(2)

AD-A276 097

Final Report N001485C0078

The attached series of reprints dating from 1985 through 1990 details the work performed with partial support from ONR under the subject contract.

In particular, via coherent effects, polarization beats were observed and the optical phase of a frequency swept pulse was measured. Using two stage pulse compression, 16 fsec, frequency tunable optical pulses were produced. New methods were introduced to reduce the wings on compressed pulses and the worlds fastest light-driven optical modulator was demonstrated. The first measurement and detailed analysis of dark pulse solitons in fibers were performed. An optical shock wave and wave-breaking were observed in the nonlinear propagation through single-mode optical fiber.

A new standard in optoelectronic performance was set with our generation and detection of subpsec electrical pulses. Subsequently, electronic shock waves were produced on coplanar transmission lines and the observations were compared in detail with theory. This work culminated in the development and application of an optoelectronic THz system. This system has been fully characterized and used to perform THz spectroscopic measurements on important electronic materials.

DTIC
ELECTE
FEB 02 1994
S

94 2 01 06 8

94-03259

93 10 8 036

Reprinted from Optics Letters, Vol. *10*, page 22, January 1985
Copyright © 1985 by the Optical Society of America and reprinted by permission of the copyright owner.

Observation of a 1.9-psec polarization beat

Joshua E. Rothenberg and D. Grischkowsky

IBM Thomas J. Watson Research Center, P.O. Box 218, Yorktown Heights, New York 10598

Received August 28, 1984; accepted October 25, 1984

We have observed polarization beats by simultaneously exciting both the D_1 (589.6-nm) and the D_2 (589-nm) lines of sodium in a vapor with a 0.4-psec resonant laser pulse. This impact excitation of both D lines produces two oscillating *macroscopic polarizations*, which interfere with each other and procedure a beat note at their difference frequency in the intensity of the light emitted from the cell. The beat period of 1.9 psec is the fastest ever observed optically.

A time-dependent beating phenomenon, which is relatively well known and has been seen in many different systems, is the so-called quantum beat.[1-6] The physical origin of this beat is an interference between indistinguishable quantum-mechanical pathways,[4] i.e., the quantum beat describes an interference between *amplitudes* that are due to different intermediate excited states (pathways) of the wave function of an individual atom or molecule evolving toward a single final state. In order to be observed with an ensemble of systems, this interference must have the same phase for each individual system. This requirement can be met by an excitation pulse that is short compared with the period of the quantum beat. A most important characteristic of the quantum beat is that it is essentially unaffected by the Doppler shift, thereby allowing quantum beats to resolve sub-Doppler atomic or molecular resonances.

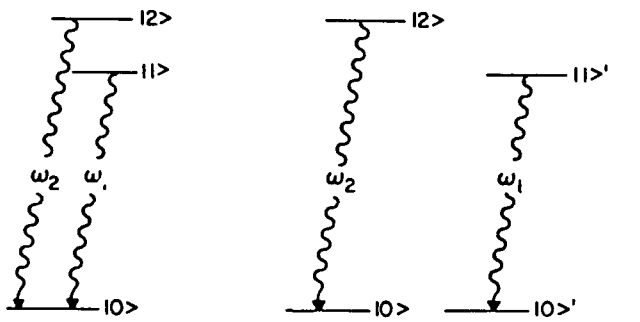

Fig. 1. Energy-level diagrams suitable for the observation of polarization beats.

In this Letter, we report the study of another type of beating phenomenon, which is understandable in purely classical terms. We have termed this phenomenon polarization beats because its origin is the interference between the *macroscopic polarizations* simultaneously excited in at least two distinct resonances by a short pulse. These resonances can be in the same or different types of atoms or molecules. For polarization beats, in contrast to quantum beats. it is the radiations from these independent polarizations at their natural frequencies that interfere with each other and produce beats at the difference frequencies. This result is a modulation in the intensity envelope emitted by the resonant system. The first experiments involving polarization beats were performed by Hartmann and Laubereau.[7]

In our experiments, we have observed a polarization beat of period 1.9 psec resulting from the interference between the D_1 and D_2 lines of sodium excited by a propagating pulse of 0.4-psec duration. This is the fastest beat observed in real time.[8] The earlier work used molecular systems, and beats slower by a factor of 8 were observed.[8] Another method with the capability of measuring (quantum) beats in the picosecond time scale is the beam-foil technique.[1]

For a simple explanation of the polarization beat, consider, as shown in Fig. 1, a three-level atom or equivalently two different types of two-level atoms (or molecules) with allowed transitions ω_1 and ω_2. A

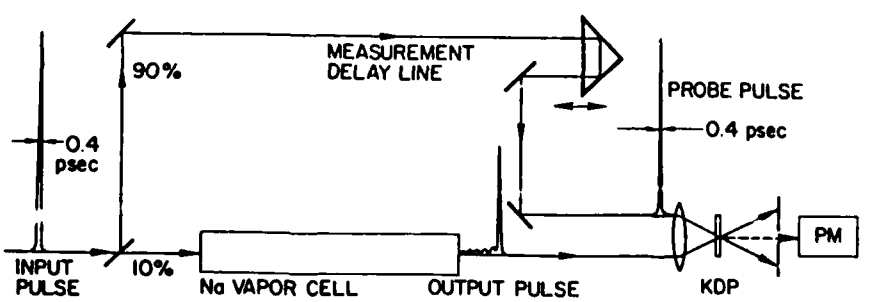

Fig. 2. Schematic diagram of the experiment.

0146-9592/85/010022-03$2.00/0 © 1985, Optical Society of America

propagating impulse excitation $E \sim \delta(\tau)$ is considered to excite both transitions simultaneously. The polarization is then given throughout the excitation region by the real part of

$$P(z,\tau) = P_1 + P_2 \propto [\mu_1^2 \exp(-i\omega_1\tau) + \mu_2^2 \times \exp(-i\omega_2\tau],$$

where z is the propagation distance, $\tau = t - z/c$ is the reduced time (which must be greater than zero), and μ_1 and μ_2 are the transition strengths. All factors common to both transitions have been deleted in this proportionality. It should be noted that since these macroscopic polarizations depend only on the reduced time τ, they are therefore phased to radiate only in the forward direction. The radiated electric field at the output of the cell ($z = L$) that is due to these phased polarizations is proportional to the real part of

$$E(L,\tau) \propto \int_0^L P(z,\tau)dz = LP(\tau),$$

or, equivalently, of

$$E(L,\tau) \propto [\mu_1^2 \exp(-i\omega_1\tau) + \mu_2^2 \exp(-i\omega_2\tau)].$$

The intensity is then given by

$$I(L,\tau) \propto (\mu_1^4 + \mu_2^4 + 2\mu_1^2\mu_2^2 \cos \Delta\omega\tau),$$

where $\Delta\omega = \omega_z - \omega_1$ is the beat frequency.

The effect described here is thus due to the interference between the macroscopic polarizations P_1 and P_2. These quantities are proportional to the off-diagonal density-matrix elements ρ_{01} and ρ_{02} for a single three-level system, and ρ_{01}' and ρ_{02} for two independent two-level systems. These elements decay with the combined homogeneous and inhomogeneous transverse relaxation rate $1/T_2 + 1/T_2^*$, and therefore the spectral resolution of the polarization beat is limited to the Doppler linewidths. This situation is to be contrasted with the case of a quantum beat whose strength is proportional to ρ_{12}, which exists only for the three-level system. This term is responsible for the sublevel coherence in the case of unresolved states under the Doppler width and is not subject to the inhomogeneous relaxation rate $1/T_2^*$ but relaxes according to $1/T_2$, the homogeneous linewidth.

The pertinent experimental configuration is shown in Fig. 2. Initially pulses of 7-psec duration were obtained from a 4-MHz-rate, cavity-dumped, synchronously pumped dye laser. This laser was tuned to 589.2 nm (between the sodium D lines) and had a linewidth of 2 cm^{-1}. These pulses were then sent through an optical-fiber pulse compressor[9] to produce pulses of width less than 0.4 psec (assuming $sech^2$ pulse shapes) and bandwidths of 125 cm^{-1}. These 0.4-psec pulses were the pulses used in our experiment. As shown in the figure, the compressed pulses were divided into two beams by a 10–90% beam splitter. The weak beam was sent through the sodium cell; its peak input power was 350 W, and the beam diameter in the cell was 0.3 cm, corresponding to an input-pulse area $\theta = \pi/150$ rad. The sodium cell consisted of a 50-cm long, 2.5-cm-diameter Pyrex glass cell containing an excess of 99.95% pure sodium metal transferred under vacuum from a sealed ampule. The cell temperature was measured by thermocouples in contact with the glass, and the absorption was calculated from the corresponding atomic density. The output-pulse envelopes from the sodium

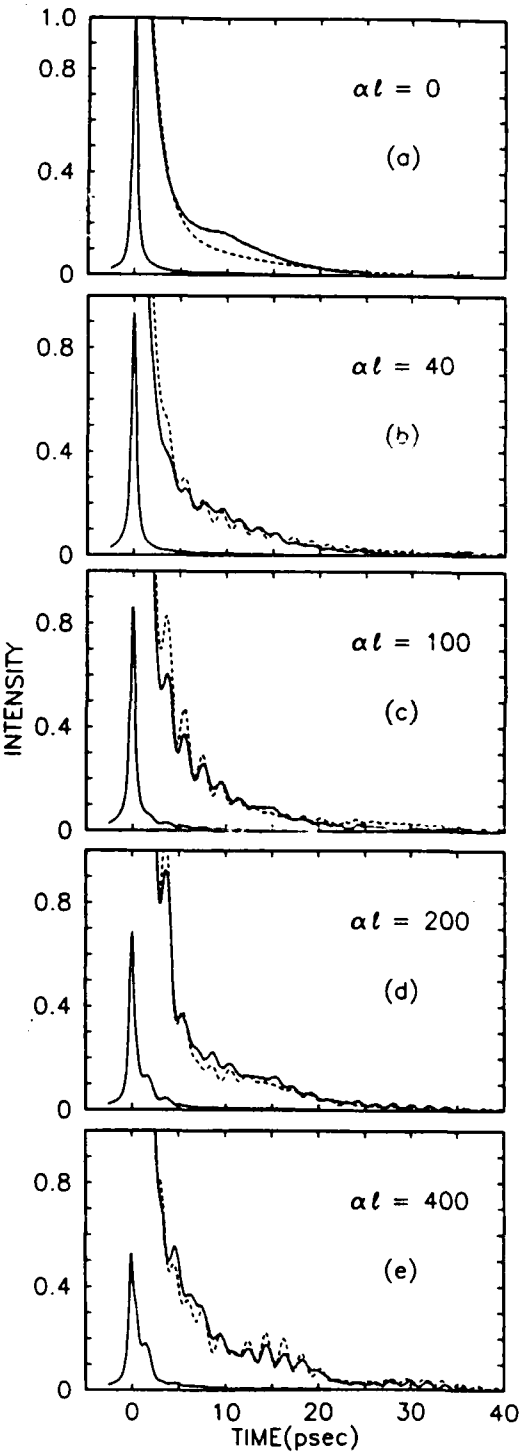

Fig. 3. Observed polarization beats (solid curves) compared with the numerical calculations (dashed curves) from the sodium-vapor cell with the indicated optical density αl. The scale for the complete output pulses is 0 to 1.0, and the trailing edges are shown on the 20× expanded vertical scale (0 to 0.05).

A-1

cell were measured with better than 0.4-psec resolution by cross correlating with the strong beam of compressed pulses by noncollinear generation of second-harmonic light in a 0.3-mm-thick KDP crystal. Thus this cross correlation represents an optical sampling measurement with 0.4-psec resolution. The second-harmonic light was monitored by a photomultiplier connected directly to a signal averager, which was synchronized with the delay setting of the probe pulses as controlled by a computer-driven stepping motor. A typical scan of the probe delay took 100 sec, and 20 such scans were averaged.

The input pulses to the sodium cell had a bandwidth exceeding the 17.1-cm^{-1} separation of the D_1 and D_2 lines by almost an order of magnitude. Also, the pulses were almost five times shorter than the period of this difference frequency. Hence we expect an experimental manifestation of the polarization beats caused by the impact excitation of the short pulse.

Figure 3 (solid curves) shows the experimental results. The entire output pulses are shown on a scale of 0 to 1.0, where the input pulse [Fig. 3(a), $\alpha l = 0$] is normalized to unity. We also show the trailing edges of the output pulses on a 20× expanded vertical scale. Figure 3(a) shows the autocorrelation of the input pulse. The observed shoulder likely represents a small satellite to the main pulse. The good signal-to-noise ratio of approximately 10^4 illustrates the sensitivity and the dynamic range of our cross-correlation technique of measuring the output-pulse intensity. Figures 3(b)–3(e) are cross correlations of the output pulse from the sodium cell with the probe pulse for increasing optical density in the cell. The peak value αl of the optical density of the 589-nm line is given in each figure. As the data demonstrate, polarization beats are indeed observed with a peak-to-peak strength typically 1/500 that of the excitation pulse. The period of 1.9 psec corresponds to the 513-GHz splitting of the D_1 and D_2 lines. This beat is the fastest ever to be observed in real time. The strength of the beat increases with αl up to about $\alpha l = 100$, and thereafter the beat continues to become stronger but also develops a more complicated amplitude modulation. This is because the input pulse is not a delta function and because of the concomitant formation of the 0π pulse.[10]

The experiment is compared (in Fig. 3) with the results of a numerical calculation based on linear dispersion theory following the procedure given in Ref. 10. The input-pulse envelope used in the calculations was obtained by fitting the experimental autocorrelation [Fig. 3(a)] with a numerically generated pulse. The experimentally unknown phase structure of the pulse was taken to be a linear chirp to account for the large experimentally observed bandwidth. This chirp was varied for the best fit and represented the only adjustable parameter in the calculation. The same chirp was used for all the theoretical curves shown in Fig. 3. The theoretical predictions show general agreement with the experimental observations. The period of the beat is well defined; its predicted phase and amplitude agree well with the observations. However, the agreement is not quantitative. We believe that the discrepancies are due to the unknown phase structure of the input pulse.

In conclusion, we have observed the polarization beat that is due to the interference of the induced macroscopic polarizations from the D_1 and D_2 lines in sodium. This beat is the fastest ever observed, and the experimental results are in good qualitative agreement with the theoretical predictions.

We would like to acknowledge the suggestion of the term polarization beats and many other useful comments on this manuscript by A. C. Balant. The careful reading of this manuscript by J. J. Wynne was most helpful.

This research was partially supported by the U.S. Office of Naval Research.

References

1. H. J. Andrä, Phys. Rev. Lett. **25**, 325 (1970).
2. S. Haroche, J. A. Paisner, and A. L. Schawlow, Phys. Rev. Lett. **30**, 948 (1973).
3. T. W. Ducas, M. G. Littman, and M. L. Zimmerman, Phys. Rev. Lett. **35**, 1752 (1975).
4. S. Haroche, in *High-Resolution Laser Spectroscopy*, K. Shimoda, ed. (Springer-Verlag, New York, 1976), p. 256.
5. W. Lange and J. Mlynek, Phys. Rev. Lett. **40**, 1373 (1978).
6. G. Leuchs, S. J. Smith, E. Khawaja, and M. Walther, Opt. Commun. **31**, 313 (1979).
7. H.-J. Hartmann and A. Laubereau, Opt. Commun. **47**, 117 (1983); J. Chem. Phys. **80**, 4663 (1984).
8. A beat of 1.9 psec that is due to the D_1 and D_2 lines of sodium was also observed recently with an incoherent echo technique [T. Yajima, Institute for Solid State Physics, University of Tokyo, Roppongi, Minato-ku, Tokyo 106, Japan (personal communication)].
9. B. Nikolaus and D. Grischkowsky, Appl. Phys. Lett. **42**, 1 (1983).
10. J. E. Rothenberg, D. Grischkowsky, and A. C. Balant, Phys. Rev. Lett. **53**, 552 (1984).

Reprinted from Journal of the Optical Society of America B, Vol. 2, page 626, April 1985
Copyright © 1985 by the Optical Society of America and reprinted by permission of the copyright owner.

626 J. Opt. Soc. Am. B/Vol. 2, No. 4/April 1985

Measurement of the phase of a frequency-swept ultrashort optical pulse

Joshua E. Rothenberg and D. Grischkowsky

IBM Watson Research Center, P.O. Box 218, Yorktown Heights, New York 10598

Received December 10, 1984; accepted December 20, 1984

We show theoretically and confirm experimentally that, by propagating a frequency-swept ultrashort pulse through an ensemble of two-level systems, it is possible to measure the time-dependent relative phase of the pulse with respect to that of the impact-excited oscillating resonant polarization. The phase is obtained from the intensity modulation of the pulse as measured by a cross-correlation technique.

1. INTRODUCTION

In the field of ultrafast optics and optical interactions, the primary emphasis has been on the generation of the ultrashort laser pulses. One line of development has led to the colliding-pulse, passively mode-locked ring dye laser (CPM laser),[1] which is capable of producing 55-fsec pulses[2]; a modified compensated design can produce 28-fsec pulses.[3] Another effort has led to the development of the optical-fiber pulse compressor,[4] which has demonstrated pulse compressions of orders of magnitude.[5] At the present time, the shortest pulses are obtained by combining these two methods, i.e., by sending the pulses from the CPM laser through the optical-fiber pulse compressor. The first application of this powerful combination was by Shank *et al.*,[6] who compressed 90-fsec amplified CPM laser pulses to 30 fsec. Exactly two years later, Fujimoto *et al.*[7] compressed 60-fsec amplified CPM laser pulses to 16 fsec. The most recent result is that of Halbout and Grischkowsky,[8] who compressed 110-fsec amplified CPM laser pulses to 12 fsec.

An associated problem that occurs with the generation of such short pulses is their complete characterization, i.e., the determination of the time-dependent amplitude and phase. All the work cited above has used background-free, noncollinear generation of second-harmonic light in thin KDP crystals to obtain autocorrelation measurements of the intensity of the ultrashort pulses. The main problem with autocorrelation is that the measurement does not give complete information concerning the actual pulse shape. The measurement is always symmetric, and the quoted pulse widths must assume a pulse shape. A cross-correlation measurement of the intensity[4,9] would be far superior, if a short enough interrogating pulse were available. Although spectral measurements of the ultrashort pulses were made, these measurements could not determine the time-dependent phase $\Phi(t)$, which is nonzero if the pulse is not transform limited. An alternative technique, the "interferometric autocorrelation" of Diels *et al.*,[10] gives information about the pulse shape and the phase modulation by an iterative fitting of the intensity autocorrelation, the interferometric autocorrelation, and the pulse spectrum. A clearly important manifestation of $\Phi(t)$ is in the intermediate stage of the optical-fiber pulse compressor,[4-8] where the pulse emerging from the fiber is frequency swept (chirped). This frequency sweep is crucial to the successful compression of the pulse by the following grating pair (dispersive delay line). Until now, it has not been possible to measure this ultrafast frequency sweep directly. Only indirect evidence has been obtained, i.e., the degree to which the pulse was compressed by the grating pair and the agreement between the experimental and calculated frequency spectra.

In this paper, we report measurements and theoretical calculations that describe a new and powerful method of measuring $\Phi(t)$ and thereby obtaining the instantaneous frequency of an ultrashort optical pulse. For this method the frequency-swept pulse is passed through a resonant vapor (ensemble of two-level systems), and the consequent time-dependent intensity modulation of the output pulse from the cell is measured by cross correlation with a shorter probe pulse. A simple approximate model that describes our method and observations quite accurately is as follows. When the frequency sweeps through the resonance of the two-level systems, the ensemble is excited in the impulse limit and thereafter oscillates with the resonance frequency ω_0. The resulting macroscopic polarization, which decays with the inhomogeneous lifetime, radiates an electric field at the resonant frequency that interferes with the propagating pulse. This self-induced heterodyne signal provides the measure of the time-dependent relative phase $\Phi(t)$ between the propagating pulse and the oscillating polarization. From knowledge of $\Phi(t)$, the instantaneous frequency is obtained. In the following sections, we present examples showing how accurately this simple model describes the more complex and complete calculations of linear dispersion theory. We show the theoretical basis of the model and discuss its limitations. Finally, we describe an experiment utilizing a sodium-vapor cell, for which the experimental results are in good agreement with the exact theory and for which the main features are well described by the simple model.

2. THEORETICAL DEMONSTRATION OF THE SIMPLE MODEL

First we calculate, using linear dispersion theory, the output pulses from a resonant vapor cell for four different input pulses with differing frequency sweeps. We test the simple

0740-3224/85/040626-08$02.00 © 1985 Optical Society of America

model by analyzing the beats on the output pulses in order to obtain the time-dependent phase $\Phi(t)$ relative to the single-frequency radiation from the excited resonant vapor. From these $\Phi(t)$ curves, we obtain the time-dependent relative instantaneous frequency $\Omega_i(t) = d\Phi/dt$. The absolute instantaneous frequency is then $\omega_o + \Omega_i$. These results are compared with the known $\Phi(t)$ and $\Omega_i(t)$; the excellent agreement shows the high accuracy of the simple approximate model.

In Fig. 1 we show the four input pulses that we analyze. Figure 1(a) represents the flat-topped linearly frequency-swept pulse typical of that from the optical fiber utilized in the pulse compressor. Figure 1(b) is the same pulse, but with a sawtooth frequency modulation chosen to test the simple model better. Figure 1(c) is a $(\text{sech})^2$ pulse with a linear frequency sweep, and Fig. 1(d) is the same $(\text{sech})^2$ pulse with a frequency sweep proportional to the time derivative of the pulse intensity. This frequency sweep corresponds to that produced by self-phase modulation with no accompanying reshaping of the pulse. The time $t = 0$ in Fig. 1 indicates when the instantaneous frequency is equal to the resonant frequency of the two-level systems. At resonance, the relative instantaneous frequency $\Omega_i = 0$. These pulses have the extensive frequency sweep required for ultrashort pulse compression.[6-8]

The calculation of the output pulse from the vapor cell of a two-level system proceeds as outlined in our earlier paper[9] and is based on linear dispersion theory following the procedure of Crisp.[11] We use the Voigt profile for the absorption coefficient and the plasma dispersion function for the index of refraction of the vapor of two-level systems. With the electric field of the input pulse written in the form

$$E(z = 0, t) = \mathrm{Re}[\mathcal{E}(0, t)\exp(-i\omega_o t)], \tag{1}$$

its spectrum is given by

$$\tilde{\mathcal{E}}(0, \Omega) = \frac{1}{2\pi}\int_{-\infty}^{\infty} \exp(i\Omega t)\mathcal{E}(0, t)\mathrm{d}t. \tag{2}$$

Thus, after a propagation distance z, the output field is given by

$$E(z, t) = \mathrm{Re}\left\{\exp(-i\omega_0 t)\int_{-\infty}^{\infty} \tilde{\mathcal{E}}(0, \Omega)\exp(-i\Omega t) \times \exp(-\alpha z/2)\exp[inz(\Omega + \omega_0)/c]\mathrm{d}\Omega\right\}, \tag{3}$$

where α and n are the frequency-dependent absorption coefficient and the index of refraction, respectively, and ω_o is both the transition frequency and the resonant laser carrier frequency. In our calculations, we assume that the absorption coefficient on line center is 4 cm^{-1}, the cell length $z = 50$ cm, and the Doppler linewidth 0.06 cm^{-1}. These are reasonable values to obtain experimentally. Performing the numerical evaluations indicated in Eq. (3) for the four input pulses of Fig. 1, we obtain the output pulses shown in Fig. 2. The time coordinate for these output pulses is the reduced time $\tau = t - z/c$, where $z = 50$ cm at the cell output. The oscillations on the output envelopes are surprisingly strong and well defined, and the changing periods of the beats are readily observed. Of course, an ultrashort probing pulse must be used to measure these oscillations.

The simple model enables one to understand these oscillations in the intensity and, in fact, to use them to determine the time-dependent phase of the input pulse. There are two contributions to the output field E_{out} from the resonant vapor, i.e.,

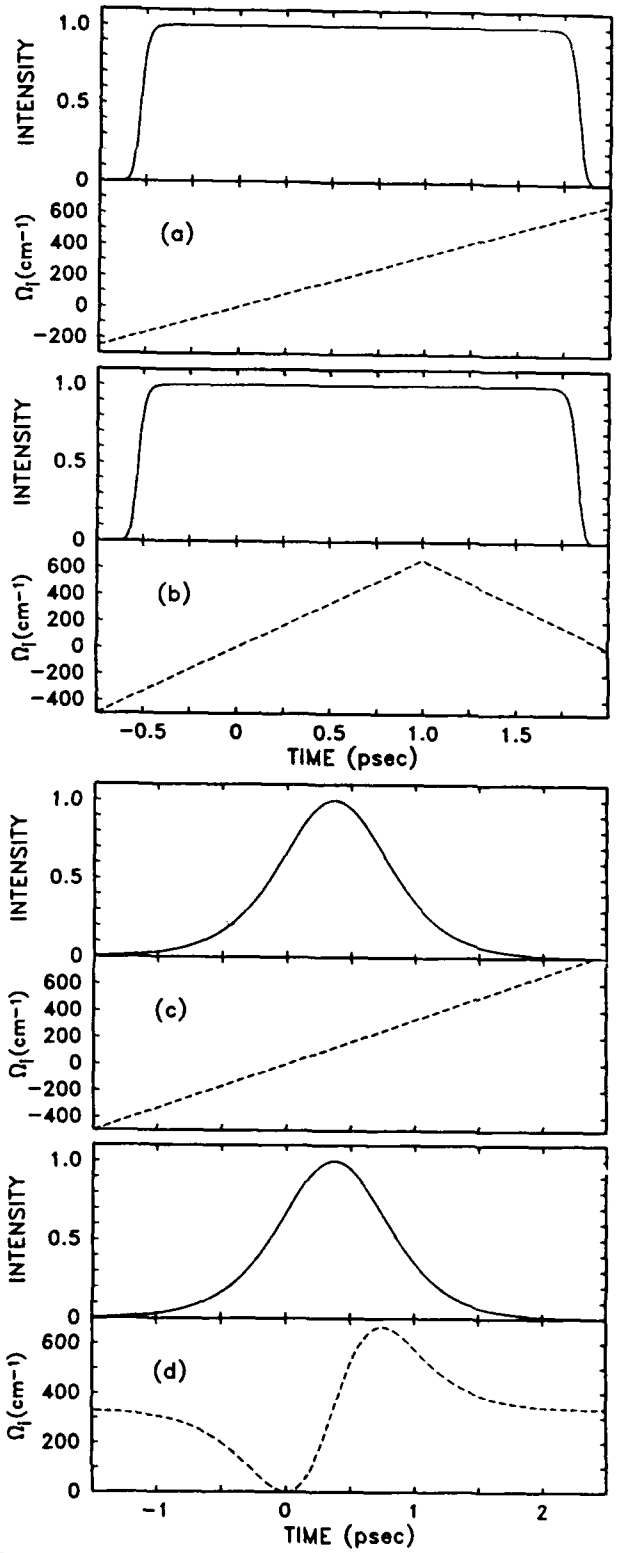

Fig. 1. Input pulses showing intensity (solid lines) and relative instantaneous frequency Ω_i (dashed lines) versus time. Relative instantaneous frequency, given in wave numbers (cm^{-1}), is equal to the resonant frequency of the two-level medium for $\Omega_i = 0$ and $t = 0$.

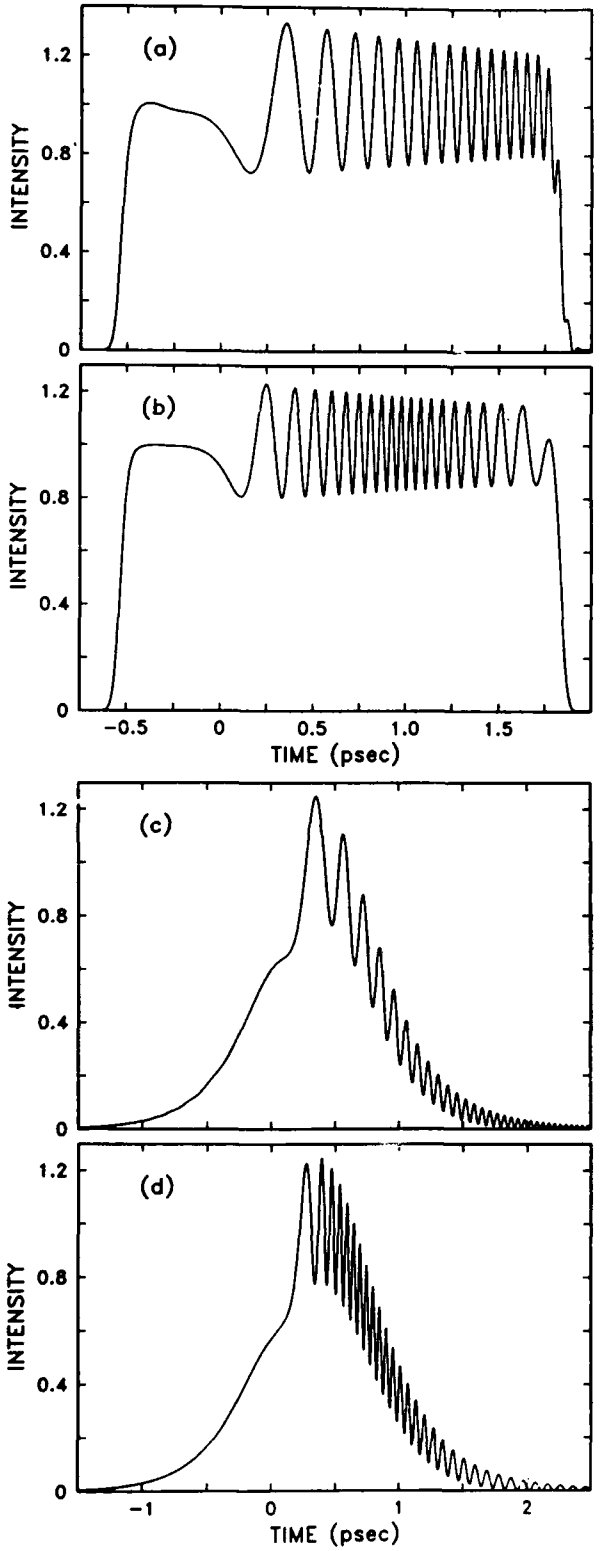

Fig. 2. Calculated output pulses, corresponding to the input pulses of Fig. 1, versus reduced time.

$$E_{out} = E_{in} + E_{rad}, \tag{4}$$

where E_{in} is the input field,

$$E_{in} = \mathcal{E}_0 \exp[-i(\omega_o \tau + \Phi(\tau) + \beta)], \tag{5}$$

β is an arbitrary phase angle that changes from pulse to pulse, τ is the reduced time, and E_{rad} is the field radiated by the excited polarization at the resonant frequency ω_o:

$$E_{rad} = a\mathcal{E}_0 \exp[-i(\omega_o \tau + \beta)]. \tag{6}$$

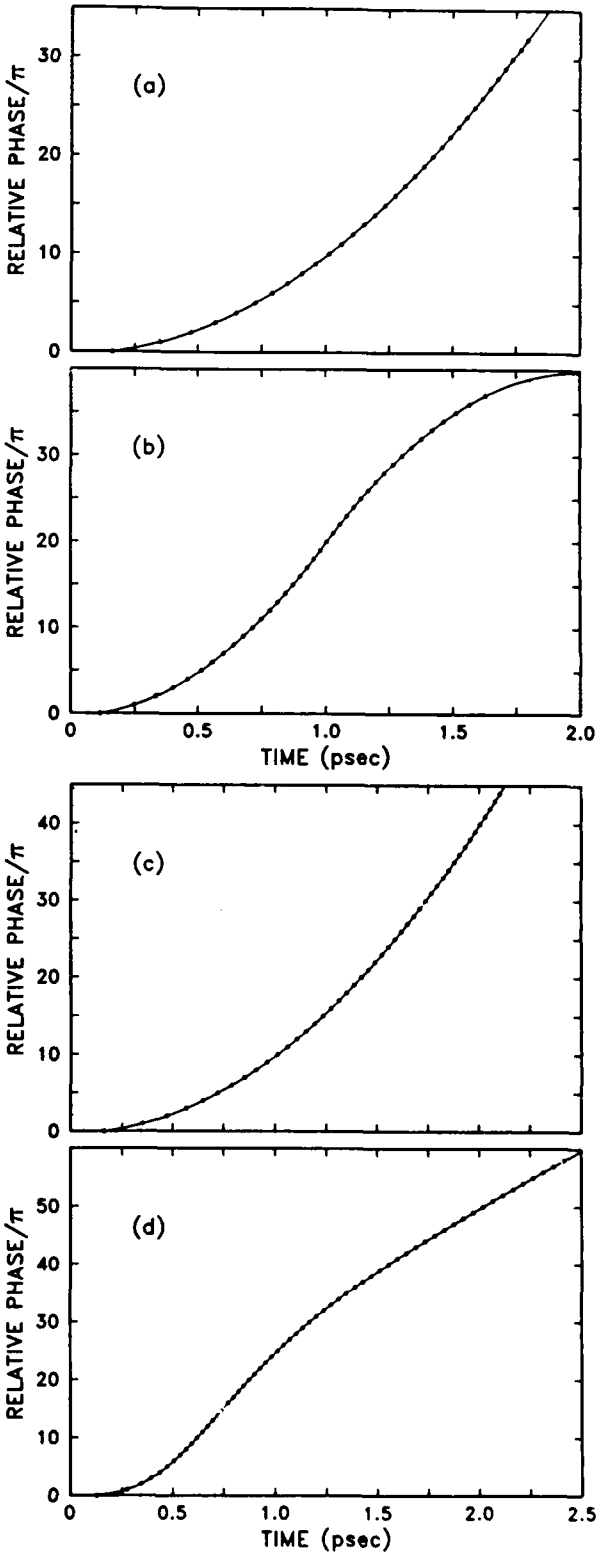

Fig. 3. Measured relative phase $\Phi(t)$ (dots) determined by counting the maxima and minima on the output pulses of Fig. 2 and $\Phi(t)$ (solid lines) from the input pulses of Fig. 1.

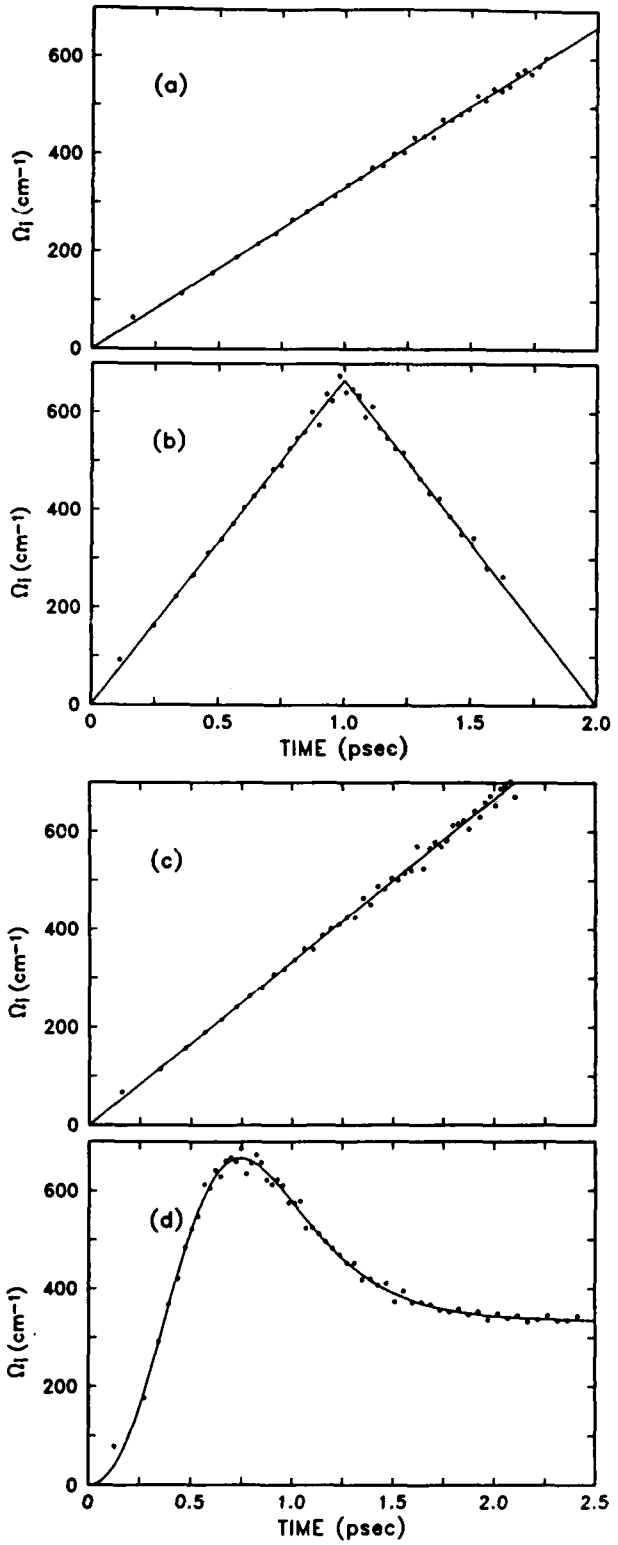

Fig. 4. Relative instantaneous frequencies Ω_i (dots) obtained from Fig. 3 and Ω_i (solid lines) determined from input pulses of Fig. 1.

In this simple picture, $\mathcal{E}_0$ is taken to be approximately constant over the time extent considered. Here, $|a|^2 \ll 1$ is a measure of the size of the excitation of the polarization and is assumed to have the form of a step function at $\tau = 0$. Consequently, it is apparent that the two-level systems are phased by the propagating excitation pulse to radiate only in the forward direction and that the output intensity I_{out} is proportional to

$$I_{out} \propto |a \exp[-i(\omega_o\tau + \dot{\rho})] + \exp[-i(\omega_o\tau + \Phi(\tau) + \beta)]|^2 = |a + \exp[-i\Phi(\tau)]|^2. \quad (7)$$

A most important feature of expression (7) is that the arbitrary phase angle β disappears from the oscillation. Consequently, there is no need for phase coherence from pulse to pulse, as would be the case for interference between different sources (hence the term "self-induced" heterodyne).

Expression (7) shows that successive extrema in I_{out} will be separated by $\Delta\Phi = \pi$, and therefore a simple counting procedure can determine the phase of the input pulse relative to the field radiated by the two-level systems for $\tau > 0$.[12] For example, we consider the first minimum to have $\Phi = 0$, the first maximum to have $\Phi = \pi$, etc. We note that a single resonance does not permit the determination of the *sign* of the phase shift, but that compressibility with a grating pair or multiple resonances can give this information. Figure 3 shows the relative phase $\Phi(t)$ obtained in this manner for each of the pulses of Fig. 2. The data points represent the phase obtained by direct counting of the extrema, and the solid line is the actual input phase of the respective pulses. The agreement between the phase obtained from the simple *approximate* model and the actual phase is nearly exact. In Fig. 4 we show the instantaneous frequencies $\Omega_i(t)$ (points) obtained by numerically differentiating the data points for $\Phi(t)$ in Fig. 3 with respect to time. These results are compared with the actual input instantaneous frequencies Ω_i shown by the solid lines in Fig. 4. As can be seen, the agreement between Ω_i obtained from the simple model and Ω_i of the input pulses is excellent. Thus, to a remarkable accuracy, this simple model approach allows one to determine the instantaneous frequency of a frequency-swept pulse.

We now consider the magnitude of the oscillations. The observed peak-to-peak excursion of $I_{out} \approx 0.4\, I_{in}$ requires that $|a| \approx 0.1$ and $|a|^2 = 0.01$. Therefore the resonant system appears to be radiating at a rate equal to 1% of the power in the propagating pulse. However, in terms of the actual absorbed energy, it is to be remembered that the absorption linewidth of 0.06 cm^{-1} is less than 1/10,000 the ~600-cm^{-1} linewidths of the input pulses. This apparent discrepancy can be understood by considering the phase shift that is due to the two-level vapor. For the case considered here ($\lambda = 5890$ Å, $z = 50$ cm, and a peak absorption of 4 cm^{-1}), we find that the detuning at which the phase shift is less than $\lambda/10$ is approximately 3 cm^{-1}. Hence the fractional bandwidth over which the pulse is strongly affected by the dispersion of the medium is orders of magnitude larger than that affected by the absorption. *Consequently, it is not the absorption of the resonance line that is responsible for the beat but rather the dispersion.*

In order to confirm the above conclusion more quantitatively, we have calculated $|a|$ to first order for a two-level Lorentzian line shape and a linearly frequency-swept pulse [$\Omega_i(t) = bt$ and $\Phi(t) = bt^2/2$]. The result is given by

$$|a| \propto N\mu^2 z/\sqrt{b}, \quad (8)$$

where N is the number density and μ is the two-level dipole moment. The magnitude of $|a|$ is independent of the Lo-

rentzian linewidth γ and is therefore solely dependent on the dispersion. This result requires that $\gamma^2 \ll b$ [for our examples $(\gamma^2/b) \sim 10^{-7}$]. To prove this independence of absorption further, we set α equal to zero in the complete calculation of Eq. (3) but left n the same. With this modification, the calculated output pulses were essentially unchanged.

Finally, we note that the size of the oscillations in Fig. 2 is seen to decay by a significant amount [most clearly in the flat-topped cases of Figs. 2(a) and (b)] on a time scale of only ~2 psec. This cannot be attributed to the decay of the excited polarization (for our simulation this decay time is approximately 100 psec) but is due to the effect of propagation on the resonant radiation emitted from the excited polarization. The effect of propagation on this impact-induced resonance radiation has been shown to lead to the so-called 0π pulse.[9] It is the interference of this 0π pulse with the input pulse that leads to the oscillations of Fig. 2, and the decay of these oscillations is simply the initial decay seen in the formation of the 0π pulse.[11] In fact, at higher density the oscillations of Fig. 2 are seen to vanish and reappear with opposite phase, in exact analogy with the 0π pulse.

3. EXPERIMENTAL DEMONSTRATION

The experimental arrangement is indicated schematically in Fig. 5. The 1.5-kW peak-power, 7-psec-duration input pulses with 2-cm^{-1} linewidths were obtained from a 4-MHz-rate, cavity-dumped, synchronously pumped dye laser. These pulses were sent through a 10-m-long, single-mode optical fiber. The coupling efficiency into the fiber was typically better than 50%. The pulses from the fiber were temporally broadened to 25-psec duration and were frequency broadened to 150 cm^{-1}. As was discussed earlier,[4,5] the pulses emerging from the fiber were frequency swept (chirped) owing to the combined effects of nonlinear self-phase-modulation and linear group-velocity dispersion. The schematic shows that 10% of the beam of frequency-swept pulses emerging from the fiber was reflected by the beam splitter and passed through the 50-cm-long Na-vapor cell. The other 90% traversed the dispersive delay line, consisting of a diffraction grating and a 90° prism. This delay line is equivalent to the more usual diffraction grating pair. The separation between the prism

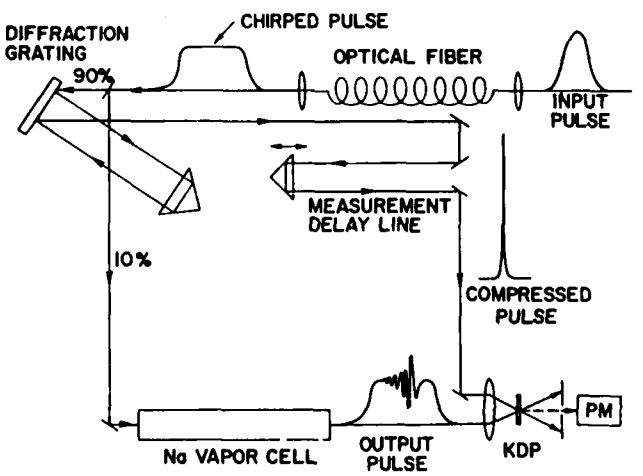

Fig. 5. Schematic diagram of the experimental apparatus. PM, photomultiplier tube.

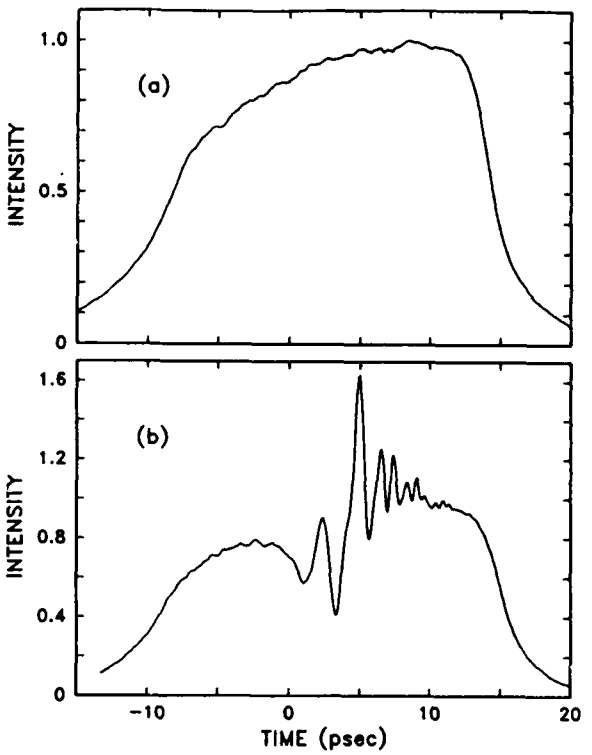

Fig. 6. (a) Measured cross correlation (resolution, 0.4 psec) of the input pulse to the Na cell. (b) Measured cross correlation of the output pulse (solid line) from the Na cell.

and the diffraction grating was adjusted to obtain the minimum compressed pulse width, which for our conditions was always less than 400 fsec. The 2.5-cm-diameter Pyrex glass cell contained an excess of 99.95% pure Na metal. The cell temperature was measured by thermocouples, and the absorption was calculated from the corresponding atomic number density. The output-pulse envelopes from the cell were measured with better than 0.4-psec resolution by cross correlating with the beam of compressed probe pulses by noncollinear generation of second-harmonic light in a 0.3-mm-thick KDP crystal. The second-harmonic light was monitored by a photomultiplier connected directly to a signal averager, which was synchronized with the delay setting of the probe pulses as controlled by a computer-driven stepping motor. A typical scan of the probe delay took 100 sec, and 20 such scans were averaged.

The experimental results are shown in Fig. 6, for which the Na-cell temperature was 160°C, corresponding to an absorption of $\alpha z = 100$ at the peak of the 5890-Å line. In Fig. 6(a), the input pulse to the Na cell is displayed, while Fig. 6(b) shows the resulting output pulse. Strong oscillations, well resolved in time and with an excellent signal-to-noise ratio, are seen on the output pulse, indicating the beating between the frequency swept pulse and the radiation emitted by the Na vapor. The observation of these oscillations demonstrates their independence of the arbitrary phase angle β of the input pulse. Unfortunately, both the D_1 (5896-Å) and the D_2 (5890-Å) lines are excited by the pulse, so that the Na vapor behaves as a vapor of two types of two-level systems whose resonant frequencies differ by 6 Å. Thus the observed beating (in terms of our simple model) is due to the fields radiated by both sets of oscillators. Consequently, after the frequency

sweeps over the resonance of the first set of oscillators, a simple beat is obtained with all the features as described in Section 2, until the sweeping frequency excites the second set of oscillators. Then, two beats of different frequency and amplitude are simultaneously present. This complicated situation makes the determination of $\Phi(t)$ for the propagating pulse much more difficult.

However, the calculation of the output pulse using linear dispersion theory still follows the same procedure as before. The input pulse used in the calculation has the experimentally determined time-dependent intensity shown in Fig. 6(a) and, for simplicity and in agreement with our previous considerations, is considered to have a linear frequency sweep consistent with the measured bandwidth. With this as the input pulse and knowing the absorption and dispersion of the two Na lines, we use the procedure of Eq. (3) to calculate the output pulse indicated in Fig. 7(a). The calculated output pulse has the dramatic and rapid time dependence illustrative of the two lines beating simultaneously and of the large frequency sweep of the input pulse. Unfortunately, as can be seen, the calculated time dependence becomes more rapid than our resolution limit of 0.4 psec (the probing pulse width) at approximately $\tau = 10$ psec, and the subsequent high-frequency detail cannot be observed. In order to compare with experiment, we must calculate the cross correlation of Fig. 7(a) with the probing pulse. The result (dashed line) is compared with our measurement in Fig. 7(b). As can be seen, the agreement between theory and experiment (solid line) is excellent. The oscillatory structure is predicted with precision, and the amplitudes agree well with the observation.

To clarify the role that the two lines in Na play in the observed output intensity, we use the computer to simulate the propagation as if each line were present alone. The results for the output pulse intensities (no cross correlations) are shown in Figs. 8(a) and 8(b) for the D_1 and D_2 lines, respectively. As can be seen, the characteristic oscillatory structure that is due to the D_2 line is shifted later in time with respect to the structure that is due to the D_1 line. This is a manifestation of the time it takes the instantaneous frequency to sweep from the D_1 to the D_2 line. In addition, it is seen that the relative strength of the D_2 line (twice that of the D_1 line) leads to a proportionately stronger oscillatory structure. The sum of the fields that lead to the output pulses of Figs. 8(a) and 8(b) then includes the contributions from both D lines and results in the output intensity of Fig. 8(c), which is the same result as the calculation of Fig. 7(a).

Even with the complications introduced by the presence of two resonance lines, we can still apply the counting proce-

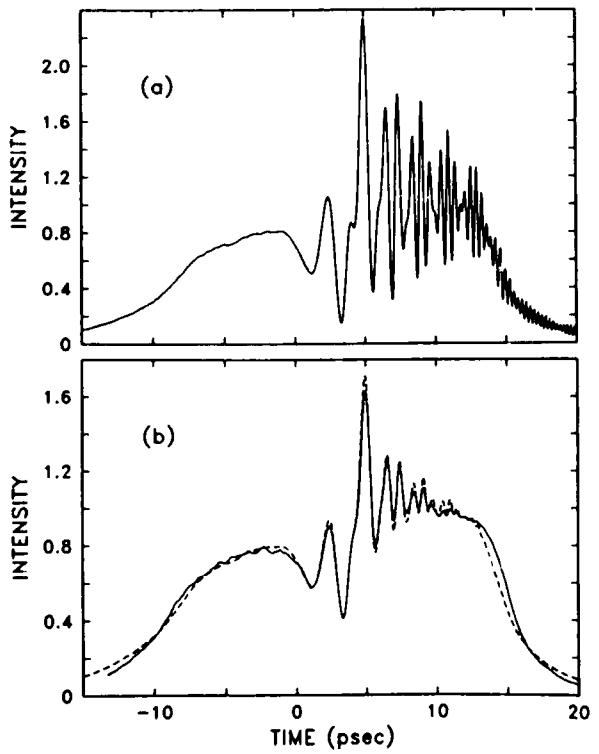

Fig. 7 (a) Calculated output pulse from the Na cell. (b) Measured cross correlation of the output pulse (solid line) compared with the cross correlation of the calculated pulse (dashed line), with a 0.4-psec probing pulse.

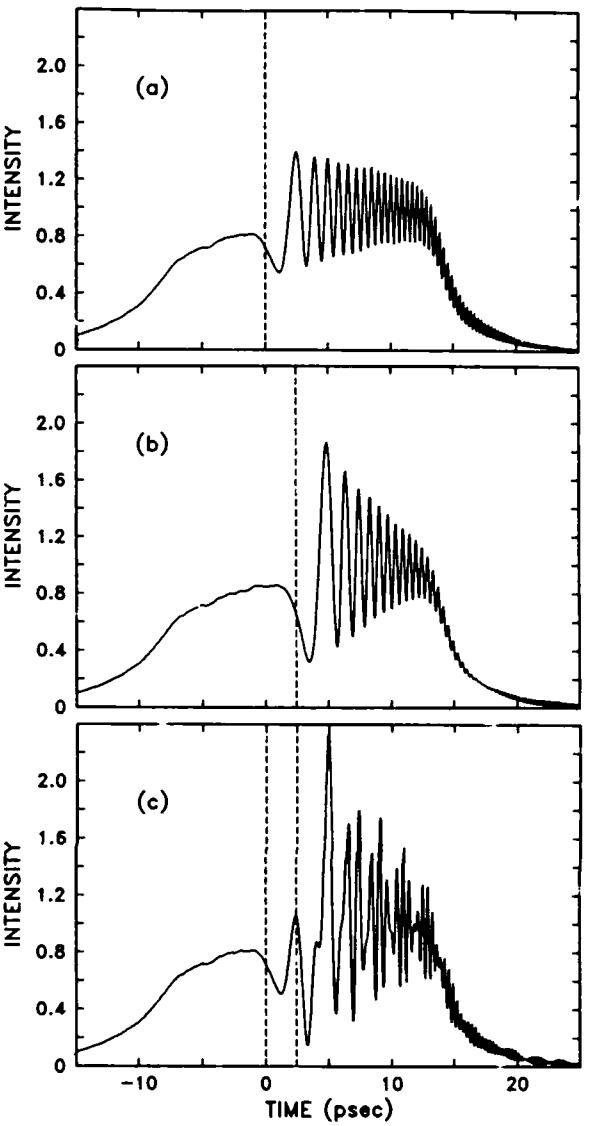

Fig. 8. (a) Calculated output pulse from the Na cell assuming that only the D_1 line is present. (b) Calculated output pulse assuming that only the D_2 line is present. (c) Calculated output pulse obtained by summation of the effects of the D_1 and D_2 lines. The dashed lines indicate when the frequency of the pulse is resonant with the D lines.

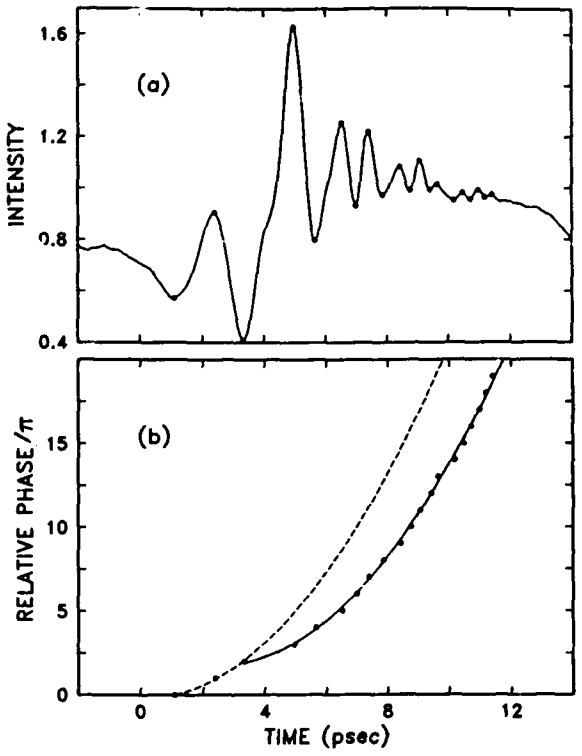

Fig. 9. (a) Measured output pulse from the Na cell shown on an expanded scale with the maxima and minima marked by dots. (b) Relative phase $\Phi(t)$ obtained from direct counting of the maxima and minima (dots) in (a). The dashed curve is the phase expected from a linearly swept pulse relative to the D_1 line, and the solid curve relative to the D_2 line.

dure for the simple model described in Section 2 to the observed output pulse [Fig. 9(a)] to determine the phase of the input pulse. The results are shown as the points in Fig. 9(b). The dashed curve is the quadratic phase (i.e., from a linear frequency sweep) that one would expect relative to the D_1 line radiation, and the solid curve is relative to the D_2 line radiation. As can be seen from the figure, the first three points up to the excitation of the D_2 line fall on the former curve, whereas the points occurring after the excitation of the D_2 line fall close to the latter curve. Although both sets of oscillators are radiating during the latter period, because the D_2 excitation is much stronger than the D_1 excitation, the location of the extrema are nearly predicted by ignoring the D_1 excitation. A close examination of Fig. 9(b) reveals that, in fact, the D_1 line only acts to perturb the location of these extrema periodically (with a 1.9-psec period) by a small amount. However, as the agreement of Fig. 9(b) shows, even for this more complicated case it is possible to determine the relative phase $\Phi(t)$ for the input pulse. Indeed, the good agreement here and in Fig. 7(b) has verified that this pulse had a linear frequency sweep.

A final comment concerning the high-frequency intensity modulation obtainable with this technique is in order here. It should be possible by nonlinear optical techniques (optical rectification) to eliminate the carrier frequency from the output pulses. These pulses could then provide phase-coherent, frequency-swept pulses well into the high-terahertz frequency range. This situation would permit an entirely new approach to spectroscopy and applications in this frequency range, where currently there are no suitable radiation sources. The pioneering demonstration of these ideas has just been reported by Auston *et al.*,[14] who generated single-cycle terahertz waves derived from the Čerenkov radiation from 100-fsec laser pulses.

4. SUMMARY

We have theoretically explained and experimentally demonstrated a new method of determining the time-dependent relative phase of frequency-swept ultrashort optical pulses. The method is based on the frequency-swept pulses impact exciting a vapor of two-level systems. The phase of the pulses is determined relative to the subsequent oscillating polarization by a simple counting of the maxima and minima in the interference between the radiation emitted by the two-level vapor and that of the optical pulse. This interference is manifested by strong beats in the intensity of the output pulse from the vapor. In fact, this modulation is more than 10 times larger than that expected from simple absorbed energy arguments. We have explained this extraordinary strength by showing that the dispersion of the vapor is responsible for the modulation. The observed intensity pattern (interference in the time domain) is independent of the initial phase angle of the input pulse. Besides the fact that this feature makes our observations possible, it should also allow for the generation of phase-coherent terahertz pulses.

ACKNOWLEDGMENT

This research was partially supported by the U.S. Office of Naval Research.

REFERENCES

1. R. L. Fork, B. I. Greene, and C. V. Shank, "Generation of optical pulses shorter than 0.1 psec by colliding pulse mode locking," Appl. Phys. Lett. 38, 671 (1981).
2. See, for example, J.-M. Halbout and C. L. Tang, "Generation of 55-fsec optical pulses," IEEE J. Quantum Electron. QE-19, 487 (1983); W. Dietel, J. J. Fontaine, and J. C. Diels, "Intracavity pulse compression with glass: a new method of generating pulses shorter than 60 fsec," Opt. Lett. 8, 4 (1983); see also Ref. 7.
3. J. A. Valdmanis and R. L. Fork, "Generation of optical pulses shorter than 30 fsec in a laser-balancing passive mode-locking with soliton-like pulse shaping," J. Opt. Soc. Am. A. 1, 1337(A) (1984).
4. H. Nakatsuka, D. Grischkowsky, and A. C. Balant, "Nonlinear picosecond-pulse propagation through optical fibers with positive group velocity dispersion," Phys. Rev. Lett. 47, 910 (1981).
5. B. Nikolaus and D. Grischkowsky, "90-fs tunable optical pulses obtained by two-stage pulse compression," Appl. Phys. Lett. 43, 228 (1983).
6. C. V. Shank, R. L. Fork, R. Yen, R. H. Stolen, and W. J. Tomlinson, "Compression of femtosecond optical pulses," Appl. Phys. Lett. 40, 761 (1982).
7. J. G. Fujimoto, A. M. Weiner, and E. P. Ippen, "Generation and measurement of optical pulses as short as 16 fs," Appl. Phys. Lett. 44, 832 (1984).
8. J.-M. Halbout and D. Grischkowsky, "12-femtosecond ultrashort optical pulse compression at a high repetition rate," Appl. Phys. Lett. 45, 1281 (1984).
9. J. E. Rothenberg, D. Grischkowsky, and A. C. Balant, "Observation of the formation of the 0π pulse," Phys. Rev. Lett. 53, 552 (1984).
10. J. C. Diels, W. Dietel, E. Dopel, J. Fontaine, I. C. McMichael, V. Rudolph, F. Simoni, R. Torti, H. Vanherzeele, and B. Wilhelmi, "Colliding pulse femtosecond lasers and applications to the

measurement of optical parameters," in *Ultrafast Phenomena IV*, D. H. Auston and K. B. Eisenthal, eds. (Springer-Verlag, Berlin, 1984), p. 30.
11. M. D. Crisp, "Propagation of small-area pulses of coherent light through a resonant medium," Phys. Rev. A 1, 1604 (1970).
12. We note that this approach has the limitation that the time variations in the input-pulse intensity must be slower than the time scale on which the phase of the pulse changes.
13. The vapor cell had two 3-mm-thick windows, which did not have a significant effect on the results. In general, the linearity of the system allows one conceptually to think of both windows being at the cell input, in which case they will have the effect of changing the frequency sweep rate of the input pulse by a small amount. In the experimental and the theoretical cases considered here, this effect is negligible.
14. D. H. Auston, K. P. Cheung, J. A. Valdmanis, and D. A. Kleinman, "Cherenkov radiation from femtosecond optical pulses in electro-optic media," Phys. Rev. Lett. 53, 1555 (1984).

Joshua E. Rothenberg

Joshua E. Rothenberg was born in New York City on September 8, 1958. He received the B.S. degree in applied physics and the M.S. degree in electrical engineering from the California Institute of Technology. In 1978, he was the recipient of a Hertz Foundation Fellowship to study at Stanford University, where he worked on XUV spectroscopy and lasers. He received the Ph.D. degree in electrical engineering from Stanford University in 1983 and is currently a research staff member at IBM Research Laboratory in Yorktown Heights, New York. Currently, his research interests include transient laser processes and ultrafast phenomena. Dr. Rothenberg is a member of the Optical Society of America, the American Physical Society, and Tau Beta Pi.

D. Grischkowsky

D. Grischkowsky is the manager of the Ultrafast Science with Lasers Group at the IBM Watson Research Center in Yorktown Heights, New York. He received the B.S. degree from Oregon State University in 1962 and the Ph.D. degree in physics from Columbia University in 1968. After one year as a research associate at Columbia University, he joined IBM in 1969. His experimental and theoretical studies of the interaction of near-resonant light with two-level systems led to the development of the adiabatic following model. An outgrowth of his investigations of nonlinear pulse propagation in single-mode optical fibers was the invention of the optical-fiber pulse compressor. He is a Fellow of the American Physical Society and a member of the Optical Society of America.

Reprinted from Optics Letters, Vol. 10, page 562, November, 1985
Copyright © 1985 by the Optical Society of America and reprinted by permission of the copyright owner.

Generation of 16-fsec frequency-tunable pulses by optical pulse compression

S. L. Palfrey* and D. Grischkowsky

IBM Watson Research Center, P. O. Box 218, Yorktown Heights, New York, 10598

Received June 20, 1985; accepted August 21, 1985

Using a two-stage optical-fiber pulse compressor together with an optical amplifier, we have compressed the 5.4-psec pulses from a synchronously pumped mode-locked dye laser to 16-fsec duration. The compressed pulses had peak powers of 80 kW and a repetition rate of 200 Hz and were tunable over the wavelength of the dye laser.

There has been steady and significant progress during the last few years toward the generation of the shortest possible optical pulses. In one line of development the optical-fiber pulse compressor[1] has been used to compress the ultrashort pulses from custom-built colliding-pulse mode-locked ring dye lasers (CPM lasers). By this method, pulses as short as 30 fsec,[2] 16 fsec,[3] 12 fsec,[4] and most recently 8 fsec (Ref. 5) have been reported. All these pulses, however, suffer from the nontunability of the CPM laser, which limits the utility of these pulses for the study of time-dependent processes in many atomic, molecular, and condensed-matter systems.

In order to generate tunable, ultrashort pulses, we have taken the alternative approach of compressing the output of a commercially available, synchronously pumped mode-locked dye laser. Using this approach with two stages of pulse compression, Nikolaus and Grischkowsky[6] previously obtained pulses as short as 90 fsec, but at this point further compression was limited by insufficient power in the pulses. We have overcome this problem by amplifying the pulses after one stage of compression before sending them into a second optical-fiber pulse compressor. Using this two-stage compression with amplification, we have obtained frequency-tunable pulses as short as 16 fsec.

Figure 1 is a schematic diagram of the pulse-compression setup. All the pulse shapes shown were measured by cross correlation with shorter pulses in the compression chain, except, of course, for the final 16-fsec pulses (shown in more detail in Fig. 2), which were measured by autocorrelation. The 5.4-psec, 1.3-kW pulses, generated by cavity dumping the synchronously pumped, mode-locked dye laser, were coupled into 3 m of polarization-preserving, single-mode optical fiber (Newport Research Corporation F-SPV) with approximately 50% coupling efficiency. As described previously,[1,6,7] the self-phase modulation and the group velocity dispersion (GVD) in the fiber act together to broaden the pulses both spectrally and temporally. The output pulses from the fiber were broadened somewhat asymmetrically to 10 psec and had a frequency sweep corresponding to their measured bandwidth of 160 cm^{-1} (5.5 nm). The initial bandwith was approximately 3 cm^{-1} (0.1 nm). These pulses were then compressed by passage through a dispersive delay line consisting of a 1800-line/mm holographic diffraction grating and a prism. Although not shown in the figure for simplicity, this delay line was actually double passed to cancel the spatial-frequency sweep that results from a single pass.[8] This technique more efficiently couples the entire frequency spectrum into the second fiber. The resulting compressed pulses were asymmetric with a 180-fsec pulse width.

These compressed pulses had peak powers of 3.3 kW, which is insufficient to obtain substantial spectral broadening in a second fiber. Intuitively, the limitation is that the pulses must have high enough intensity in the fiber to cause significant spectral broadening before GVD broadens them temporally and reduces their intensity. To overcome this problem, we amplified the pulses by a factor of 30 before passing them through the second fiber. The amplifier consisted of a 1-cm cell of Rhodamine 610 in water and was longitudinally pumped by the frequency-doubled output of a mode-locked Nd:YAG laser Q switched at 1 kHz.[4] The pulse trains from the YAG pump and the dye laser were synchronized by driving the mode locker in the YAG laser with the same source used to mode lock the argon-ion laser that pumped the dye laser. The am-

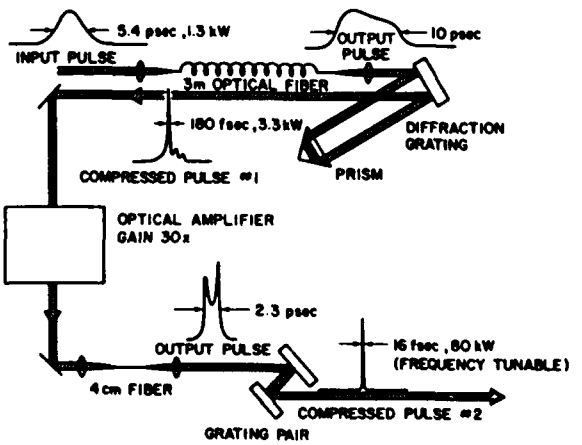

Fig. 1. Schematic diagram of the pulse-compression chain. The pulses are drawn as they appear spatially.

0146-9592/85/110562-03$2.00/0 © 1985, Optical Society of America.

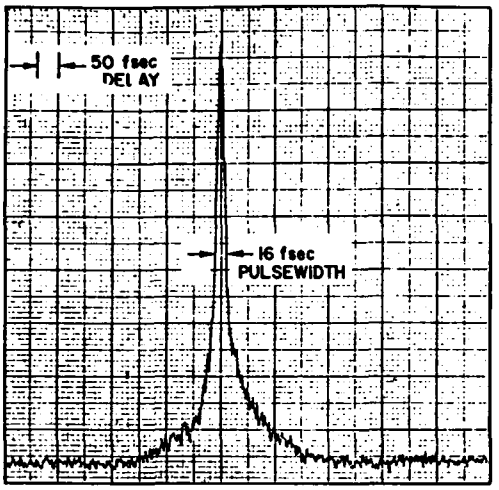

Fig. 2. Measured autocorrelation of the compressed output pulse.

plified pulses had a peak power of 100 kW and were temporally broadened only slightly.

In order to reduce the effect of pulse-to-pulse energy fluctuations, to make our measured compressed pulses more stable, and to have less amplitude noise, an electronic selection procedure based on threshold detection was used. This requirement was due to the 20% peak-to-peak amplitude noise on the pulse train of the dye laser and to the 25% peak-to-peak variations in the gain of the optical amplifier. For this selection part of the beam of the amplified 180-fsec pulses was focused on a 0.3-mm-thick KDP crystal, and the resulting second-harmonic light was monitored with a photomultiplier (PM). The output pulses from the PM then triggered a boxcar integrator only if they were above a preselected threshold level. Typically, the threshold triggering rate was 200 Hz. The output of the boxcar was then directly displayed by a chart recorder. For the cross-correlation measurements displayed in Figs. 3(a) and 4(a), the boxcar output was connected to a signal averager, which was synchronized with the delay setting of the correlator as controlled by a computer-driven stepping motor. Typically, a scan of the correlator delay took 100 sec, and 10 such scans were averaged.

For the second stage of compression the amplified pulses were coupled into 4 cm of polarization-preserving single-mode fiber (ITT 1605). The output of the fiber was then recompressed by a single pass through a pair of 600-line/mm holographic diffraction gratings. The optimum separation between the gratings was 4 cm, and changes of 0.5 mm significantly broadened the measured pulse width. The autocorrelation of the compressed pulses, obtained with a 200-μm-thick KDP crystal, is shown in Fig. 2. The FWHM of the autocorrelation is 25 fsec, which for a $(\text{sech})^2$ pulse shape corresponds to a pulse width of 16 fsec. This is a conservative value for the pulse width, because the measured autocorrelation is better fitted by a pulse shape with a shorter pulse width and more-extensive wings than the $(\text{sech})^2$ pulse shape. For these results the initial source was operating at 587 nm. Similar results were obtained when the source was tuned anywhere within the tuning range (585 to 605 nm) of the dye-laser amplifier. Tunability refers to moving the entire 30-nm-wide spectrum of the compressed pulses. Even though the 20-nm tunability is less than the linewidth, tuning to material resonances can cause significant effects. As is apparent from an inspection of Fig. 2, this compressed pulse has a relatively sharp pulse shape with little energy in the wings. The observed asymmetry was due to a slight optical misalignment of the correlator. The excellent signal-to-noise ratio is due to the relatively high repetition rate (200 Hz) of the selected pulses and the high power (80 kW) in the compressed pulses

As our first measurement application with these ultrashort compressed pulses, we used them for probing pulses to study the pulse reshaping at various stages in the pulse-compression chain. These measurements were made by cross correlation in a 60-μm-thick KDP crystal. In Fig. 3(a) we show the measured 180-fsec compressed pulses. Our subpicosecond time resolution is immediately apparent, and details of the pulses are seen that cannot be obtained any other way. The fact that these pulses could not be compressed to their bandwidth limit of 70 fsec was not due to the higher-order dispersion of the grating prism delay line, which was calculated to be too small an effect,[9] but is thought to have been caused by the fiber output pulses' having a frequency sweep that was not precisely linear with time. Given that our compression of the

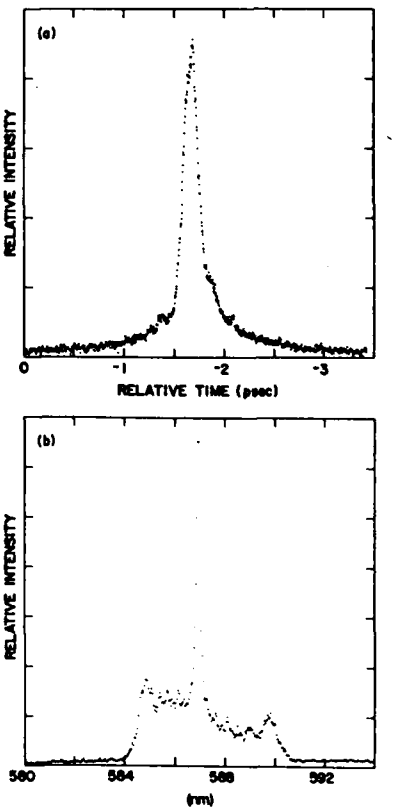

Fig. 3. (a) Measured cross correlation of the intermediate compressed pulse. Note that the leading edge of the pulse is to the right. (b) Intensity spectrum of the intermediate compressed pulse.

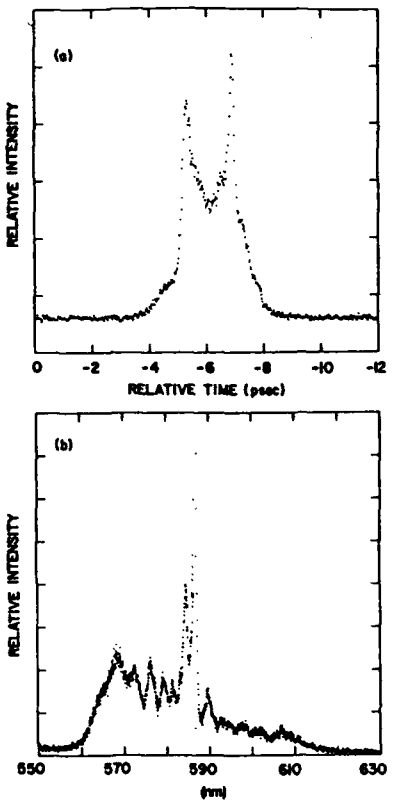

Fig. 4. (a) Measured cross correlation of the output pulse from the second fiber. Note that the leading edge of the pulse is to the right. (b) Intensity spectrum of the output pulse from the second fiber.

output pulse from the fiber was limited to a factor of 50 times, the nonlinearity of this sweep seems to be about a 2% effect, which is too large to be due to the higher-order dispersion in the fiber. Furthermore, the overall asymmetric compressed pulse shape with its small oscillation on the trailing edge is strongly suggestive of fiber output pulses with a slightly nonlinear frequency sweep. The intensity spectrum of the pulses is displayed in Fig. 3(b), illustrating the relatively compact spectral distribution of energy and the 160-cm^{-1} (5.5-nm) bandwidth. The central spike at 587 nm in the spectrum comes from the satellite pulses present in the initial laser output, which, because of their low intensity, pass through the entire system unchanged.

The measured output pulses from the second fiber, shown in Fig. 4(a), have been dramatically reshaped and broadened by passage through the fiber. The pulse width has increased from 180 fsec to 2.3 psec, and the two sharp spikes of 200 fsec define the front and the back of the pulses. The observed compression of these output pulses from the second fiber by more than 100 times indicates that the corresponding frequency sweep was linear with time to better than 1%. As illustrated in Fig. 4(b), the spectral bandwidth increased from 160 to 900 cm^{-1} (300 nm) by passage through the second fiber. This 900-cm^{-1} bandwidth is reasonably close to the 650-cm^{-1} bandwidth required by a transform-limited, $(sech)^2$, 16-fsec pulse. The sharp spike at 587 nm again marks the starting laser frequency and is caused by the satellite pulses.

In summary, 16-fsec frequency-tunable optical pulses have been generated. In addition, they have been used to study nonlinear propagation effects in the single-mode fibers used in the two-stage optical-fiber-pulse compressor.

The many incisive discussions with Joshua E. Rothenberg and his help with many aspects of the experiment are gratefully acknowledged.

This research was partially supported by the U. S. Office of Naval Research.

*Present address, RCA Laboratories, Princeton, New Jersey 08540.

References

1. H. Nakatsuka, D. Grischkowsky, and A. C. Balant, Phys. Rev. Lett. 47, 910 (1981).
2. C. V. Shank, R. L. Fork, R. Yen, and R. H. Stolen, Appl. Phys. Lett. 40, 761 (1982).
3. J. G. Fujimoto, A. M. Weiner, and E. P. Ippen, Appl. Phys. Lett. 44, 832 (1984).
4. J. M. Halbout and D. Grischkowsky, Appl. Phys. Lett. 45, 1281 (1984).
5. W. H. Knox, R. L. Fork, M. C. Downer, R. H. Stolen, C. V. Shank, and J. A. Valdmanis, Appl. Phys. Lett. 46, 1120 (1985).
6. B. Nikolaus and D. Grischkowsky, Appl. Phys. Lett. 43, 228 (1983).
7. D.Grischkowsky and A. C. Balant, Appl. Phys. Lett. 41, 1 (1982).
8. A. M. Johnson, R. H. Stolen, and W. M. Simpson, Appl. Phys. Lett. 44, 729 (1984).
9. J. D. McMullen, Appl. Opt. 18, 737 (1979).

Generation of subpicosecond electrical pulses on coplanar transmission lines

M. B. Ketchen, D. Grischkowsky, T. C. Chen, C-C. Chi, I. N. Duling, III, N. J. Halas,[a)]
J-M. Halbout, J. A. Kash, and G. P. Li
IBM Watson Research Center, P.O. Box 218, Yorktown Heights, New York 10598

(Received 8 October 1985; accepted for publication 28 January 1986)

Electrical pulses shorter than 0.6 ps were generated by photoconductively shorting a charged coplanar transmission line with 80 fs laser pulses. After propagating 8 mm on the line the electrical pulses broadened to only 2.6 ps.

It has been demonstrated that by using fast photoconductive switches driven by short laser pulses, very short electrical pulses can be produced and measured.[1] The shape of the electrical pulse depends on the laser pulse shape, the material properties of the semiconductor, the nature of the charge source, and the characteristics of the associated electrical transmission line onto which it is coupled. The standard microstrip line configuration suffers from reflections (ringing) at the generation site[1] and from strong frequency dispersion.[1,2] Due to structural factors it is difficult to eliminate these problems by shrinking the microstrip line geometry to dimensions below 0.1 mm while maintaining 50 Ω impedance. However, these problems can be bypassed by eliminating the line altogether, as was demonstrated by Auston *et al.*[3] They used a Hertzian dipole configuration of fast photoconductive switches to generate and detect freely propagating 1.6 ps (FWHM) electrical pulses. An alternative measurement approach has been to use the electro-optic effect in a nonlinear crystal. In this case, the field of the electrical pulse is sampled through the rotation of the polarization of the optical sampling pulse.[4] Recent work using this approach has shown a temporal resolution of less than 500 fs by measuring the fast rising edge of a longer pulse propagating on a 100-μm coplanar transmission line.[5]

In this letter we report the generation of subpicosecond electrical pulses obtained by photoconductively shorting a charged 5-μm coplanar transmission line with 80 fs laser pulses. The electrical pulses were measured by a fast photoconductive switch (gap), driven by a time delayed beam of the same 80 fs laser pulses, which connected the transmission line to an electrical sampling probe. This method of excitation seems to be especially well matched to the propagating mode of the transmission line in that shorter pulses are obtained and they broaden less with propagation than their counterparts generated via photoconductive gaps. After 8 mm of propagation on this line, the pulses broadened to only 2.6 ps.

The geometry of the experiment is illustrated in Fig. 1. The 20-mm-long transmission line with a design impedance of 100 Ω is made of three parallel 5-μm-wide aluminum lines separated from each other by 10 μm. The dc resistance of a single 5-μm line is 200 Ω. Because of the small dimensions, the geometrical dispersion of this line is much less than an equivalent microstrip line. The laser spot diameters are both 10 μm. It is important to note that we can continuously move the excitation beam and that no special lithographic features are required for the pulse generation. We thus have the equivalent of a "sliding contact" for the excitation beam.

The transmission line together with its pads and sampling gaps was fabricated on an undoped commercial (Union Carbide UCC-O) silicon on sapphire (SOS) wafer. The transmission line pattern was defined by conventional photolithographic lift-off techniques. The wafer with the photoresist stencil in place was precleaned with buffered HF before it was loaded into an electron beam evaporation system. The surface of the sample was further cleaned with an Ar plasma just prior to the deposition of a 0.5-μm-thick Al film. A clean Al-SOS interface is required to prevent an excessive interface resistance due to oxides. To ensure the required short carrier lifetime, the wafer with the Al transmission line pattern was implanted with two doses of O^+ ions, $1.0\times10^{15}/cm^2$ at 200 keV and $1.0\times10^{15}/cm^2$ at 100 keV.

The laser source is a compensated, colliding pulse, passively mode-locked dye laser producing 80 fs pulses at a 100-MHz repetition rate.[6,7] The average power was 2 mW (20 pJ/pulse) in the excitation beam and 4 mW in the sampling beam. The measurements were made with the standard excite and sample arrangement for the beams of optical pulses.[1-7] The time delay between the exciting and sampling beams was mechanically scanned by moving an air-spaced retroreflector with a computer-controlled stepping motor, which was synchronized with a multichannel analyzer (MCA) used in the signal averaging mode. The exciting beam was chopped at 2.5 kHz, and a lock-in amplifier was

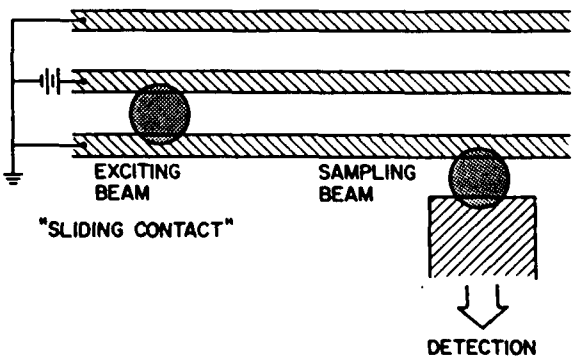

FIG. 1. Coplanar transmission line consisting of three parallel 5-μm-wide Al lines separated by 10 μm. Also shown is the 25-μm-wide sampling probe separated by a 10-μm gap from the transmission line. The exciting and sampling laser beams are indicated by the circles. The dc bias was 20 V.

[a)] Bryn Mawr College, Bryn Mawr, Pennsylvania.

 0003-6951/86/120751-03$01.00 © 1986 American Institute of Physics

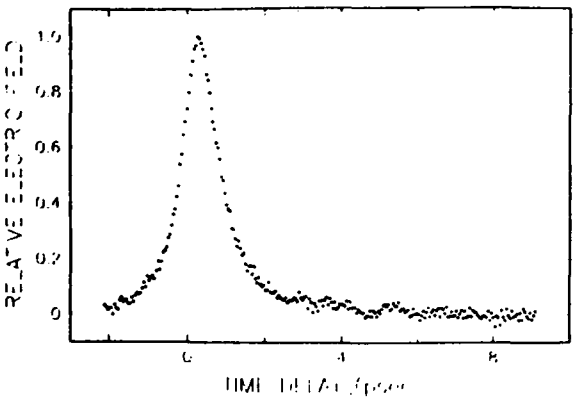

FIG. 2. Measured cross-correlation electrical pulse with less than 50 μm separation between the exciting and sampling beams. Zero delay corresponds to the exciting and sampling pulses hitting the sample simultaneously.

connected to the electrical probe switched by the sampling beam. The output of the lock-in was connected to the MCA, and repetitive scans were acquired.

The cross-correlation measurement of our subpicosecond electrical pulse is shown in Fig. 2. The magnitude of 10 mV was determined from sampling oscilloscope measurements and estimates based on the measured photocurrent. Here the spatial separation between the exciting and sampling beams was approximately 50 μm. As can be seen, the measured pulse has an excellent signal to noise ratio. The observed noise is a sum of laser oscillations which occur within the detection bandwidth of the lock-in amplifier and amplitude modulation on the laser slower than the averaging time (0.1 s) but faster than the scan duration of 50 s. Only four scans were averaged to obtain this figure.

We will now describe our procedure for determining that the actual pulse width was less than 0.6 ps. We follow the theory presented by Auston[1] and use his notation throughout. An important experimental observation was that when, instead of using the sliding contact, we generated the electrical pulse with a photoconductive gap of the same type as shown in Fig. 1, the pulse width of the autocorrelation measurement broadened by 1.5 times to 1.7 ps. This measurement had the characteristic asymmetric shape (Fig. 10, Ref. 1) of a gap generated and detected pulse for which the carrier lifetimes and the driving laser pulses were short compared to the measured autocorrelation pulse.

This result will now be explained, and the sampling gap capacitance C_s and the sliding contact capacitance C_{sc} will be calculated in the short pulse limit of Ref. 1. For this, the photoconductances $g_1(t)$ and $g_2(t)$ for the excitation and sampling gaps, respectively, are assumed to be delta functions, thereby implying infinitely short laser pulses and carrier lifetimes. For this limiting case with similar gaps we can estimate C_s from the relationship $\Delta\tau = 3.67 Z_0 C_s$, where $\Delta\tau$ is the autocorrelation pulse width and $Z_0 = 100\ \Omega$ is the characteristic impedance of the transmission line. With $\Delta\tau = 1.7$ ps, we obtain $C_s = 4.6$ fF. The actual pulse width Δt is given approximately by $\Delta t \approx Z_0 C_s \approx 0.5$ ps, corresponding to the unphysical shape of an infinitely sharp rising edge decaying exponentially with the time constant $(3/2)Z_0C_s$. Now the fact that with the sliding contact excitation we measure the shorter cross-correlation pulse width $\Delta\tau = 1.1$ ps implies that the effective capacitance C_{sc} of the sliding contact is less than $C_s/2.4$. This result is obtained from Eq. (32) of Ref. 1. For this simple limiting case, reducing the generation capacitance by 2.4 reduces the generated pulse width by 2.4. However, if this limit was valid the measured cross correlation would remain strongly asymmetric, in disagreement with experiment.

We then made the more reasonable assumption that $g_1(t)$ and $g_2(t)$ were given by the convolution of the laser pulse (allowing for its spatial extent) with an exponential response function describing the carrier lifetime τ_c. It should be clear that the value of $C_s = 4.6$ fF obtained above in the delta function limit is only an upper limit for C_s obtained from a numerical fit to the measured cross correlation using the realistic $g_1(t)$ and $g_2(t)$, i.e., the inclusion of other broadening mechanisms only broadens the observed pulse width and thereby less capacitance is required for a fit. The same reasoning holds for C_{sc}. With these $g_1(t)$ and $g_2(t)$, we numerically calculated [via Eq. (32) of Ref. 1] the predicted cross-correlation pulse shape, using the parameters $\tau_c = 250$ fs, $C_{sc} = 1$ fF, and $C_s = 4$ fF. The result agrees well with the slightly asymmetric cross-correlation measurement in Fig. 2 and corresponds to an electrical pulse duration of less than 0.6 ps. An additional point is that this value of C_{sc} compares well with that obtained from the calculated capacitance per unit length of the transmission line (0.7 pF per cm) multiplied by the laser spot size.

In Fig. 2 the measured delay of 0.25 ps is consistent with the group velocity for the pulse and indicates a rapid response of the sampling gap. By changing the separation between the exciting and sampling beams, we measured the pulse as it propagated down the line. When the separation was increased to 0.3 mm the cross-correlation pulse only slightly broadened to 1.2 ps. At 8 mm separation the pulse changed as shown in Fig. 3. The 65.4 ps delay indicates a group velocity of $v_g = c/2.45$. The low-frequency dielectric constant of sapphire is 9.95,[2] and neglecting the small frequency dispersion, v_g would be $v_g = c/3.15$. However, for our case the field is partially in air so that the pulse should

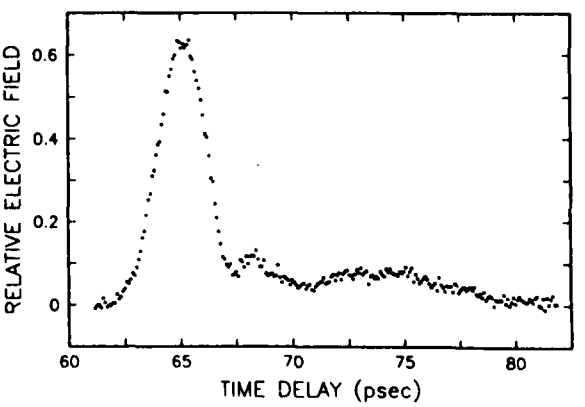

FIG. 3. Measured cross-correlation electrical pulse with 8 mm separation between the exciting and sampling beams. Zero delay corresponds to the exciting and sampling pulses hitting the sample simultaneously.

travel faster. The energy of this pulse is 0.5 of that of the pulse shown in Fig. 2, indicating an absorption length of 12 mm for our line. The measured pulse width of 2.6 ps is surprisingly short and illustrates the advantages of the small dimension coplanar transmission line compared to the microstrip line.[8]

In conclusion, we have generated electrical pulses shorter than 0.6 ps on a coplanar transmission line by using a new method of pulse generation, "the sliding contact." This method does not require any special lithographic features, allows pulse generation anywhere on the transmission line, and generates shorter pulses than the standard photoconductive gaps. We have also measured the exceptionally small dispersion of the 5-μm-wide coplanar transmission lines.

We acknowledge the Yorktown Silicon Facility and J. F. Ziegler's Ion Implantation Group for their support in sample preparation. This research was partially supported by the U. S. Office of Naval Research.

[1]D. H. Auston, in *Picosecond Optoelectronic Devices*, edited by C. H. Lee (Academic, London, 1984), pp. 73–116.
[2]D. E. Cooper, Appl. Phys. Lett. 47, 33 (1985).
[3]D. H. Auston, K. P. Cheung, and P. R. Smith, Appl. Phys. Lett. 45, 284 (1984).
[4]J. A. Valdmanis, G. A. Mourou, and C. W. Gabel, IEEE J. Quantum Electron. QE-19, 664 (1983).
[5]G. A. Mourou and K. E. Meyer, Appl. Phys. Lett. 45, 492 (1984).
[6]J-M. Halbout and D. Grischkowsky, Appl. Phys. Lett. 45, 1281 (1984).
[7]J. A. Valdmanis, R. L. Fork, and J. P. Gordon, Opt. Lett. 10, 131 (1985).
[8]We have also performed the same measurements with a two-line transmission line of the same dimensions. The initial pulse was similar (1.1 ps), and it broadened to only 2.2 ps after 6.5 mm of propagation.

Simultaneous optical pulse compression and wing reduction

N. J. Halas[a] and D. Grischkowsky
IBM Watson Research Center, Yorktown Heights, New York 10598

(Received 21 November 1985; accepted for publication 3 February 1986)

We report the compression of picosecond optical pulses with a simultaneous reduction of the pulse wings by using a combination of both the self-phase modulation and nonlinear birefringence effects in a modified optical-fiber pulse compressor.

Optical pulse compression via the optical-fiber pulse compressor[1] has become an important experimental technique to achieve shorter pulses for many different applications and at a variety of wavelengths. The operation of the pulse compressor is based on the self-phase modulation effect which increases the bandwidth of the input pulse and which together with the group velocity dispersion of the fiber produces the frequency sweep (chirp) that makes compression with the subsequent dispersive delay line possible. A recent example was that by using two-stage optical pulse compression together with amplification, the 5 ps pulses from a synchronously pumped, mode-locked dye laser were compressed to only 16 fs.[2] Other examples include the compression of the 33 ps, 0.53 μm second harmonic pulses (generated by a mode-locked YAG laser) to 0.4 ps,[3] and the compression of the 80 ps, 1.06 μm fundamental output pulses to 1.8 ps[4] and then to 1.3 ps.[5] In addition, the shortest optical pulses have for some time been produced by compressing the pulses from the colliding pulse mode-locked ring dye laser.[6-9]

However, for the above examples of pulse compression, the compressed pulses had relatively broad low power wings, which can be detrimental to energy integrating measurements. One method of eliminating these wings is based on the nonlinear birefringence effect in single-mode optical fibers.[10-13] This effect causes a different amount of intensity-dependent phase to be acquired by the field components along the two axes of the optical fiber. The consequent phase difference $\phi(t)$ between the components causes a change in the state of the output polarization. For sufficient intensity, the output polarization becomes strongly intensity dependent. Therefore, if a polarizer at the output end of the fiber, in conjunction with a Soleil–Babinet compensator, is set to block the low intensity light it will operate to transmit the peak of the pulse and attenuate the pulse wings. For this simplest mode of operation the output pulse shape is proportional to the cube of the input pulse shape. This application was first discussed by Stolen *et al.*,[10] and was demonstrated for picosecond pulses in the visible by Nikolaus *et al.*[11] and with soliton propagation in the infrared by Mollenauer *et al.*[12] Unfortunately, for subpicosecond pulses, with reasonable phase differences $\phi(t)$, the accompanying self-phase modulation becomes so strong that the pulses are severely broadened by group-velocity dispersion, and this approach can no longer be used. Another method of wing clipping recently introduced by Heritage *et al.*[5] involves spectral windowing of a pulse in the optical-fiber pulse compressor. This method eliminates the spectral components at the edges of the spectral envelope that do not compress well in the subsequent dispersive delay line.

In this letter we report the usage of both self-phase modulation and nonlinear birefringence to achieve optical pulse compression together with optical pulse reshaping on the subpicosecond time scale in a modified optical-fiber pulse compressor. We have compressed the 6 ps pulses from a mode-locked dye laser to 0.38 ps; simultaneously, we have severely clipped the wings of this pulse so that it compares favorably with a $(\text{sech})^2$ pulse shape.

We will now describe our experimental method and results in detail. The experimental setup is as shown in Fig. 1. The commercial laser source was a synchronously pumped, mode-locked tunable dye laser,[1] whose output at 5900 Å consisted of 6 ps FWHM pulses, cavity dumped at a repetition rate of 4 MHz. A variable disk attenuator was placed permanently in the beam to attenuate the incident light yet not interfere with the coupling efficiency into the optical fiber. The input beam was then transmitted through a crystal polarizer to ensure a high degree of linear polarization. A polarization rotator (half-wave plate) was used to vary the polarization angle of the beam incident on the optical fiber. The light was then coupled with 40% efficiency into five meters of ITT-1601 nonpolarization-preserving single-mode optical fiber, by means of a Newport fiber coupler[14] and a 10× microscope objective lens. The fiber had a core diameter of 4 μm; the nonlinear index n_2 and the group velocity dispersion (GVD) were that of fused quartz.[1,15] The fiber was loosely wound on a 20-cm-diam spool. The beat length of the mounted fiber was of the order of its 5 m length, and this value was relatively insensitive to temperature changes. However, if the fiber was moved, the linear birefringence and the axes of the fiber changed,[16] but on a daily basis this experimental setup for the fiber was quite stable. At the fiber output, the beam, recollimated by another 10× objective lens, was passed through a Soleil–Babinet compensator to cancel any acquired phase shift in the fiber due to its small linear birefringence, and then passed through the output polarizer, which blocked the low intensity light. Another polarization rotator optimized the diffraction efficiency for the dispersive delay line, consisting of a 1800 line/mm holographic grating, and a right angle prism. The optimum separation between the grating and prism was 13 cm. The autocorrelation traces were obtained by noncollinear generation of second harmonic light in a 200-μm-thick KDP crystal; the time delay was scanned by a computer-driven stepping motor synchronized with a multichannel analyzer used in the signal averaging mode. Following a procedure similar to

[a] Bryn Mawr College, Bryn Mawr, Pennsylvania.

 0003-6951/86/130823-03$01.00 © 1986 American Institute of Physics

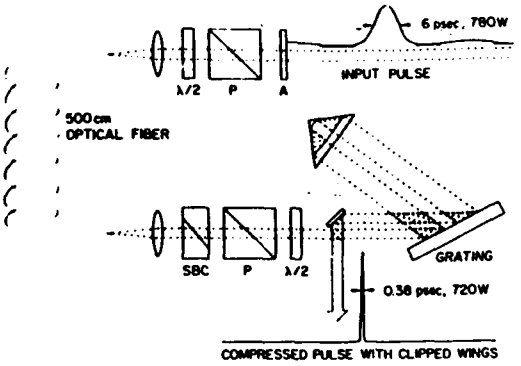

FIG. 1. Schematic diagram of experiment. *A* indicates the variable attenuator; *P* indicates a crystal polarizer; $\lambda/2$ indicates a half-wave plate; SBC indicates the Soleil–Babinet compensator.

that described in Ref. 2, electronic pulse selection was employed to minimize the effect of laser pulse fluctuations.

Figure 2 is a plot of the average output power transmitted through the crossed output polarizer as a function of the average input power. The characteristic curve is nearly cubic over more than an order of magnitude. For low levels of input light the slope is less than cubic, and at the lowest levels the slope becomes linear. This is due to a slight linear depolarization of the light upon propagation through the fiber, which at very low power levels is responsible for the transmitted power. For this case, the measured polarization ratio for the output light from the optical fiber was consistently less than 1/1000. The cubic region of the curve (and below) corresponds to a maximum induced phase difference $\phi_m < \pi$ at the peak of the pulse. Above this cubic regime (for higher input powers than shown in Fig. 2) the curve again acquires a subcubic slope. In this region $\phi_m > \pi$, and the curve saturates because the maximum transmission no longer occurs at the peak of the pulse. In this region of operation we have observed a three-peaked pulse autocorrelation corresponding to a dip in the center of the transmitted pulse.

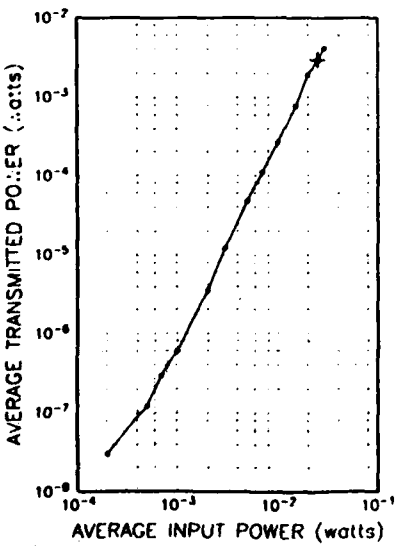

FIG. 2. Measured characteristic curve.

The strength of the nonlinear birefringence depends on the angle of the input polarization with respect to the effective fiber axes.[16] In the cubic regime of the characteristic curve we have measured a factor of three change in the output power as this angle was varied. The maximum and minimum values occurred with the polarization along the effective axes. These results disagree with the theories of Refs. 10 and 13. Both theories predict no effect when the polarization is aligned along an axis of the fiber. Reference 10 neglects linear birefringence, the effect of which was later analyzed in Ref. 13. Both theories neglect circular birefringence (optical activity) which is induced by twists in the fiber.[17] The inclusion of circular birefringence weakens the strong angular dependence of the nonlinear birefringence as predicted above. However, the self-phase modulation effect does not show any significant angular dependence.

In order to optimize the system for simultaneous pulse compression and wing clipping the following procedure is recommended. The length of the fiber is determined in the ordinary way for pulse compression as described in Refs. 1 and 18, although for this application we recommend nonpolarization preserving fiber.[19] To properly optimize the rotation, characteristic curves such as Fig. 2 should be taken as a function of angle with respect to the fiber axes. One then adjusts the strength of the nonlinear birefringence to obtain a polarization change of 90° ($\phi_m = \pi$) at the peak of the pulse for the maximum possible input power. This procedure gives the best throughput with the maximum bandwidth. For the results shown in Figs. 2 and 3, the input polarization was aligned along the axis for which the nonlinear birefringence was a minimum. An added advantage was that this situation eliminated the need for the Soleil–Babinet compensator.

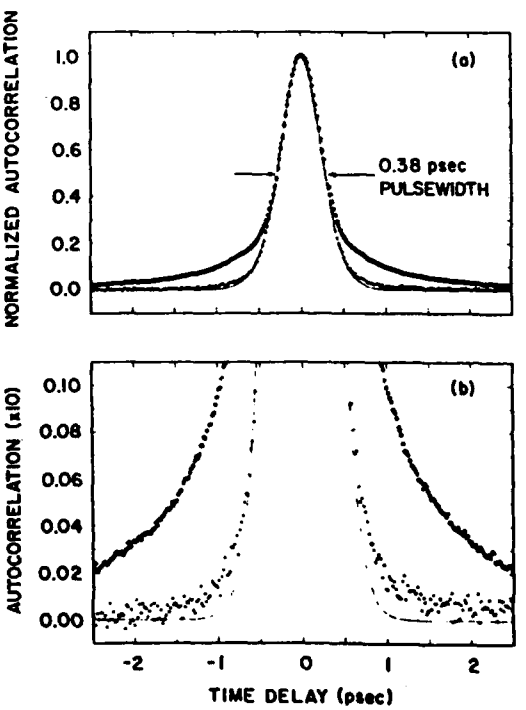

FIG. 3.(a). Autocorrelation measurements. Compressed pulse obtained using this technique (points); standard compressed pulse (open circles); calculated autocorrelation of $(\text{sech})^2$ (solid line). (b) 10× magnified view of (a).

The cross on the characteristic curve marks the conditions for the experimental results shown in Fig. 3. The indicated 25 mW average input power yielded an average output power from the polarizer of 2.8 mW, for a final average output power from the compressor of 1.1 mW. One can understand this 2.8 mW output power in terms of the following considerations. The coupling efficiency of 40% gave 10 mW of power coupled into the fiber. Since we have separately measured our laser pulses by cross correlation with compressed pulses, we know that approximately 1/4 of the energy of the laser output pulses resided in satellite pulses and low level wings that surrounded the main pulse. Consequently, only 7.5 mW of the coupled power was in the pulses that drove the nonlinear effects of self-phase modulation and nonlinear birefringence. Knowing the 4 MHz repetition rate and the input pulse width of 6 ps, we calculate that the driving pulses in the fiber had peak powers of 310 W. If we assume that the switching efficiency was 100% at the peak of these pulses ($\phi_m = \pi$), and because the transmitted pulse shape is proportional to $\sin^2(\phi/2)$,[10,11] the transmitted energy would be 60% for our typical laser pulse shapes. Thus, for $\phi_m = \pi$, the transmission of the 7.5 mW average power of the 310 W driving pulses would be 60% giving the predicted average output power of 4.5 mW compared to the measured value of 2.8 mW. This difference indicates that ϕ_m was approximately 0.7π for our measurement. The loss in the dispersive delay line was mainly due to the 65% diffraction efficiency of the grating. The 1.1 mW average compressed power corresponds to a peak power of 720 W for the 380 fs compressed pulses.

The intensity autocorrelation measurement of the compressed and reshaped optical pulses is shown in Fig. 3. For this result the separation between the grating and prism was optimized for the shortest pulses with the cleanest pulse shapes. The measured bandwidth for these compressed pulses was 35 cm^{-1}, to be compared to 29 cm^{-1} required for a transform limited $(sech)^2$ pulse shape with the same pulse width. For comparison a standard compressed pulse shape (normalized to the same pulse width) is also shown. One sees a marked reduction in the wings of the optical pulses obtained via this new technique. Also, one sees that with this method of pulse compression/reshaping the resulting pulses compared favorably to the calculated $(sech)^2$ autocorrelation shown as the solid line.

In conclusion, we have demonstrated an optical pulse compression and reshaping technique based on the use of a modified optical-fiber pulse compressor. The simple modifications are the substitution of a nonpolarization-preserving fiber and the addition of one polarizer. The wings of the compressed pulses were strongly reduced, and any low power satellite pulses from the laser source were also eliminated.

We acknowledge with gratitude the tireless and expert help of D. Krokel for much of the data taking. This work was partially sponsored by the U.S. Office of Naval Research.

[1]H. Nakatsuka, D. Grischkowsky, and A. C. Balant, Phys. Rev. Lett. 47, 910 (1981); D. Grischkowsky and A. C. Balant, Appl. Phys. Lett. 41, 1 (1982); B. Nikolaus and D. Grischkowsky, Appl. Phys. Lett. 42, 1 (1983).
[2]S. L. Palfry and D. Grischkowsky, Opt. Lett. 10, 562 (1985).
[3]A. M. Johnson, R. H. Stolen, and W. M. Simpson, Appl. Phys. Lett. 44, 729 (1984).
[4]J. D. Kafka, B. H. Kolner, T. Baer, and D. M. Bloom, Opt. Lett. 9, 505 (1984).
[5]J. P. Heritage, R. N. Thurston, W. J. Tomlinson, A. M. Weiner, and R. H. Stolen, Appl. Phys. Lett. 47, 87 (1985).
[6]C. V. Shank, R. L. Fork, R. Yen, and R. H. Stolen, Appl. Phys. Lett. 40, 761 (1982).
[7]J. G. Fujimoto, A. M. Weiner, and E. P. Ippen, Appl. Phys. Lett. 44, 832 (1984).
[8]J.-M. Halbout and D. Grischkowsky, Appl. Phys. Lett. 45, 1281 (1984).
[9]W. H. Knox, R. L. Fork, M. C. Downer, R. H. Stolen, C. V. Shank, and J. A. Valdmanis, Appl. Phys. Lett. 46, 1120 (1985).
[10]R. H. Stolen, J. Botineau, and A. Ashkin, Opt. Lett. 7, 512 (1982).
[11]B. Nikolaus, D. Grischkowsky, and A. C. Balant, Opt. Lett. 8, 189 (1983).
[12]L. F. Mollenauer, R. H. Stolen, J. P. Gordon, and W. J. Tomlinson, Opt. Lett. 8, 289 (1983).
[13]H. G. Winful, Appl. Phys. Lett. 47, 213 (1985).
[14]Instead of using the standard fiber collet to hold the input end of the fiber, a 3-in. brass rod of equivalent diameter with a 90° radial trough was used. The cleaved and mechanically stripped end of the optical fiber was placed in this trough and held in place with Eastman 910 adhesive. This adhesive possesses excellent mode-stripping qualities, and thereby eliminated much of the low-level light that would have otherwise propagated through this short fiber by means of the cladding modes.
[15]H. Nakatsuka and D. Grischkowsky, Opt. Lett. 6, 13 (1981).
[16]We always found two orthogonal effective axes for which low power linearly polarized input light resulted in linearly polarized output light. This is not to say that the light remained linearly polarized during its total passage through the fiber. For an input polarization along an effective axis, the Soleil–Babinet compensator was not needed.
[17]R. Ulrich and A. Simon, Appl. Opt. 18, 2241 (1979).
[18]W. J. Tomlinson, R. H. Stolen, and C. V. Shank, J. Opt. Soc. Am. B 1, 139 (1984).
[19]With a polarization preserving (strong linear birefringence) single-mode fiber, we could not observe any nonlinear birefringence under similar experimental conditions.[13]

Reprinted from Journal of the Optical Society of America B, Vol. 3, page 1235, October 1986
Copyright © 1986 by the Optical Society of America and reprinted by permission of the copyright owner.

Subpicosecond transient excitation of atomic vapor and the measurement of optical phase

Joshua E. Rothenberg and D. Grischkowsky

IBM Watson Research Center, P.O. Box 218, Yorktown Heights, New York 10598

Received April 14, 1986; accepted June 17, 1986

The transient behavior of a frequency-swept optical pulse transmitted through a resonant vapor cell is observed by an optical sampling technique with ~20-fsec time resolution. The observed 200-fsec transients are the fastest intensity sampling measurement ever made on an atomic vapor and provide a precise determination of the time-varying phase of the pulse. The observed phase shows deviations from a linear frequency sweep, which may account for previous limits on pulse compression.

A two-stage pulse-compression result was recently reported,[1] whereby the 5.4-psec pulses from a synchronously pumped mode-locked dye laser were compressed to 16 fsec. An important question raised in this paper, which has relevance to all applications of the optical-fiber pulse compressor,[2] is: How linear is the frequency sweep of the frequency-broadened pulse from the optical fiber? A conjectured nonlinearity of only a few percent appeared to limit the first stage of pulse compression.

The possibility of measuring these small deviations from a linear sweep is now provided by a new experimental technique,[3] based on the "self-induced optical heterodyne effect,"[4] in which one measures the slowly varying phase of an optical pulse and thereby determines the frequency sweep. In this technique, a pulse of unknown phase is first directed through a resonant vapor cell. The transmitted pulse develops an intensity modulation that is a direct measure of the phase of the input pulse. The modulation can be very rapid (with a single oscillation for every 2π change of phase in the input pulse) and therefore must be observed by cross correlation with a sufficiently short probe pulse. The initial demonstration[3] of this method confirmed its potential but was limited in accuracy because a 400-fsec probing pulse was used for cross correlation.

This method is based on a simple model for the interaction of a frequency-swept pulse with a resonant medium.[3,4] We can summarize this model here as follows. When the frequency of the pulse sweeps through the medium resonance, the medium (atomic, molecular, etc.) is excited in the impact limit and thereafter radiates at its resonance frequency. This reference radiation interferes (heterodynes) with the input pulse, thereby leading to modulation on the output pulse. Therefore each change from a minimum to a maximum in this modulation corresponds to a change of π rad in the phase of the input pulse relative to the resonance reference radiation.

In this paper we report the combination of two-stage pulse compression with the self-induced optical heterodyne effect to achieve phase measurements with ~20-fsec time resolution. This accuracy was sufficient to allow us to determine that, depending on the initial pulse shape, the frequency sweep of the output pulse from the fiber used in the optical-fiber pulse compressor can deviate from linearity and thereby limit the obtainable pulse compression. An additional feature of this optical sampling measurement is that, to our knowledge, we have observed the fastest transients (less than 200 fsec) ever measured directly from an atomic vapor.

The apparatus used in this measurement is shown in Fig. 1. The 5.4-psec pulses from a frequency-tunable, synchronously pumped, cavity-dumped dye laser were sent through a single-mode polarization-preserving optical fiber 3 m in length. Passage through this fiber broadened the pulses to 10 psec and increased their spectral bandwidth from 1 to 50 Å. This large increase in bandwidth appeared as a frequency sweep across the pulse. A fraction of the frequency-swept pulse train was sent directly through the sodium-vapor cell, with the rest of the pulse train being compressed by a diffraction grating and prism arrangement. The resulting compressed pulses (approximately 250 fsec in duration) were then amplified 100 times. The amplifier was a 1-cm cell containing Rhodamine 610 in water, which was pumped by the frequency-doubled output of a mode-locked Nd:YAG laser, Q switched at 1 kHz. The amplified pulses were then sent through a second, shorter fiber only 2 cm long. The pulses transmitted by the second fiber were compressed in a grating-pair arrangement to approximately 20 fsec. In order to reduce the shot-to-shot fluctuations in the experiment and to stabilize the second-stage compressed pulses, an electronic-pulse-selection procedure similar to that described in Ref. 1 was used. This procedure significantly improved the time resolution and the signal-to-noise ratio of our measurements, but it decreased the accepted pulse-repetition rate to about 200 Hz.

The pulses transmitted by the vapor cell were cross correlated with the ~20-fsec probing pulses in a 50-μm-thick KDP crystal. A noncollinear geometry was used so that the correlation signal was background free. The resulting second-harmonic signal was monitored by a boxcar integrator triggered by the pulse-selection electronics. The output from the boxcar was connected to a signal averager synchronized with the time delay of the probing pulse, as controlled by a computer-driven stepping motor. A single scan took approximately 100 sec, and usually 10 scans were averaged. This optical sampling technique permitted the observation

0740-3224/86/101235-04$02.00 © 1986 Optical Society of America

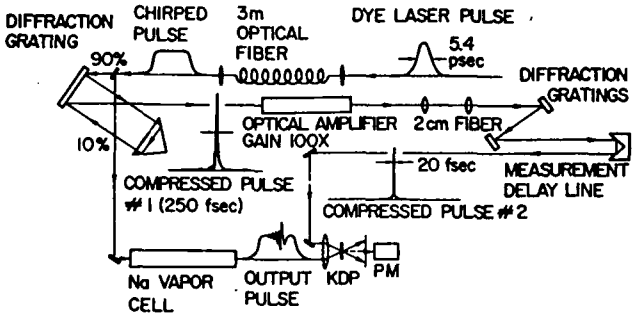

Fig. 1. Schematic diagram of the apparatus used to measure the phase of a frequency-swept optical pulse. PM, photomultiplier.

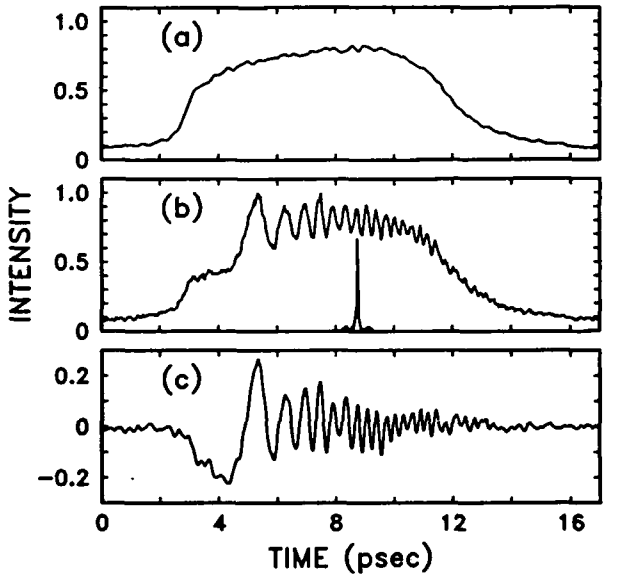

Fig. 2. (a) Measured cross correlation (resolution 22 fsec) of the input pulse to the sodium cell. (b) Measured cross correlation of the output pulse from the sodium cell. The 22-fsec probing pulse's autocorrelation (FWHM of 34 fsec) is also shown. (c) Smoothed difference between the modulated output pulse (b) and the input pulse (a).

of the intensity of the transmitted pulse with ~20-fsec resolution. The 50-cm-long vapor cell contained an excess of sodium metal sealed under vacuum. The atomic-number density corresponding to the saturated vapor pressure was given by the heated cell temperature. The absorption coefficient was then calculated from this number density.

The frequency-swept input pulses to the vapor cell (i.e., the output pulses from the cold cell with negligible sodium-vapor pressure) are shown in Fig. 2(a). Here we see that passage through the 3-m fiber has broadened the 5.4-psec incident pulses to 10 psec and shaped them to the characteristic square, flat-topped shape. Our numerical calculations agree with this general shape, but the difference in the rise and fall times has not yet been adequately explained. In addition, until this measurement, we did not know the time-dependent phase of these frequency-swept pulses. When these pulses were passed through the heated sodium-vapor cell, we obtained the output pulses shown in Fig. 2(b). The cell temperature was 160°C, corresponding to an atomic-number density of $3 \times 10^{11}/\text{cm}^3$, which gives an optical density of $\alpha l = 95$ on the center of the 5890-Å sodium line. As discussed earlier,[3,4] the strong modulation on these output pulses is a measure of the relative phase of the frequency-swept pulses with respect to the resonance radiation emitted by the impact excited sodium atoms. The resolution of this cross-correlation measurement is illustrated by the autocorrelation of the narrow probing pulse that is also shown in the figure. The FWHM of this autocorrelation is 34 fsec, which for an assumed sech^2 pulse shape, implies a pulse width of 22 fsec. The observed modulation frequency increases with time and is resolved out to ~14 psec, where the frequency has increased to approximately 5 THz.

In order to obtain the relative phase from Fig. 2(b), all that needs to be done is to locate the maxima and minima as a function of time. This is most accurately accomplished by subtracting the intensity of Fig. 2(a) from that of Fig. 2(b), using a simple three-point smoothing routine to minimize the effects of noise, and finding the extrema of this smoothed difference, shown in Fig. 2(c). This procedure eliminates the effects of the slowly changing amplitude to first order and enhances the visibility of the extrema. The simple model of the self-induced heterodyne effect[3,4] tells us that the phase of the pulse changes by exactly π rad from one extremum to the next. Hence a simple counting procedure may be used to determine the phase. The result of this procedure is given by the filled circles in Fig. 3, which are compared with a quadratic dependence shown as the dashed line for a linear frequency sweep of 18.2 cm^{-1}/psec, or, equivalently, 0.55 THz/psec. The measurement error is indicated by the approximate $\pi/4$ scatter of the points about the curve shown in Fig. 3. Clearly, the measured frequency sweep is not linear on the trailing edge of the pulse. We consider this deviation to be at least partially responsible for previous limits on pulse compressibility.[1] The deviation also explains the success of the spectral windowing technique recently used by Heritage *et al.*[5] to clip the edges of the broadened frequency spectrum and thereby obtain better pulse compression. Johnson and Simpson[6] have also used this technique in a case in which, similarly to our situation, there is significant group-velocity dispersion. Similar to our results, they deduce that the frequency sweep is linear over most of the pulse.

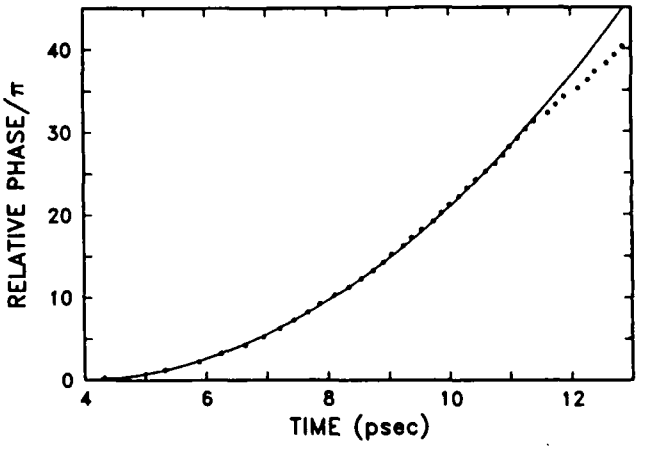

Fig. 3. The relative phase of the frequency-swept input pulse the sodium-vapor cell. The measured points are obtained from direct counting of the maxima and minima of the modulation of the output pulse shown in Fig. 2(b). The measurement is compared with the quadratic relationship (solid line) corresponding to a linear frequency sweep of 18.2 cm^{-1}/psec.

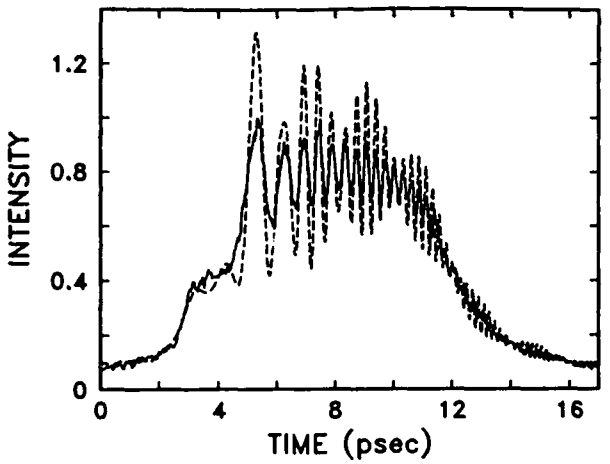

Fig. 4. Experimental results (solid line) compared with a linear dispersion theory calculation (dashed line) for a linear frequency sweep of 18.2 cm^{-1}/psec.

As pointed out in Ref. 4, the method described is valid only when the amplitude of the pulse changes more slowly than its phase. From the figures it appears that this condition is fulfilled, but since the deviation from quadratic phase occurs on the trailing edge of the pulse one might argue that it is the rapidly changing amplitude that leads to this deviation. In order to eliminate this possibility, we compare an exact linear dispersion theory calculation with the experimental results in Fig. 4. The theory assumes a perfectly linear frequency sweep and has only two adjustable parameters, the magnitude of the frequency sweep and the relative position of the sodium resonance. Although the amplitude of the modulations do not agree, the time positions agree well for most of the pulse. However, at the time (~11.5 psec) when the dots in Fig. 3 deviate from the quadratic dependence, the oscillations of the theory in Fig. 4 slip from synchronization with the data. This slip is more clearly apparent in Fig. 5, where we have obtained a much better fit of the amplitudes of the oscillations by allowing a pulse-to-pulse jitter in the magnitude of the frequency sweep. A Gaussian distribution of frequency sweeps centered around 18.2 cm^{-1}/psec with a FWHM of 2 cm^{-1}/psec was used. In addition, the fit assumed an atomic-number density 30% less than that indicated by the cell thermocouples. On the expanded scale of Fig. 5, it is clearly apparent that the oscillations of the data slip from synchronization with the theory on the trailing edge of the pulse. Since the theory assumes an absolutely linear frequency sweep and includes all the effects of the rapidly changing amplitude of the input pulse, we can confidently conclude from a comparison of Figs. 3 and 5 that there is a deviation from linearity in the frequency sweep of the input pulse.

It has been pointed out in Ref. 3 that the data can be difficult to interpret if the two D lines of sodium interfere to cause significant additional structure in the transmitted pulse. However, in Figs. 2–5 we see that this effect is quite small. The reason is simply that the center frequency of the pulse was adjusted so that the spectral overlap was limited almost completely to the D_2 line. Indeed, in Fig. 2 the initial absorption, the single dip at the beginning of the pulse, corresponds to a single line. In Fig. 6 we show the contrasting case in which the center frequency of the pulse was adjusted so that both lines were clearly excited. Thus we see the two dips at the beginning of the pulse and a beat note superimposed upon the heterodyne modulation. This beat, approximately 2 psec in period, is due to the ~500-GHz separation between the two D lines.[7] Note carefully the nodal points in the data at which the heterodyne modulation nearly disappears. At these points, there is a phase change of approximately π resulting from the phase change in the resonance reference signal because of the destructive interference of the D lines at the nodes. Figure 6(b) shows a linear dispersion theory calculation for this case using the same experimental parameters as for Figs. 4 and 5.

In summary, by using an optical sampling technique with ~20-fsec resolution, we have directly measured atomic transients as fast as 200 fsec. These transients were excited by the passage of a frequency-swept optical pulse through a resonant atomic vapor, and they provided a measure of the

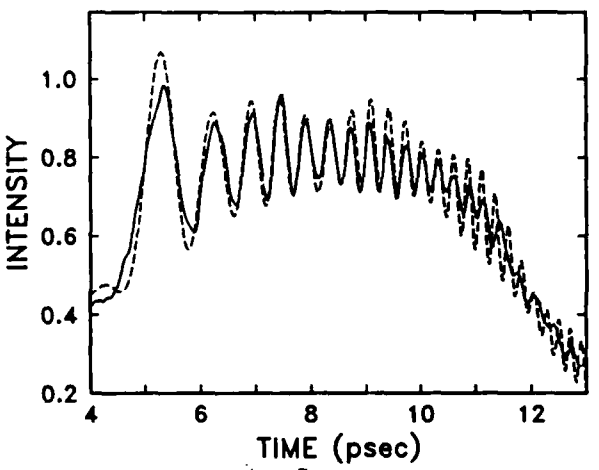

Fig. 5. Experimental results (solid line) compared with linear dispersion theory calculation (dashed line) for a Gaussian distribution of linear frequency-sweep strengths centered about 18.2 cm^{-1}/psec with a FWHM of 2 cm^{-1}/psec.

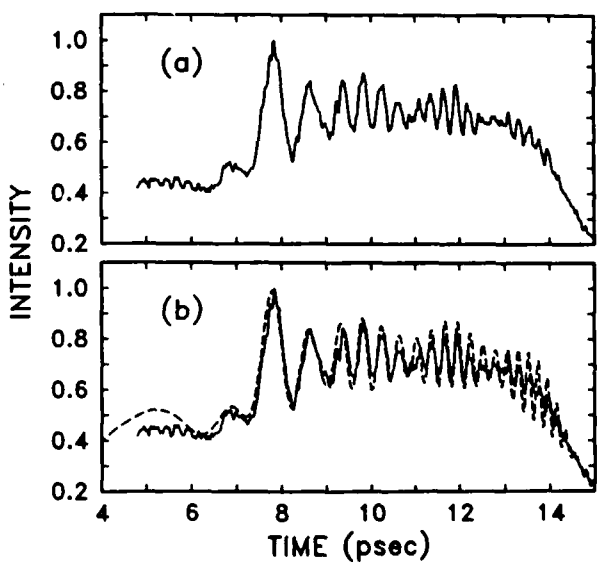

Fig. 6. (a) Measured cross correlation of the output pulse from the sodium cell when the center frequency was tuned to excite both the sodium D lines. (b) Experimental results (solid line) compared with a linear dispersion theory calculation (dashed line).

phase of the optical pulse. From the time dependence of the phase, we determined that the frequency sweep of the pulse was not exactly linear. These deviations from linearity may explain previously measured limits for pulse compression.

ACKNOWLEDGMENTS

The authors gratefully acknowledge the assistance of D. Krökel in this work. This research was partially supported by the U.S. Office of Naval Research.

REFERENCES

1. S. L. Palfrey and D. Grischkowsky, "Generation of 16-fsec frequency tunable pulses by optical pulse compression," Opt. Lett. **10**, 562 (1985).
2. H. Nakatsuka, D. Grischkowsky, and A. C. Balant, "Nonlinear picosecond-pulse propagation through optical fibers with positive group velocity dispersion," Phys. Rev. Lett. **47**, 910 (1981); D. Grischkowsky and A. C. Balant, "Optical pulse compression based on enhanced frequency chirping," Appl. Phys. Lett. **41**, 1 (1982); B. Nikolaus and D. Grischkowsky, "12× pulse compression using optical fibers," Appl. Phys. Lett. **42**, 1 (1983).
3. J. E. Rothenberg and D. Grischkowsky, "Measurement of the phase of a frequency-swept ultrashort optical pulse," J. Opt. Soc. Am. B **2**, 626 (1985).
4. J. E. Rothenberg, "Self-induced heterodyne: the interaction of a frequency-swept pulse with a resonant system," IEEE J. Quantum Electron. **QE-22**, 174 (1986).
5. J. P. Heritage, R. N. Thurston, W. J. Tomlinson, A. M. Weiner, and R. H. Stolen, "Spectral windowing of frequency-modulated optical pulses in a grating compressor," Appl. Phys. Lett. **47**, 87 (1985).
6. A. M. Johnson and W. M. Simpson, "Optically biased tunable femtosecond dye laser and spectral windowing of the compressed second harmonic of Nd:YAG," IEEE J. Quantum Electron. **QE-22**, 133 (1986).
7. J. E. Rothenberg and D. Grischkowsky, "Observation of a 1.9 psec polarization beat," Opt. Lett. **10**, 22 (1985).

Reprinted from Optics Letters, Vol. 12, page 99, February 1987.
Copyright © 1987 by the Optical Society of America and reprinted by permission of the copyright owner.

Measurement of optical phase with subpicosecond resolution by time-domain interferometry

Joshua E. Rothenberg and D. Grischkowsky

IBM Watson Research Center, P.O. Box 218, Yorktown Heights, New York 10598

Received September 8, 1986; accepted October 26, 1986

A new and extremely general interferometric technique has been experimentally demonstrated that permits the direct measurement of optical phase on a subpicosecond time scale. The intensity is characterized by cross correlation, and thus the optical field is completely determined.

A major unsolved technical problem in the field of ultrafast phenomena is the complete characterization of the optical excitation pulses. Traditionally, these ultrashort laser pulses are described by measuring their intensity autocorrelation by the generation of second-harmonic light in thin nonlinear crystals. These autocorrelation measurements do not, however, give complete information regarding the pulse shape. The measurement is always symmetric, and the quoted pulse widths must assume a pulse shape. A cross-correlation measurement[1] of the intensity would be preferable if a short enough interrogating pulse were available.

In order to characterize an optical pulse completely, one must also measure the slowly varying phase $\phi(t)$. This measurement is experimentally much more difficult, although significant progress has recently been made. Usually, short-pulse characterizations include an intensity spectrum, which determines $\phi(t)$ only if the pulse is transform limited. Dietel *et al.*[2] have developed the interferometric autocorrelation technique, which gives more information about the pulse shape and $\phi(t)$ by an iterative fitting of the intensity autocorrelation, the interferometric autocorrelation, and the pulse spectrum.

A recent experimental technique,[3] based on the self-induced optical heterodyne effect,[4] allows one to measure $\phi(t)$ directly. For this, a pulse of unknown phase is directed through a resonant vapor cell. The phase of the input pulse is determined from the intensity modulation that develops on the transmitted pulse by means of a simple counting procedure[3,4] that assumes that adjacent modulation extrema are separated by π rad. The modulation originates from the interference between the input pulse and the nearly monochromatic radiation emitted by the resonantly excited vapor. Although this method is quite powerful, it has a few shortcomings. A suitable atomic or molecular resonant vapor must be available within the bandwidth of the laser pulse; the modulation begins only after the instantaneous frequency has swept through the vapor resonance, and if the pulse amplitude is changing more rapidly than the phase, then the simple counting procedure[3,4] may lead to an erroneous measured phase.

In this Letter we report a new and more general technique whereby the resonant vapor is replaced by a Mach–Zehnder interferometer with a Fabry–Perot étalon in one arm (Fig. 1). The étalon, tuned to be resonant with the input pulse, provides the monochromatic reference pulse. The delay and the alignment of the interferometer are adjusted to ensure that this reference pulse interferes (heterodynes) with the input pulse, which passes unaltered through the other arm of the interferometer. Conceptually this arrangement is similar to that of the resonant vapor technique. In both techniques an ultrashort probe pulse is required for resolution of the intensity modulation on the transmitted pulse. However, because of the flexibility of the étalon, the resonant condition as well as all constraints on $\phi(t)$ are thereby eliminated. In addition, because of the ease of adjustment of the delay of the interferometer, the phase of the entire pulse can be obtained, and both quadratures of the field relative to the carrier frequency (i.e., the resonance frequency) of the étalon can be determined. It should also be noted that, just as with the resonant vapor, the reference pulse is phase locked to the input pulse. Therefore any shot-to-shot fluctuation in the overall (absolute)

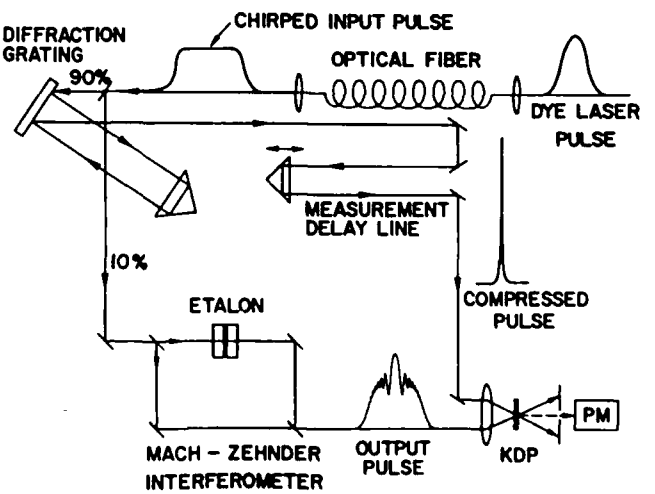

Fig. 1. Apparatus used to measure the phase of an optical pulse. PM, photomultiplier.

0146-9592/87/020099-03$2.00/0 © 1987, Optical Society of America

phase of the input pulse cancels out in the interferometer.

The apparatus is shown in Fig. 1. The 6-psec, 605-nm output of a synchronously pumped cavity-dumped dye laser was sent through a 3-m single-mode optical fiber. It emerged with a pulse width broadened to 10 psec and with a bandwidth increased from 0.1 to ~5.5 nm. A portion (10%) of this frequency-swept pulse from the fiber was directed through the Mach–Zehnder interferometer, while the rest was sent through a grating-prism compressor. The resulting compressed pulse, ~200 fsec in duration, was used to cross correlate the output of the interferometer in a 200-μm-thick KDP crystal. In order to keep the relative length of the arms of the Mach–Zehnder interferometer stable to a small fraction of a wavelength during the measurements, the interferometer was constructed on a small-area Al plate (20 cm × 20 cm × 1 cm) using mechanically stiff optical mounts and was surrounded by a polyethylene sheet to reduce air currents. The resulting stability was much less than a fringe over tens of minutes. The Fabry–Perot étalon was chosen with a free spectral range such that the bandwidth of the input pulse overlapped only one resonance, and the finesse was made large enough so that the decay time of the reference pulse was longer than the input pulse. The étalon was constructed of 99% reflectivity fused-quartz plates polished to $\lambda/200$. The plates were mechanically pressed together using 31-μm thick In metal shims as spacers. The free spectral range was 57 Å (160 cm^{-1}).

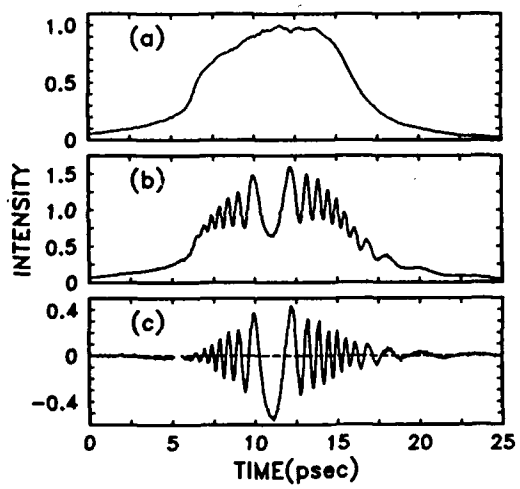

Fig. 2. (a) Input pulse to Mach–Zehnder interferometer. (b) Output pulse from the interferometer. (c) Difference between (b) and the sum of (a) and the reference pulse.

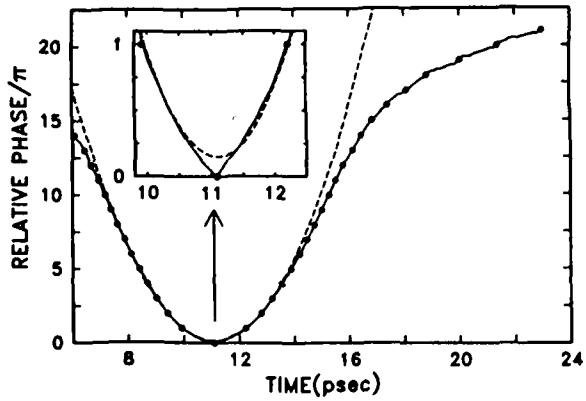

Fig. 3. The relative phase (radians, solid curve) determined from the counting of extrema in Fig. 2(c) and quadratic phase (dashed) due to a 22-cm^{-1}/psec frequency sweep.

The pulse transmitted by the Fabry–Perot étalon, as measured by cross correlation, showed a sharp subpicosecond rise time followed by a 7-psec exponential decay, corresponding to a pass bandwidth of the étalon of ~0.75 cm^{-1} and a finesse of 215. In order to broaden this pulse further and to eliminate some residual oscillations due to the nature of the frequency-swept excitation, an additional étalon (150 μm thick, 80% reflectivities, free spectral range of 22 cm^{-1}, finesse of 14, and 1.6-cm^{-1} linewidth) was put in series with the first. The resulting reference pulse had a rise time of ~5 psec and a 12-psec pulse width. Calculations show that this pulse has a constant phase to much less than 1 rad over its duration.

The input pulse to the interferometer shown in Fig. 2(a) is measured by blocking the arm containing the Fabry–Perot étalon. When the reference pulse from the étalon interferes with the input pulse, we obtain the modulated pulse shown in Fig. 2(b). The modulation is better analyzed and displayed [Fig. 2(c)] by subtracting the sum of the intensities of Fig. 2(a) and the measured reference pulse from the intensity of Fig. 2(b).

For the analysis, consider the unknown field to be the real part of $E(t)\exp\{i[\phi(t)+\omega_0 t]\}$ and the reference pulse to be $\mathrm{Re}[R(t)e^{i\omega_0 t}]$. The intensity in Fig. 2(b) then corresponds to

$$I(t) = |E(t)\exp\{i[\phi(t)+\omega_0 t]\} + R(t)e^{i\omega_0 t}|^2 = E^2(t) + R^2(t) + 2\,\mathrm{Re}[E(t)R(t)e^{i\phi(t)}], \quad (1)$$

and that in Fig. 2(c) corresponds to

$$I(t) - E^2(t) - R^2(t) = 2\,\mathrm{Re}[E(t)R(t)e^{i\phi(t)}]. \quad (2)$$

For smoothly varying amplitudes $E(t)$ and $R(t)$, which we have from intensity cross correlations, we can assume that $\phi(t)$ changes by π from one extremum in Fig. 2(c) to the next. Thus each dot in Fig. 3 corresponds to an extremum in Fig. 2(c), and we have assumed (based on the further measurements described below) that there is a point of stationary phase [$\dot{\phi}(t) = 0$] near the middle of the pulse. Otherwise one could not determine the *direction* of the phase change from one extremum to the next [i.e., the absolute sign of $\dot{\phi}(t)$]. The solid line in Fig. 3 is the cosinusoidal interpolation of the data of Fig. 2(c) according to Eq. (2). The dashed line is the parabolic phase for a linear frequency sweep.

Note that there is a deviation from the dashed curve at the point of stationary phase (see the blowup inset of Fig. 3). This point is not necessarily separated by π rad from the adjacent extrema, because it is due to the extremum in $\phi(t)$ and not to the cosinusoidal variation of Eq. (2). Therefore the phase at this point cannot be

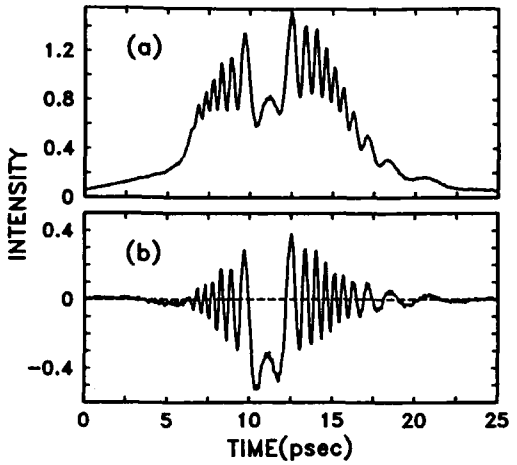

Fig. 4. (a) Output pulse from the interferometer. This quadrature is obtained by a relative phase change of $\pi/2$ of the reference pulse compared with Fig. 2(b). (b) Difference between (a) and the sum of the input pulse [Fig. 2(a)] and the reference pulse.

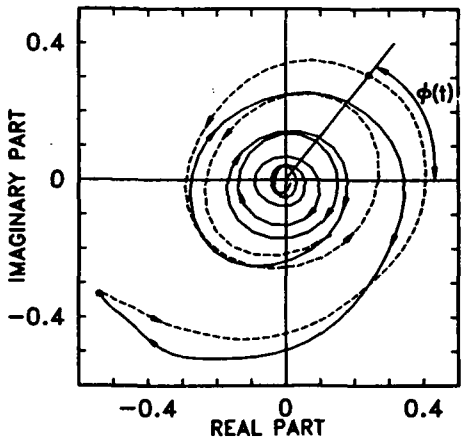

Fig. 5. One quadrature of the field [Fig. 4(b)] plotted versus the other [Fig. 2(c)]. This is equivalent to plotting the slowly varying field in the complex plane. The phase $\phi(t)$ is then the angle subtended from the origin by the corresponding data point.

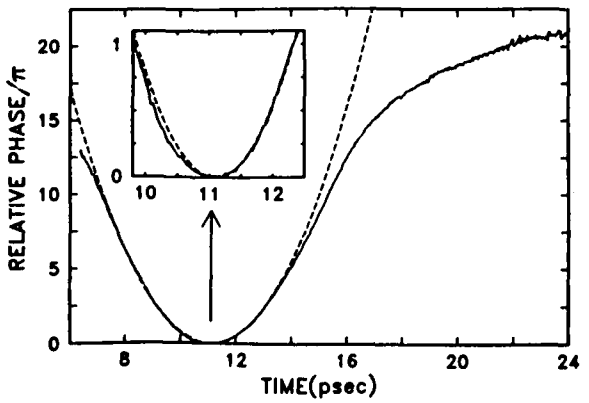

Fig. 6. The relative phase (radians, solid curve) determined from Fig. 5 and the quadratic phase (dashed) due to a 22-cm^{-1}/psec frequency sweep.

easily determined. The amplitude variation of the oscillations, which prevents one from interpolating from the adjacent extrema, has a number of sources: (1) the factor $E(t)R(t)$, (2) the limited resolution of the cross-correlating pulse, which causes the more rapid oscillation to appear smaller, and (3) shot-to-shot variations in the frequency sweep, which blur out the rapid oscillations in the averaged ensemble.

The difficulties described above can be eliminated to a great extent by obtaining the other quadrature of the field, i.e., the imaginary part of Eq. (2). This was achieved by tilting a microscope slide in one arm of the interferometer to give an additional $\lambda/4$ of delay. The resulting interference pattern is shown in Fig. 4(a) and the difference corresponding to Eq. (2) in Fig. 4(b). *Having now measured both the real and the imaginary parts of Eq. (2), we can obtain $\phi(t)$ directly from the arctangent of their ratio, including the absolute sign of $\dot{\phi}(t)$.* In addition, because this is a ratio measurement, the amplitude variation of the modulation is effectively canceled out. An illustrative way of displaying the phase is to plot one quadrature of the field versus the other in the complex plane. Then, as shown in Fig. 5, we obtain the phase as simply the angle subtended by any point from the origin. $\phi(t)$ is continuous because one keeps track of the winding number. Thus we see that the plot winds around the origin first in the direction of decreasing phase (solid line) to the point of stationary phase and then in the direction of increasing phase (dashed line). Note that the curve spiraling down toward the origin is just the result of the decreasing size of the oscillations in Figs. 2 and 4.

The phase obtained from Fig. 5, shown by the solid line in Fig. 6, is compared with a parabolic phase (dashed line). While the agreement in the central region is quite good (see the blowup inset of Fig. 6), it is interesting to note that the disagreement on the edges is quite asymmetric. This could be due to the effects of phase modulation in the fiber for an asymmetric input pulse or to the effects of concomitant Raman scattering.[5] This asymmetry may be the origin of the limits of compression observed recently.[6,7]

This research was partially supported by the U.S. Office of Naval Research.

References

1. H. Nakatsuka, D. Grischkowsky, and A. C. Balant, Phys. Rev. Lett. 47, 910 (1981).
2. W. Dietel, J. J. Fontaine, and J. C. Diels, Optics Lett. 8, 4 (1983).
3. J. E. Rothenberg and D. Grischkowsky, J. Opt. Soc. Am. B 2, 626 (1985); 3, 1235 (1986).
4. J. E. Rothenberg, IEEE J. Quantum Electron. QE-22, 174 (1986).
5. R. H. Stolen and A. M. Johnson, in *Digest of Conference on Lasers and Electro-Optics* (Optical Society of America, Washington, D.C., 1986); A. M. Weiner, J. P. Heritage, and R. H. Stolen, ibid.
6. W. Knox, R. Fork, M. Downer, R. Stolen, C. V. Shank, J. A. Valdmanis, Appl. Phys. Lett. 46, 1120 (1985).
7. S. L. Palfrey and D. Grischkowsky, Opt. Lett. 10, 562 (1985).

Subpicosecond optoelectronic study of resistive and superconductive transmission lines

W. J. Gallagher, C.-C. Chi, I. N. Duling, III, D. Grischkowsky, N. J. Halas,[a)]
M. B. Ketchen, and A. W. Kleinsasser
IBM Thomas J. Watson Research Center, Yorktown Heights, New York 10598

(Received 11 August 1986; accepted for publication 9 December 1986)

We have studed the propagation of subpicosecond electrical pulses on coplanar resistive and superconductive Nb transmission lines. Pulses with 0.9 ps full width at half-maximum were generated and detected by shorting fast photoconductive switches with 80 fs laser pulses. Dramatic improvements in propagation characteristics were achieved when the Nb was superconductive. We observed the strong dispersion and attenuation predicted to occur for frequency components near the superconducting energy gap frequency.

In a recent letter, Ketchen *et al.*[1] reported on the generation, propagation, and detection of subpicosecond electrical pulses on coplanar transmission lines. They were able to generate pulses with measured 1.1 ps (and inferred true 0.6 ps) full width at half-maximum (FWHM) which broadened to 2.6 ps after propagating 8 mm on a low resistance (10 Ω/mm for each line) coplanar aluminum transmission line. In this letter we report on the use of these subpicosecond electrical pulse techniques at variable temperatures (2–300 K) to study transmission lines of vastly varying resistivities, ranging from superconductive to highly lossy. In doing so we have made the fastest optoelectronic sampling measurements on a superconductor and have observed for the first time the predicted sharp onset of attenuation and strong dispersion near the superconducting pair-breaking frequency. In addition, measurements above and below the transition temperature show the dramatic improvement in pulse propagation afforded by superconductive transmission lines. Our optoelectronic sampling technique has proven to be well suited to operation inside a Dewar since all fast electrical signals (0–1 THz) are confined to the sample and only slow signals (0–2 kHz) must leave the Dewar. The technique has distinct advantages in this regard when compared to Josephson sampling techniques[2] which require high-speed electrical inputs to the cryogenic sample. Our use of fast photoconductive switches has allowed the generation and detection of pulses, in contrast to fast rise time steps used in other cryogenic optical sampling measurements.[3]

The transmission line geometries we studied consisted of two equal width (1–5 μm wide) parallel metal lines with separations equal to twice the metal linewidths (see Fig. 1). The lines were made of Nb and fabricated on commercial silicon-on-sapphire substrates (500 nm thick silicon). Lift-off patterning was used for defining 80-nm-thick Nb lines, and plasma etching was used to pattern 150- and 300-nm-thick Nb lines. Subsequent to the Nb deposition and patterning the samples received two blanket oxygen implants of 10^{15} cm^{-2} at 100 and 200 keV. The implant dosage and energy were chosen to heavily damage the Si substrate layer and thereby give the photoexcited carriers a subpicosecond lifetime for the ultrafast operation of the excitation and probe switches. The implant also slightly degraded the superconducting transition temperature of the Nb lines. In the worst case, the 80-nm-thick line had its transition temperature lowered 0.2 to 8.9 K and had a room temperature to 10 K resistivity ratio of 3 and a resistivity at 10 K of $\sim 2\,\mu\Omega$ cm.

After being diced into chips, the transmission line samples were mounted on an insert in a variable temperature Dewar with an optical access window. Cold He vapor provided cooling for the sample, while temperature regulation was achieved by a feedback controlled resistive heater. The Dewar was positioned on an optical bench and 4 cm focal length lenses were used to focus two beams of 80 fs optical pulses from a dispersion compensated, colliding pulse, mode-locked ring dye laser onto the sample generation and detection points.

Electrical pulses were generated when the laser pulses momentarily shorted the photoconductive substrate in the gap region between the two charged lines of the transmission line structure. A fast photoconductive switch that connected the transmission line to an electrical probe sampled the propagating pulses produced at the movable generation point ("sliding contact"). The photoconductive switch at the sampling point was driven by a time delayed probe beam from the same laser that generated the initial electrical pulse. The electrical field of the propagating pulse was sampled by a phase sensitive measurement of the ac current induced in the sampling arm at the frequency at which either the generating or probing laser beam was chopped. By varying the time delay of the probe beam relative to the exciting beam, the time development of the electrical field as it passed the

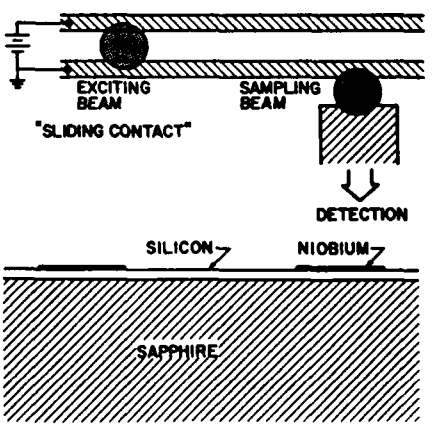

FIG. 1. Top and cross-sectional view of the transmission line geometry.

[a)] Present address: Dept. of Physics and Astronomy, Vanderbilt University, Nashville, TN 37235.

 0003-6951/87/060350-03$01.00 © 1987 American Institute of Physics

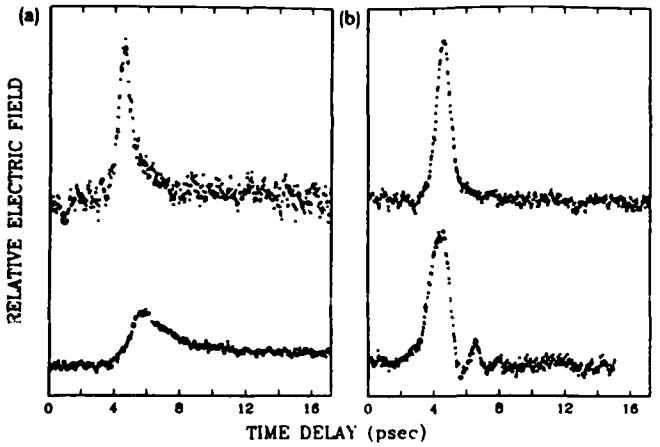

FIG. 2. (a) Pulse shapes after propagating distances of 0.5 (top) and 3 mm (bottom) on a coplanar transmission line composed of 20 Ω/mm Nb lines at 10 K. (b) Pulses after propagating the same distances on the line in the superconducting state at 2.6 K.

sampling point was mapped out. By changing the separation between the sliding contact generation point and the fixed sampling point we could study the evolution of the shape of the electrical pulse as it propagated varying distances.

Figure 2 shows the measured electric field amplitude of pulses propagated distances of 0.5 and 3 mm at temperatures of 10 and 2.6 K on the two-line coplanar transmission line. The 300-nm-thick, 5-μm-wide Nb lines comprising the transmission line had resistances of 20 Ω/mm at 10 K and a superconducting transition temperature of ~9.4 K. The top trace in Fig. 2(a) shows a pulse at 10 K after propagating 0.5 mm. It has a FWHM of 0.9 ps and shows the beginning of a tail developing on its falling edge. By the time the pulse has propagated 3 mm [lower trace in Fig. 2(a)], the pulse energy has degraded to 40% of its initial value and the pulse consists of an initial spike with a 2.3-ps FWHM superimposed on a steplike structure with a height that is 1/3 of the amplitude of the spike. This appearance of a long tail is a characteristic of propagation on lossy lines[4] (as we will discuss later), but the resistance that would be needed to explain the size of the step is about an order of magnitude larger than the dc resistance of this line. For comparison, we note that this pulse is rather severely degraded compared to the relatively good propagation characteristics of pulses on roughly comparable resistivity Al transmission lines at room temperature. Reference 1 reported that similar pulses propagated on a 10-Ω/mm aluminum line broadened to only 2.6 ps after propagating 8 mm.

Figure 2(b) shows the pulses after propagating 0.5 and 3 mm on the same Nb line when it is well into the superconducting state at 2.6 K. After the pulse has propagated 0.5 mm (top trace) on the superconducting line, its FWHM is 1.0 ps, 10% greater than it was for the normal metal state, but there is only a slight tail on the trailing edge. After propagating 3 mm (lower trace) the pulse energy degraded by only 5% and its FWHM broadened to 1.4 ps, but more significantly there is clear ringing on the trailing edge. The ringing is due to the strong dispersion at frequencies approaching the superconducting energy gap frequency of Nb at 0.7 THz and is the first observation of this phenomenon which was predicted by the superconducting transmission line calculations of Kautz[5] based on the Mattis–Bardeen[6] theory for the complex conductivity of superconductors.

Further insight into how superconductivity influences pulse propagation on lines that are highly lossy in the normal state can be gleaned by looking at Fig. 3 where we plot the electric field of a pulse after propagating 0.5 mm on a transmission line composed of two 70-nm-thick, 1.2-μm-wide Nb lines (with $T_c = 8.9$ K) at temperatures of 2.6, 6, and 10 K. The resistance at 10 K of each line in this case was ~450 Ω/mm. There is no evidence of an initial spike on the propagation characteristic in the normal state, which instead appears as a step with a very long tail. The pulses are well preserved on the superconducting lines. The measurement at 2.6 K shows ringing qualitatively similar, but of somewhat smaller relative amplitude than that in Fig. 2(b). The period of the ringing is ~23% shorter in the 2.6 K data than in the 6 K data. If for fixed distance the change in the frequency of the ringing scaled directly with the gap frequency at which strong dispersion occurs, we would have expected a ~15% decrease in the period of the ringing.

Examining the amplitude spectra of pulses propagated on the superconducting transmission line gives insight into the frequency-dependent absorption near the superconduct-

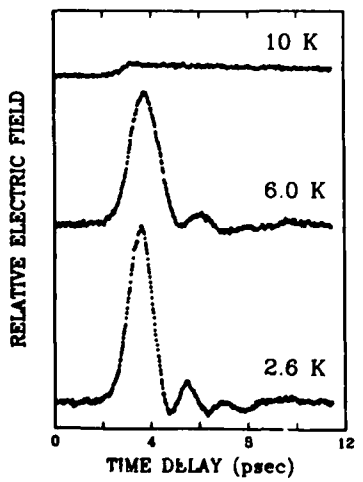

FIG. 3. Pulses after propagating 0.5 mm on a coplanar transmission line composed of 450 Ω/mm Nb lines at 10 K (top trace), 6K (middle trace), and 2.6 K (bottom trace).

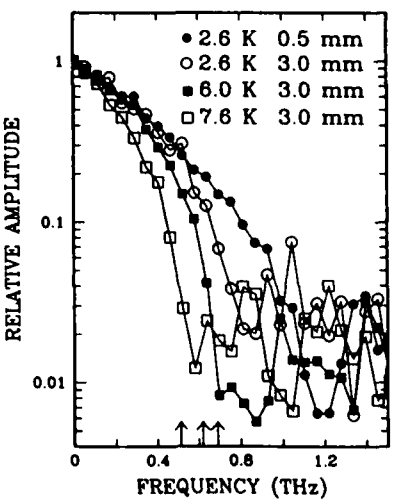

FIG. 4. Amplitude spectra of pulses propagated 3 mm on the 20 Ω/mm Nb line when superconducting at temperatures of 2.6, 6.0, and 7.6 K compared to the amplitude spectrum of the "initial" pulse (i.e., after 0.5 mm of propagation at 2.6 K). The arrows indicate the calculated pair-breaking frequencies at the three temperatures.

ing gap frequency. Figure 4 displays the amplitude spectra of data in Fig. 2(b) for the pulses propagated 0.5 and 3 mm at 2.6 K along with additional data for pulses propagated 3 mm at 6.0 and 7.5 K. With increasing temperature there is a clear decrease in the frequency at which the power is rapidly absorbed into the noise level. The increases in absorption fall very near the estimated values of the pair-breaking frequencies at 2.6, 6.0, and 7.5 K indicated by the arrows in the plot. With increasing temperature there is also an increase in absorption below the pair-breaking frequency due to energy being absorbed by the increasing density of thermally excited quasiparticles. The absorption below the pair-breaking frequency can also be seen to be increasing with frequency. The onset of strong attenuation at the gap frequency and increase in absorption below the gap with increasing temperature and frequency are both in qualitative agreement with the theoretical expectations.[5,6]

The propagation in the normal state is much worse than is expected for propagation on lossy lines characterized by the measured dc resistances. Pulses on lossy lines characterized by (frequency independent) resistances per unit length R, capacitances per unit length C, and inductances per unit length L are exponentially attenuated with a time constant $2L/R$ and have a diffusivelike tail that develops as the main pulse is attenuated. The origin of the two parts of the propagated pulse is easily understood by examining the terms in the lossy line equation

$$\frac{\partial^2 V}{\partial x^2} = LC\frac{\partial^2 V}{\partial t^2} + RC\frac{\partial V}{\partial t}. \tag{1}$$

For $R=0$ this is the ordinary wave equation. For $R>0$ there is an additional diffusive term. The crossover from wavelike behavior to diffusive behavior occurs for frequencies $f<R/2\pi L$. For our most resistive line (the 450 Ω/mm line of Fig. 3), the crossover is at $f\sim 0.09$ THz. Only 10% of the area of our pulses, estimated to have 0.6 ps FWHM (and approximated as Gaussian shaped), is below this frequency. Thus according to Eq. (1) the pulses should mainly propagate as waves and have only small diffusive tails. In contrast, after traveling only 0.5 mm on the 450 Ω/mm line in the normal state at 10 K, the pulse shape shows only a long steplike characteristic. The step rise time of ~0.65 ps is comparable to that of the launched pulse, but the tail is very long. Further measurements on a longer time scale showed that the amplitude of the tail was still 13% of the initial step height 90 ps after the initial rise. Another highly lossy line showed similar propagation characteristics. On the 80-nm-thick, 5-μm-wide Nb lines at room temperature with resistances of 500 Ω/mm, we likewise observed only the step and diffusivelike tail on pulses after they had propagated 0.5 mm.

The frequency dependence of the losses due to the skin effect could account for the observed pulse degradation on the very lossy lines. At 1 Thz the skin depth of the 450 Ω/mm line (~4 μΩ cm) is 100 nm. Current crowding would thus result in an increase of the line resistance near 1 Thz, and an increase of the crossover frequency.[7] In this case, a substantial fraction of the pulse area is in the regime where diffusive propagation dominates. Frequency-dependent losses must also be the source of the observed broadening of propagated pulses on lower resistance normal state Al and Nb lines. [No pulse broadening is expected from Eq. (1) unless some of the transmission line parameters are frequency dependent.] However, the skin effect alone cannot account for the substantially greater distortion of pulses propagating on 20 Ω/mm normal state Nb lines than that of pulses propagating on 10 Ω/mm Al lines.

It is interesting to note that the resistances per unit length of the resistive lines studied in Figs. 2 and 3 span the range of the resistances of metal interconnects in present and future very large scale integrated circuitry. Present minimum feature sizes on integrated circuits are ~1 μm and the ultimate dimensions are believed to be near 0.25 μm.[8] Near room temperature, the resistivity of good metallic films (e.g., Al) is 1–2 μΩ cm, that of typical silicides is > 10 μΩ cm, and that of polysilicon is > 1000 μΩ cm. A 1-μΩ cm conductor with a 1×1 μm cross section has a resistance per unit length of 10 Ω/mm while at 0.25×0.25 μm it would have 160 Ω/mm. It is clear that picosecond pulses on micron sized polysilicon lines will have difficulties propagating any but the shortest of distances (as is well known). Our normal state Nb data suggest that submicron silicide lines will also have trouble maintaining pulse integrity over millimeter distances. For lines with ~0.25 μm cross sections, possibly even the best conductors at room temperature will show the same problems over millimeter distances.

In conclusion, we have demonstrated subpicosecond electrical sampling capability at cryogenic temperatures and used it to study the propagation of subpicosecond electrical pulses on resistive and on superconductive transmission lines. On Nb lines with resistivities on the order of those expected for ~0.25-μm-diam wire, we observed degradation of subpicosecond pulses to diffusivelike pulse with long tails in less than 0.5 mm of propagation. On the same lines well into the superconductive state, we observed good pulse propagation, with significant absorption only above the pair-breaking frequency, but with some ringing associated with strong dispersion near the pair-breaking frequency.

We acknowledge the capable assistance of C. Jessen, R. L. Sandstrom, and M. Smyth for sample preparation and E. Shapiro for pointing out Ref. 4. This research was partially supported by the U.S. Office of Naval Research.

[1] M. B. Ketchen, D. Grischkowsky, T. C. Chen, C.-C. Chi, I. N. Duling, III, N. J. Halas, J.-M. Halbout, J. A. Kash, and G. P. Li, Appl. Phys. Lett. **48**, 751 (1986).

[2] P. Wolfe, B. J. Van Zeghbroeck, and U. Deutsch, IEEE Trans. Magn. MAG-21, 226 (1985).

[3] D. R. Dykaar, T. Y. Hsiang, and G. A. Mourou, in *Picosecond Electronics and Optoelectronics*, edited by G. A. Mourou, D. M. Bloom, and C.-H. Lee (Springer, Berlin, Heidelberg, and Tokyo, 1985), p. 249; D. R. Dykaar, R. Sobolewski, T. Y. Hsiang, G. A. Mourou M. A. Hollis, B. J. Clifton, K. B. Nichols, C. O. Bozler, and R. A. Murphy, Topical Meeting on Ultrafast Phenomena, June 1986, Snowmass, Colorado.

[4] O. Heaviside, Electrician **19**, 295 (1887), reprinted in O. Heaviside, *Electrical Papers* (Chelsea, New York, 1970), Vol. 2, pp. 137–141; E. Hallen, *Electromagnetic Theory* (Wiley, New York, 1962), pp. 409–414.

[5] R. L. Kautz, J. Appl. Phys. **49**, 308 (1978).

[6] D. C. Mattis and J. Bardeen, Phys. Rev. **111**, 412 (1958).

[7] The current concentration also lowers the inductance, cf. R. E. Matick, *Transmission Lines for Digital and Communication Networks* (McGraw-Hill, New York, 1969), pp. 310–354. For our coplanar transmission line geometry, the inductance change is much less significant than the resistance change.

[8] P. M. Solomon, Proc. IEEE **70**, 489 (1982).

Carrier lifetime versus ion-implantation dose in silicon on sapphire

F. E. Doany, D. Grischkowsky, and C.-C.Chi
IBM T. J. Watson Research Center, P. O. Box 218, Yorktown Heights, New York 10598

(Received 10 November 1986; accepted for publication 16 December 1986)

We have measured the dependence of the free-carrier lifetime on O^+ ion-implantation dose in silicon-on-sapphire. At low implant doses, the carrier trapping rate increased linearly with the trap density introduced by ion implantation. At doses above 3×10^{14} cm^{-2} the measured carrier lifetime reached a limit of 600 fs.

The generation of short electrical pulses via optical methods has for some time been performed by driving Auston switches (photoconductive gaps) with short laser pulses.[1] The same techniques can also measure the generated electrical pulses by sampling methods. An alternate measurement approach has been to use the electro-optic effect in a nonlinear crystal.[2] In this case, the field of the electrical pulse is sampled through the rotation of the polarization of the optical sampling pulse. Because the electro-optic method has demonstrated 460 fs time resolution,[3] it is presently considered to be the fastest measurement technique. However, in recent work photoconductive switches have generated and measured subpicosecond electrical pulses.[4] This order of magnitude reduction in the generated pulsewidth demonstrates the ultrafast capability of the Auston switches and challenges the ultrafast time resolution of electro-optic methods. The shape of the electrical pulse generated by the Auston switch depends on the laser pulse shape, the nature of the charge source and the characteristics of the electrical transmission line, and the material properties of the semiconductor. Since laser pulses shorter than 100 fs are routinely obtained from colliding-pulse-mode-locked dye lasers, the laser pulse width can be made negligible compared to the generated electrical pulse. Furthermore, the limiting factors on the time response due to the circuit reactance may be eliminated if the capacitance of the generation site is reduced to negligible amounts. Under these conditions the duration of the electrical pulse would be mainly determined by the carrier lifetime in the semiconducting materials. However, until the measurements presented here, the limits of the carrier lifetimes obtainable were not known.

Although a variety of photoconductive materials has been used in picosecond optoelectronic devices,[1-5] ion-implanted silicon-on-sapphire (SOS) and amorphous silicon have proven to be the fastest materials due to their relatively short free-carrier lifetimes. The reduction of the free-carrier lifetimes is the result of the introduction of defects into the crystalline semiconductor which act as traps and recombination centers. With increasing doses of ion implantation, a systematic series of materials ranging from low defect density to amorphous can be produced thus facilitating studies of the dependence of carrier lifetimes on the density of traps. Previous studies on O^+ implantation dosage deduced carrier lifetimes from photoconductivity measurements and were limited to about 8 ps by laser pulse widths and circuit response times.[6] Later work used a Hertzian dipole configuration of fast photoconductive switches fabricated from ion-implanted SOS to generate and detect freely propagating 1.6 ps electrical pulses,[7] thereby demonstrating that the carrier lifetime was at least this fast. The work describing the generation of subpicosecond electrical pulses[4] ascribed the measured pulse limit to circuit parameters, and a numerical analysis was consistent with a carrier lifetime of 250 fs. In this work we present direct measurements of the carrier lifetimes of a systematic series of SOS samples with a wide range of defect densities introduced through ion implantation.

Optical excitation of silicon generates an electron-hole plasma. The temporal and spatial evolution of the photogenerated free carriers can be probed directly by time-resolved reflectivity and transmission measurements. The contribution of the *e–h* plasma to the reflectivity (and transmission) can be estimated from the Drüde expression for the refractive index:

$$n = n_0(1-\omega_p^2/\omega^2)^{1/2}, \tag{1}$$

where n_0 is the refractive index of the silicon, ω is the probe angular frequency, and the plasma angular frequency ω_p is given by

$$\omega_p^2 = 4\pi N_e e^2/\epsilon m^*. \tag{2}$$

In the above expression N_e is the electron density, m^* is the reduced effective mass for electrons and holes, and ϵ is the background dielectric constant. At high excitation levels, the plasma frequency will exceed the probing frequency. In this case, the index of refraction becomes imaginary leading to strong reflection. At low excitation levels the plasma frequency is less than the probe frequency resulting in a decrease in reflectivity. For the low levels of excitation ($\omega_p < \omega$) the fractional index change due to the *e-h* plasma is directly proportional to the carrier density:

$$\Delta n/n_0 = -(2\pi e^2/\epsilon m^*\omega^2)N_e. \tag{3}$$

Numerous experiments have been carried out to investigate the kinetics of laser-generated electron-hole plasmas and their influence on phase transitions in silicon.[8-12] These experiments used amplified picosecond and femtosecond optical pulses to investigate ultrafast heating dynamics in silicon following pulsed excitation near the melting threshold fluence of approximately 0.1 J cm^{-2} (carrier density $> 10^{20}$ cm^{-3}). At these excitation levels, the reflectivity dynamics are dominated by Auger recombination with carrier-density-dependent rates,[11,12] plasma diffusion in bulk silicon,[10] and lattice heating produced primarily by Auger recombination.[9,11,12] In addition, these high pump laser fluences, even below the melting threshold, can produce temperature in-

 0003-6951/87/080460-03$01.00 © 1987 American Institute of Physics

creases of several 100 °C[9,11] which can partially anneal out the lattice defects. In our experiment the pump laser fluence is kept approximately four to five orders of magnitude below the melting threshold in order to minimize lattice heating effects and carrier-carrier recombination processes (e.g. Auger recombination). The low carrier densities used here (10^{16}–10^{17} cm^{-3}) also eliminate possible effects due to saturation of occupied traps. Furthermore, the use of optically thin films of silicon minimize diffusion of the free carriers from the probing region, since carriers are injected throughout the silicon in the optically pumped region. These conditions assure that the measured carrier lifetimes are primarily determined by the free-carrier trapping and recombination.

The samples used in this study consist of 0.5 μm silicon-on-sapphire wafers that were implanted at room temperature with O^+ ions at 200 and 100 keV energies. These ion energies were chosen to provide a 0.5-μm implant depth with damage dispersed throughout the entire silicon film. The samples with doses ranging from 1×10^{12} cm^{-2} to 1×10^{14} cm^{-2} were implanted with 200 keV ions while the more highly implanted samples (up to 7.5×10^{15} cm^{-2}) received approximately equal doses at both energies.

Time-resolved reflectivity and transmission measurements were obtained following excitation with femtosecond optical pulses. The laser source is a compensated colliding-pulse, mode-locked dye laser producing 70 fs pulses at 625 nm (2.0 eV) at a repetition rate of 100 MHz. These pulses are split into two beams to provide the pump and probe pulses. The average power of the pump beam was in the range 0.1–2.0 mW (1–20 pJ/pulse) and is focused to a diameter of about 10 μm. The probe beam, attenuated to 1–5% of the pump power, is focused to a diameter of about 5 μm. The polarization of the probe beam is rotated by 90° to suppress interferences between the two beams on the sample surface. The pump is incident on the sample at an angle of 30° relative to the normal while the probe is incident on the opposite side of the normal at an angle of 60°. The pump beam is chopped at 1 kHz. Before reaching the sample, the probe beam is additionally split into two beams: one is reflected off the sample onto a photodiode detector and the other, incident directly onto a matched photodiode, is used as a reference. The reflection signal is derived as the difference of these two photocurrents and is detected, using a lock-in amplifier, as a function of time delay between the pump and probe pulses. The sensitivity of our apparatus to changes in the probe beam reflectance is approximately 1 part in 10^6.

Without pumping, the reflectivity at normal incidence of the samples used in this study at 625 nm is relatively constant at a value of 0.2 and increases only slightly at the highest implantation dose. The reflectivity of unimplanted SOS and amorphous silicon is also very similar with values of 0.2 and 0.25. The absorption, however, increases monotonically from 0.3 at a dose 1×10^{12} cm^{-2} to 0.65 at the highest dose of 7.5×10^{15} cm^{-2}. For the unimplanted SOS and amorphous silicon (0.3 μm thickness) the measured absorptions are 0.25 and 0.6, respectively.

The time evolution of the change in reflectivity following photoexcitation of two representative samples is shown in Fig. 1. Figure 1(a) was obtained for an SOS sample ion

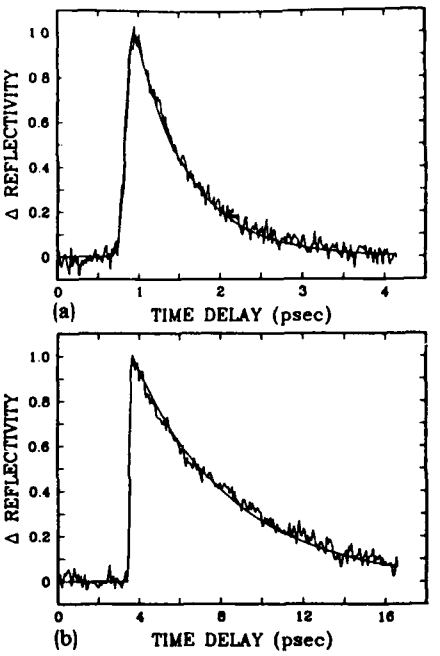

FIG. 1. Measured change in reflectivity for SOS samples ion implanted at doses of (a) 2×10^{15} cm^{-2} and (b) 1×10^{14} cm^{-2}. Smooth curves are fits obtained using a 140 fs instrument response convoluted with (a) 0.65 ps and (b) 4.8 ps exponential decays.

implanted at a dose of 2×10^{15} cm^{-2}, while Fig. 1(b) was obtained at a dose of 1×10^{13} cm^{-2}. The data exhibit a fast rise (<150 fs) followed by a slower recovery back toward normal reflectivity. The peak change in reflectivity ($\Delta R/R$) of the data in Fig. 1 is approximately 10^{-5}. This value is in agreement with the expected index change predicted by Eq. (3) for our experimental conditions ($\Delta n/n_0 \sim 10^{-5}$).

The time evolution of the change in reflectivity is consistent with a pulse width limited rise and an exponential recovery. To obtain fits to the data, we approximated our pump/probe experimental response function as a 140 fs Gaussian. The smooth curves also shown in Fig. 1 were obtained by a convolution of the instrument response with exponential decays of 650 fs [Fig. 1(a)] and 4.8 ps [Fig. 1(b)]. At the signal-to-noise levels of these results, a simple exponential recovery accurately describes the time evolution of the change in reflectivity.

Femtosecond resolved reflectivity data were obtained for a series of SOS samples with a range of implantation doses covering four orders of magnitude and also for amorphous silicon and unimplanted SOS. In attempting to interpret these data, each curve was fit to a single exponential decay time, which varied from >300 ps for the unimplanted SOS wafer down to about 600 fs for the amorphous and the highly implanted samples. These results are summarized in Fig. 2. There are two major regions of interest: the variation of the lifetime at low ion-implantation doses, $<1\times10^{14}$ cm^{-2}, and the lack of dependence at the higher doses, $>3\times10^{14}$ cm^{-2}.

At low implant levels, the lifetime decreases linearly with increasing ion-implantation dose. This is clearly demonstrated by the fit of the low dose data points in Fig. 2 to a

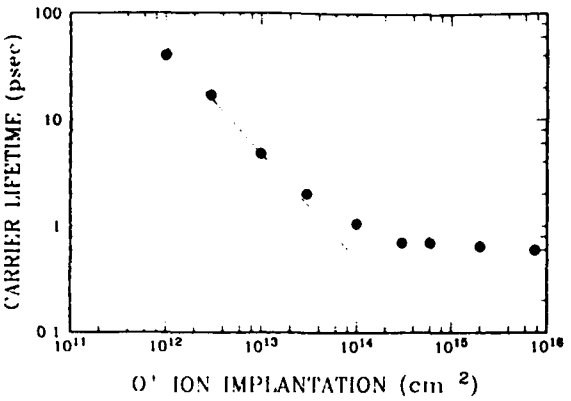

FIG. 2. Carrier lifetime vs ion-implantation dose. Lifetimes are derived from individual reflectivity data at each dose. The solid line shown has a slope of unity.

slope of unity. The linear dependence in this region is consistent with recombination rates proportional to the density of traps introduced by the ion implantation. This behavior is predicted by an expression, valid for low carrier densities, that estimates the capture time τ by traps in crystals as[13]

$$1/\tau = N_t \sigma \langle v \rangle, \tag{4}$$

where N_t is the trap density, σ is the capture cross section, and $\langle v \rangle$ is the average carrier thermal velocity. In this case, the trap density and therefore the free-carrier trapping rate will vary linearly with ion-implantation level.

The variation of lifetime with implantation dosage saturates at a level 3×10^{14} cm^{-2}. Above this dose, the lifetime reaches a limit of 600 fs. This lifetime does not vary even as the implantation dose is increased by more than a factor of 20. Shorter lifetimes are clearly resolvable by our experimental resolution as evidenced by the <150 fs rise times of the data presented in Fig. 1. The approximate 600-fs limit is therefore due to the response of the semiconductor itself. This behavior is not expected from Eq. (4) which predicts a continuous decrease in lifetime with implantation dose.

One possible explanation for the lack of the carrier lifetime dependence on ion-implantation dose is hot-carrier relaxation. The photoexcitation energy of 2.0 eV is significantly larger than the band gap (1.15 eV for pure Si). The 600-fs lifetime limit may therefore represent the thermalization time of the photoexcited carriers as they relax toward the band edge. This process will act as a bottleneck to trapping of the carriers. However, one would not necessarily expect the same relaxation rate for Si at all implant doses, or that only thermalized carriers are trapped. Furthermore, no experimental evidence such as nonexponential behavior in the reflectivity measurements, was observed.

The most probable process limiting the carrier lifetime is amorphization of the crystalline silicon. Above a critical dose of 3×10^{14} cm^{-2} the density of effective traps introduced by implantation saturates and the sample is essentially amorphous. The reflectivity data obtained for amorphous silicon also exhibit the same carrier lifetime of 600 fs. This interpretation is supported by electron spin resonance[14] and third harmonic generation[15] studies on ion-implanted SOS which showed similar saturation effects occurring at critical implantation doses of 10^{14}–10^{15} cm^{-2}.

In summary, we have measured the dependence of the free-carrier lifetime on ion-implantation dose in silicon. At low implant doses, the carrier trapping rate ($1/\tau$) increased linearly with the trap density introduced by radiation damage. At doses above a critical dose of 3×10^{14} cm^{-2} the measured carrier lifetime reaches a limit of 600 fs. This limit is believed to be due to amorphization or a saturation of the effective trap density in the crystalline silicon. For high-speed optoelectronics, the carrier lifetime saturation effect implies that the 0.6-ps electrical pulses produced by Ketchen *et al.*[4] is the limiting pulse width that can be produced using devices fabricated on ion-implanted SOS.

We would like to acknowledge the many stimulating and informative discussions with I. N. Duling, III and J. A. Kash. This research was partially supported by the U. S. Office of Naval Research.

[1]D. H. Auston, in *Picosecond Optoelectronic Devices*, edited by C. H. Lee (Academic, London, 1984), pp. 73–116.
[2]J. A. Valdmanis, G. A. Mourou, and C. W. Gabel, IEEE J. Quantum Electron. QE-19, 664 (1983).
[3]G. A. Mourou, and K. E. Meyer, Chem. Phys. Lett. 45, 492 (1984).
[4]M. B. Ketchen, D. Grischkowsky, T. C. Chen, C. -C. Chi, I. N. Duling, III, N. J. Halas, J-M. Halbout, J. A. Kash, and G. P. Li, Appl. Phys. Lett. 48, 751 (1986).
[5]See, for example, *Picosecond Electronics and Optoelectronics*, edited by G. A. Mourou, D. H. Bloom, and C-H. Lee (Springer, New York, 1985).
[6]P. R. Smith, D. H. Auston, A. M. Johnson, and W. M. Augustyniak, Appl. Phys. Lett. 38, 47 (1981).
[7]D. H. Auston, K. P. Cheung, and P. R. Smith, Appl. Phys. Lett. 45, 284 (1984).
[8]D. von der Linde and N. Fabricius, Appl. Phys. Lett. 41, 991 (1982).
[9]L. A. Lompre, J. M. Liu, H. Kurz, and N. Bloembergen, in *Ultrafast Phenomena IV*, edited by D. H. Auston and K. B. Eisentahal (Springer, New York, 1984), p. 122.
[10]C. V. Shank, R. Yen, and C. Hirlimann, Phys. Rev. Lett. 50, 454 (1983).
[11]L-A. Lompre, J-M. Liu, H. Kurz, and N. Bloembergen, Appl. Phys. Lett. 44, 3 (1984).
[12]M. C. Downer and C. V. Shank, Phys. Rev. Lett. 56, 761 (1986).
[13]C. T. Sah, R. N. Noyce, and W. Shockley, Proc. IRE 45, 1228 (1957).
[14]J. R. Dennis and E. B. Hale, J. Appl. Phys. 49, 1119 (1978).
[15]C. C. Wang, J. Bomback, W. T. Donlon, C. R. Huo, and J. V. James, Phys. Rev. Lett. 57, 1647 (1986).

Ultrafast light-controlled optical-fiber modulator

N. J. Halas,[a] D. Krökel, and D. Grischkowsky
IBM Watson Research Center, P. O. Box 218, Yorktown Heights, New York 10598

(Received 24 November 1986; accepted for publication 3 February 1987)

We report the ultrafast operation of a light-controlled optical-fiber modulator, driven by subpicosecond, compressed, and amplified (6000 Å) dye laser pulses, controlling frequency-doubled (5320 Å) yttrium aluminum garnet laser pulses. The operation of the modulator is based on the optical Kerr effect, and its main component is 7 mm of single-mode optical fiber. Using this system as a light-controlled shutter, we produced either 0.4 ps green light pulses or 0.5 ps holes on the much longer duration second harmonic pulses.

The idea of using one beam of light to modulate a second beam of light has been implemented in many ways based on a number of different physical effects. The pioneering work of Duguay and Hansen[1,2] demonstrating the optically driven Kerr gate, has been a particularly productive approach. Here the driving beam changes the index of refraction of a material by the optical Kerr effect, and thereby changes the polarization of a second beam which is then switched out by a polarizer. This concept is the basis for a number of different modulators using different Kerr materials.[2] A recent example was the switching out of 0.5 ps pulses by optical Kerr gating a 100 ps optical pulse with powerful ultrashort pulses at 1 kHz repetition rates.[3]

One important application is the use of the optical Kerr effect in single-mode fibers for a light-driven optical modulator.[4–6] Here one has the advantage of an enormous reduction in driving power requirements together with an increase in stability due to the long single-mode interaction path. In the initial demonstration of the optical-fiber modulator, response times of microseconds were obtained.[4] Later work has obtained nanosecond response times.[5,6] The closely related nonlinear birefringence effect in fibers has also been proposed for pulse reshaping,[7] which has been demonstrated on the picosecond time scale.[8–10]

In this letter we report the ultrafast operation of a light-controlled optical-fiber modulator, driven by subpicosecond, compressed, and amplified (6000 Å) dye laser pulses controlling either frequency-doubled (5320 Å) YAG laser pulses or Ar ion (5145 Å) laser pulses. The operation of the modulator is based on the optical Kerr effect, and the main component of the modulator is a 7-mm length of low-birefringence single-mode optical fiber. Using this system as a light-controlled shutter, we produced either 0.37 ps green light pulses or 0.46 ps holes (dark pulses) on the much longer duration second harmonic pulses.

A schematic diagram of the experiment is shown in Fig. 1. The driving pulses were the compressed and amplified pulses from a synchronously pumped, mode-locked, tunable dye laser. The initially 6 ps, 6000 Å dye laser pulses were compressed to typically 0.20 ps by passage through an optical-fiber pulse compressor.[11] These compressed pulses were then amplified up to 100 times to a peak power of 400 kW. The amplifier was a 1-cm cell containing rhodamine 610 in water and was pumped by the frequency-doubled output of a mode-locked Nd:YAG laser, Q switched at 700 Hz. The long duration green signal pulses were from either the mode-locked Ar ion laser which pumped the dye laser or the second harmonic pulses from the YAG laser used to pump the amplifier. In order to achieve the shortest switched out pulses, the input powers of the driving pulses and the long duration green pulses were attenuated to 40 kW and to below 1 kW, respectively. These driving and signal pulses were combined on the dichroic beam splitter, adjusted to be temporally coincident, overlapping, and collinear, and were then coupled into the short length of single-mode optical fiber (ITT 1601). The polarization angle of the linearly polarized input signal beam was adjusted by the $\lambda/2$ plate to obtain the best linear polarization of the output signal beam with typical extinction ratios of 1000:1. The input polarization angle of the driving beam was then rotated to obtain the strongest modulation effect. The two output beams from the fiber were recollimated by the output lens and were then separated by the prism. Usually, the driving beam was simply blocked as shown, but with a simple insertion of one mirror it could be measured by the same cross-correlation arrangement. The green signal beam then traversed the polarizer which is shown in the figure to be oriented to transmit the signal beam in the absence of the driving pulses. This configuration produced dark pulses when the driving pulses were applied. The corresponding light pulses were reflected from the polarizer. Alternatively, the polarizer could be set to pass the light pulses and reflect the dark pulses. The output pulses from the polarizer were measured by cross correlation with the 0.20 ps probing pulses obtained by a partial reflection from the beam of amplified pulses. All the pulse widths stated are the deconvolved values taking into account the 0.20 ps width of the probing pulse. Typically, the deconvolved pulse width is 0.1 ps less than the measured cross-correlation value.

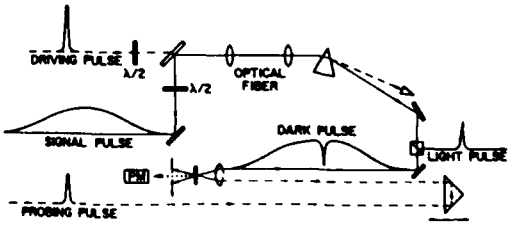

FIG. 1. Schematic diagram of the experiment.

[a] Present address: The Center for Atomic and Molecular Physics at Surfaces, Department of Physics and Astronomy, Vanderbilt University, Nashville, TN 37235.

 0003-6951/87/140886-03$01.00 © 1987 American Institute of Physics

The actual cross-correlation signal was obtained by the noncollinear generation of second harmonic light in a 300-μm-thick potassium dihydrogen phosphate (KDP) crystal. The generated light was monitored by a photomultiplier connected directly to a boxcar integrator, which in turn was connected to a multichannel analyzer. The analyzer was synchronized with the delay setting of the correlator as determined by a computer-controlled stepping motor. In order to reduce the effect of pulse to pulse fluctuations, the light pulse was monitored by a photodiode connected to a discriminator, which triggered the boxcar only if the energy of the light pulse was within a narrow window. Although this selection procedure reduced the data rate to about 200 pulses per second, it increased the signal-to-noise ratio so that only single scans of the correlator delay were required. A typical scan was made in about 100 s.

Our measurement of the 0.46 ps dark pulse on the 103 ps output signal pulse is shown in Fig. 2(a). The modulation depth of 1/4 was partially limited by the response time of our detection system. A slower higher resolution scan is shown in Fig. 2(b), where the modulation depth and pulse width are measured to be 1/3 and 0.46 ps, respectively. When the polarizer was rotated by 90°, we obtained the 0.37 ps light pulse displayed in Fig. 2(c). The switched-out light pulse is quite sharp with not much energy in the wings. This is in accord with the wing clipping feature of the modulator[8,10] with respect to the driving pulse. The peak of the light pulse is approximately as strong as the dark pulse, i.e., 1/3 of the strength of the coupled 500 W signal pulse. This gives an energy of 70 pJ in the light pulse. The fact that these pulse widths are approximately twice that for the 0.20 ps amplified pulses calls for some explanation to be given below.

We show the autocorrelation of the probing pulse in Fig. 3(a); the basic pulse shape is quite good and the narrow wings indicate that the optical fiber pulse compressor was operating in the enhanced chirping mode.[12] These data were numerically deconvolved and a good fit was obtained with a pulse width of 0.20 ps and a pulse shape similar to a sech^2 in the central region, but with more extensive wings. The measured driving pulse after passage through the 7-mm-long fiber is shown in Fig. 3(b). Here we see that the initial 0.20 ps amplified pulse has broadened to 0.37 ps. Initially we thought the observed broadening was due to passage through the 7 mm fiber. However, subsequent theoretical analysis could not account for this broadening, and later experimental measurements showed that the pulses were broadened mainly by the focusing and collimating lenses used with the fiber. With the fiber removed, the initially 0.20 ps pulses broadened to approximately 0.35 ps due to passage through these lenses. Passage through the fiber did not significantly further broaden the driving pulse. The driving pulse coupled into the fiber was about 0.3 ps due to broadening by the focusing lens. The collimating lens should not broaden the switched-out dark and light pulses because of their much narrower bandwidths.

A broadening effect on the switched-out pulses is the group velocity difference between the input (5320 Å) and driving (6000 Å) pulses. For 7 mm of fused quartz the difference in transit times for the two pulses is 0.18 ps, which

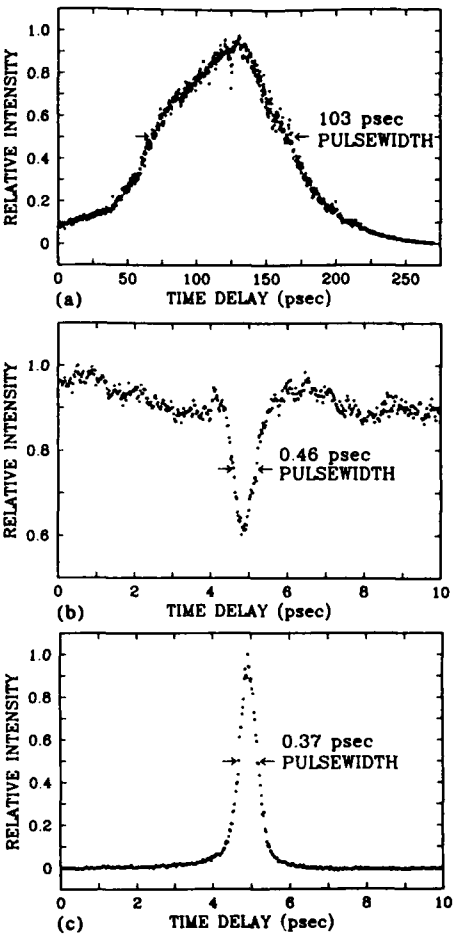

FIG. 2. (a) Cross-correlation measurement of the dark pulse on the second harmonic YAG pulse. (b) Cross-correlation measurement of the dark pulse. (c) Cross-correlation measurement of the light pulse.

implies that for an infinitely narrow driving pulse, the output dark and light pulses would have pulse widths of 0.18 ps. Another effect is phase modulation of the output signal pulses. The optical Kerr effect, due to the linearly polarized driving pulse, induces onto the weak optical signal beam a different amount of intensity-dependent phase parallel and perpendicular to the polarization axis of the driving pulse. Because we are using a low-birefringence optical fiber, we are in the short-fiber limit for our 7 mm fiber length, and can assume the optical fiber to be isotropic. The intensity-dependent phase of the signal component along the axis of the driving pulse is $\Phi_1(t) = 2\pi n_2 E(t)^2 z/\lambda$, whereas the component of the weak signal beam perpendicular to the driver acquires the intensity-dependent phase $\Phi_2(t) = 4\pi n_2 E(t)^2 z/3\lambda$, where n_2 is the nonlinear index, E is the field strength of the driving beam, z is the propagation distance (fiber length), and λ is the wavelength of the signal beam. For switching applications, this leads to a phase difference between these two components of

$$\phi(t) = \Phi_1(t) - \Phi_2(t) = 2\pi n_2 E(t)^2 z/3\lambda \, .$$

The optical phase transmitted through the polarizer can be shown to be $\Phi_T(t) = [\Phi_1(t) + \Phi_2(t)]/2$. For a maximum phase difference $\phi(t)$ of $2\pi/5$, corresponding to the observed depth of modulation of the dark pulse, we obtain a predicted bandwidth due to phase modulation of $(\partial\Phi_T)/\partial t = 48\ \mathrm{cm}^{-1}$ or 14 Å. This value compares well to the mea-

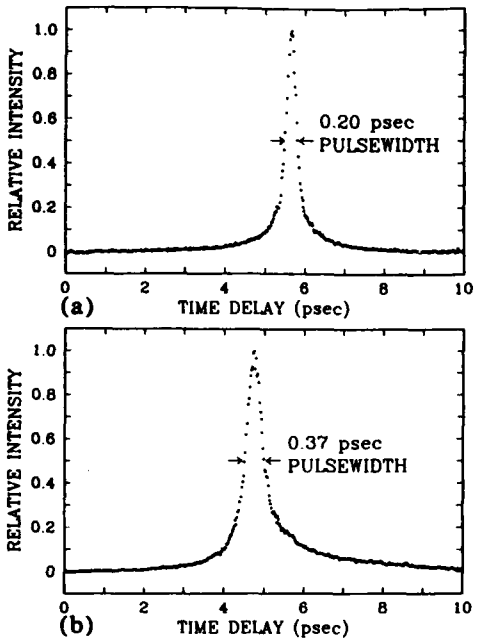

FIG. 3. (a) Autocorrelation measurement of the probing pulse. (b) Cross-correlation measurement of the output driving pulse.

sured bandwidth of 10 Å for the output light pulse. As the driving power was reduced the bandwidth of the light pulse decreased to a limiting value of 8 Å, which is equal to the transform limit of a 5300 Å, 0.4 ps, $\mathrm{sech}^2(t)$ pulse. The bandwidth of the driving pulse was 50 Å and did not change due to passage through the fiber.

These effects were treated quantitatively in a numerical calculation based on the theory of the Kerr effect in an isotropic, single-mode fiber. Our calculation included group velocity mismatch between the driver and the signal beams, group velocity dispersion at both the driver and signal wavelengths, and the third-order nonlinear polarization terms relevant for self-phase modulation, intensity-dependent polarization change, and the two-frequency interaction of the Kerr effect.[13] The calculated output dark and light pulses for our experimental conditions[14] are shown in Fig. 4, as well as the calculated output driving pulse (not to scale). The calculated output driving pulse shape does not significantly change due to passage through the fiber. Because of the group velocity difference between the driving and signal pulses, the switched-out light and dark pulses are broader than that of the driving pulse squared.[8,10] Also, the peak of the driving pulse comes before the peaks of the switched-out pulses. As can be seen, agreement with our experimentally obtained modulation depth and output pulse widths is good considering the nonlinear nature of the problem.

It is of interest to consider that this modulator can transfer information from one light beam to another at a potentially very high data rate. In the present experiment the data rate was limited to the 700 Hz repetition rate of the laser amplifier. However, if the wavelengths of the signal and driver beams are closer together and operate closer to the wavelength of minimum group velocity dispersion of the optical fiber, fiber lengths of the order 100 cm or more could be used. This situation would eliminate the need for the laser amplifier and repetition rates of 100 MHz, typical of mode-

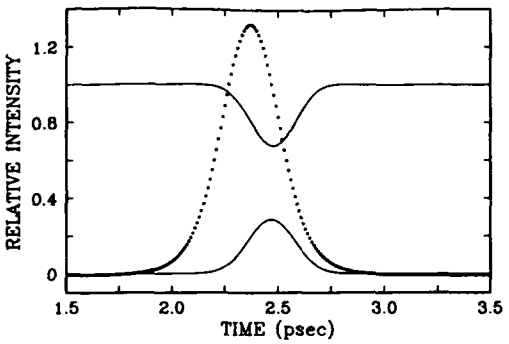

FIG. 4. Calculated dark and light pulses. The dotted line shows the calculated output driving pulse.

locked lasers, would be possible. A factor of ten increase in the data rate above the laser pulse rate would be reasonable using pulse splitting procedures. However, further increases are limited by the power handling capabilities of optical fibers and by the output powers of present day laser systems. One way of bypassing the power limit of a single fiber would be to use a matrix of fibers and sequentially switch from one to the other. A more fundamental approach would be to develop nonlinear materials compatible with fiber technology. A cw data rate, limited only by the response time of the modulator, requires a fiber core 1000 times more nonlinear than fused silica and pulse splitting techniques capable of generating 10 000 uniformly spaced pulses from a single powerful subpicosecond pulse.

In summary, we have demonstrated subpicosecond operation of an ultrafast light-controlled optical-fiber modulator, which can produce either dark or light pulses. The modulator can also operate as an AND gate with subpicosecond response times. Such a modulator can transfer information from one light beam to another at potentially very high data rates. In addition, the modulator can provide a source of synchronized, subpicosecond, tunable, second-frequency pulses for ultrafast measurement applications.

This work was partially supported by the U.S. Office of Naval Research.

[1]M. A. Duguay and J. W. Hansen, Appl. Phys. Lett. 15, 192 (1969).
[2]M. A. Duguay, Prog. Opt. 14, 163 (1976).
[3]I. N. Duling III (private communication).
[4]R. H. Stolen and A. Ashkin, Appl. Phys. Lett. 22, 294 (1973).
[5]J. M. Dziedzic, R. H. Stolen, and A. Ashkin, Appl. Opt. 20, 1403 (1981).
[6]K. Kitayama, Y. Kimura, K. Okamoto, and S. Seikai, Appl. Phys. Lett. 46, 623 (1985).
[7]R. H. Stolen, J. Botineau, and A. Ashkin, Opt. Lett. 7, 512 (1982).
[8]B. Nikolaus, D. Grischkowsky, and A. C. Balant, Opt. Lett. 8, 189 (1983).
[9]L. F. Mollenauer, R. H. Stolen, J. P. Gordon, and W. J. Tomlinson, Opt. Lett. 8, 289 (1983).
[10]N. J. Halas and D. Grischkowsky, Appl. Phys. Lett. 48, 823 (1986).
[11]H. Nakatsuka, D. Grischkowsky, and A. C. Balant, Phys. Rev. Lett. 47, 910 (1981); B. Nikolaus and D. Grischkowsky, Appl. Phys. Lett. 42, 1 (1983); A. C. Balant and D. Grischkowsky, U.S. Patent No. 4 588 957 (13 May 1986).
[12]D. Grischkowsky and A. C. Balant, Appl. Phys. Lett. 41, 1 (1982).
[13]N. J. Halas, "Ultrafast Modulation of Light by Light," Ph.D. thesis, Bryn Mawr College, Bryn Mawr, PA, 1986.
[14]50% of the energy of the input 0.3 ps driving pulse was coupled into the 4-μm-diam fiber. The best fit was obtained with a peak power in the fiber of 25 kW, compared to the experimental value of 15 kW. The nonlinear index $n_2 = 1.1 \times 10^{-13}$ esu. GVD at 5300 Å was 1.3 times larger than the GVD at 6000 Å, where GVD = (0.034 ps/Å m).

Far infrared spectroscopy with subpicosecond electrical pulses on transmission lines

R. Sprik,[a] I. N. Duling, III, C.-C. Chi, and D. Grischkowsky
IBM T. J. Watson Research Center, P. O. Box 218, Yorktown Heights, New York 10598

(Received 30 April 1987; accepted for publication 18 June 1987)

Optically generated and detected electrical pulses on transmission lines in the subpicosecond range have frequencies extending up to 1 THz, thereby covering the far infrared region of the spectrum from 0 to 30 cm^{-1}. We have studied the propagation of these short pulses through a section of the transmission line covered with erbium iron garnet which shows distinct absorption lines in the far infrared at low temperatures (2–30 K). The absorption and dispersion of the garnet modify the shape of the pulse, and the absorption spectrum is obtained by Fourier transforming the propagated pulse shape.

Recently optoelectronic techniques have been used to generate and detect subpicosecond electrical pulses on coplanar transmission lines.[1,2] The frequency bandwidth of these short electrical pulses ranges up to 1 THz and covers an interesting part of the far infrared energy spectrum (0–30 cm^{-1}, $\lambda > 330\,\mu m$) in which can be found the gap frequencies of superconductors, magnetic excitations, and the far infrared modes in lattices and molecules. This situation, plus the fact that the earlier observations showed that the subpicosecond pulses broadened to only 2.6 ps after propagating 8 mm on the transmission line, encouraged us to consider spectroscopic applications of these guided wave electrical pulses.

The recent use of superconducting transmission lines showed that by observing pulse reshaping as a function of propagation distance, the frequency-dependent absorption and dispersion of the line could be obtained. The absorption sharply increased at the frequency associated with the breaking of the Cooper pairs in the superconducting niobium metal lines.[2] In this letter we demonstrate that this time domain optoelectronic technique can be more generally used for far infrared spectroscopy by covering a section of the transmission line with an absorbing material and studying the consequent reshaping of the transmitted pulse. We demonstrate the feasibility of this spectroscopic method by measuring the magnetic resonances in erbium iron garnet (ErIG) and studying the temperature dependence of the frequencies between 2 and 30 K. The particular choice of ErIG was guided by the fact that this system is known to have sharp absorption resonances in the currently accessible spectral range of the technique and was readily available to us.

The optoelectronic generation of short electrical pulses is based on the temporary shorting of the charged transmission line by carriers excited in the photoconductive material (ion-implanted Si on sapphire) underneath the lines with a short laser pulse. The minimum electrical pulse width, which is measured by the same electro-optic technique, appears to be limited by the lifetime of the photoexcited carriers in the photoconductive material.[3] Figure 1 shows the experimental arrangement, the coplanar transmission line, and the focused spots of the laser, where the electrical pulse is generated by focusing the exciting beam between the lines ("sliding contact") and detected after propagation by the sampling beam focused on the gap. By scanning the time delay between the exciting beam and the sampling beam one measures the pulse shape. Both beams are derived from the same laser, a prism-compensated, colliding-pulse, mode-locked, dye laser producing 70-fs pulses at a repetition rate of 100 MHz.[4] The exciting beam is chopped at 2 kHz and the resulting photocurrent signal is detected as a function of time delay with a lock-in amplifier, whose output is stored in a computer for further processing.

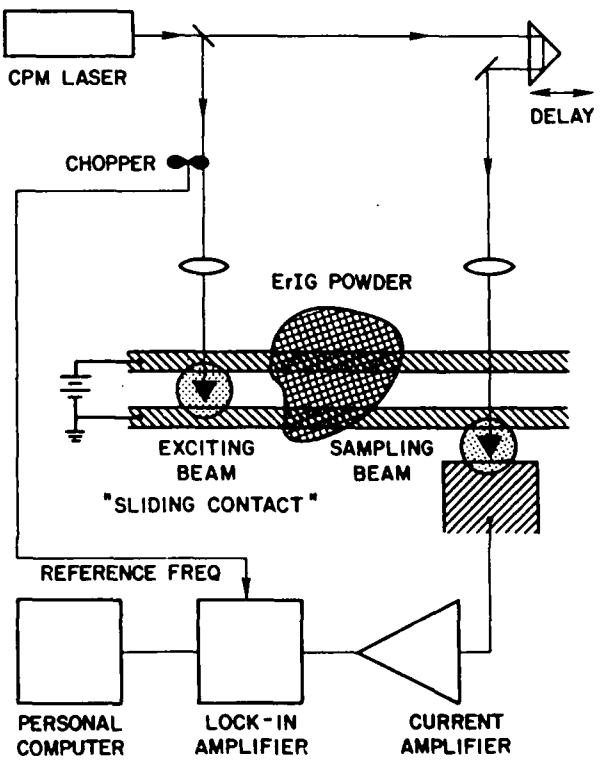

FIG. 1. Schematic diagram of the experimental arrangement together with the coplanar transmission line configuration.

[a] Permanent address: Natuurkundig Laboratorium, Universiteit van Amsterdam, Valckenierstraat 65, 1018 XE Amsterdam, The Netherlands.

 0003-6951/87/330548-03$01.00 © 1987 American Institute of Physics

The transmission lines used in this work have a characteristic impedance of 100 Ω and are composed of two coplanar aluminum lines with a linewidth of 5 μm and a spacing double the linewidth. The metal lines were deposited on commercial silicon-on-sapphire substrates. After lift-off patterning of the aluminum, the samples were implanted with oxygen to shorten the lifetime of the photoexcited carriers below 1 ps. Performances of these lines are described in detail by Gallagher *et al.*[2] A small section (2–3 mm) of the transmission line was covered with a thin layer of powder of the infrared-absorbing material. The samples were mounted in an optical ^{4}He flow cryostat enabling measurements between 2 and 300 K. Since the photocurrent was modulated at 2 kHz, the electrical wiring of the cryostat could be simple and did not require high-frequency performance.

Figure 2(a) shows the shape of the propagated electrical pulse without any powder sample on the transmission line at 5 K. The pulse is shown as it was used for the numerical analysis, with the data truncated at 10 ps. Room-temperature scans have confirmed that no extraneous reflections are present in the truncated region. When the line was covered with ErIG the pulse shape dramatically changed to that shown in Fig. 2(b), where strong oscillation is now seen for the longer time delays. This time domain measurement is converted to the frequency domain in Fig. 2(c), by Fourier transforming the two propagated pulse shapes. The resulting spectra show that when the sample is in place, strong resonances appear at the frequencies 10.0 and 4.3 cm^{-1} at $T = 5$ K. A crude estimate of the spectral resolution of the technique based on a total delay time scan of 45 ps is $\simeq$0.7 cm^{-1}. The measured linewidth, especially for the higher frequency mode, is $\simeq$1.5 cm^{-1}, clearly broader than the spectral resolution. We identify these observed lines as magnetic resonances in ErIG, which we will now discuss.

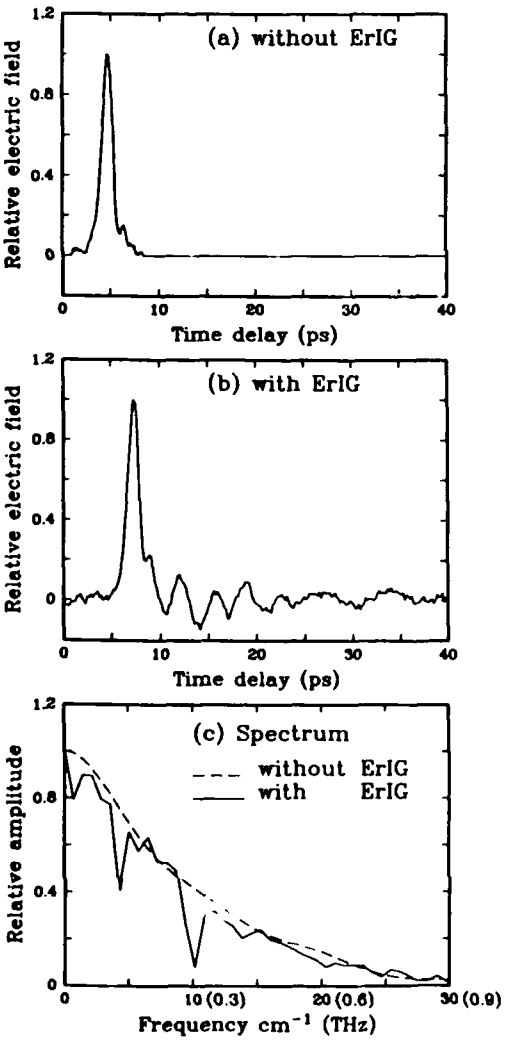

FIG. 2. Pulse shape after propagation on a transmission line without (a) and with (b) ErIG powder covering the line. The Fourier transform (c) of the propagated pulse (b) shows distinct absorption at the exchange 10.0 cm^{-1} and the ferrimagnetic 4.3 cm^{-1} resonance in ErIG ($T = 5$ K).

Rare-earth iron garnets ($5Fe_2O_3 \cdot 3R_2O_3$) display a number of well-known sharp resonances in the far infrared range of the spectrum relevant for the current experiments.[6,7] These garnets have two magnetic modes which originate from the exchange resonance[8] between the iron and the rare-earth sublattices in the ferrimagnetic ordered material. The anisotropy in the coupling results in a low frequency mode of ferrimagnetic nature.[7] At somewhat higher frequency are two resonances in the rare-earth garnets associated with the exchange field splitting induced by the iron lattices. These resonances have all been observed and extensively studied in YbIG. The exchange resonance has been observed for the first time by Sievers and Tinkham[9,10] in YbIG using a far infrared monochromator. The temperature dependence of the frequency confirmed their model[7] for the anisotropic coupling in the rare-earth iron garnets. Using a spectrometer with an extended spectral range, Richards[11] observed the exchange resonance and in addition the predicted ferrimagnetic resonance in YbIG. ErIG, which we used for our study, is expected to behave analogously to YbIG and has been studied in some detail by Sievers and Tinkham.[10] In particular for ErIG the exchange resonance was observed at 10.0 cm^{-1} ($T = 2$ K), which is consistent with our measurement of 9.6 cm^{-1} ($T = 2.5$ K). Sievers and Tinkham could not observe the ferrimagnetic resonance in ErIG because it was outside their detection range. To our knowledge the ferrimagnetic resonance in ErIG which we observe at 4.3 cm^{-1} has not been reported previously. Based on simple arguments considering the observed exchange field splitting and exchange resonance, the ferrimagnetic resonance should be at $\simeq$2 cm^{-1}. The same arguments in the case of YbIG predict the ferrimagnetic resonance to be at 4 cm^{-1},[6,7] while the observed line is at 3 cm^{-1}.[11] A better agreement between theory and experiment can only be expected after a more detailed analysis of the garnet system. We do not observe the resonances in ErIG associated with the exchange splitting which Sievers and Tinkham measured at 18.2 and 21.6 cm^{-1}, most likely because our available IR power is considerably reduced between 20 and 30 cm^{-1}, compared to the lower frequency ranges. With an improved signal-to-noise ratio, we should also be able to resolve these lines.

As mentioned before, the magnetic resonances display a frequency shift as a function of temperature which depends intricately on the various coupling parameters in the garnet

system. Figure 3 shows the temperature dependence of the exchange and the ferrimagnetic resonance in ErIG derived from our far infrared absorption measurements. Especially the exchange resonance shifts upwards as a function of temperature from 9.6 cm^{-1} at 2.5 K to 12.1 cm^{-1} at 25 K. This temperature dependence is qualitatively consistent with the measurements on YbIG and the report by Tinkham[6] for ErIG. We did not try a more detailed analysis of the temperature dependence, since the appropriate anisotropy coefficients are not well known for ErIG. The observed shifts clearly illustrate the fact that the observed absorption lines are an intrinsic property of the garnet powder and not an artifact of the transmission line technique.

The new technique has a number of advantages and disadvantages in comparison with the traditional cw far infrared spectroscopic techniques based on a mercury arc light source and a monochromator or interferometer.[5] A cw light source has typically $\simeq 10^{-10}$ W available in a bandwidth of 1 cm^{-1},[6] and an infrared interferometer has a spectral resolution better than 0.1 cm^{-1}. The accessible spectral range of such a system is usually from a few cm^{-1} to many hundreds of cm^{-1}. The generated 1-ps electrical pulse (10 mV amplitude) at a 100-MHz repetition rate generates an average cw power of 10^{-10} W. This power is distributed in amplitude of the spectral components as shown in Fig. 2(c). From this spectrum we calculate that for the frequency of 10 cm^{-1}, $\simeq 2\times 10^{-12}$ W is available within a 1 cm^{-1} bandwidth. However, the effective power is enhanced a factor $\simeq 250$ due to the fact that the actual measurement occurs only during the 45 ps-scan time. This makes the effective available infrared power comparable with cw sources. Similar to an infrared interferometer, the optoelectronic technique detects the electric field and not the intensity. This feature makes the technique sensitive to changes in phase and amplitude of the interfering spectral components resulting in an excellent signal-to-noise ratio with modest infrared power. The current spectral resolution of $\simeq 0.7$ cm^{-1} can be increased simply by extending the delay time scan beyond 45 ps. In order to be able to do this, it is essential to eliminate reflection from the ends of the transmission lines, because these will disturb the actual measurements. Currently the spectral range of the pulse technique is between 1 and 30 cm^{-1}, covering frequencies from the microwave range up to the more readily accessible far infrared frequencies. Because the electrical pulses propagate as a guided wave along the transmission line, the electric and magnetic fields are strongly localized at the surface. This feature makes the technique quite suitable for studying surface excitations. Furthermore, the required amount of sample is very limited since only the area near the transmission lines has to be covered. Perhaps the most attractive feature is the possibility of time-resolved far infrared spectroscopy on a picosecond time scale, especially when the available far infrared power can be enhanced to a level where the population of the magnetic levels is strongly influenced. For this case, one can consider applying the technique to observe spin echos from magnetic excitations in the far infrared. The power of the pulse can be increased significantly by amplifying the exciting laser pulses. Preliminary attempts show that electrical pulses of the order of 1 V can be produced, thereby increasing the available power by four orders of magnitude. These unique features of the optoelectronic technique clearly offer new possibilities for the study of far infrared transitions.

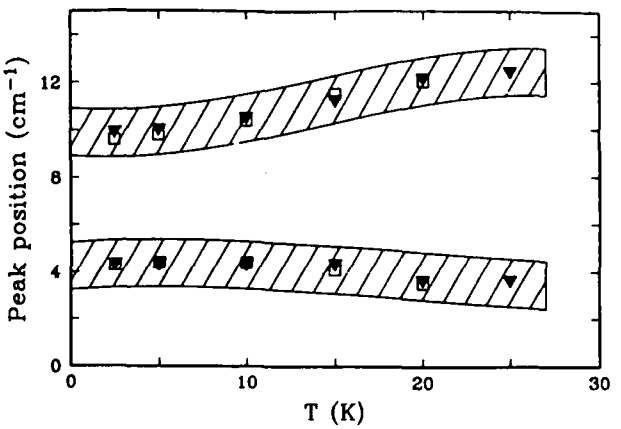

FIG. 3. Temperature dependence of the exchange and the ferrimagnetic resonance in ErIG. The different symbols are of two different runs with the same sample. Shaded area indicates the resolution of the data.

We thank E. Giess for the ErIG sample, M. B. Ketchen for the chip design, and C. Jessen for help fabricating the transmission lines. This work was partially supported by the U.S. Office of Naval Research.

[1]M. B. Ketchen, D. Grischkowsky, T. C. Chen, C.-C. Chi, I. N. Duling III, N. J. Halas, J.-M. Halbout, J. A. Kash, and G. P. Li, Appl. Phys. Lett. **48**, 751 (1986).
[2]W. J. Gallagher, C.-C. Chi, I. N. Duling, III, D. Grischkowsky, N. J. Halas, M. B. Ketchen, and A. W. Kleinsasser, Appl. Phys. Lett. **50**, 350 (1987).
[3]F. E. Doany, D. Grischkowsky, and C.-C. Chi, Appl. Phys. Lett. **50**, 460 (1987).
[4]J. A. Valdmanis, R. L. Fork, and J. P. Gordon, Opt. Lett. **10**, 131 (1985).
[5]In the present discussion we will only consider broadband sources and exclude monochromatic sources based on nonlinear generation schemes with laser pulses. For a discussion of these methods see, e.g., K. H. Yang, J. R. Morris, P. L. Richards, and Y. R. Shen, Appl. Phys. Lett. **23**, 669 (1973) and Y. R. Shen, ed., *Nonlinear Infrared Generation* (Springer, Berlin, 1977).
[6]M. Tinkham, J. Appl. Phys. Supp. **33**, 1248 (1962).
[7]M. Tinkham, Phys. Rev. **124**, 311 (1961).
[8]J. Kaplan and C. Kittel, J. Chem. Phys. **21**, 760 (1953).
[9]A. J. Sievers, III and M. Tinkham, Phys. Rev. **124**, 321 (1961).
[10]A. J. Sievers, III and M. Tinkham, J. Appl. Phys. **34**, 1235 (1963).
[11]P. L. Richards, J. Appl. Phys. **34**, 1237 (1963).

Electromagnetic Shock Waves from Transmission Lines

D. Grischkowsky, I. N. Duling, III, J. C. Chen, and C.-C. Chi
IBM Watson Research Center, Yorktown Heights, New York 10598
(Received 15 June 1987)

We have observed subpicosecond electrical pulses to propagate on 5-μm coplanar transmission lines at velocities faster than the phase velocity in the underlying dielectric. This situation produces an electromagnetic shock wave in a manner similar to Cherenkov radiation and electro-optic Cherenkov radiation. Using time-domain spectroscopy, we have measured the strong frequency-dependent loss of energy in the propagating electrical pulse due to this radiation.

PACS numbers: 41.10.−j, 03.50.−z, 84.40.−x

Electromagnetic radiation is emitted when electric charges are accelerated while the uniform motion of electric charges does not cause the emission of radiation. However, Cherenkov has shown that, when charges move faster than the phase velocity for electromagnetic radiation in a material, radiation is emitted as an electromagnetic shock wave.[1] The initial analysis of this effect was for electric monopoles, but the physical picture holds true for higher-order moments as well.

Auston has recently demonstrated that it is possible to produce an electric dipole moving faster than the appropriate phase velocity in a dielectric, and thereby to produce an electromagnetic shock wave.[2,3] This dipole, which is caused by an ultrashort laser pulse driving the optical rectification effect in a nonlinear dielectric material, has the same spatial distribution as the laser pulse. When the group velocity of light (and, consequently, the speed of the dipole) is faster than the phase velocity for terahertz radiation, an electromagnetic shock wave is produced. This situation has been verified in detail in Auston's experiments and theoretical analyses.

In this paper we describe another very general physical situation which can also yield emission of electromagnetic shock-wave radiation. This case involves the propagation of ultrashort electrical pulses on a metallic transmission line on the surface of a semi-infinite dielectric substrate. Associated with these propagating electrical pulses are electric multipoles determined by the number of metal lines making up the transmission line and the characteristics of the propagating mode. For example, with two metal lines the TEM mode has an electric dipole moment and a consequent dipolar field distribution, while for three lines a quadrupole moment is possible. When the dielectric constant is greater than unity, the group velocity for electric pulses propagating on these lines (and consequently the associated multipoles) will be faster than the phase velocity in the dielectric. Thus in the dielectric we have the situation shown in Fig. 1(a), which includes radiation of an electromagnetic shock wave in the form of a Cherenkov-type cone.

In this Letter we present time-domain measurements of the attenuation versus frequency for the spectral components of the propagating electrical pulse, due to the radiation of the electromagnetic shock wave. This loss is so severe that after propagating only 1 mm, power at 0.8 THz is reduced to $1/e$ of its original value. Previous frequency-domain studies have calculated the radiative loss for single-frequency transmission on coplanar metal lines on dielectrics.[4] These results have been confirmed by experimental measurements up to 1 GHz,[4] where the radiation loss is only 10^{-9} of that reported here. Our observed frequency-dependent absorption remains in

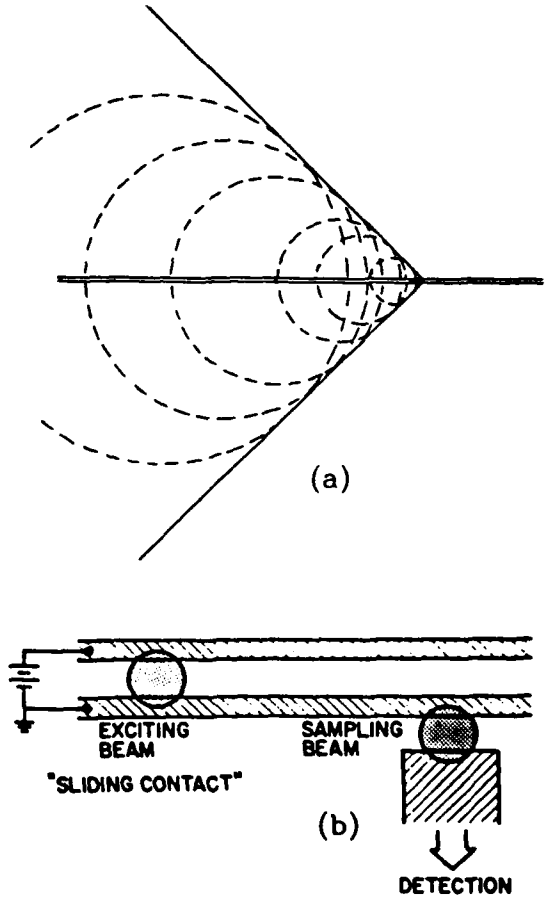

FIG. 1. (a) Cherenkov cone in the dielectric half space; (b) experimental geometry.

© 1987 The American Physical Society

good agreement with this calculation, even though our spectrum extends to 1 THz. At these high frequencies, the time-domain Cherenkov picture provides a simple intuitive description of the generation of the electromagnetic shock wave and of the radiation process associated with the propagating ultrashort electrical pulse.

The experimental situation shown in Fig. 1(b) is similar to that used previously.[5] Here the subpicosecond electrical pulses are obtained by photoconductive shorting of the charged coplanar transmission line with 70-fsec pulses from a colliding-pulse mode-locked dye laser. This method of pulse generation ensures a pure dipolar pulse. The resulting electrical pulses were measured by a fast photoconductive switch, driven by a time-delayed beam of the same 70-fsec laser pulses, which connected the transmission line to an electrical probe. In order to measure propagation effects, the excitation point (sliding contact) was moved variable distances away from the sampling photoconductive switch.

The 20-mm–long transmission line had a design impedance of 150 Ω and consisted of two parallel 5-μm-wide, 0.5-μm-thick aluminum lines separated from each other by 15 μm. The measured dc resistance of a single 5-μm line was 200 Ω. The transmission line was fabricated on an undoped silicon-on-sapphire wafer, which was then heavily implanted with O^+ ions to ensure the required short carrier lifetime.[6] The measurements were made with the standard excite-and-probe arrangement for the beams of optical pulses.

In Fig. 2(a), we show the measured subpicosecond electrical pulse. For this result the spatial separation between the exciting and sampling beams was approximately 50 μm, while the laser spot diameters were 15 μm. When the sliding contact was moved 6 mm from the optical sampling gap, we observed the pulse propagation effects shown in Fig. 2(b). The Fourier analyses of these pulses are shown in Fig. 2(c), where it is seen that the amplitude spectrum of the initial pulse extends to beyond 1 THz and that the transmitted pulse has suffered a significant frequency-dependent loss. From these spectra it is straightforward to obtain the absorption coefficient as a function of frequency, as shown in Fig. 2(d). For some time, previous to this paper, we had considered this absorption to be due to the aluminum lines.

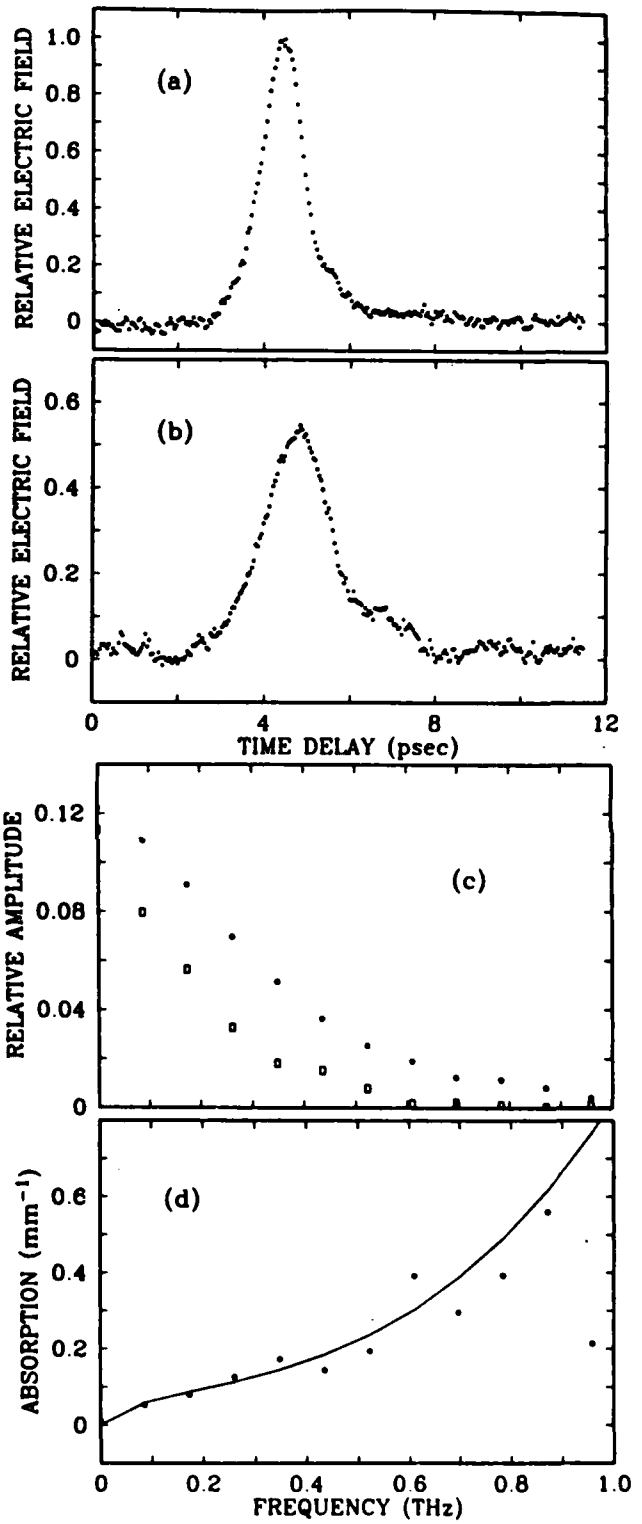

FIG. 2. Room temperature: (a) measured input pulse; (b) measured pulse after propagating 6 mm on the transmission line; (c) amplitude spectrum of input pulse (dots) compared with propagated pulse (squares); (d) amplitude absorption coefficient α from (c) (dots) compared with theory (solid line).

In order to test this assumption, we reduced the resistivity of the Al lines by approximately 12 times by cooling the transmission line to liquid-helium temperatures. Instead of the expected reduction in the absorption coefficient by at least $\sqrt{12}$ due to the consequent reduction in the surface resistance controlled by the frequency-dependent skin effect, we obtained the results shown in Fig. 3. The initial pulse looks almost identical to the room-temperature result. The unexpected feature was that the propagated pulse, illustrated in Fig. 3(b), broadened considerably and developed a slight ringing. In addition, as shown in Fig. 3(c), the Fourier spectra of the input and propagated pulses at 2.5 K look very similar to the room-temperature results. This comparison is made more precise when the absorption coefficient is plotted [Fig. 3(d)].

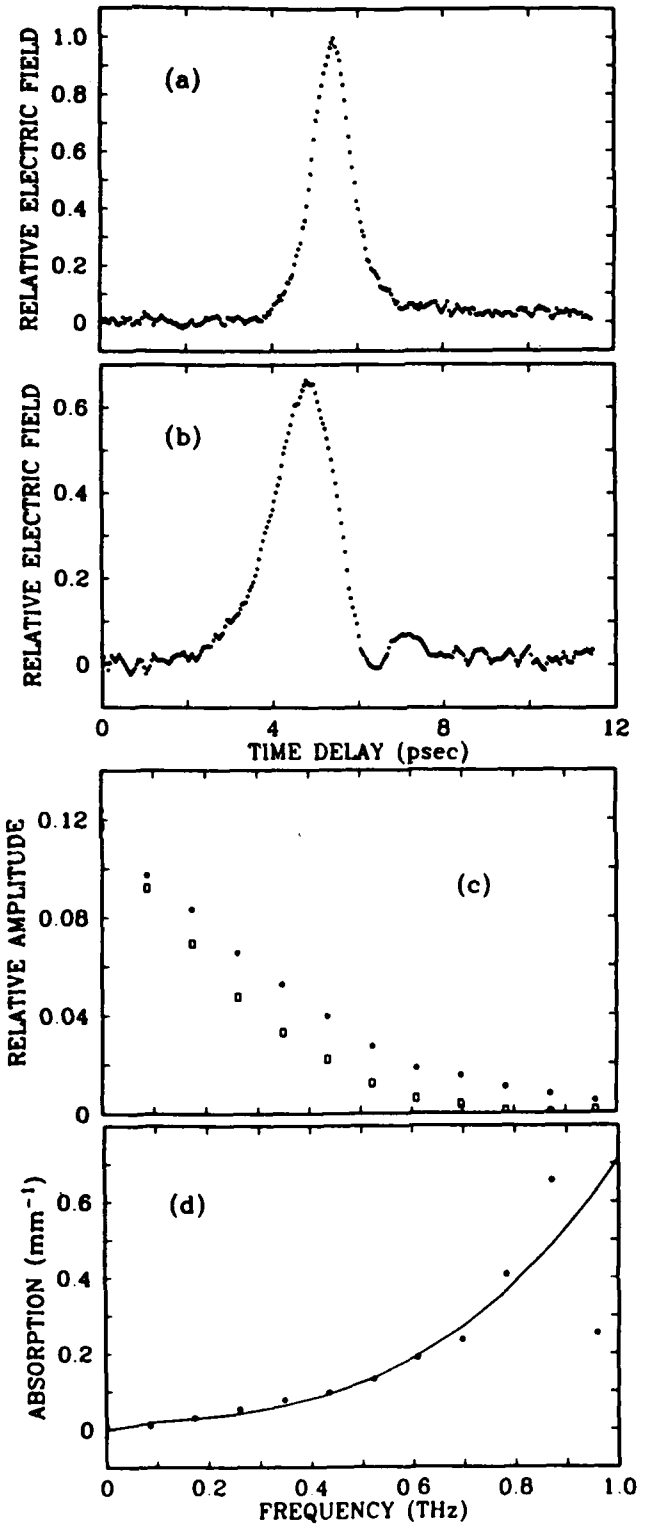

FIG. 3. 2.5 K: (a) measured input pulse; (b) measured pulse after propagating 6 mm on the transmission line; (c) amplitude spectrum of input pulse (dots) compared with propagated pulse (squares); (d) amplitude absorption coefficient α from (c) (dots) compared with theory (solid line).

Thus it is clear that the main component of the observed loss is not due to the aluminum metal film. The absorption of the thin 0.5-μm layer of silicon is relatively insignificant[7] and cannot explain the large absorption observed. The same is true for the sapphire substrate whose absorption coefficient in this frequency range is also insignificant.[8] Therefore, the apparent absorption must be due to radiation by the moving electric dipole associated with the electrical pulse. This pulse is produced by the transfer of approximately 2000 electrons between the two lines at the generation site. Consequently, two dipoles with charges of $1000e$ and separations of 15 μm move down opposite directions of the line at the group velocity. By measuring the total optical delay required for the sampling pulses, we determined that the electrical pulses (dipole moments) propagate on the line with the group velocity of $v_g = c/2.45$. This velocity is significantly faster than the phase velocity of approximately $c/3.3$ for terahertz radiation in sapphire.

The above measured value for v_g is to be compared with that obtained from the relationship $v_g = c/[\frac{1}{2}(1+\epsilon)]^{1/2}$, which applies for our dielectric half-space geometry in the quasistatic approximation.[9] The low-frequency dielectric constants ϵ of sapphire are 9.4 for the ordinary ray and 11.6 for the extraordinary ray.[8] These values give the corresponding group velocities of $c/2.28$ and $c/2.51$, which bracket our measured value of $c/2.45$ obtained on sapphire of unknown orientation. This good agreement confirms the first-order validity of the quasistatic approximation and allows the calculation of the deviations from the TEM mode responsible for the radiative loss.

The solution for the radiation loss at frequency ω from a coplanar line on a dielectric is given by[4]

$$\alpha = \left(\frac{\pi}{2}\right)^5 \frac{\sqrt{2}(3-\sqrt{8})(1-1/\epsilon)^2 W^2}{\lambda_d^3 K(k) K'(k)} (1+1/\epsilon)^{1/2}. \quad (1)$$

For Eq. (1), λ_d is the wavelength in the dielectric; $W = 25$ μm is the width of the transmission line; $k = 0.6$ is the ratio of the separation of the two lines to the total width; $K(k)$ and $K'(k)$ are standard tabulated elliptic integrals.[10]

Evaluating Eq. (1) for our conditions, we obtain the amplitude absorption coefficient to be $\alpha = (0.4\ \text{mm}^{-1}) \times f^3$, where f is the frequency in terahertz. This result is to be compared with the measurements in Figs. 2(d) and 3(d). The solid line fitted to the data in Fig. 2(d) is given by the relationship $\alpha = (0.2\ \text{mm}^{-1}) f^{1/2} + (0.65\ \text{mm}^{-1}) f^3$. The first term gives the frequency-dependent loss due to the resistive skin effect for the Al lines, while the second term with the f^3 dependence describes the loss due to the radiation. In Fig. 3(d), the solid line fitted to the measured absorption is again the sum of two terms, $\alpha = (0.06\ \text{mm}^{-1}) f^{1/2} + (0.65\ \text{mm}^{-1}) f^3$. It is to be noticed that the radiative term, as expected, remained the same, while the resistive-loss term decreased by approximately $1/\sqrt{12}$, corresponding to the reduction of 12

in the resistance of the lines. The measured loss due to the radiation is approximately 1.5 times the calculated value; we consider this good agreement and especially the cubic frequency dependence to confirm definitely the nature of the effect.

As an additional test of our conclusions, we performed the same measurements on a transmission line composed of 2.5-μm-wide lines separated by 5 μm. Here, because W was reduced by 2.5 times compared with the measurements of Figs. 2 and 3, and in agreement with the prediction of Eq. (1), the radiative loss was negligible. The measured absorption was well described by the single-term expression $\alpha = (0.4\ \text{mm}^{-1}) f^{1/2}$ at room temperature. When the sample was cooled to liquid-helium temperatures, the resistivity of the lines dropped by 4 times and the absorption was fitted by the function $\alpha = (0.2\ \text{mm}^{-1}) f^{1/2}$, which agrees with the expected reduction of $\frac{1}{2}$ due to the factor-of-4 decrease in resistivity.

This research was partially supported by the U.S. Office of Naval Research.

[1]J. V. Jelley, *Cherenkov Radiation and Its Applications* (Pergamon, New York, 1958).

[2]D. H. Auston, Appl. Phys. Lett. **43**, 713 (1983).

[3]D. A. Kleinman and D. H. Auston, IEEE J. Quantum Electron. **20**, 964 (1984).

[4]D. B. Rutledge, D. P. Neikirk, and D. P. Kasilingham, in *Infrared and Millimeter Waves,* edited by K. J. Button (Academic, New York, 1983), Vol. 10, Pt. II.

[5]M. B. Ketchen, D. Grischkowsky, T. C. Chen, C.-C. Chi, I. N. Duling, III, N. J. Halas, J-M. Halbout, J. A. Kash, and G. P. Li, Appl. Phys. Lett. **48**, 751 (1986).

[6]F. E. Doany, D. Grischkowsky, and C.-C. Chi, Appl. Phys. Lett. **50**, 460 (1987).

[7]C. M. Randall and R. D. Rawcliffe, Appl. Opt. **6**, 1889 (1967).

[8]E. E. Russell and E. E. Bell, J. Opt. Soc. Am. **57**, 543 (1967).

[9]R. E. Collin, *Field Theory of Guided Waves* (McGraw-Hill, New York, 1960).

[10]*Handbook of Mathematical Functions,* edited by M. Abramowitz and I. A. Stegun, National Bureau of Standards Applied Mathematics Series No. 55 (U.S. GPO, Washington, D.C., 1971); see p. 608.

J-QE/24/2// 17793

Capacitance Free Generation and Detection of Subpicosecond Electrical Pulses on Coplanar Transmission Lines

Daniel R. Grischkowsky
Mark B. Ketchen
C.-C. Chi
Irl N. Duling, III
Naomi J. Halas
Jean-Marc Halbout
Paul G. May

Reprinted from
IEEE JOURNAL OF QUANTUM ELECTRONICS
Vol. 24, No. 2, February 1988

Capacitance Free Generation and Detection of Subpicosecond Electrical Pulses on Coplanar Transmission Lines

DANIEL R. GRISCHKOWSKY, MEMBER, IEEE, MARK B. KETCHEN, MEMBER, IEEE, C.-C. CHI, IRL N. DULING, III, NAOMI J. HALAS, JEAN-MARC HALBOUT, MEMBER, IEEE, AND PAUL G. MAY

(Invited Paper)

Abstract—**Based on a reanalysis of previous work and new experimental measurements, we conclude that the parasitic capacitance at the generation site is negligible for sliding contact excitation of small dimension coplanar transmission lines.**

THE generation of short electrical pulses via optical methods has for some time been performed by driving Auston switches (photoconductive gaps) with short laser pulses [1]. The generated electrical pulse is determined by the laser pulse, the carrier lifetime in the semiconductor, the capacitance of the switch, and the characteristic impedance of the electrical transmission line. The same techniques can also measure the resulting electrical pulses by sampling methods. Recent work utilizing photoconductive gaps has generated and measured subpicosecond electrical pulses [2]. This large reduction in the generated pulsewidth demonstrates the ultrafast capability of the Auston switches and calls for an understanding of the fundamental limits of their generation and detection processes.

Stimulated by recent direct measurements [3], [4] of the carrier lifetime in ion-implanted silicon-on-sapphire (SOS), we have reanalyzed the results of [2]. Based on this analysis, we have come to the conclusion that, for the so-called "sliding-contact" method of excitation [2], [5], to first order the capacitance of the photoconductive switch at the generation site is zero. This conclusion is further supported by an experimental measurement of an ultrashort electrical pulse using the double sliding-contact method of generation and detection [6] where, to first order, the capacitances at both the generation and detection sites are zero. This measurement is in excellent agreement with a theoretical analysis which assumes that the duration of the generated electrical pulse was limited only by the laser pulsewidth and the carrier lifetime. This conclusion removes one of the most severe limitations, associated with the circuit parameters, on the generation of ultrashort electrical pulses by photoconductive switches. The remaining limitations are the carrier lifetime, where recent progress has been made [4], and the laser pulsewidth itself.

We will briefly review the initial experiment and its analysis to provide the background for this recent advance. The geometry of the experimental arrangement [2] is illustrated in Fig. 1(a). The 20 mm long transmission line had a design impedance of 100 Ω and consisted of three parallel 5 μm aluminum lines separated from each other by 10 μm. The dc resistance of a single 5 μm line was 200 Ω. The transmission line, composed of a 0.5 μm thick Al film, was fabricated on an undoped silicon-on-sapphire (SOS) wafer, which was heavily implanted with 0+ ions to ensure the required short carrier lifetime.

The laser source is a compensated, colliding-pulse, passively mode-locked dye laser producing 80 fs pulses at a 100 MHz repetition rate. The measurements were made with the standard excite and probe arrangement for the beams of optical pulses. The time delay between the exciting and sampling beams was mechanically scanned by moving an air-spaced retroreflector with a computer-controlled stepping motor synchronized with a multichannel analyzer. The measured subpicosecond electrical pulse with an excellent signal-to-noise ratio is shown in Fig. 1(b). For this result, the spatial separation between the exciting and sampling beams was approximately 50 μm, while the laser spot diameters were 10 μm.

Our initial analysis [2] of this pulse followed Auston's theory [1], which is extremely general and applies to practically any transmission line configuration. The theory only assumes (for both the generation and detection sites) a conductance, given by the convolution of the laser pulse and the carrier lifetime, charging a capacitance. Each capacitance C discharges with time constant ZC where Z is approximately the transmission line impedence. The numerical fit shown as the solid line in Fig. 1(b) was obtained with the following parameters. The conductances of both the sliding contact generation site and the sampling gap site $g_1(t)$ and $g_2(t)$, respectively, were assumed to be given by the convolution of the laser pulse (allowing for its spatial extent) with an exponential

Manuscript received June 9, 1987; revised August 7, 1987. This work was supported in part by the U.S. Office of Naval Research.

D. R. Grischkowsky, M. B. Ketchen, C.-C. Chi, I. N. Duling, III, J.-M. Halbout, and P. G. May are with the IBM T. J. Watson Research Center, Yorktown Heights, NY 10598.

N. J. Halas was with the IBM T. J. Watson Research Center, Yorktown Heights, NY 10598. She is now with AT&T Bell Laboratories, Holmdel, NJ 07733.

IEEE Log Number 8717793.

0018-9197/88/0200-0221$01.00 © 1988 IEEE

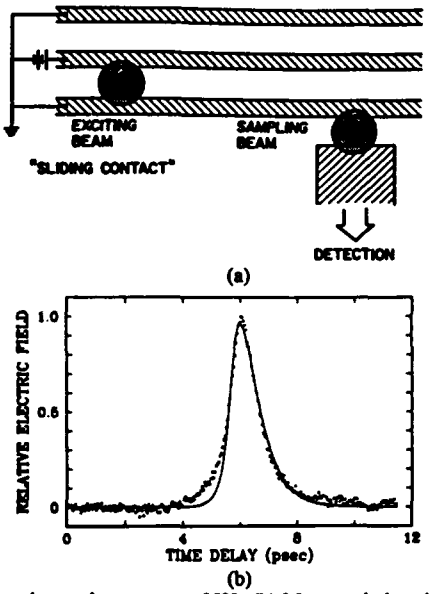

Fig. 1. Experimental geometry of [2]. (b) Measured electrical pulse (dots) compared to theory of [2] with $t_c = 250$ fs, $C_{sc} = 1$ fF, and $C_s = 4$ fF.

response function describing the carrier lifetime t_c. For this initial analysis, t_c was assumed to be 250 fs. An intuitive argument presented in [2] led to the values of the capacitance at the generation site $C_{sc} = 1$ fF and at the sampling site to be $C_s = 4$ fF. As can be seen, the fit is reasonably good, with the exception that the leading edge of the calculated pulse rises much faster than the experiment. Later analysis indicated that the shortness of the assumed carrier lifetime (compared to the measured pulse) was responsible for this deviation. A recent direct measurement of the carrier lifetime for heavily implanted SOS obtained the value of $t_c = 600$ fs [3], and thereby confirmed this situation. This measurement forced the following reanalysis of the generation process for the electrical pulse.

We will now discuss some general aspects of transmission line theory in the quasi-static limit (QSL) for which the wavelengths involved are large compared to the transverse dimensions of the line. For this case, the number of transverse electromagnetic (TEM) modes is one less than the number of metal lines making up the transmission line. Consequently, a two-line transmission line has a single propagating TEM mode. In the QSL, the electric field distribution of this mode is the same as for the static case when the lines are equally and oppositely charged. Any pulse propagating on this line can be described mathematically as a Fourier sum of single frequency components, all with this same TEM modal distribution. Likewise, a transient "purely electric" pulse of a limited spatial extent can be considered to be the sum of two counterpropagating pulses with the same spatial extent. For this "stationary" electrical pulse, the zero H field comes from the superposition of the two counterpropagating pulses where the E fields add, but the H fields subtract. The key point in the argument to follow is that for sliding-contact excitation, the resulting electrical transient is equivalent to the superposition of two counterpropagating electrical pulses due to the zero H field and to the excellent match of the E field lines to the propagating TEM mode. This essentially perfect coupling eliminates the parasitic capacitance (and inductance) at the excitation site.

Consideration of the sliding-contact excitation site shows that, to first order, charge is simply transferred from one line to the other, creating a symmetrical field distribution with respect to the two lines. During the excitation process, a current flow is induced between the lines. Localized charge accumulations of opposite sign build up on the segments of the two metal lines under the laser excitation spot, creating a dipolar field distribution similar to that illustrated in Fig. 2(a). The response time of this field pattern is approximately the time required for electromagnetic radiation to cross the separation between the two lines. For the simplified quasi-static picture to apply, this time should be short compared to either the laser pulse duration or the carrier lifetime, whichever is longer. This is simply a restatement that the wavelengths involved should be large compared to the transverse dimensions of the line. Because the electric field lines of the TEM mode have the same pattern as the dc field lines [illustrated in Fig. 2(a)] when the lines are equally and oppositely charged [7], the sliding-contact excitation is well matched to the TEM mode. The major part of generated field pattern is the same as this TEM mode which is perfectly coupled to the line.

A most important feature of a coplanar transmission line (of negligible thickness) on an infinite dielectric half-space is that for a constant voltage between the two conducting lines, the electric field lines are the same as for the lines immersed in free space [8]. This result is due to the geometric symmetry with respect to the dielectric boundary and is a consequence of the fact that no electric field lines cross this boundary. The effect of the dielectric (with dielectric constant ϵ) is to increase the surface charge density on the conductors in contact with the dielectric to $\epsilon\sigma_0$ where σ_0 is the surface charge density in free space. However, because there is a polarization surface charge density of $(\epsilon - 1)\sigma_0$ of the opposite sign, the net surface charge remains σ_0, keeping the electric field the same. Consequently, the main effect of the dielectric is to increase the distributed line capacitance. This increase will now be evaluated following the procedure of [8]. Consider the capacitance per unit length of the line to be C_0 in free space. In the dielectric medium, the surface charge density is $\epsilon\sigma_0$, but for the side of the line in free space, the surface charge density remains σ_0. Therefore, for the same voltage between the lines, the charge has increased by $(1 + \epsilon)/2$, and the corresponding capacitance has increased to $C = (1 + \epsilon)C_0/2$. Because we assume the dielectric medium has a magnetic permeability equal to unity, the inductance L_0 per unit length does not change in the presence of the dielectric.

The predicted group velocity can now be evaluated following the logic of [8]. For the transmission line in free

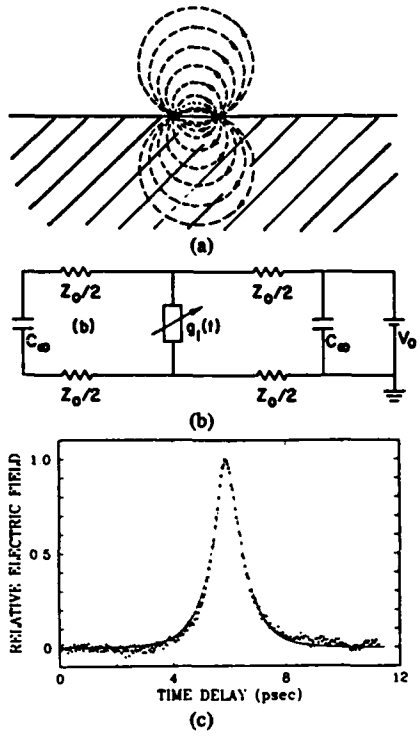

Fig. 2. (a) Electrical field lines for the propagating TEM mode (differential mode) of a two-line transmission line in a uniform dielectric and on the surface of a uniform dielectric. (b) Equivalent circuit for sliding-contact excitation of a two-line transmission line. (c) Measured electrical pulse (dots) of [2] compared to theory with $t_c = 600$ fs, $C_{sc} = 0$, and $C_s = 1$ fF.

space, the group velocity v_g is given by $v_g = (1/(L_0C_0))^{1/2} = c$ [9], [10]. In the presence of the dielectric, the capacitance has increased to $(1 + \epsilon)C_0/2$, while the inductance remained the same. This situation gives the result $v_g = c(2/(\epsilon + 1))^{1/2}$. The low-frequency dielectric constants of sapphire are 9.4 for the ordinary ray and 11.6 for the extraordinary ray [11]. These values give the corresponding group velocities of $c/2.28$ and $c/2.51$, which bracket our measured value [2] of $c/2.45$ obtained on sapphire of unknown orientation. This good agreement confirms the validity of the quasi-static approximation and shows that the TEM mode remains a good approximation for this split dielectric case, even though it is no longer an exact solution. Consequently, all of the above arguments also apply to the split dielectric case, i.e., sliding-contact excitation produces a field distribution which matches the propagating mode of the line, and thereby the parasitic capacitance at the generation site is negligible.

An equivalent circuit illustrating this situation is shown in Fig. 2(b) where the photoconductance $g_1(t)$ created by the laser excitation is connected directly across the characteristic (resistive) impedance Z_0 in either direction. The infinite capacitances simply illustrate that the line extends without end in both directions. Because this circuit has no capacitance at the generation site, the voltage pulses launched in both directions down the line are given by $V(t) = V_0Z_0/(Z_0 + 1/g_1(t))$. For our case where $V(t) \ll V_0$, this result simplifies to $V(t) = V_0Z_0g_1(t)$. Consequently, the generated electrical pulse has the same time dependence as the conductance $g_1(t)$.

We again numerically analyzed the measured electrical pulse of Fig. 1(b), but with the following parameters. The conductances $g_1(t)$ and $g_2(t)$ were obtained as before, except now the carrier lifetime is known to be 600 fs. The capacitance at the generation site was set equal to zero, $C_{sc} = 0$. Thus, the capacitance at the sampling site was the only adjustable parameter to be determined by numerically fitting to the measured pulse. With the optimized value $C_s = 1$ fF, we obtained the excellent agreement with theory shown as the solid line in Fig. 2(c). For this situation, the actual generated electrical pulse was calculated and is shown in Fig. 3 to have a pulsewidth of only 0.52 ps. The sharp rising edge is due to the short laser pulse excitation, while the slower falling edge of the pulse is due to the 600 fs carrier lifetime. This pulse is directly proportional to $g_1(t)$ in accordance with the analysis of the equivalent circuit of Fig. 2(b).

The good agreement between theory and experiment in Fig. 2(c) gave us confidence in our new understanding of the pulse generation process and suggested as a further confirmation the experiment illustrated in Fig. 4(a). This more symmetrical arrangement is called the double sliding-contact and has no observable capacitance [6]. It is to be noted that we used a two-line transmission line, so that the above arguments about matching to the propagating TEM mode are more precise. The electrical pulse is generated as before, but here the sampling measurement is also made by shorting the transmission line with the sampling laser pulse. For this case, the two laser beams are mechanically chopped at incommensurate frequencies and the signal is measured as a modulation of the photocurrent on the transmission line at the sum of the two chopping frequencies. Because to first order this arrangement has no capacitance at both the generation and sampling sites, the measured electrical pulse had a pulsewidth of only 0.85 ps compared to the previous measurement of 1.1 ps using a sampling gap. This measurement was made on a smaller geometry coplanar line with line dimensions of 1.2 μm separated by 2.4 μm. The design impedance was 100 Ω and the bias was 1.5 V. In order to compare to theory, the conductances $g_1(t)$ and $g_2((t)$ were obtained as before with the carrier lifetime of 600 fs, but now the capacitances at both the generation and sampling sites were set to zero. The resulting fit to the data is shown as the solid line in Fig. 4(b). This theoretical prediction is equivalent to the autocorrelation of the electrical pulse shown in Fig. 3. The agreement between theory and experiment showing the sharpness of the peak of the pulse is good. This extremely sharp peak is due to the sharp leading edge of the generated electrical pulse in Fig. 3.

However, the data in Fig. 4(b) definitely show a faster time dependence than the calculations which only assume an excitation pulse of 130 fs (the square root of the sum of the squares of the laser pulse width plus the transit time due to the 10 μm diameter spot size) and the 600 fs carrier lifetime.

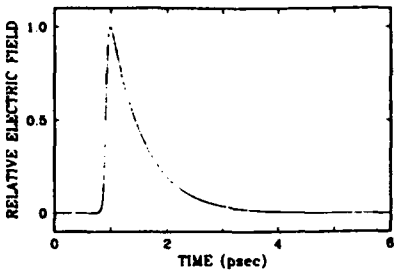

Fig. 3. Generated electrical pulse.

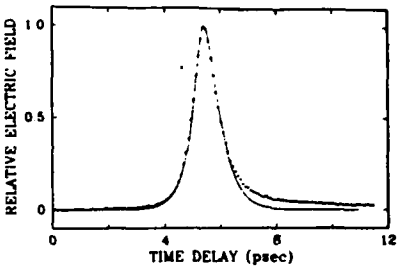

Fig. 5. Measured electrical pulse (dots) compared to theory with t_c = 400 fs, C_{sc} = 0 fF, and C_s = 2.5 fF.

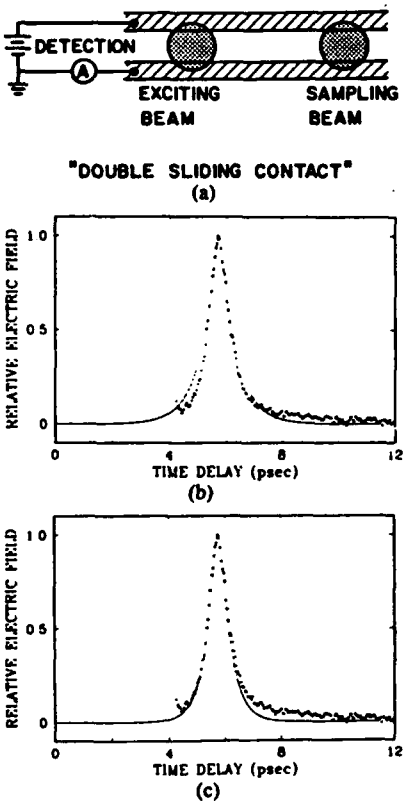

Fig. 4. (a) Experimental geometry for double sliding contact. (b) Measured electrical pulse (dots) compared to theory with t_c = 600 fs, C_{sc} = 0 fF, and C_s = 0 fF. (c) Measured electrical pulse (dots) compared to theory with t_c = 400 fs, C_{sc} = 0 fF, and C_s = 0 fF.

Because the 600 fs data were obtained by reflectivity measurements [3], [4], it is natural to assume that they were a surface-sensitive measure of the carrier lifetime. However, a recent analysis [12] has shown that this was not the case, and that for a 0.5 μm thick layer of silicon on a sapphire substrate, the main component on the signal obtained with 620 nm light was due to the induced change in the optical length of the silicon, due to the change in the index of refraction. This thin-film, interference-enhanced signal can be as much as 20 times larger than the comparable change in reflectivity from the single surface of a thick silicon wafer. Consequently, the measurements of the carrier lifetime of [3], [4] are representative of the entire silicon film and not just the surface layer. As such, it is possible that the relevant carrier lifetime for optoelectronic pulse generation and measurement could be shorter due to their surface sensitivity and the presence of additional traps at the surface.

This conjecture was tested by reanalyzing the data of Fig. 4, using a carrier lifetime of 400 fs, which appears to give a significantly better fit as shown in Fig. 4(c). The capacitances were, of course, kept equal to zero.

In order to provide more information on this point, we compare a calculation to some recently measured high signal-to-noise data shown in Fig. 5. This pulse was generated by sliding-contact excitation of a two-line transmission line consisting of 5 μm lines separated by 10 μm, and was detected with a side gap similar to that shown in Fig. 1. As previously mentioned, the zero capacitance argument is more precise for this two-line case. The theoretical comparison shown as the solid line in the figure fits the rising edge and the main pulse itself exceedingly well. The deviation on the falling edge is thought to be due to resistive line effects. Again, this was fit with a 130 fs excitation pulse, a 400 fs carrier lifetime, zero capacitance at the generation site, and for this gap, a 2.6 fF capacitance. These parameters correspond to a generated electrical pulse of only 0.45 ps with a shape similar to that shown in Fig. 3.

In summary, by reanalyzing the first experiment to generate subpicosecond pulses using photoconductive switches, we have shown that to first order, the sliding-contact generation site has no capacitance. This conclusion is further supported by a double sliding-contact experiment where, to first order, neither the generation nor the detection site has any capacitance. This result removes the parasitic capacitance of the electrical circuit as one of the major difficulties to short electrical pulse generation using photoconductive switches.

Acknowledgment

D. R. Grischkowsky would like to acknowledge stimulating and informative discussions with D. H. Auston, H. Melchior, and M. J. W. Rodwell concerning this work.

References

[1] D. H. Auston, "Impulse response of photoconductors in transmission lines," *IEEE J. Quantum Electron.*, vol. QE-19, pp. 639–648, 1983.
[2] M. B. Ketchen, D. Grischkowsky, T. C. Chen, C.-C. Chi, I. N. Duling, III, N. J. Halas, J.-M. Halbout, J. A. Kash, and G. P. Li, "Generation of subpicosecond electrical pulses on coplanar transmission lines," *Appl. Phys. Lett.*, vol. 48, pp. 751–753, 1986.
[3] F. E. Doany, D. Grischkowsky, and C.-C. Chi, "Carrier lifetime

versus ion-implantation dose in silicon on sapphire," *Appl. Phys. Lett.*, vol. 50, pp. 460–462, 1987.
[4] ——, "Photoconductive generation of sub-picosecond electrical pulses and their measurement applications," in *Proc. 2nd Topical Meet. Picosecond Electron. Optoelectron.*, Incline Village, NV, Jan. 1987.
[5] D. R. Dykaar, T. Y. Hsiang, and G. A. Mourou, "Development of a picosecond cryo-sampler using electro-optic techniques," in *Picosecond Electron. Optoelectron., Proc. Topical Meet.*, Lake Tahoe, NV, Mar. 1985, G. A. Mourou, D. M. Bloom, and C.-H. Lee, Eds. Berlin, Heidelberg: Springer-Verlag, 1985, pp. 249–252.
[6] P. G. May, G. P. Li, J.-M. Halbout, M. B. Ketchen, C.-C. Chi, M. Scheuermann, I. N. Duling, III, D. Grischkowsky, and M. Smyth, "Picosecond electrical pulses in microelectronics," in *Ultrafast Phenomena V*, G. R. Fleming and A. E. Siegman, Eds. New York: Springer-Verlag, 1986, pp. 120–122.
[7] R. E. Collin, *Field Theory of Guided Waves*. New York: McGraw-Hill, 1960.
[8] C. J. Chen and D. Grischkowsky, "Cerenkov radiation from coplanar transmission lines," to be published.
[9] R. E. Matick, *Transmission Lines for Digital and Communication Networks*. New York: McGraw-Hill, 1969.
[10] This is the usual expression for the phase velocity, but for a dispersion-free dielectric, it also describes the group velocity.
[11] E. E. Russell and E. E. Bell, "Optical constants of sapphire in the far infrared," *J. Opt. Soc. Amer.*, vol. 57, pp. 543–544, 1967.
[12] F. E. Doany and D. Grischkowsky, "Measurement of ultrafast 'hot' carrier relaxation in silicon by thin-film-enhanced, time-resolved reflectivity," to be published.

Daniel R. Grischkowsky (A'84) was born in St. Helens, OR, on April 17, 1940. He received the B.S. degree from Oregon State University, New York, in 1968. His dissertation work, supervised by S. R. Hartmann, involved electron spin resonance investigations, which led to the explanation of the observed dependence of photon echoes in ruby to the direction of the applied magnetic field.

In 1969 he joined the IBM Research Division at the IBM T. J. Watson Research Center, Yorktown Heights, NY, where he now manages the Ultrafast Science with Lasers Group. His initial experimental and theoretical research involved studying the interaction between near-resonant light and the two-level system. The "adiabatic following model" which he originally proposed as a result of these studies subsequently explained the observed effects of self-focusing, self-defocusing, self-steepening, and slow group velocities in vapors of two-level systems (alkali metals). His more recent work has been the experimental and theoretical studies of nonlinear propagation of picosecond laser pulses in single-mode optical fibers. An outgrowth of this work was the invention of the optical fiber pulse compressor, for which he was awarded The Boris Pregel Award for Applied Science and Technology (1985) by The New York Academy of Sciences.

Dr. Grischkowsky is a member of Optical Society of America and a Fellow of the American Physical Society.

Mark B. Ketchen (M'79) received the B.S. degree in physics from the Massachusetts Institute of Technology, Cambridge, in 1970 and the Ph.D. degree in physics from the University of California, Berkeley, in 1977.

From 1972 to 1976 he served as an officer teaching thermodynamics and nuclear reactor physics in the U.S. Naval Nuclear Power Program. As a graduate student he specialized in the design, fabrication, and use of low-noise superconducting devices. He joined the IBM Research Division, IBM T. J. Watson Research Center, Yorktown Heights, NY, in 1977. As a research staff member and manager he has worked on the electrical aspects of logic, memory, power, package, and analog detectors in Josephson Technology. For the last four years he has worked in Silicon Technology where he managed the Silicon Bipolar Technology Group and is now manager of the Yorktown Silicon Facility. His personal research activities include picosecond optoelectronics in silicon technology and analog magnetic detectors in Josephson technology.

Dr. Ketchen is a member of the American Physical Society.

C.-C. Chi, photograph and biography not available at the time of publication.

Irl N. Duling, III, for a photograph and biography, see this issue, p. 410.

Naomi J. Halas, photograph and biography not available at the time of publication.

Jean-Marc Halbout (M'87), for a photograph and biography, see this issue, p. 239.

Paul G. May, for a photograph and biography, see this issue, p. 239.

Measurement of ultrafast hot-carrier relaxation in silicon by thin-film-enhanced, time-resolved reflectivity

F. E. Doany and D. Grischkowsky
IBM Watson Research Center, Yorktown Heights, New York 10598

(Received 30 July 1987; accepted for publication 4 November 1987)

Time-resolved reflectivity measurements with ~ 100 fs resolution have revealed an initial 350 fs relaxation time in silicon, believed to be the time it takes hot, photoinjected carriers to relax to the band edge. The measurements were made at low carrier densities ($\sim 10^{17}$ cm^{-3}) for which carrier-carrier processes are negligible, and were facilitated by the greater than order of magnitude enhancement of the change in reflectivity signals that can be produced by the use of thin films.

Picosecond and femtosecond optical techniques have been extensively utilized in studies of the dynamics of nonequilibrium carrier relaxation in semiconductors.[1] When a semiconductor is excited with photons of energy $\hbar\omega$ greater than its band gap E_g, electron-hole pairs are created with excess kinetic energy $\hbar\omega - E_g$. This excess energy will then redistribute among the electronic and lattice degrees of freedom until equilibrium is reached with the surroundings. To date, most time-resolved reflectivity experiments in silicon have probed carrier relaxation after the thermalized distribution has been established. Numerous studies have examined the dynamics of dense electron-hole plasmas in silicon, particularly related to ultrafast heating and pulsed annealing.[2-10] Shank *et al.*[4] have recently used high intensity, 90 fs pulses to time resolve the transition to the melted state in silicon. In addition to the plasma reflectivity signal, the reflectivity dynamics near the melting threshold fluence exhibited an additional ~ 1 ps component. This fast component was believed to arise from lattice heating resulting from phonon emission due to hot-carrier relaxation toward the band edge. Lattice heating above the melting threshold leading to disorder in crystalline silicon was also probed by second-harmonic generation[5,10] and the results are consistent with thermally induced disorder occurring within ~ 0.5 ps. Reflectivity changes monitored slightly below the melting threshold[8] also suggest that direct heating of the lattice resulting from the hot-carrier relaxation occurs within 1 ps.

The above measurements are all indicative of a subpicosecond cooling time (energy relaxation time) for photoexcited carriers, although no direct experimental measurement is yet available. The carrier lifetime in amorphous silicon was measured as 0.8 ps by time-resolved reflectivity indicating the relaxation time is at least this fast.[7] Hot-carrier relaxation times of approximately 0.5–1.0 ps in amorphous silicon have been estimated from photoinduced absorption measurements using laser pulse widths of ~ 0.8 ps.[11] Carrier lifetimes as short as 600 fs have been measured in ion-implanted Si suggesting that the cooling time is <600 fs.[9] Steady-state measurements have also been used to obtain estimates of the energy relaxation times.[12] Analysis of the temperature dependence of these electron drift velocity measurements in silicon[12,13] is consistent with energy relaxation times ranging from ~ 3 to ~ 0.4 ps for hot electrons (~ 300–500 K) in a 300-K silicon lattice. These rates have also been calculated by the Monte Carlo method[12,14] as a function of the difference between the average and the thermal energies. At a carrier density of 10^{17} cm^{-3}, this time varied from ~ 250 fs for carriers near the band gap to ~ 450 fs for carriers with 1 eV excess energy.

We report here results on the carrier relaxation dynamics in silicon obtained with high temporal resolution (~ 100 fs) and under low carrier densities ($\sim 10^{17}$ cm^{-3}) where carrier-carrier processes were negligible. The samples used in this study are 0.5-μm-thick silicon films on sapphire (SOS) wafers. High signal-to-noise reflectivity measurements were obtained by taking advantage of the thin-film properties to enhance the observed changes in the reflectivity of silicon by more than an order of magnitude. This experimental technique is ideally suited for investigating the carrier dynamics in thin films of semiconductors.

Time-resolved reflectivity measurements were obtained using a system described elsewhere.[9] Briefly, the laser source consists of a dispersion-compensated colliding-pulse modelocked (cpm) ring dye laser producing 70 fs pulses at 2.0 eV (625 nm) and operating at a repetition rate of 100 MHz. A probe beam was split off the main pump beam and attenuated to about 2% of the ~ 1 mW pump power. The pump was incident onto the sample at an angle of $\sim 45°$ to the surface normal and focused to a diameter of 10 μm, while the probe was incident normal to the surface and focused to a diameter of 5 μm. The polarization of the probe beam was rotated by 90° relative to the pump in order to suppress interferences between the two beams at the sample surface. Prior to reaching the sample, the probe beam was additionally split into two beams: one was reflected off the sample and detected on a large surface area photodiode, and the second was directed onto a matched photodetector and used as a reference. The signal and reference photocurrents were subtracted and the difference was detected using a lock-in amplifier referenced at the 2.7 kHz pump beam chopping frequency. This differential detection compensated for small fluctuations in the incident laser intensity and allowed for detection of changes in the probe beam reflectance of less than 1 part in 10^6.

Using this apparatus, we have previously measured the time evolution of the reflectivity following photoexcitation of a SOS wafer on the ~ 100 ps timescale.[9] The maximum change in reflectivity for the 1 mW pump power used in that study was $\Delta R/R \sim 3 \times 10^{-5}$. The observed change in reflectivity exhibited a pulse width limited rise time (<150 fs) with a long time recovery of approximately 100 ps, consis-

 0003-6951/88/010036-03$01.00 © 1987 American Institute of Physics

tent with carrier diffusion out of the 10 μm pump region with a drift velocity 10^7 cm/s.[12]

Both n- and p-type bulk silicon wafers exhibited similar time evolution as the SOS wafer. However, the maximum signals observed in these bulk samples at 1 mW pump power were only $\Delta R/R \sim 2\times 10^{-6}$, less than 1/10 of that from SOS. The recovery of the reflectivity in these samples was slightly faster ($\sim$50 ps) than in SOS. This recovery is consistent with previous measurements[4] and is due to carrier diffusion into the bulk. In SOS carriers are injected throughout the 0.5 μm film and thus can only diffuse laterally out of the 10 μm pump region. In the bulk wafers, however, diffusion into the bulk will dominate since the absorption depth is only 3 μm.[15]

The signal strength ($\Delta R/R$) observed in the bulk silicon is consistent with the index change associated with the plasma generated by the 1 mW pump power (10 pJ/pulse). Without pumping, the reflectivity at normal incidence of the bulk silicon wafers at 625 nm was 0.35. This same value can be calculated from the simple expression for the reflectance at normal incidence,

$$R_1 \equiv r_1^2 = [(n_1 - 1)/(n_1 + 1)]^2, \tag{1}$$

where the refractive index of silicon at 625 nm is $n_1 = 3.9$. In the Drüde formalism the change in refractive index due to the presence of a low density electron-hole plasma is

$$\Delta n/n = -(2\pi e^2/\epsilon m\omega^2)N, \tag{2}$$

where ϵ is the background dielectric constant at low frequencies, m is the effective mass, and ω is the probe angular frequency. From Eq. (2), the calculated index change due to the plasma at our experimental conditions for which the injected carrier density $N \sim 2\times 10^{17}$ cm^{-3} is $\Delta n_1 \sim 4\times 10^{-6}$. This value, together with the change in reflectivity dR_1/dn_1 derived from Eq. (1), gives the predicted value $\Delta R_1/R_1 = 4\times 10^{-6}$, in approximate agreement with the measurement $\Delta R_1/R_1 \sim 2\times 10^{-6}$.

The above simple analysis does not apply to SOS, where the change in reflectivity was approximately an order of magnitude greater than that observed for bulk silicon under identical experimental conditions. Associated with this point is the fact that for SOS the reflectance was not constant across the wafer. At normal incidence, the reflectance varied from 0.18 to 0.55 for different positions on the surface of the 3-in. wafer indicating interferences arising from multiple reflections at the air/silicon and silicon/sapphire interfaces. The absorption, however, remained nearly constant at 0.3. For our $\sim$0.5 μm film this corresponds to an absorption depth $\alpha^{-1} \sim 1.5$ μm, consistent with earlier measurements on epi films.[16]

Figure 1(a) shows the calculated reflectance at normal incidence of a SOS film with thickness variation 0.45–0.55 μm. The solid curve was obtained from the thin-film equations[17] including absorption ($\alpha^{-1} = 1.5\,\mu$m) but neglecting the small reflection at the sapphire/air interface. The reflectance varies from 0.15 to 0.55, depending on the film thickness l. For a simple but informative analysis we need only to consider two reflections. With an incident electric field E_0, these first two reflections are $E_1 = r_1 E_0$ and $E_2 = T_1 r_2 E_0 e^{-\alpha l}$, where r_2 is the silicon/sapphire reflection coefficient $r_2 = (n_2 - n_1)/(n_2 + n_1)$, T_1 is the transmission of the silicon/air interface ($T_1 = 1 - R_1$), and n_2 is the refractive index of sapphire. The reflectance is then given by the time average of $[E_1(t) + E_2(t)]^2/E_0(t)^2$,

$$R = R_1 + 2(1 - R_1)r_1 r_2 e^{-\alpha l}\cos 2\phi + (1 - R_1)^2 R_2 e^{-2\alpha l}, \tag{3}$$

where $\phi = 2\pi n_1 l/\lambda$ is the phase delay introduced by propagation through the film; λ is the probe wavelength in air. This calculation (dashed line) is shown to be qualitatively similar to the full thin-film result (solid curve) in Fig. 1(a).

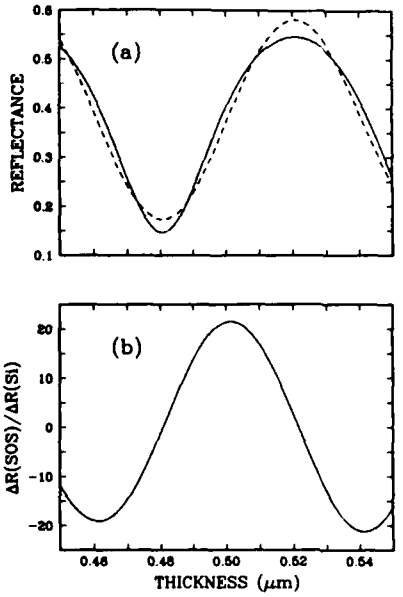

FIG. 1. (a) Calculated reflectance at 625 nm for a 0.5-μm film of silicon-on-sapphire (SOS) substrate. Solid line is from the full thin-film equations. Dashed line uses only the first two reflections. (b) Calculated change in reflectivity for SOS normalized to the change in reflectivity for a single Si surface $\Delta R(\mathrm{SOS})/\Delta R(\mathrm{Si}) = (dR/dn_1)/(dR_1/dn_1)$.

Calculating dR/dn_1 from Eq. (3), we obtain the change in reflectivity for SOS,

$$\frac{dR}{dn_1} = \frac{dR_1}{dn_1} + (F_1\cos 2\phi + F_2 \sin 2\phi)e^{-\alpha l} + F_3 e^{-2\alpha l}. \tag{4}$$

The first term and third terms in this expression correspond to first and second surface reflections while the middle term arises from the interference between the two reflections. The functions F_1 and F_3 are independent of l, while F_2 varies linearly with l. Evaluating them for our conditions, we obtain $F_1 \sim 0.1$, $F_2 \sim -3.6l/\lambda$ (~ -3), and $F_3 \sim -0.06$. Because of the relatively large value of F_2, the associated oscillating term dominates the changes in reflectivity since $dR_1/dn_1 \sim 0.1$. In Fig. 1(b) we show dR/dn_1 vs ϕ (sample thickness) normalized to the value for a single surface dR_1/dn_1. Here one can see that for most thicknesses the magnitude of the thin-film interference term is far greater than the single surface term and peaks at a value of 20×. Thus, in agreement with our observation, changes in reflectivity for SOS can be more than an order of magnitude greater than for bulk silicon.

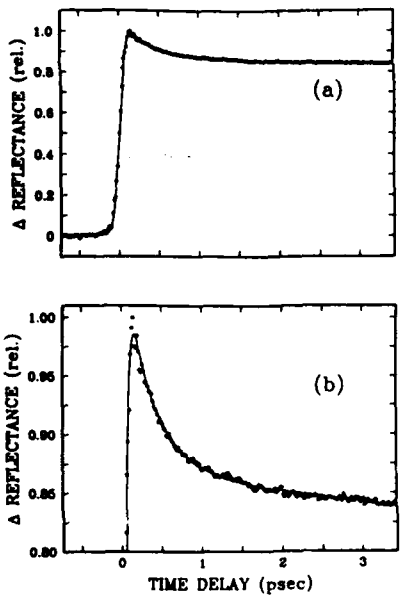

FIG. 2. (a) Transient reflectivity changes for SOS. (b) The top 15% of the data above on an expanded scale. The smooth curve in (a) and (b) is a biexponential fit with $\tau_1 = 350$ fs and $\tau_2 \sim 100$ ps.

Figure 2(a) shows the reflectivity signal for SOS during the first ~ 3 ps following photoinjection of carriers. In addition to the previously discussed ~ 100 ps component, the time evolution exhibits a fast component near $t = 0$. These data were modeled using a biexponential decay together with a 120-fs Gaussian experimental response function. By fixing the long time constant at 100 ps and using a least-squares fitting routine, the fast decay component was determined to be ~ 350 fs. This short time is clearly resolvable as evidenced by the < 150 fs rise time of the data in Fig. 2. The enhanced signal-to-noise levels of the data and the agreement of the model are evident from Fig. 2(b) which show in an expanded scale the top 15% of the data and the fit of Fig. 2(a). The power dependence of this decay time was also checked since relaxation rates may depend on carrier density at densities $> 10^{17}$ cm^{-3}.[18,19] The carrier density for the experimental conditions used in obtaining the data in Fig. 2 is $\sim 2 \times 10^{17}$ cm^{-3}. Identical time evolution was observed when the laser power was reduced by a factor of 4.

The initial fast component is believed to be the hot-carrier cooling rate in silicon. The 2.0 eV excitation generates carriers with substantial excess kinetic energy since the band gap of silicon is only 1.15 eV at 293 K. Thus initially, the electron and hole share an excess energy of ~ 0.85 eV. The measured 350 fs decay in the reflectivity represents the cooling time of these hot carriers. The dependence of the energy relaxation time on the excess energy of the electrons in silicon at 293 K has been calculated by the Monte Carlo method.[12,14] For a carrier density of 10^{17} cm^{-3} this time varied smoothly from ~ 450 fs at an excess energy of 1.0 eV down to ~ 250 fs near the band gap (excess energy < 0.02 eV).[13] These values bracket our experimental result of 350 fs and are consistent with our interpretation.

The dependence of the reflectivity on the carrier temperature (excess energy) is not predicted by the simple Drüde expression presented in Eq. (2). This expression, however, is only an approximation and does not include several factors which may contribute to the observed dependence on carrier temperature. The effective mass m of the carriers is not a constant, as assumed in Eq. (2), but varies with the curvature (nonparabolicity) of the potential. Similarly, the dielectric background is commonly taken as the long wavelength limiting value ϵ_∞, thus ignoring its energy dependence and response to the plasma resonances. Additionally, free-carrier absorption, which has a strong dependence on carrier excess energy,[11] will also contribute to the change in reflectivity. Further considerations show that the fast component should also contain a small contribution due to lattice heating. Equation (2) shows that the change in index due to the plasma is negative, $\Delta n < 0$. The change in index associated with heating, however, is positive, $\Delta n > 0$.[6,8,15] Thus, a rise in lattice temperature results in a change in reflectivity in the opposite direction to the plasma signal. This direct lattice heating is derived from the emission of phonons by the hot carriers as they relax toward the band edge. The time constant associated with this process is therefore an upper limit to the carrier cooling time. Estimates of the magnitude of this component, however, suggest that direct lattice heating would be only a minor contribution to the observed reflectivity signal. For 2 eV excitation, the ratio of the change in index due to direct heating to that of the plasma has been estimated as ~ 0.1 for probe wavelength of 0.485 μm and < 0.01 for 1.0 μm.[8] In our experiment at a probe wavelength of 0.625 μm, the measured ratio of the fast/slow component is ~ 0.25, much too large to be explained by lattice heating.

We would like to acknowledge the many helpful discussions with J. Kash and the use of computer modeling routines developed by J. Misewich. This research was partially supported by the U.S. Office of Naval Research.

[1]See, for example, *Ultrafast Phenomena V*, edited by G. R. Fleming and A. E. Siegman (Springer, New York, 1986).
[2]P. Liu, R. Yen, N. Bloembergen, and R. T. Hodgson, Appl. Phys. Lett. **34**, 864 (1979).
[3]D. von der Linde and N. Fabricius, Appl. Phys. Lett. **41**, 991 (1982).
[4]C. V. Shank, R. Yen, and C. Hirlimann, Phys. Rev. Lett. **50**, 454 (1983).
[5]C. V. Shank, R. Yen, and C. Hirlimann, Phys. Rev. Lett. **51**, 900 (1983).
[6]L. A. Lompre, J-M. Liu, H. Kurz, and N. Bloembergen, in *Ultrafast Phenomena IV*, edited by D. H. Auston and K. B. Eisenthal (Springer, New York, 1984), p. 122.
[7]J. Kuhl, E. O. Gobel, Th. Pfeiffer, and A. Jonietz, Appl. Phys. A **34**, 105 (1984).
[8]M. C. Downer and C. V. Shank, Phys. Rev. Lett. **56**, 761 (1986).
[9]F. E. Doany, D. Grischkowsky, and C-C. Chi, Appl. Phys. Lett. **50**, 460 (1987).
[10]H. W. K. Tom, G. D. Aumiller, and C. H. Brito-Cruz, in *XV International Quantum Electronics Conference Technical Digest Series 1987* (Optical Society of America, Washington, D. C., 1987), Vol. 21, p. 26.
[11]Z. Vardenay and J. Tauc, Phys. Rev. Lett. **18**, 1223 (1981).
[12]G. Canali, C. Jacocboni, F. Nava, G. Ottaviani, and A. Alberigi-Quaranta, Phys. Rev. B **12**, 2265 (1975).
[13]B. R. Nag, in *Semiconductors Probed by Ultrafast Laser Spectroscopy*, edited by R. R. Alfano (Academic, New York, 1984), Vol. I, p. 3.
[14]E. Constant, in *Hot Electron Transport in Semiconductors*, edited by L. Reggiani (Springer, New York, 1985), p. 227.
[15]G. E. Jellison, Jr. and F. A. Modine, J. Appl. Phys. **53**, 3745 (1982).
[16]R. Hulthen, Phys. Scr. **12**, 342 (1975).
[17]O. S. Heavens, *Thin Film Physics* (Methuen & Co., London, 1970).
[18]J. A. Kash and J. C. Tsang, in *Ultrafast Phenomena V*, edited by G. R. Fleming and A. E. Siegman (Springer, New York, 1986), p. 188.
[19]W. Z. Lin, J. G. Fujimoto, E. I. Ippen, and R. A. Logan, Appl. Phys. Lett. **50**, 124 (1987).

Dark-Pulse Propagation in Optical Fibers

D. Krökel, N. J. Halas,[a] G. Giuliani, and D. Grischkowsky
IBM Watson Research Center, Yorktown Heights, New York 10598
(Received 8 September 1987)

We report measurements of the reshaping of 0.3-psec dark pulses due to their passage through 10 m of single-mode optical fiber. The measurements were performed as a function of intensity and the observed strong reshaping agrees qualitatively with the predictions of the nonlinear Schrödinger equation which suggest that we have observed the formation of dark-pulse solitons.

PACS numbers: 42.30.—d, 41.10.Hv, 42.10.Qj

Propagation of short optical pulses through single-mode optical fibers appears to be the best physical example of a system described by the nonlinear Schrödinger equation (NLSE).[1-10] In the traditional and simplest description of the problem, the single-mode propagation permits the problem to be reduced to the equivalent problem of plane waves.[1-7,9,10] The solutions of this equation divide into two regimes depending on the relative sign of the fiber's group-velocity dispersion (GVD), a combination of the material GVD and the fiber waveguide dispersion. In the region of negative GVD, it is possible to have optical soliton propagation, where for the lowest-order soliton the effects of the nonlinear index of refraction balance the pulse-broadening effect of GVD and the pulse can propagate without distortion. Higher-order soliton solutions show periodic pulse-reshaping behavior. These features have been investigated and confirmed in a beautiful series of experiments.[4] In the region of positive GVD the combined effects of self-phase modulation (SPM) and GVD lead to a frequency and temporal broadening of the propagating optical pulse. The combined action of these two effects can lead to the formation of a flat-topped optical pulse with a linear frequency sweep. This behavior is the key to the operation of the optical-fiber pulse compressor.[6]

Another solution of the NLSE for positive GVD, which has been much discussed but never observed, is the "dark-pulse soliton."[1,5,7,9] In this case, one has a cw or a long optical pulse with a rapid intensity dip, "dark pulse." Because the sign of the SPM is reversed for the dark pulse, it becomes possible to balance GVD to allow the dark pulse to propagate without distortion. This picture has been challenged by recent theoretical work which claims that the full three-dimensional NLSE has no dark-pulse soliton solution for positive GVD.[8] Independent of this theoretical controversy, there have been no previous experimental investigations of this important problem.

In this Letter we describe a series of measurements of 0.3-psec dark-pulse propagation through a 10-m single-mode optical fiber. The observations were made as a function of the dark-pulse intensity, and good qualitative agreement was obtained with numerical solutions of the plane-wave NLSE. At the highest intensity, our observations showed the formation of two 0.6-psec dark pulses from single 0.3-psec input dark pulses. According to our numerical calculations, these two observed dark pulses may indicate the formation of dark-pulse solitons. When these calculations were performed for the experimental fiber length, as well as for longer propagation distances, the calculated dark pulses had converged to the analytical description of dark-pulse solitons.

The experiment shown in Fig. 1 was made possible by the newly developed "ultrafast light-controlled optical fiber modulator."[11] The operation of the modulator is based on the optical Kerr effect, and its main component is 15 mm of single-mode optical fiber. Driving the modulator by subpicosecond, compressed and amplified 6000-Å dye-laser pulses, we produced 0.3-psec holes (dark pulses) on the much longer duration (100 psec) second-harmonic (5320 Å) yttrium aluminum garnet pulses. The driving pulse is shown in Fig. 2(a), the resulting dark pulse is Fig. 2(b), and the calculated dark pulse[11,12] in Fig. 2(c) for the experimental conditions. The output pulses from the modulator were measured by cross correlation with the 0.3-psec probing pulses obtained by a partial reflection from the beam of driving pulses. The linearly polarized beam of dark pulses from the modulator was coupled into a 10-m single-mode, polarization-preserving optical fiber (Newport Research F-SPA). The resulting linearly polarized output beam from the fiber was recollimated and directed into the same cross correlator, where the beam of 0.3-psec probing pulses (suitably delayed) was used for the measurement. The 10-m optical-fiber length was limited by the delay line of the cross correlator; because of beam-

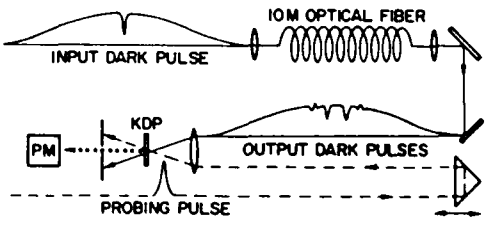

FIG. 1. Schematic diagram of the experiment.

© 1987 The American Physical Society

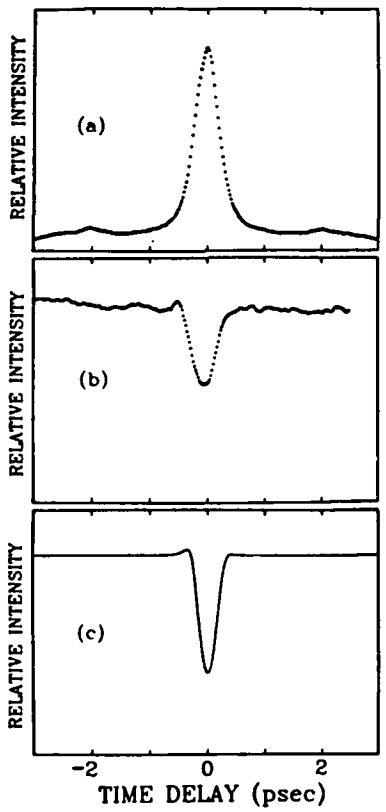

FIG. 2. (a) Autocorrelation measurement of the driving pulse. (b) Cross-correlation measurement of the input dark pulse. (c) Input dark pulse used in numerical integration of the nonlinear Schrödinger equation. For all traces, the base line is zero.

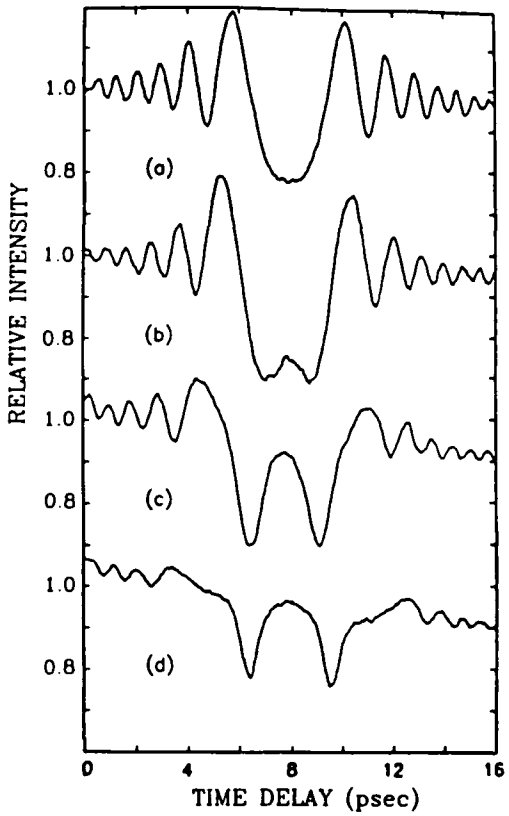

FIG. 3. Measured output dark pulses from the 10-m fiber vs peak coupled input power: (a) 0.2 W, low intensity; (b) 2 W; (c) 9 W; (d) 20 W.

stability problems, further extensions significantly degraded the time resolution and reduced the signal-to-noise ratio. The cross-correlation signals were obtained by the noncollinear generation of sum-frequency light in a 300-μm-thick potassium dihydrogen phosphate crystal. The generated light was monitored by a photomultiplier connected directly to a boxcar integrator, which in turn was connected to a multichannel analyzer synchronized with the correlator delay. In order to reduce the effect of pulse-to-pulse fluctuations, the light pulse and the driving pulse were monitored at the output of the modulator by two photodiodes connected to discriminators driving a coincidence trigger. This arrangement triggered the boxcar amplifier only if the energies of both pulses were simultaneously within narrow preset energy windows. Usually twenty scans were averaged with a typical scan requiring about 100 sec.

The measured dark pulses from the 10-m fiber are shown in Fig. 3 as a function of the coupled input power[13] for the dark pulse of Fig. 2(b). As shown in Fig. 3(a), at low powers (under 0.5 W) the output dark pulses have broadened by an order of magnitude, and a strong symmetric ringing structure has developed. At these power levels, nonlinear effects are negligible and the propagation can be described by linear dispersion theory. Therefore, a transform-limited dark pulse can be considered as the superposition of a constant cw background at the carrier frequency and an optical pulse out of phase by π radians with respect to the cw field. In the fiber these two fields propagate independently. As the pulse propagates it broadens monotonically because of GVD. When the broadened pulse width becomes much greater than the initial pulse width, the reshaped pulse has acquired a linear frequency sweep as a result of the action of GVD. The observed intensity modulation is simply the interference between the broadened frequency-swept pulse and the carrier wave. The beat frequency increases quadratically from the center of the pulse to the wings, showing the quadratic time dependence of the phase corresponding to a linear frequency sweep.[14] We calibrated the broadening of this out-of-phase hypothetical pulse by propagating through the fiber at low intensity the light pulse simultaneously produced by the modulator. For a 0.3-psec input light pulse, we observed a 9-psec output pulse. Given GVD=0.044 psec/Å·m of the fiber, this gives a bandwidth of approximately 20 Å, indicating strong phase modulation compared with the transform limit of 11 Å.

When the coupled input power was increased to 2 W, the output pulse developed a slight peak at the center in-

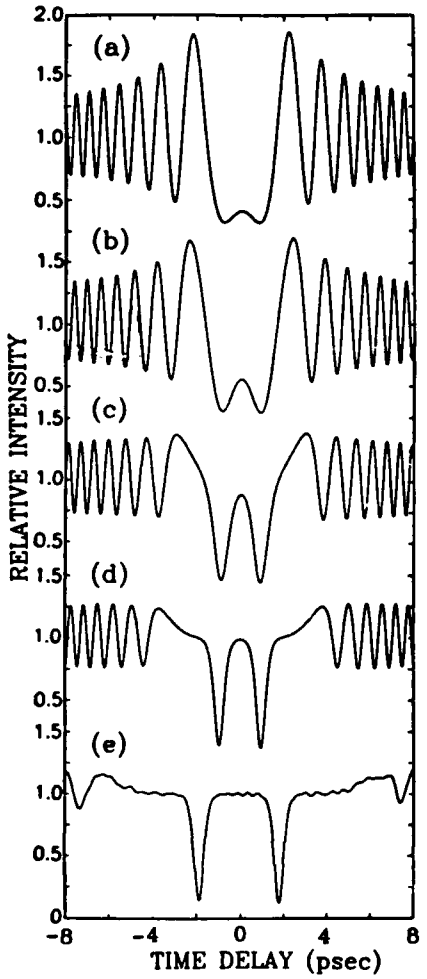

FIG. 4. Calculated output dark pulses from the fiber vs peak coupled input power and fiber length: (a) 0.2 W, 10 m; (b) 4 W, 10 m; (c) 18 W, 10 m; (d) 40 W, 10 m; and (e) 40 W, 20 m.

dicating a small phase shift at the carrier frequency caused by the nonlinearity. The output modulation pattern shifted slightly outwards from the center and was no longer described by a simple linear frequency sweep. Increasing the power to 9 W caused the central pulse to split into two clearly resolved dips, and the modulation on the wings was again pushed outwards. At 20-W input power, the modulation was pushed completely out of the central region and two well-defined 0.6-psec dark pulses developed.

The above observations were studied by the numerical integration of the plane-wave NLSE (with use of a split step routine described in Refs. 1 and 12) through the 10-m optical fiber starting with the input pulse shown in Fig. 2(c). In the low-intensity limit, we calculated the fiber output dark pulse of Fig. 4(a). Here, a well-developed symmetric ringing is obtained over a large time interval and is almost perfectly described by the interference between a broad weak pulse with a linear frequency sweep and the cw carrier wave. The experimental time resolution of 0.3 psec strongly attenuates the predicted higher-frequency modulation on the wings. In order to obtain better agreement with our observations in the nonlinear regime, the power (or equivalently the nonlinear index n_2) was increased by 2 times in the calculation compared with the experimental value. Given the difficulties in measuring peak instantaneous power,[13] the uncertainty in $n_2 = 1.1\times10^{-13}$, and the problem of knowing the effective fiber core area because of the transverse intensity variation,[5] we consider this adjustment to be within our experimental limits. With the input power raised to 4 W, the calculated output pulse in Fig. 4(b) shows a slight increase of the center bump, caused by the nonlinearity. For 18-W input pulses, the double-dip structure in the center of the pulse continues to develop into two separate pulses, while the amplitude of the ringing pattern is reduced together with a phase shift. Finally, with an input power of 40 W, we calculate in agreement with experiment the double-pulse structure shown in Fig. 4(d). Because the soliton velocity depends on the modulation depth of the input pulse, the fact that the time separation between the pulses is shorter than observed is indicative of our experimental uncertainty in measuring the input dark-pulse modulation depth.

The following considerations led to our preliminary conclusion that the dark pulses in Fig. 4(d) and consequently Fig. 3(d) may represent the formation of dark-pulse solitons. Initially, when the dark pulse enters the fiber, self-phase modulation causes a phase change that follows the pulse shape. However, the time-dependent phase $\phi(\xi)$ for the dark-pulse soliton has one of the two possible time dependences

$$\sin\phi(\xi) = \pm A\tanh(\xi)/[1-A^2\mathrm{sech}^2(\xi)]^{1/2}$$

over the $A^2\mathrm{sech}^2(\xi)$ dark pulse.[1] Consequently, to first order the phase dependence and the input pulse shape are an approximate superposition of two $(+/-)$ solitons. Recent calculations have shown that a single dark pulse can evolve into two $(+/-)$ dark-pulse solitons which continue to move apart with propagation distance.[9] The dark-pulse shapes in Fig. 4(d) are quite accurately fitted by a 0.6-psec $\mathrm{sech}^2(\xi)$ pulse shape. In addition, the calculated time-dependent phase also quite accurately fits the expression given above for the first $(-)$ soliton and the second delayed $(+)$ soliton. As a further indication that soliton formation has possibly occurred, we extended the numerical calculation to 20 m as shown in Fig. 4(e). Here the dark pulses further separated into two well-defined pulses, and the ringing on the wings was reduced in amplitude and pushed out in time. As expected for solitons, the pulse shapes did not change nor did the time-dependent phase. This convergence to the soliton solutions indicates that our experimental results are consistent with the formation of dark-pulse solitons as predicted by the plane-wave nonlinear

Schrödinger equation.

This research was partially supported by the U.S. Office of Naval Research.

---

[a]Present address: AT&T Bell Laboratories, Holmdel, NJ 07733.

[1]A. Hasegawa and F. Tappert, Appl. Phys. Lett. **23**, 142, 171 (1973).

[2]G. B. Whitham, *Linear and Nonlinear Waves* (Wiley, New York, 1974).

[3]*Solitons in Action*, edited by K. Lonngren and A. Scott (Academic, New York, 1978).

[4]L. F. Mollenauer, R. H. Stolen, and J. P. Gordon, Phys. Rev. Lett. **45**, 1095 (1980).

[5]B. Bendow, P. Gianino, N. Tzoar, and M. Jain, J. Opt. Soc. Am. **70**, 539 (1980).

[6]H. Nakatsuka, D. Grischkowsky, and A. C. Balant, Phys. Rev. Lett. **47**, 910 (1981); D. Grischkowsky and A. C. Balant, Appl. Phys. Lett. **41**, 1 (1982); A. C. Balant and D. Grischkowsky, U.S. Patent No. 4 588 957 (1986).

[7]B. Crosignani, A. Cutolo, and P. DiPorto, J. Opt. Soc. Am. **72**, 1136 (1982).

[8]D. N. Christodoulides and R. I. Joseph, Opt. Lett. **9**, 229, 408 (1984).

[9]K. J. Blow and J. J. Doran, Phys. Lett. **107A**, 55 (1985).

[10]H. G. Winful, in *Optical Fiber Transmission*, edited by E. E. Basch (Sams, Indianapolis, Indiana, 1986).

[11]N. J. Halas, D. Krökel, and D. Grischkowsky, Appl. Phys. Lett. **50**, 886 (1987).

[12]N. J. Halas, Ph.D. thesis, Bryn Mawr College, 1986 (unpublished).

[13]This is the background power level corresponding to unity on the intensity scales of Figs. 3 and 4. This power was obtained by the measurement of the energy of the 100-psec, 5320-Å pulse with a photodiode, calibrated by measurement of the average power of the second-harmonic yttrium aluminum garnet pulse train with a calorimeter.

[14]J. E. Rothenberg and D. Grischkowsky, Opt. Lett. **12**, 99 (1987).

Point source terahertz optics

Ch. Fattinger and D. Grischkowsky
IBM Watson Research Center, P.O. Box 214, Yorktown Heights, New York 10598

(Received 12 July 1988; accepted for publication 19 August 1988)

We demonstrate an ultrafast 10 μm sized, electric dipole source of terahertz radiation closely coupled to a 1 cm spherical mirror. This optical approach has the advantages of subpicosecond response times with essentially complete collection efficiency. Using this technique, we have generated and detected subpicosecond freely propagating electrical pulses.

The idea of using a transient electric dipole as a source of broadband radiation goes back to the original work of Hertz,[1] described in standard textbooks on electromagnetic theory. A modern integrated circuit version of Hertz's experiment has been performed by Auston *et al.*[2] using fast photoconductive switches on silicon-on-sapphire (SOS) wafers as the dipole sources and detectors. This work demonstrated the generation and detection of 1.6 ps pulses of radiation freely propagating through the SOS wafer.

The experiments by Ketchen *et al.*[3] describe the generation of extremely short-lived electric dipoles by the "sliding contact" method of shorting charged, micron-sized, coplanar transmission lines with ultrashort laser pulses. The extremely fast response time was mainly due to the fact that the field pattern of the electric dipole created by the sliding contact excitation matched the field pattern of the propagating TEM mode of the transmission line.[4] Therefore, in addition to the freely propagating radiation produced by the creation of the electric dipoles, the essentially perfect coupling to the line resulted in the production of two counterpropagating subpicosecond electrical pulses on the coplanar transmission line. By adding an impedence matched antenna to the coplanar line geometry, DeFonzo and Lutz have transmitted and detected freely propagating 10 ps electrical pulses.[5] Subpicosecond pulses have been generated, transmitted, and detected by Smith *et al.*[6] who fabricated ultrafast dipolar antennas terminated by coplanar transmission lines.

The above approaches using antennas extend radio and microwave techniques into the terahertz regime. In this letter we demonstrate an alternative approach, whereby optical techniques are adapted to terahertz frequencies. Our approach is distinguished by excellent time resolution and essentially complete collection of the radiation. We use an ultrafast point dipole source (Hertzian dipole) with dimensions small compared to any of the radiated wavelengths. This source is located at the focal point of a spherical lens or mirror which can focus the radiated pulse on a detector or collimate the emission to produce a beam of freely propagating ultrashort electrical pulses. Our method has extremely high coupling efficiency in that we capture essentially all of the dipolar radiation. In addition, our excellent focusing properties preserve the subpicosecond response times of the source.

The experimental geometry illustrated in Fig. 1(a), used to generate the transient electric dipole responsible for the terahertz radiation emitted into the sapphire substrate, is similar to that used earlier for transmission line studies.[3,4] Here, the subpicosecond electric dipoles are created by photoconductive shorting the charged coplanar transmission line with 70 fs pulses from a colliding-pulse, mode-locked dye laser. For short propagation distances, the electrical pulse coupled to the transmission line has the same time

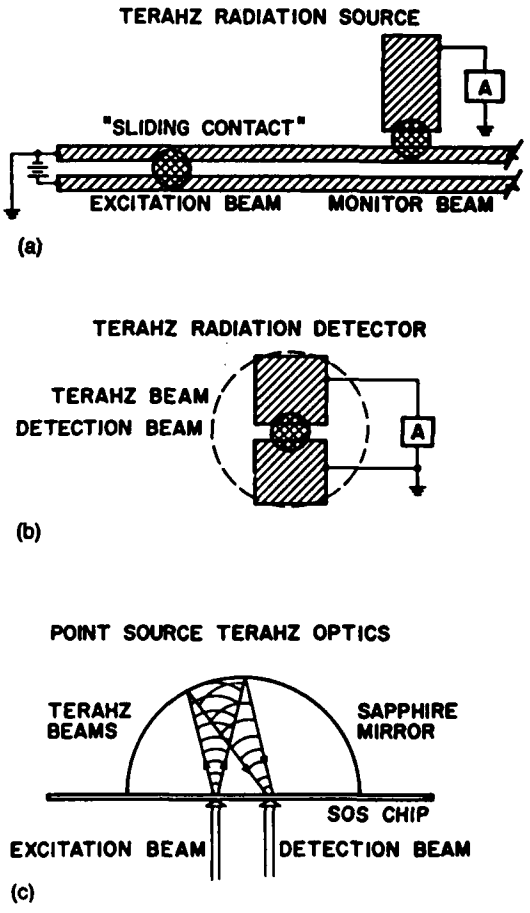

FIG. 1. (a) Schematic diagram of the charged coplanar transmission line. The laser excitation beam spot defines the location of the transient electric dipole. The monitor beam measures the electrical pulse coupled to the line. (b) Schematic diagram of the terahertz detector. The laser detection beam spot is shown centered on the gap in the focal spot of the terahertz radiation. (c) Schematic diagram of the focusing optics consisting of a gold-coated, solid-hemispherical sapphire mirror with a diameter of 9.5 mm in contact with the backside (sapphire side) of the SOS chip.

 0003-6951/88/421480-03$01.00 © 1988 American Institute of Physics

dependence as the transient electric dipole responsible for the terahertz radiation.[4] This electrical pulse on the line was measured by a fast photoconductive switch driven by the monitor beam, a time-delayed beam of the same 70 fs laser pulses, which connected the transmission line to the electrical probe. The 20-mm-long transmission line had a design impedance of 100 Ω and consisted of two parallel 5-μm-wide, 0.5-μm-thick aluminum lines separated from each other by 10 μm. The measured dc resistance of a single 5 μm line was 10 Ω/mm. The transmission line was fabricated on an undoped silicon-on-sapphire wafer, which was heavily implanted to ensure the required short carrier lifetime.[7] The measurements were made with the standard excite and probe arrangement for the beams of optical pulses.

The terahertz radiation detector shown in Fig. 1(b) is simply a photoconductive gap of 10 μm spacing with a width of 25 μm. This gap was fabricated together with the coplanar transmission line on the same SOS chip. With respect to the orientation of the transmission line shown in Fig. 1(a), the detection gap of Fig. 1(b) is located 1.7 mm below the line. One side of the gap is grounded, and a current amplifier is connected across the gap as indicated. During operation the gap is biased by the incoming terahertz radiation pulse. The measurement is made by shorting the gap via the 70 fs ultrashort optical pulses in the detection beam and measuring the collected charge (current) versus the time delay between the excitation and detection pulses.

The point-source terahertz optics illustrated in Fig. 1(c) are quite simple and consist of a gold-coated section of a 9.5-mm-diam hemisphere of sapphire contacted to the backside (sapphire side) of the SOS chip. The center of the hemisphere is located in the plane of the 0.5-μm-thick silicon layer on top of the 0.43-mm-thick SOS chip. This ensures that the terahertz radiation from the transient dipole excited in this plane will be refocused in the plane. Because we work in reflection, alignment is simple in that the focus of the excitation optical beam is imaged at the focus of the terahertz radiation and can be easily observed with an optical microscope. Thus, the hemisphere and the sliding contact are adjusted until the reflected image of the excitation laser focus appears on the gap of the terahertz radiation detector, corresponding to the center of the hemisphere adjusted to be midway between the sliding contact and the detection gap. It is important to note that most of the radiation from the transient electric dipole is contained in a 40° full angle cone normal to the surface of the SOS chip and directed into the sapphire.[8] This is a consequence of the relatively high dielectric constant of approximately 10 of sapphire. This situation gives good focusing of the terahertz radiation, because only the central portion of the spherical mirror is involved.

The generated electrical pulse on the line is shown in Fig. 2(a). This measurement was made in a single 2 min scan of the relative time delay between the excitation and monitor pulses. For this result the spatial separation between the sliding contact excitation spot and the monitor gap was 120 μm so that propagation effects were negligible. The measured FWHM as shown is 1.0 ps. Taking into account the response time of the monitor gap we consider that the actual pulse width of the transient dipole was 0.6 ps.

In Fig. 2(b), the detected terahertz radiation pulse is displayed, where the indicated amplitude scale is normalized with respect to the electrical pulse on the transmission line [Fig. 2(a)]. Again, this measurement was made in a single 2 min scan of the relative time delay between the excitation and detection pulses. The 99 ps time delay shown on Fig. 2(b) with respect to Fig. 2(a) is the measured propagation time from the generation site to the detection gap. For this particular case the radiation detection gap was located 1.7 mm below (with respect to Fig. 1) the sliding contact excitation site with the center of the hemisphere midway between. Thus, the total distance from the excitation point to the surface of hemispherical mirror and back to the gap was 9.7 mm. Using this value we obtain a propagation speed of $c/3.06$ corresponding to a dielectric constant of 9.36 in good agreement with the tabulated value of 9.42 for the ordinary ray in sapphire.[9] This agreement confirms that we have observed the freely propagating radiation pulse.

Although the observed pulse shape approximates the derivative of the time dependence of the transient electric dipole, as predicted by theoretical analysis,[6] it does not agree in detail. This slight disagreement is probably due to a combination of the following three effects. The first effect involves the strong birefringence of the sapphire, the fact that the source is polarized perpendicular to the transmission lines and the feature that the detector measures only the field component perpendicular to the gap. In order to minimize this effect the c axes of the SOS wafer and the sapphire mirror were aligned parallel to the transmission line. Second,

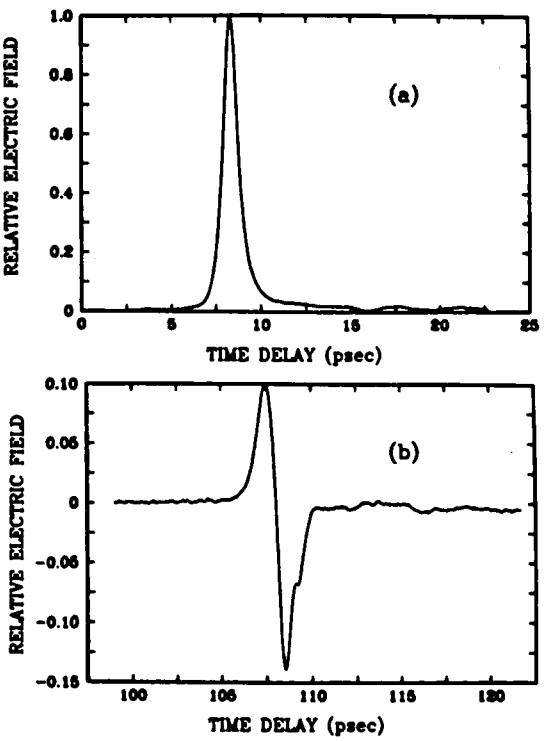

FIG. 2. (a) Measured electrical pulse with 120 μm separation between the excitation and monitor beams. (b) Measured electrical pulse of the focused freely propagating terahertz pulse at the detector.

the detection efficiency is better for higher frequencies. This is due to the fact that the focused spot size is proportional to the wavelength while the much smaller detector size is fixed. Third, we believe that the main reshaping mechanism is due to the dielectric dispersion of the sapphire crystal.[9] This effect reshapes the propagating pulse by delaying the higher frequency components with respect to the lower frequencies. Thus, the more rapid time dependence would occur on the trailing edge of the pulse in agreement with the observation.

The two main features of our method are clearly evidenced by the measurement of Fig. 2(b). First, excellent time resolution is obtained as shown by the 1 ps duration from maximum to the minimum. Second, the collection is extremely efficient. The measured pulse has a good signal-to-noise ratio and is approximately 1/10 the amplitude of the pulse coupled to the lines. Considering that we measure only the central 10-μm-diam of the total 100-μm-diam focal spot of the terahertz radiation, the power in the radiated terahertz pulse appears to be approximately the same as that coupled to the transmission lines. Our experimental results show that, by using standard optical components and techniques combined with point sources of terahertz radiation, it will be possible to generate well collimated beams of freely propagating subpicosecond electrical pulses for a multitude of applications.

We thank Joshua E. Rothenberg for stimulating and clarifying discussions concerning crystal optics and the effects of dielectric dispersion. This research was partially supported by the U.S. Office of Naval Research.

[1]H. Hertz, Weidemann's Ann. 34, 551 (1881); for a translation of this and related papers see, *Electric Waves*, by H. Hertz, translated by D. E. Jones (Dover, New York, 1962).
[2]D. H. Auston, K. P. Cheung, and P. R. Smith, Appl. Phys. Lett. 45, 284 (1984).
[3]M. B. Ketchen, D. Grischkowsky, T. C. Chen, C-C. Chi, I. N. Duling, III, N. J. Halas, J-M. Halbout, J. A. Kash, and G. P. Li, Appl. Phys. Lett. 48, 751 (1986).
[4]D. Grischkowsky, M. B. Ketchen, C-C. Chi, I. N. Duling III, N. J. Halas, J-M. Halbout, and P. G. May, IEEE J. Quantum Electron. QE-24, 221 (1988).
[5]A. P. DeFonzo, M. Jarwala, and C. R. Lutz, Appl. Phys. Lett. 50, 1155 (1987); A. P. DeFonzo and C. R. Lutz, Appl. Phys. Lett. 51, 212 (1987).
[6]P. R. Smith, D. H. Auston, and M. C. Nuss, IEEE J. Quantum Electron. 24, 255 (1988).
[7]F. E. Doany, D. Grischkowsky, and C-C. Chi, Appl. Phys. Lett. 50, 460 (1987).
[8]W. Lukosz, J. Opt. Soc. Am. 69, 1495 (1979).
[9]E. E. Russell and E. E. Bell, J. Opt. Soc. Amer. 57, 543 (1967).

Terahertz beams

Ch. Fattinger and D. Grischkowsky
IBM T. J. Watson Research Center, P. O. Box 218, Yorktown Heights, New York 10598

(Received 10 October 1988; accepted for publication 29 November 1988)

We have generated freely propagating, diffraction-limited beams of single-cycle 0.5 THz electromagnetic pulses from a 5-mm-diam coherent source. After propagating 100 cm in air, there was little change in the measured subps pulse shape, even though the signal strength was reduced by 20 times compared to the strength at 10 cm.

The importance of integrated circuit versions of the Hertzian dipole as generators and detectors of terahertz radiation was first demonstrated by Auston *et al.*[1] In a recent paper an optical approach was introduced to focus and to manipulate the terahertz radiation emitted by the Hertzian dipole source with an ultrafast time dependence.[2] The dipole had small dimensions compared to any of the radiated wavelengths and was produced by shorting a charged coplanar transmission line with an ultrashort laser pulse. When this dipole source was located at a focal point of a spherical mirror, essentially all of the emitted radiation was captured by the mirror and could be focused on an ultrafast optically driven photoconductive switch. Besides the extremely high coupling efficiency, the excellent focusing properties preserved the subps time dependence of the source. This approach represents an alternative and complementary method to recent works extending radio and microwave techniques into the terahertz regime through the use of antennas.[3,4]

In this letter we report the application of the optical technique to the generation of diffraction-limited terahertz beams with a relatively large source size, by locating the ultrafast dipole source at the focal point of a collimating lens. This technique allowed us to produce, for the first time, diffraction-limited beams of single-cycle 0.5 terahertz pulses from a coherent source (the time dependence is much faster than the transit time across the source) of 5 mm diameter. Because of their relatively low divergence, the single-cycle pulses were easily measured after a propagation distance of 100 cm. The detection was accomplished by focusing the terahertz beam on a photoconductive switch driven by a subpicosecond laser pulse.

The terahertz radiation source is similar to that used before[2,5,6] and is illustrated in Fig. 1(a). Here, the 20 μm sized subps electric dipoles are created by photoconductive shorting of the charged coplanar transmission line with 70 fs pulses from a colliding-pulse, mode-locked dye laser. As described previously, the electrical pulse coupled to the transmission line has the same time dependence as the transient electric dipole responsible for the terahertz radiation.[6] This electrical pulse on the line was measured by a fast photoconductive switch (driven by the monitor beam, a time-delayed beam of the same 70 fs laser pulses), which connected the transmission line to the electrical probe. The 20-mm-long transmission line had a design impedance of 125 Ω and consisted of two parallel 5-μm wide, 0.5-μm-thick aluminum lines separated from each other by 15 μm. The measured dc resistance of a single 5 μm line was 10 Ω/mm. The transmission line was fabricated on an undoped silicon-on-sapphire (SOS) wafer, which was heavily implanted to ensure the required short carrier lifetime.[7]

The terahertz radiation detector shown in Fig. 1(b) is simply a photoconductive gap of 5 μm spacing with a width of 25 μm. This gap was fabricated as above on a separate SOS chip. One side of the gap is grounded, and a current amplifier is connected across the gap as indicated. During operation the gap is biased by the incoming terahertz radiation pulse polarized across the gap. The measurement is made by shorting the gap via the 70 fs ultrashort optical pulses in the detection beam and measuring the collected charge (current) versus the time delay between the excitation and detection pulses.

The terahertz optics illustrated in Fig. 1(c) consist of two crystalline sapphire, spherical lenses contacted to the backside (sapphire side) of the SOS chips. For the radiation

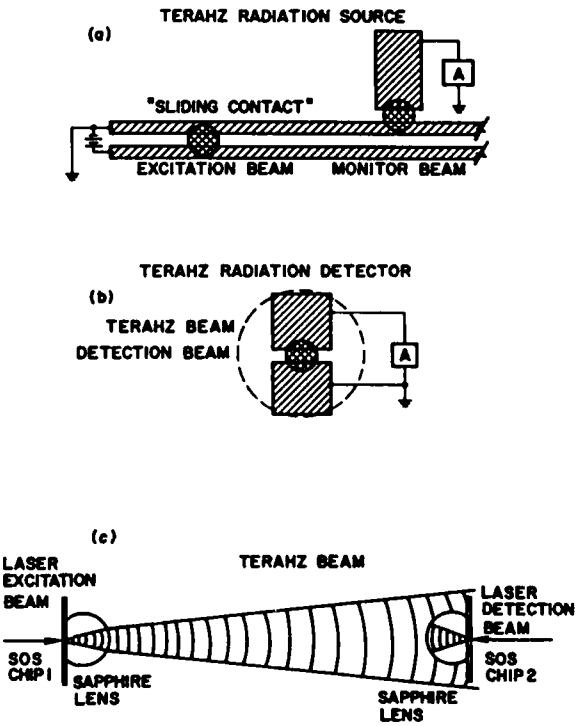

FIG. 1. (a) Schematic diagram of the charged coplanar transmission line. The laser excitation beam spot defines the location of the transient electric dipole. The monitor beam measures the electrical pulse coupled to the line. (b) Schematic diagram of the terahertz detector. The laser detection beam spot is shown centered on the gap in the focal spot of the terahertz radiation. (c) Schematic diagram of the collimating and focusing optics consisting of crystalline, sapphire lenses in contact with the backside (sapphire side) of the SOS chips.

 0003-6951/89/060490-03$01.00 © 1989 American Institute of Physics

source the center of the truncated 9.5-mm-diam sphere (lens) is 2.3 mm above the Hertzian dipole located at the focus of the lens. The same situation holds for the detector where the photoconductive switch is at the focus of the lens. For both lenses the C axis of the sapphire is perpendicular to the optical axis of the lens. For the source lens and the source chip the C axes are oriented parallel to the transmission line, while for the detecting lens and the detecting chip the C axes are perpendicular to the gap (parallel to the 25 μm dimension of the gap). Consequently, for both generation and detection the C axes are perpendicular to the polarization of the terahertz radiation. These orientations of the C axes are required in order to generate and detect the cleanest and shortest terahertz pulses. It is important to note that, because of the relatively high dielectric constant of approximately 10 of sapphire, most of the radiation emitted from the transient electric dipole is contained in a 40° full angle cone normal to the surface of the SOS chip and directed into the sapphire.[8] This situation gives exceptionally good collection and collimation of the terahertz radiation, because the central portion of the spherical lens captures essentially all of the emitted radiation. After collimation we obtain a beam diameter of 5 mm with a diffraction-limited divergence. Thus, we have changed the effective source size from 20 μm to 5 mm while at the same time preserving the ultrafast time response.

The generated electrical pulse on the line is shown in Fig. 2(a). This measurement was made in a single 2 min scan of the relative time delay between the excitation and monitor pulses. For this result the spatial separation between the sliding contact excitation spot and the monitor gap was 200 μm so that propagation effects were negligible. The measured full width at half maximum (FWHM) as shown is 0.95 ps. Taking into account the response time of the monitor gap, we consider that the actual pulse width of the transient dipole was 0.6 ps.

Figures 2(b) and 2(c) display the detected terahertz radiation pulses after propagation distances of 10 and 100 cm, respectively. The indicated amplitude scales are normalized with respect to the electrical pulse on the transmission line [Fig. 2(a)]. As can be seen, the signal strength dropped by about 20 times as the propagation distance was increased from 10 to 100 cm, indicating a full angle beam divergence of about 100 mrad. This is an average value with respect to the frequency content of the pulse, because the diffraction angle and the divergence are proportional to the wavelength. Both of these high signal-to-noise measurements of the freely propagating pulses were made in single 2 min scans of the relative time delay between the excitation and detection pulses.

With the exception of the initial dip in the observed pulse shape, the measured time dependence roughly approximates the time derivative of the transient dipole source. However, the response time of the detector is believed to be limiting the observed fast time dependence of the signal. One effect that we did not observe was an expected changing of the pulse shape as the detector was moved away from the source. This effect would have been due to a selective spectral filtering, caused by the wavelength-dependent diffraction angle, enhancing the higher frequency components of the pulse. As illustrated in Fig. 2 the main component of the signal was independent of propagation distance for distances greater than 10 cm, corresponding to the far field of the 5-mm-diam source. However, the oscillations on the trailing edge [observable in Fig. 2(c)] increased with propagation distance. We have determined that these oscillations are due to absorption by water vapor. When the 100 cm space between the source and the detector was filled by a large plastic bag inflated with helium, the oscillations disappeared. But, when a water soaked sponge was placed in the bag, the oscil-

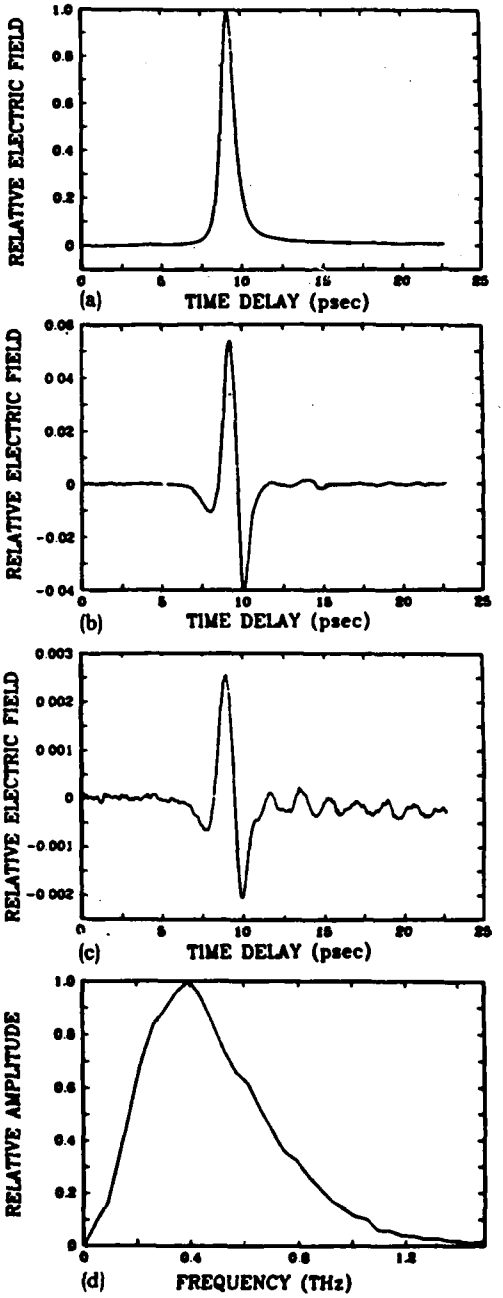

FIG. 2. (a) Measured electrical pulse on the transmission line with 200 μm separation between the excitation and monitor beams. (b) Measured electrical pulse of the freely propagating terahertz beam with the detector located 10 cm from the source. (c) Measured electrical pulse of the freely propagating terahertz beam with the detector located 100 cm from the source. (d) Amplitude spectrum of the transmitted pulse shown in (b).

lations increased in size until equilibrium was reached corresponding to 100% relative humidity.

The amplitude spectrum of the measured pulse of Fig. 2(b) is displayed in Fig. 2(d), where it is seen that the spectrum peaks at approximately 0.4 THz and extends from low frequencies up to above 1 THz. Consequently, these beams are immediately useful for transmission spectroscopy, where by Fourier analysis of the input and transmitted pulses the absorption and disperison of the investigated materials can be obtained. The importance of this conclusion is demonstrated by the water vapor observation. Finally, the wide bandwidth of these beams shows their enormous capacity as a potential communications channel.

This research was partially supported by the U.S. Office of Naval Research.

[1]D. H. Auston, K. P. Cheung, and P. R. Smith, Appl. Phys. Lett. **45**, 284 (1984).
[2]Ch. Fattinger and D. Grischkowsky, Appl. Phys. Lett. **53**, 1480 (1988).
[3]A. P. DeFonzo, M. Jarwala, and C. R. Lutz, Appl. Phys. Lett. **50**, 1155 (1987); A. P. DeFonzo and C. R. Lutz, Appl. Phys. Lett. **51**, 212 (1987).
[4]P. R. Smith, D. H. Auston, and M. C. Nuss, IEEE J. Quantum Electron. **24**, 255 (1988).
[5]M. B. Ketchen, D. Grischkowsky, T. C. Chen, C-C. Chi, I. N. Duling III, N. J. Halas, J-M. Halbout, J. A. Kash, and G. P. Li, Appl. Phys. Lett. **48**, 751 (1986).
[6]D. Grischkowsky, M. B. Ketchen, C-C. Chi, I. N. Duling III, N. J. Halas, J-M. Halbout, and P. G. May, IEEE J. Quantum Electron. **QE-24**, 221 (1988).
[7]F. E. Doany, D. Grischkowsky, and C-C. Chi, Appl. Phys. Lett. **50**, 460 (1987).
[8]W. Lukosz, J. Opt. Soc. Am. **69**, 1495 (1979).

Observation of the Formation of an Optical Intensity Shock and Wave Breaking in the Nonlinear Propagation of Pulses in Optical Fibers

Joshua E. Rothenberg and D. Grischkowsky
IBM Thomas J. Watson Research Center, P.O. Box 218, Yorktown Heights, New York 10598
(Received 11 October 1988)

We have observed the formation of an optical intensity shock and the subsequent wave breaking in the nonlinear propagation of 1-psec pulses in an optical fiber. The wave breaking manifests itself as the appearance of oscillations trailing the shock, which are due to the beating of widely separated frequency components which bridge the shock. The experimental results are in good agreement with numerical solutions of the nonlinear Schrödinger equation.

PACS numbers: 41.10.-j, 42.10.-s, 42.81.-i

Nonlinear wave propagation has received much attention recently, both because it is rich in unique phenomena relevant to many physical systems and because the theoretical treatment involves a high degree of mathematical sophistication and challenge.[1] In this class of problems the nonlinear Schrödinger equation (NLSE) is of fundamental importance because it represents the general situation of dispersive wave propagation with a weak nonlinearity.[2] Optical propagation in single-mode fibers provides an excellent physical system for study of the NLSE because the single-mode propagation allows the problem to be reduced to the equivalent 1D (plane) wave propagation problem, and because the fibers have extremely low loss. The NLSE includes two physical effects, group-velocity dispersion (GVD) and self-phase modulation (SPM) due to the intensity-dependent refractive index. Depending on their relative signs, they combine to allow bright solitary waves,[3-5] or (in the visible region of optical fibers) dark solitary waves,[3,4,6,7] enhanced frequency chirping,[8] and "optical wave breaking."[9]

A prominent class of phenomena in nonlinear wave propagation is that of shocks and breaking,[1] which are known to occur in many diverse physical systems. Breaking, a phenomenon inseparable from shocks, occurs when the top of the shock overtakes the bottom, similar to the breaking of water waves.[1,9] The possibility of so-called optical intensity "envelope" shocks was first theoretically suggested by several researchers[10,11] some twenty years ago. In the descriptions of Ref. 10, a higher-order nonlinear term was considered which results in an intensity-dependent group velocity, but because they ignored the effects of dispersion, the shock formation proposed there has never been observed. Although, for optical pulses propagating in strongly nonlinear, dispersive near-resonant vapors, nsec observations of self-steepening have been reported.[12] In addition, Hasegawa and Tappert[4] have pointed out that the dark pulse solitary wave is, in fact, an example in the class of envelope shocks proposed by Ostrovskii.[11]

In this Letter we describe the first high-resolution (0.1 psec) measurements of the formation of an intensity (envelope) shock and the subsequent oscillations due to wave breaking. We measured the reshaped output pulse from a 250-cm single-mode optical fiber versus the power of a 1-psec input pulse. Over a wide range of input powers, the output pulse has remarkably sharp self-steepened shocks of less than 0.2-psec duration. At a critical peak power of 250 W, well-defined 0.3-psec oscillations due to optical wave breaking begin to develop adjacent to the shocks.

Previous measurements of nonlinear visible pulse propagation in single-mode fibers established the characteristic rectangular reshaping and enhanced frequency chirping of the output pulses.[8] There and in subsequent numerical calculations[9,13,14] it was found that the combined effects of SPM and GVD resulted in the following pulse-shape evolution during propagation through a nonlinear fiber. Initially, pulse-intensity reshaping is minimal and all that occurs is simple SPM, where the central portion of the pulse develops a positive frequency sweep and the edges develop negative sweeps. As the pulse propagates further, the positive sweep stretches under the influence of normal GVD, but the edges compress. The result is a broadening rectangular pulse of positive frequency sweep with increasingly sharp edges which have accordingly more rapid frequency transitions from their maximum frequency shifts back to the carrier. At a critical distance, the negative frequency sweep and the edges go through a singularity, indicating the formation of the shocks. Subsequently, the edges of the rectangular pulse overlap (break) the wings of the pulse and the resulting interference between the shifted frequency components and the carrier frequency causes oscillations to appear on the wings of the pulse. This phenomenon was first termed "optical wave breaking" by Tomlinson, Stolen and Johnson.[9] Their high-resolution numerical calculations showed these oscillations in detail and explained the accompanying change in the power spectra observed in fiber-transmission experiments.[15] There have been a few attempts to observe this effect with streak cameras, both in the spectral and in the time

© 1989 The American Physical Society

domain.[16-18] Nelson *et al.*[16] observed the intensity time dependence, and Gomes, Gouveia-Neto, and Taylor[17] and Hamaide and Emplit[18] observed the spectral time dependence. In these cases the temporal resolution was insufficient to observe the predicted intensity oscillations of wave breaking.

To understand why this observation has eluded workers in the past, consider the experimental configuration of Fig. 1. A synchronously pumped, cavity-dumped dye laser with an intracavity saturable absorber supplies 608-nm, 1-psec pulses at a repetition rate of 4 MHz. The output beam is split and focused into two separate polarization-preserving fibers with core diameters of 4 μm. One fiber is 60 cm long and after compression of the output through a grating pair we obtain 120-fsec probe pulses. The other fiber is 250 cm long and its output (signal) pulse is the subject of our investigation. In the simplest configuration (shown in the dashed box of Fig. 1), one samples the signal pulse with the probe pulse in a noncollinear cross-correlation arrangement,[8] where the beams cross at their focus in a 0.3-mm $LiIO_3$ crystal. The delay of the probe beam is varied and the second harmonic is detected with a photomultiplier tube (PMT) and recorded. Unfortunately, observation of the very fast signal-pulse edge is difficult because its time position is extremely sensitive to the dye-laser input pulse power, shape, and frequency. For example, since the signal-pulse width is approximately proportional to the input pulse power, a power stability of better than 5% is required to observe an edge with a resolution of 120 fsec. Probably even more critical is the input pulse-shape stability. Consequently, this standard cross-correlation technique yielded none of the fast features predicted.

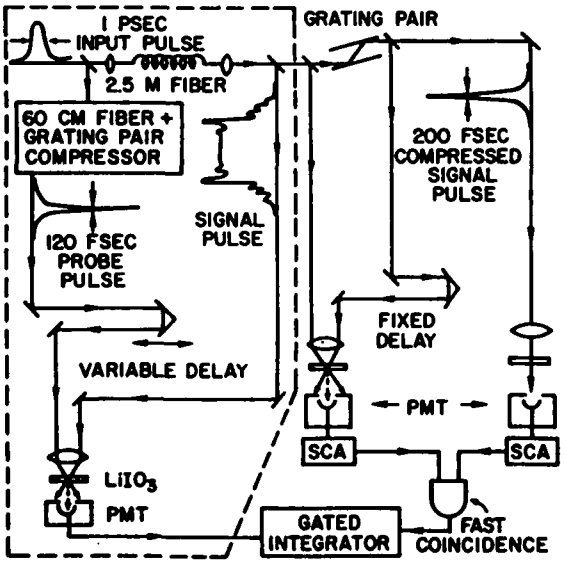

FIG. 1. Schematic of experimental arrangement, with the standard cross correlator inside the dashed box, and the pulse selection apparatus outside.

To overcome this stability problem, we use one of the sharp pulse edges (either leading or trailing) as a criterion to select and sample only those output pulses whose edges occur at a specified time. This effectively locks the time position of that edge. This is accomplished by taking a portion of the signal output pulse and cross correlating it with another portion of the signal pulse which has been compressed by a (second) grating pair. This second cross correlator is set with a *fixed* delay corresponding to the 50% point of either edge of the pulse, and the output of its PMT is selected to be within a certain range by a single-channel analyzer. The signal was further improved by simultaneous restriction of the peak power of the compressed signal pulse by detection of the second harmonic it generates with a PMT connected to a second single-channel analyzer. The outputs of the two single-channel analyzers drove a fast coincidence detector, which triggered a gated integrator. The gated integrator sampled the PMT of the (first) signal cross correlator which was scanned (typically ten times) and thus measured the intensity profile of only those pulses meeting both selection criteria. These coincident sampling rates were only 1–10 kHz compared to the optical pulse rate of 4 MHz. In the following measurements of the trailing edge of the pulse, we have selected on that edge; similar results are found for the leading edge when it is selected upon.

In Fig. 2 we show a measured sequence of the input pulse [Fig. 2(a)] and output pulses together with the corresponding numerical calculations, for increasing input-pulse peak power. At 125 W [Fig. 2(b)], the observed output pulse has broadened to a rectangularlike pulse with a sharp ~300-fsec trailing edge. The observed asymmetry is not completely understood; however, when the selection is set on the leading edge of the pulse, it sharpens up just as the trailing edge. In addition, phase modulation of the input pulse, whose spectrum is about twice the transform limit, may be contributing to the asymmetry. As the power is further increased, our observations concentrated on the development of the trailing edge of the rectangular pulse. At 250 W [Fig. 2(c)], shown on a higher-resolution time scale, the trailing edge has steepened to a ~200-fsec shock (80% to 20% fall time) and oscillations are just appearing, indicating the onset of wave breaking. In Fig. 2(d), at 500 W, wave breaking is clearly seen; the oscillations are prominent both before and after the shock, which has steepened to ~160 fsec. The ~300-fsec period of the trailing oscillations corresponds to a frequency difference of ~100 cm^{-1}, which is consistent with the observed spectrum. We note a striking similarity between these data and those obtained in shock formation in plasmas.[19] At the still higher power of 750 W [Fig. 2(e)], the shock steepened no further, indicating that we reached our resolution limit, while the contrast of the oscillations decreased as they formed an increasingly larger trailing

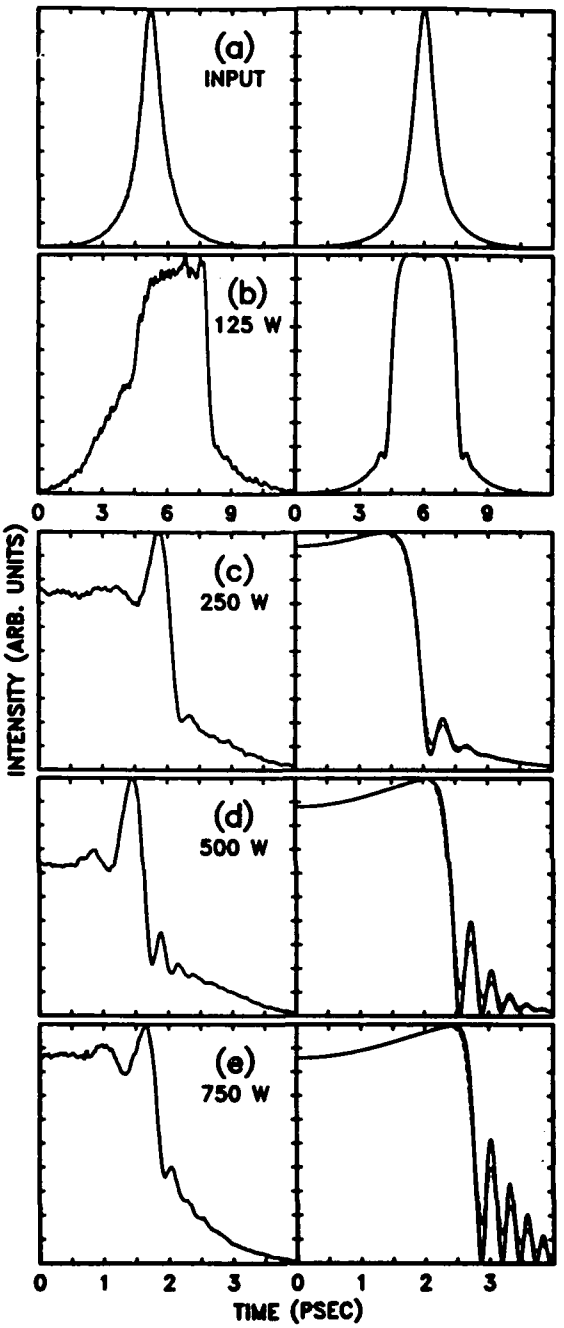

FIG. 2. Observed (first column) and calculated pulse intensities (second column), solid curves. (a) input pulse; (b)–(e) output pulse for indicated input pulse peak powers. Dashed curves are blurred with 120-fsec sech^2 resolution function.

wing.

The numerical integrations of the NLSE use an implicit centered difference method with an input pulse obtained from a fit [Fig. 2(a)] to the measured input pulse assuming no phase modulation and the indicated peak intensities. Because the calculations give a symmetric output pulse as shown in Fig. 2(b), we show only the trailing half of the calculated pulse in Figs. 2(c)–2(e).

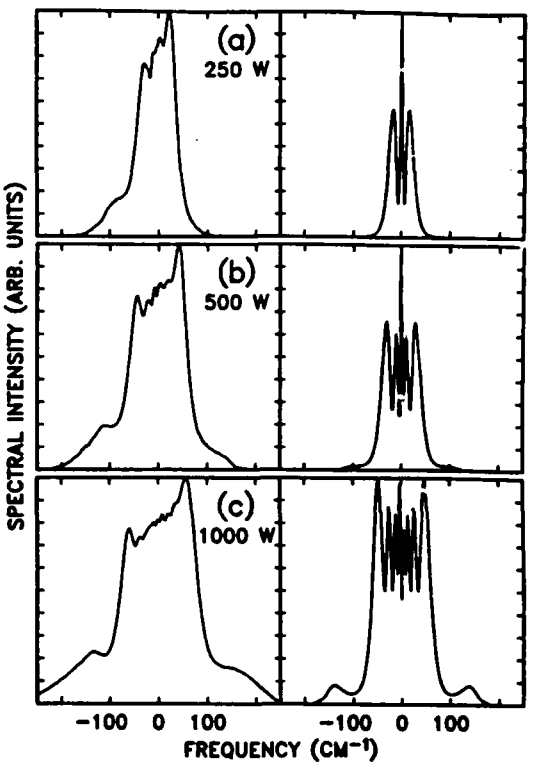

FIG. 3. Observed (first column) and calculated output pulse spectra (second column) for indicated input peak powers.

At 250 W [Fig. 2(c)], the calculation shows a ~250-fsec pulse edge and the onset of oscillations as the shock is just forming. For 500 and 750 W [Figs. 2(d) and 2(e)], the shock has steepened to 150 and 130 fsec, respectively, and wave breaking is clearly seen as indicated by the 330-fsec oscillations. For comparison with the data, these calculations are cross correlated with a sech^2 probing pulse of 120 fsec FWHM (dashed curves). It appears from the data that our resolution is slightly poorer than the probe width of 120 fsec, which is indicative of residual timing jitter in our selection technique.

The measured spectra (4 cm^{-1} resolution) and calculations are shown near the onset of wave breaking in Fig. 3. Here one should focus on the high-frequency side, since this corresponds to the trailing pulse edge. The sharp high-frequency edge in Fig. 3(a) shows the spectrum at the formation of the optical shock and before significant wave breaking has occurred (note the absence of any satellite on the high-frequency side). The satellite on the low-frequency side is not predicted by the calculations and is most likely due to stimulated Raman scattering. As the power is increased, we see a broadening of the spectrum and then, commensurate with the development of the intensity oscillations, we observe the formation of satellites[15] [Figs. 3(b) and 3(c)], which, on the high-frequency side, are in good agreement with the calculations. It should be noted that once the SPM nonlinearity has set up the negative frequency sweeps in the

pulse, subsequent linear propagation will lead to breaking that is very similar to what has been observed here. However, in the linear case, although intensity oscillations appear, no spectral satellites are formed. These satellites are the result of nonlinear mixing of the overlapping frequencies to create new frequencies at $\pm$ the frequency difference.[9] This mixing process is related to "modulation instability" as has been noted by Agrawal.[20]

In general, our calculations are in good qualitative agreement with our observations and verify that indeed the optical intensity shock and wave breaking have been observed. However, a departure from our own and previous calculations[8,9,13] is the appearance of oscillations and a peak immediately before the shock. Although Lassen *et al.*[14] have found peaks in their NLSE solutions for very lossy fibers, the linear loss of our fiber is too small to be responsible for the observed peak. Therefore, the addition of higher-order terms to the NLSE may be indicated.[21] The inclusion of the nonlinear group-velocity term mentioned earlier is about a factor of 10 too small to have any significant effect at our power levels. However, Raman scattering has led to some important effects at these power levels in soliton experiments,[22] and appears to have affected our spectral data. Therefore, its investigation in the normal dispersion regime may be warranted.

This work was supported in part by the U.S. Office of Naval Research.

[1]G. B. Whitham, *Linear and Nonlinear Waves* (Wiley, New York, 1974).

[2]H. C. Yuen and B. M. Lake, in *Solitons in Action*, edited by K. Lonngren and A. Scott (Academic, New York, 1978).

[3]V. E. Zakarov and A. B. Shabat, Zh. Eksp. Teor. Fiz. **61**, 118 (1971), and **64**, 1627 (1973) [Sov. Phys. JETP **34**, 62 (1972), and **37**, 823 (1973)].

[4]A. Hasegawa and F. Tappert, Appl. Phys. Lett. **23**, 142, 171 (1973).

[5]L. F. Mollenauer, R. H. Stolen, and J. P. Gordon, Phys. Rev. Lett. **45**, 1095 (1980).

[6]P. Emplit, J. P. Hamaide, F. Reynaud, C. Froehly, and A. Barthelemy, Opt. Commun. **62**, 374 (1987).

[7]D. Krokel, N. J. Halas, G. Giuliani, and D. Grischkowsky, Phys. Rev. Lett. **60**, 29 (1988).

[8]H. Nakatsuka, D. Grischkowsky, and A. C. Balant, Phys. Rev. Lett. **47**, 910 (1981); D. Grischkowsky and A. C. Balant, Appl. Phys. Lett. **41**, 1 (1982).

[9]W. J. Tomlinson, R. H. Stolen, and A. M. Johnson, Opt. Lett. **10**, 457 (1985).

[10]R. J. Joenk and R. Landauer, Phys. Lett. **24A**, 228 (1967); F. DeMartini, C. H. Townes, T. K. Gustafson, and P. L. Kelley, Phys. Rev. **164**, 312 (1967).

[11]L. A. Ostrovskii, Zh. Eksp. Teor. Fiz. **54**, 1235 (1968) [Sov. Phys. JETP **27**, 660 (1968)].

[12]D. Grischkowsky, E. Courtens, and J. A. Armstrong, Phys. Rev. Lett. **31**, 422 (1973).

[13]W. J. Tomlinson, R. H. Stolen, and C. V. Shank, J. Opt. Soc. Am. B **1**, 139 (1984).

[14]H. E. Lassen, F. Mengel, B. Tromborg, N. C. Albertsen, and P. L. Christiansen, Opt. Lett. **10**, 34 (1985).

[15]A. M. Johnson and W. M. Simpson, J. Opt. Soc. Am. B **2**, 619 (1985).

[16]D. P. Nelson, D. Cotter, K. J. Blow, and N. J. Doran, Opt. Commun. **48**, 292 (1983).

[17]A. S. L. Gomes, A. S. Gouveia-Neto, and J. R. Taylor, Electron. Lett. **22**, 41 (1986).

[18]J.-P. Hamaide and P. Emplit, Electron. Lett. **24**, 818 (1988).

[19]K. Saeki, J. Phys. Soc. Jpn. **35**, 251 (1973).

[20]G. P. Agrawal, Phys. Rev. Lett. **59**, 880 (1987).

[21]E. Bourkoff, W. Zhao, R. I. Joseph, and D. N. Christodoulides, Opt. Lett. **12**, 272 (1987).

[22]F. M. Mitschke and L. F. Mollenauer, Opt. Lett. **11**, 659 (1986).

Subpicosecond electrical pulse generation using photoconductive switches with long carrier lifetimes

D. Krökel, D. Grischkowsky, and M. B. Ketchen
IBM T. J. Watson Research Center, P.O. Box 218, Yorktown Heights, New York 10598

(Received 24 October 1988; accepted for publication 20 December 1988)

Using a new mechanism of electrical pulse generation, we have generated 350 fs (full width at half maximum) electrical pulses on a coplanar transmission line, fabricated on an unimplanted silicon-on-sapphire substrate.

A powerful method of generating picosecond and subpicosecond electrical pulses is based on driving photoconductive switches with ultrashort laser pulses.[1] Recent work has adapted this approach to the so-called "sliding contact" method of pulse generation.[2–4] Here, a charged transmission line fabricated on a photoconductive substrate is shorted via the photocarriers generated by an ultrashort laser pulse focused between the lines. Due to the exceptionally good coupling of the generated pulse to the propagating mode of the line, the response time is very fast and is predicted to follow the transient conductivity of the photoconductive switch.[4] Usually the photoconductive substrate is a silicon-on-sapphire (SOS) wafer, which has been heavily ion implanted to ensure a short carrier lifetime.[5] For this case, the generated electrical pulse has a rapid rise followed by an exponential decay determined by the carrier lifetime of approximately 600 fs. For an unimplanted wafer a step-function pulse is generated with an initial rapid rise time followed by a long pulse tail whose duration is given by the carrier lifetime of approximately 100 ps. The electrical pulse generated on the transmission line can be measured with either a probing photoconductive switch[1,3,4] or by using electro-optic techniques.[2,6]

In this letter we report observations of a new mechanism to generate subpicosecond electrical pulses whose duration is not determined by the carrier lifetime. The key to this approach is the asymmetric irradiation of a charged coplanar transmission line fabricated on an unimplanted SOS wafer. Using this method we have generated and measured electrical pulses as short as 350 fs.

The schematic diagram of the experimental arrangement is illustrated in Fig. 1. The 21-mm-long transmission line had a design impedance of 100 Ω and consisted of two parallel 5-μm-wide, 1-μm-thick aluminum lines separated from each other by 10 μm. The measured dc resistance of a single 5 μm line was 9 Ω/mm. The $LiTaO_3$ crystal had dimensions of 2 mm × 3 mm × 0.1 mm and was contacted to the silicon side of the SOS substrate with the z axis in the 2 mm × 3 mm plane of the crystal and perpendicular to the transmission line. We used the same 20× microscope objective lens to focus both the 4 mW exciting and 4 mW sampling beams on the 0.5-μm-thick silicon layer. The 625 nm, 70 fs laser pulses were from a compensated, colliding-pulse, mode-locked dye laser with a 100 MHz pulse repetition rate. The beams entered the wafer from the polished sapphire side and exited at the silicon side, where the focused beam size was approximately 4 μm in diameter. The generated electrical pulse was measured by monitoring the change in polarization of the sampling beam due to the presence of the pulse, using an optical arrangement similar to that previously described.[6] As shown in the figure, in order for our new pulse generation mechanism to operate, the laser beam must be focused to a spot smaller than the separation between the two lines of the coplanar transmission line. For optimum performance the small laser spot should partially illuminate the back side of the positively charged line.

Our measurement of the generated pulse under the above conditions is illustrated in Fig. 2(a). This measurement was taken 100 μm away from the excitation site. Here the rise time is 260 fs with a full width at half maximum (FWHM) pulsewidth of only 350 fs. This result showing our shortest electrical pulse was obtained by optimizing the position of the excitation beam with respect to the positive line. From our calibration of the strength of the electro-optic effect versus voltage on the transmission line, we determined the amplitude of the generated pulse to be approximately 180 mV. This value is to be compared with the bias voltage of + 10.5 V. Characteristically, we always observed a strong short pulse followed by a much weaker step function. Although the signal strength is proportional to the bias voltage across the line, the general features of the observed pulse are independent of bias voltage from approximately + 1.5 to + 20 V. However, when the voltage polarity is changed, the initial short pulse changes sign and is reduced in amplitude by 10 times, as shown in Fig. 2(b). The small rapid oscillations are an optical interference effect at the detector and are independent of the electrical pulse on the line. When the focal spot size is increased to completely fill the space between the two lines, the short pulse disappears and the expected step function for unimplanted material is obtained as shown in Fig. 2(c). The rise time of 690 fs is almost three times that of Fig. 2(a), and the pulse amplitude has more than doubled. This pulse decays with the carrier lifetime of

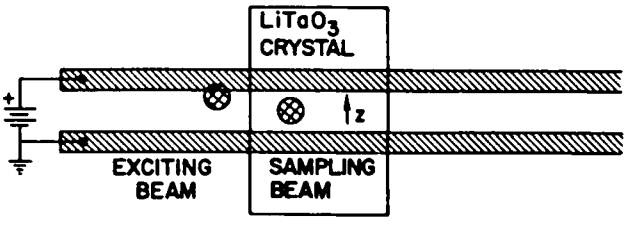

FIG. 1. Schematic diagram of the experiment. The coplanar transmission line consists of two 5-μm-wide by 1-μm-thick aluminum lines separated from each other by 10 μm, fabricated on a silicon-on-sapphire substrate.

 0003-6951/89/111046-02$01.00 © 1989 American Institute of Physics

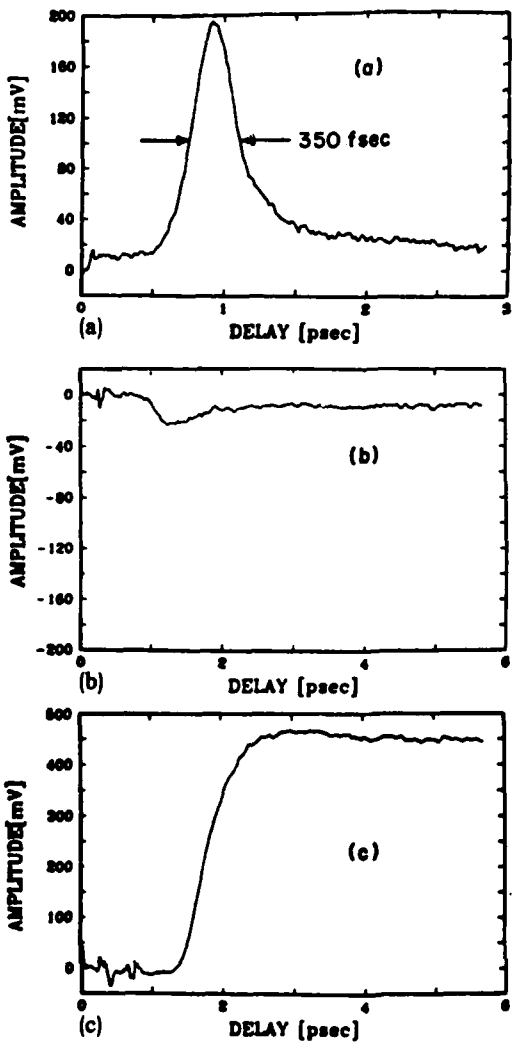

FIG. 2. Measured electrical pulse with 10.5 V across the lines. (a) Small diameter exciting beam in contact with the positive line. (b) Polarity reversed; small diameter exciting beam in contact with the negative line. (c) Diameter of the exciting beam increased to completely fill the separation between the two lines.

approximately 100 ps. In contrast to the observations of Figs. 2(a) and 2(b), for the step function changing the voltage polarity reduces the amplitude by approximately 30% together with changing the polarity of the observed pulse. We have repeated these measurements using ion-implanted photoconductive switches (gaps) for the detection. The same effects were observed, but with somewhat lower time resolution due to the longer response time of the gap. We have also observed changes in shape due to propagation on the line. In this regard it is important to note that, because of the asymmetric excitation for Fig. 2(a), the generated pulse does not match the propagating (differential) mode of the transmission line. Rather, the pulse is a linear superposition of both the common mode and the differential mode. This superposition causes the pulse to broaden more rapidly as it propagates down the line.

We are currently working to understand the physics of this new pulse generation mechanism. An intuitively appealing model involves the instantaneous formation of a very conductive region, defined by the laser spot, which becomes an equipotential with the positive line. This change in conductor geometry gives rise to a capacitance increase δC to produce an electrical pulse comparable to that which would be produced by the instantaneous addition of a charge $\delta Q = V\delta C$ to the line. Such a simple picture does not by itself explain the asymmetry in the polarity of the bias voltage. Possible explanations of this asymmetry require a more detailed examination of the metal-silicon-metal transmission line structure which, in the simplest case, consists of two ideal back-to-back Schottky barrier diodes. The diode at the one line is reverse biased while the diode at the other line is forward biased. For this case almost all of the dc voltage applied to the transmission line is dropped across the depletion region of the reverse biased diode. Thus, at one line our intuitive model should apply, while at the other line little if any effect is expected, since that entire region is already nearly an equipotential. Another possible explanation is that there are a large number of mobile surface ions (Na for example) on the unpassivated silicon surface which move to the vicinity of the negative electrode when a voltage is applied, leaving most of the potential drop near the positive electrode. Again the mechanism of our intuitive model would imply a much larger effect at the positive electrode. As evidence of the asymmetry of the electric field in the silicon between the lines, we have detected a 5% asymmetry for the dc electric field above the lines via the sampling beam passing through the electro-optic crystal. Additional experiments are in progress to help develop a more detailed picture of the pulse generation mechanism.

We would like to acknowledge Tak Ning for informative discussions on the metal-silicon interface. This research was partially supported by the U.S. Office of Naval Research.

[1]D. H. Auston, IEEE J. Quantum Electron. QE-19, 639 (1983).
[2]D.R. Dykaar, T. Y. Hsiang, and G. A. Mourou, in *Picosecond Electronics and Optoelectronics*, Proceedings of the Topical Meeting, Lake Tahoe (Incline Village), Nevada, March 13–15, 1985, edited by G. A. Mourou, D. M. Bloom, and C.-H. Lee (Springer, Berlin, Heidelberg, 1985), pp. 249–252.
[3]M. B. Ketchen, D. Grischkowsky, T. C. Chen, C.-C. Chi, I. N. Duling III, N. J. Halas, J.-M. Halbout, J. A. Kash, and G. P. Li, Appl. Phys. Lett. 48, 751 (1986).
[4]D. Grischkowsky, M. B. Ketchen, C.-C. Chi, I. N. Duling III, N. J. Halas, J.-M. Halbout, and P. G. May, IEEE J. Quantum Electron. QE-24, 221 (1988).
[5]F. E. Doany, D. Grischkowsky, and C.-C. Chi, Appl. Phys. Lett. 50, 460 (1987).
[6]J. A. Valdmanis, G. A. Mourou, and C. W. Gabel, IEEE J. Quantum Electron. QE-19, 664 (1983).

Observation of Electromagnetic Shock Waves from Propagating Surface-Dipole Distributions

Ch. Fattinger and D. Grischkowsky
IBM Watson Research Center, P.O. Box 218, Yorktown Heights, New York 10598
(Received 27 January 1989)

We have directly measured the time-dependent electromagnetic shock wave generated by an electric surface-dipole distribution propagating faster than the phase velocity in the underlying dielectric substrate. The results are in good agreement with a theory describing the moving volume-dipole distribution with the inclusion of an equal strength surface reflection.

PACS numbers: 41.10.−j, 03.50.−z, 84.40.−x

In a recent experiment,[1] evidence was presented which indicated that an electromagnetic shock wave is produced when an ultrashort electric pulse propagates on a coplanar transmission line at speeds faster than the phase velocity in the underlying dielectric substrate. Because these electrical pulses propagate as the differential (TEM) mode of the two-line coplanar transmission line, there is a positive pulse on one line and a negative pulse of identical shape on the other. Therefore, the total electric field of the pulse is described by a propagating electrical dipole distribution. Consequently, as seen from the underlying dielectric, the situation is that of an electric dipole distribution propagating on the surface faster than the phase velocity in the dielectric. This situation produces an electromagnetic shock wave in a manner similar to Cherenkov radiation[2] and electro-optic Cherenkov radiation.[3–5] The initial indirect observation[1] was the measurement of the frequency-dependent loss from the propagating electric pulse due to the Cherenkov radiation. In this Letter we present the first direct observation of the shock wave and a measurement of its time dependence. In addition, we obtain good agreement between our experiment and a new theoretical result.

Because our physical situation is related to electro-optic Cherenkov radiation, we briefly review this earlier work. Auston created a moving volume electric dipole distribution by driving the optical rectification effect in a nonlinear dielectric material with an ultrashort laser pulse.[3,4] Because the speed in the dielectric for both the visible light pulse and the volume dipole was much faster than the phase velocity for the THz frequencies describing the electric field of the volume-dipole distribution, an electromagnetic shock wave was produced. For a laser pulse focused to transverse dimensions smaller than the spatial pulse length, Kleinman and Auston (KA) have calculated the time-dependent electric field of the shock wave.[5]

In the limit as a time-dependent dipole inside a dielectric approaches the dielectric surface to arbitrarily small distances, the emitted radiation remains the vector sum of the field radiated into the dielectric and the field reflected from the surface.[6,7] For a time-dependent dipole oriented parallel to the surface, both the total radiated power and the angular distribution of radiation are continuous as the dipole is moved across the surface; the solution of the electromagnetic boundary-value problem is the same for the dipole located either in the proximity of the surface or on the surface.[7] When the dipole is some distance away from the surface, the resulting so-called "wide-angle interference" depends on the magnitude and the relative phase of the reflected radiation and on the optical path difference between the interfering waves. As the distance between the dipole and the surface approaches zero, the phase difference between the two waves is due only to the reflection. Using this theoretical approach, we obtain the time dependence and the spatial distribution of the electromagnetic field generated by the propagating surface-dipole distribution.

These results will now be applied to the situation illustrated in Fig. 1, after a brief description of the experimental parameters. The index of refraction n_0 for the ordinary ray in the sapphire substrate is approximately constant at 3.07 from low frequencies up to more than 1 THz.[8] The corresponding group velocity of the electrical pulse and the associated surface-dipole distribution on the transmission line is $v_g = c/2.28$.[9] Given n_0 and v_g, we calculate the angle θ_0 of the (ordinary) shock wave to be 42°.[5] Therefore, the shock wave hits the sapphire/air interface at an angle of incidence well above the critical angle $\alpha_c = 19°$ for total internal reflection. This complete reflection at the interface changes the shock wave due to the accompanying phase shift Φ.[10] The reflected and directly emitted shock waves (Cherenkov cones) spatially coincide. Therefore, our predicted shock wave is the sum of two equal-strength time-dependent terms, the directly radiated electric field E_D with the KA time dependence[5] shown in Fig. 2(a), and the reflected field E_R with a different time dependence due to its total reflection. Before reflection, the E_R term also had the KA time dependence. Because the radiation emitted from the surface-dipole distribution is highly directional,[6] only those conical rays emitted in directions close to the two rays shown in Fig. 1(b) have significant amplitudes. For the ordinary ray propagating in the x-z plane

© 1989 The American Physical Society

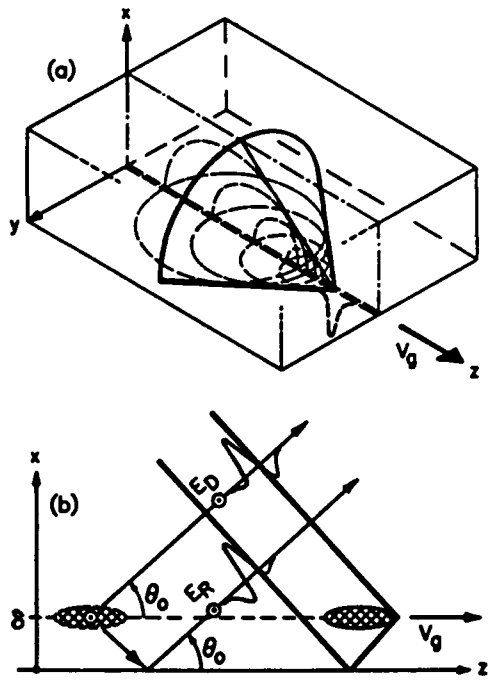

FIG. 1. (a) Cherenkov cone (shock wave) in the dielectric half-space for the propagating surface-dipole distribution. (b) Cross-sectional view of the directly radiated and reflected Cherenkov cones from a moving volume-dipole distribution near the surface of a dielectric.

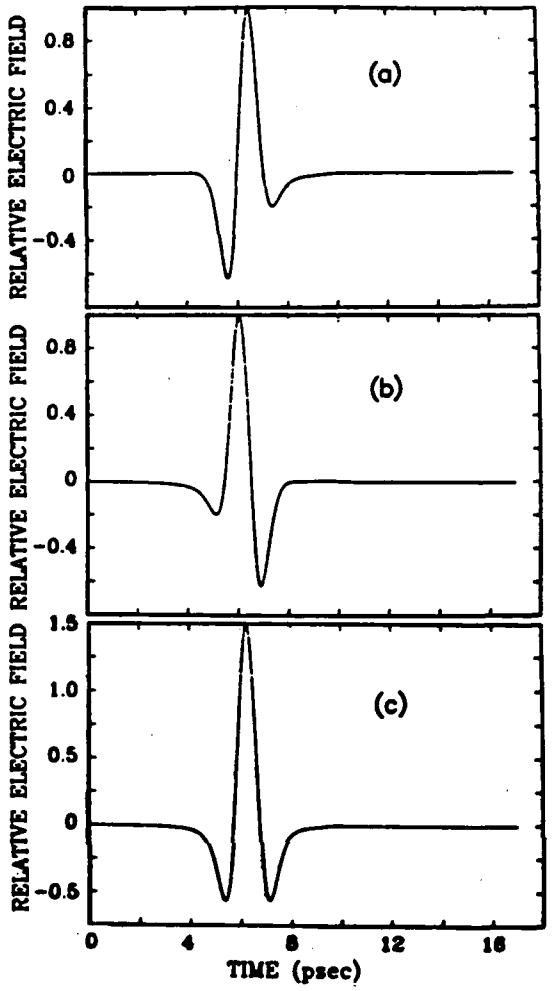

FIG. 2. (a) The Kleinman-Auston (KA) solution for the volume-dipole distribution shock wave. (b) The KA solution after a phase shift of $\Phi_0 = -89.8°$ for all frequencies. (c) The surface-dipole distribution shock wave, the sum of (a) and (b).

as shown in Fig. 1(b), the phase shift upon reflection is $\Phi_0 = -89.8°$ for all the frequency components of the pulse.[11] This phase shift changes the shock wave of Fig. 2(a) to that of Fig. 2(b). The predicted freely propagating shock wave shown in Fig. 2(c) is the sum of Figs. 2(a) and 2(b). This situation is depicted in Fig. 1(b) as the sum of E_D and E_R in the limit as δ approaches zero. The sum is equivalent to a phase shift of the KA solution by $\Phi_0/2$, together with an amplitude change of $2\cos(\Phi_0/2)$.

The observation of the shock wave was made possible by the focusing geometry illustrated in Fig. 3(a). A section of a crystalline sapphire cylinder is contacted to the backside (sapphire side) of the silicon-on-sapphire (SOS) wafer used to generate the shock wave. Because sapphire is strongly birefringent at THz frequencies with refractive indices of $n_0 = 3.07$ for the ordinary ray and $n_e = 3.41$ for the extraordinary ray, two shock waves with orthogonal polarization and propagating with different speeds are emitted into the sapphire.[12] The cyclindrical symmetry of the experimental configuration preserves, during reflection from the cyclindrical mirror, the orthogonal polarization of the ordinary and extraordinary shock waves, which are polarized perpendicular and parallel to the plane of incidence, respectively. As indicated in Fig. 3, the cylindrical mirror focuses shock-wave radiation on the detection gap from only one point on the line, the emission point. The excitation site was 7.1 mm from the gap and was located outside of the sapphire cylinder in order to prevent the cylinder from collecting the burst of radiation accompanying the creation of the electrical pulse on the transmission line.[13] Knowing Θ_0 and the 5.1-mm diam of the cylinder, we obtain 5.6 mm for the separation between the emission point and the detection gap, and 7.4 mm for the total free-flight distance of the focused ordinary shock wave.

The coplanar transmission-line structure[1,9] used to generate the ultrashort electrical pulses is designated as the generation line in Fig. 3(c). By photoconductively shorting the charged line at the excitation site with the excitation beam of 70-fsec pulses from a colliding pulse mode-locked dye laser, subpicosecond electrical pulses are produced. This method of pulse generation ensures a pure dipolar pulse[9] with a field distribution which matches the differential (TEM) mode of the coplanar line. The resulting electrical pulses propagating on the generation line are measured by a fast photoconductive switch, driven by the time-delayed monitor beam of the

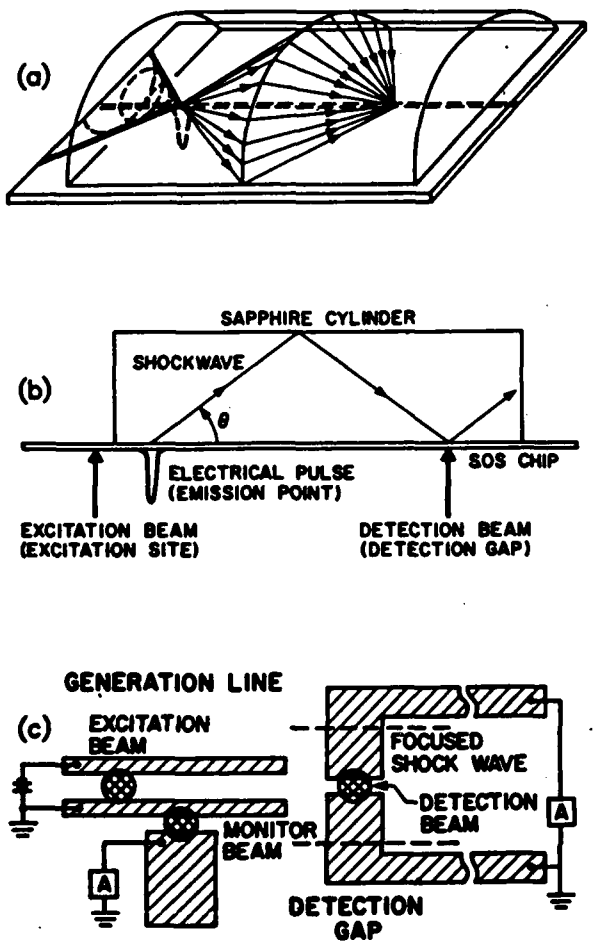

FIG. 3. (a) Focusing optics for the shock wave. (b) Cross-sectional view of the focusing optics. (c) Schematic diagram of the charged coplanar transmission line and the detection gap.

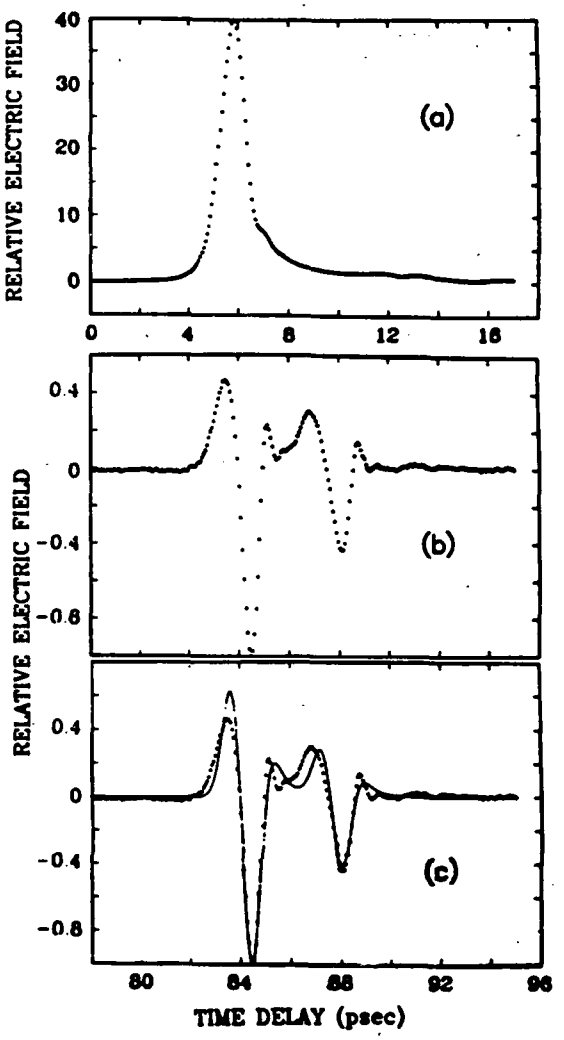

FIG. 4. (a) Measured electrical pulse on the transmission line. (b) Measured focused electromagnetic shock waves. (c) Measured shock waves compared with theory.

same 70-fsec laser pulses. The generation line consisted of two parallel 5-μm-wide, 1-μm-thick, aluminum lines separated from each other by 10 μm. Typically, the bias voltage was 10 V. The shock wave is measured with the detection gap, separated by 1 mm from the generation line. The shock wave electrically biases the gap, which is driven by the detection beam. The detection-gap spacing was 5 μm with a width of 20 μm. The gap itself was at the end of a second transmission line consisting of two parallel 10-μm-wide, 1-μm-thick aluminum lines separated from each other by 30 μm. Both transmission lines were fabricated on an undoped-SOS wafer, heavily implanted with O^+ ions.

Figure 4(a) displays the measured 1.2-psec (FWHM) electrical pulse on the generation line. Considering the relatively slow 0.7-psec response time of the monitor side gap, we estimate that the actual (FWHM) pulse width was approximately 1.0 psec. For this result the spatial separation between the exciting and sampling beams was 1.5 mm, equal to the separation between the excitation site and the emission point.

The measured electric field of the focused shock wave is shown in Fig. 4(b), where the 78-psec delay indicates the propagation time from the emission point to the detection gap. The amplitude is normalized relative to the 40× larger pulse on the line [Fig. 4(a)]. The observed time dependence is expectionally fast with well resolved features down to the 0.5-psec response time of the detection gap. This measurement is the sum of four 2-min scans of the relative time delay of the detection beam; the resulting signal-to-noise ratio is better than 100:1. The appearance of two similar shock waves is due to the birefringence of sapphire. The first is the ordinary shock wave while the second, arriving 3.6-psec later, is the extraordinary shock wave.[12]

In order to compare experiment and theory, we now explain how our predicted shock wave is changed to the inverted KA solution by the two total internal reflections shown in Fig. 3(b). When the emergent (ordinary)

shock wave hits the cylindrical mirror, it is totally reflected; all its spectral components are phase shifted by Φ_0, and the time dependence is changed. This reflection focuses the wave on the detector where another total reflection occurs. The detector measures the total field, the sum of the incident and equal strength reflected wave (phase shifted by Φ_0), with the net phase shift of $\Phi_0/2$. In summary, the initial shock wave of Fig. 2(c) is equivalent to the KA solution with a $\Phi_0/2$ phase shift. This wave is then phase shifted Φ_0 by the mirror and $\Phi_0/2$ at the detector. Consequently, the total phase shift is $2\Phi_0$ which is approximately equal to $-\pi$. Thus, the observed shock wave should be the inverted KA solution. For the extraordinary shock wave three different planes of incidence must be considered. The phase shifts of approximately $-180°$ for the emission point and detection gap have almost no effect on the time dependence due to the relative polarization of the directly emitted and reflected components. Thus, the emergent extraordinary shock wave has the original KA time dependence. The total reflection at the cylindrical mirror shifts the phase by $-170°$, which remains as the net phase shift at the detection gap. Therefore, the inverted KA dependence is also predicted for the measured extraordinary shock wave.

In Fig. 4(c), the measurements are compared with the inverted KA result for two overlapping shock waves separated by 3.6 psec.[12] The relative strengths of these waves have been adjusted for the best fit to be 1:0.4, indicating the different radiation and detection efficiences for the ordinary and extraordinary shock waves, respectively. They both correspond to the radiation from 0.65-psec $1/e$ half-width, or equivalently 1.1-psec FWHM, Gaussian dipolar electrical pulses moving on the transmission line with $v_g = c/2.28$. The 1.1-psec pulse width is only slightly longer than our measured value of 1.0 psec for the electrical pulse propagating on the transmission line. Even though the above analysis neglects several minor complicating effects,[14] the agreement between theory and experiment is quite good. In summary, the measurements have verified the existence of the shock wave produced by the propagating surface-dipole distribution, and the agreement between theory and experiment for the time dependence has confirmed the importance of the surface reflection. In addition, this shock-wave radiation is a fundamental limitation for the propagation of ultrafast signals as surface waves.

We acknowledge Martin van Exter and Joshua E. Rothenberg for stimulating and clarifying discussions. This research was partially supported by the U. S. Office of Naval Research.

[1]D. Grischkowsky, I. N. Duling, III, J. C. Chen, and C.-C. Chi, Phys. Rev. Lett. **59**, 1663 (1987).

[2]J. V. Jelley, *Cherenkov Radiation and Its Applications* (Pergamon, New York, 1958).

[3]D. H. Auston, Appl. Phys. Lett. **43**, 713 (1983).

[4]D. H. Auston, K. P. Cheung, J. A. Valdmanis, and D. A. Kleinman, Phys. Rev. Lett. **53**, 1555 (1984).

[5]D. A. Kleinman and D. H. Auston, IEEE J. Quantum Electron. **20**, 964 (1984).

[6]W. Lukosz, J. Opt. Soc. Am. **69**, 1495 (1979).

[7]W. Lukosz, Phys. Rev. B **22**, 3030 (1980).

[8]E. E. Russell and E. E. Bell, J. Opt. Soc. Am. **57**, 543 (1967).

[9]D. Grischkowsky, M. B. Ketchen, C.-C. Chi, I. N. Duling, III, N. J. Halas, J.-M. Halbout, and P. G. May, IEEE J. Quantum Electron **24**, 221 (1988).

[10]K. P. Cheung and D. H. Auston, Opt. Lett. **10**, 218 (1985).

[11]M. Born and E. Wolf, *Principles of Optics* (Pergamon, Oxford, 1980), 6th ed.; see Chap. 1.5.4, p. 49, Eqs. (59) and (60). Birefringent media are treated in the original work of F. Fockels, *Lehrbuch der Kristalloptik* (Teubner, Berlin, 1906).

[12]With the c axis of both the cylinder and the wafer parallel to the transmission line, the extraordinary shock wave has a cylindrical shape and the Cherenkov angle θ_e is given by $\tan\theta_e = (n_0/n_e)\tan\theta_0$. For the extraordinary shock wave the conical rays are no longer perpendicular to the wave surface and have the phase velocity

$$v_e = (c/n_e)[\sin^2\theta_e + (n_0/n_e)^2\cos^2\theta_e]^{-1/2}.$$

This yields a 3.8-psec delay (in agreement with experiment) of the extraordinary shock wave relative to the ordinary wave at the detection gap.

[13]Ch. Fattinger and D. Grischkowsky, Appl. Phys. Lett. **53**, 1480 (1988).

[14]These effects are (1) a weak frequency dependence of n_0 and n_e, (2) a slight reshaping of the pulse as it approaches the focal line of the cylindrical mirror (Guoy effect for cylindrical focusing), and (3) the higher frequencies are focused more tightly as $\omega^{1/2}$.

High-brightness terahertz beams characterized with an ultrafast detector

Martin van Exter, Ch. Fattinger, and D. Grischkowsky
IBM Watson Research Center, P. O. Box 218, Yorktown Heights, New York 10598

(Received 9 March 1989; accepted for publication 15 May 1989)

We have significantly improved the emission and detection of electromagnetic beams of single-cycle 0.5 THz pulses, through the use of new dipolar antenna structures. The frequency response was extended to well beyond 1 THz, and the beam power was increased by more than 15 times. The antennas were located at the foci of sapphire lenses and were photoconductively driven by ultrafast laser pulses. An additional collimation by a paraboloidal mirror produced a beam with a 25 mrad divergence, and subsequent focusing by a second identical mirror improved the coupling between the transmitting and receiving antenna by orders of magnitude.

Since the initial experiments of Hertz,[1] the Hertzian dipole has been known to be an important emitter and receiver of radiation with wavelengths large compared to the dipole. Modern integrated circuit techniques have now made possible the precise fabrication of micron-sized dipoles, which when driven with subpicosecond excitation can radiate well into the terahertz regime. The importance of these integrated circuit versions of the Hertzian dipole as generators and detectors of terahertz radiation was first demonstrated by Auston *et al.*[2] Recent work has introduced an optical technique to collect, collimate, and focus the terahertz radiation emitted by Hertzian dipoles,[3,4] produced by shorting a charged coplanar transmission line with ultrashort laser pulses.[5] When these dipole sources were located at the foci of spherical mirrors or lenses, most of the emitted radiation was captured and could be focused on detectors or collimated to produce relatively large diameter diffraction limited beams. Besides the high coupling efficiency, the excellent focusing properties preserved the subpicosecond time dependence of the source.

The above optical approach represents an alternative and complementary method to recent works extending radio and microwave techniques into the terahertz regime through the use of antennas.[6–10] For example, Mourou *et al.*[6] used a subpicosecond laser pulse to trigger a GaAs photoconductive switch driving a coaxial cable terminated by a millimeter-sized dipole antenna. This combination produced a microwave transient of several picoseconds. Later, Heidemann *et al.*[7] demonstrated the importance of planar antennas by exciting a larger, exponentially tapered, slot-line antenna with a laser-driven photoconductive switch to obtain nanosecond bursts of radiation. As discussed in their paper, this planar design is readily adaptable to integrated circuit fabrication with a consequent increase in bandwidth as the size is reduced. Defonzo *et al.*[8] demonstrated picosecond performance of an integrated circuit version of an antenna similar to that of Ref. (7). Later, Defonzo *et al.* developed and demonstrated an improved impedance-matched antenna consisting of an exponentially flared transmission line.[9] This design reduced antenna reflections and produced clean 10 ps bursts of radiation. In the most recent work, subpicosecond pulses have been generated, transmitted, and detected by Smith *et al.*,[10] who used integrated circuit techniques to fabricate ultrafast dipolar antennas terminated by coplanar transmission lines.

In this letter we report the use of a new ultrafast dipole antenna structure, optimized for photoconductive excitation, as the radiation source for the optical method.[3,4,11] Using this antenna we achieve an increase in transmitted beam power of more than 15 times, compared to the earlier work.[4] The antenna was located at the focus of a collimating sapphire lens in contact with the sapphire side of an ion-implanted,[12] silicon-on-sapphire (SOS) chip on which the antenna was fabricated. In addition, when the simple gap structure initially used for detection[3,4] was replaced with this antenna, the frequency response was significantly extended. In fact, we show that the signal measured by the antenna is the time derivative of the signal measured by the gap. Through the use of paraboloidal collimating and focusing mirrors, we have obtained a frequency-independent divergence of only 25 mrad and have increased the coupling between the transmitter and receiver by orders of magnitude. This tight coupling is evidenced by the fact that we measure electrical signals of many millivolts after a free-flight path of 80 cm.

The terahertz radiation source is illustrated in Fig. 1(a). Because this antenna directs all of the photocurrent into the antenna arms, it performs somewhat better than a dipole antenna at the end of a transmission line.[10] For comparable dimensions, more power is radiated and the noise level is lower due to the larger separation between the lines. A simple scaling argument compares the efficiency of the new antenna with that achieved by the earlier "sliding contact" technique[3,4] of simply shorting-out a coplanar transmission line. For this case the photocarrier density is inversely proportional to the area of the focused laser spot with a diameter approximately equal to the spacing between the lines. The area of contact of the photoconductive spot with the lines is proportional to the diameter of the laser spot. Consequently, with the same electric field between the lines, the photocurrent is inversely proportional to the line separation. Therefore, the main advantage of the new antenna design is that the total photocurrent from a 5 μm gap is put into a 30 μm antenna. Directly shorting a coplanar line with 30 μm separation between the two lines and with a six times higher bias voltage, would produce a current only 1/6 of that obtained by the antenna. The 20-μm-wide antenna structure was located in the middle of a 20-mm-long transmission line consisting of two parallel 10-μm-wide, 1-μm-thick, 5 Ω/mm, aluminum lines separated from each other by 30 μm. The antenna was driven by photoconductive shorting the 5 μm antenna gap with 70 fs pulses coming at a 100 MHz rate in a

 0003-6951/89/300337-03$01.00 © 1989 American Institute of Physics

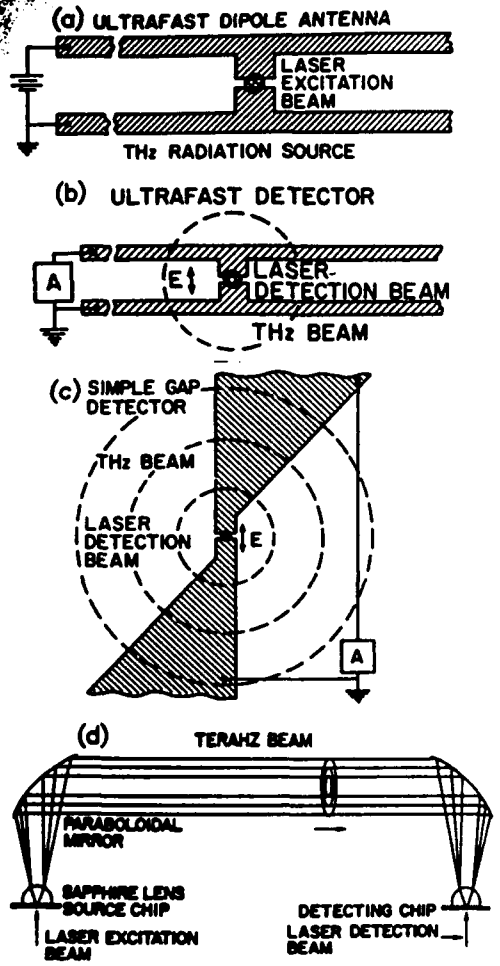

FIG. 1. (a) Ultrafast dipolar antenna terminated by the charged coplanar transmission line. (b) Ultrafast antenna used a a detector centered in the focal disk of the incoming 1.2 THz radiation. (c) Simple gap detector centered in the overlapping focal disks of the incoming 0.4, 0.6, and 1.2 THz radiation. (d) Collimating and focusing optics consisting of crystalline sapphire lenses in contact with the SOS chips, near the foci of paraboloidal collimating and focusing mirrors.

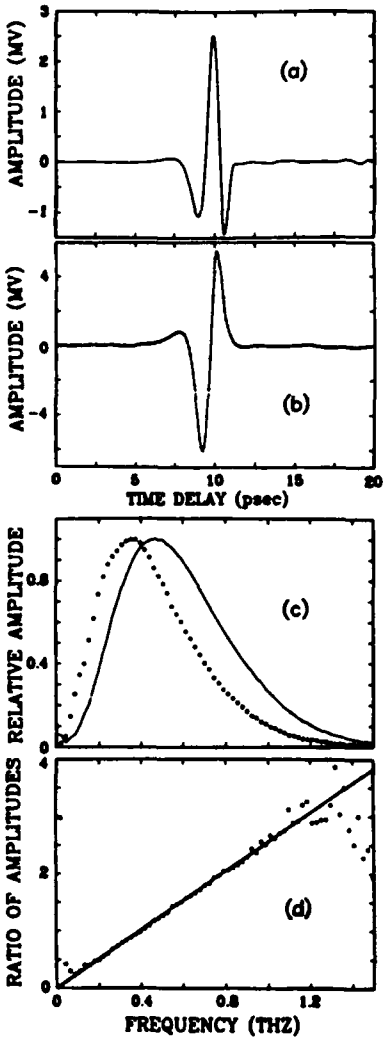

FIG. 2. (a) Measured electrical pulse of the freely propagating terahertz beam with the ultrafast dipolar antenna detector. (b) Measured electrical pulse of the freely propagating terahertz beam with the simple gap detector. (c) Amplitude spectra of the measured pulse shapes shown in (a) (solid line) and (b) (dots). (d) Ratio of the spectral amplitudes of (c).

1.5 mW beam from a colliding-pulse, mode-locked dye laser.

We have used two different terahertz radiation detectors. The one shown in Fig. 1(b) uses the same ultrafast antenna and terminating transmission line as the transmitter. Via the transmission line one side of the antenna is grounded, and a current amplifier is connected across the antenna. During operation the antenna is driven by the incoming terahertz radiation pulse polarized parallel to the antenna; this excitation causes a time-dependent voltage to appear across the antenna gap. This induced voltage is measured by shorting the antenna gap with the 70 fs optical pulses in the detection beam and monitoring the collected charge (current) versus the time delay between the excitation and detection laser pulses. The detector shown in Fig. 1(c) has a simple photoconductive gap of 10 μm spacing, an initial width of 25 μm, and a total length of 1 mm. This detector is similar to those used previously[3,4] and has some similarity to the bow tie antenna.[11,13] The measurements made using the simple gap are performed in the same manner.

The terahertz optics illustrated in Fig. 1(d) consist of two matched crystalline sapphire, spherical lenses contacted to the sapphire side of the SOS chips located near the foci of two identical paraboloidal mirrors. For both the radiation source and the detector, the center of the truncated 9.5-mm-diam sphere (lens) is 2.3 mm above the ultrafast dipolar antenna located at the focus of the lens. The orientations of the c axes of the sapphire lenses and SOS chips have been described earlier.[4] Due to the relatively high dielectric constant of approximately 10 for sapphire, most of the radiation emitted from the ultrafast antenna is contained in a 60° full angle cone normal to the surface of the SOS chip and directed into the sapphire.[13,14] This situation gives good collection and collimation of the terahertz radiation, because the central portion of the spherical lens captures most of the emitted radiation. After collimation we obtain a beam diameter of 5 mm; the calculated field pattern shows a strongly defined structure.[13] Although the 70 mm aperture paraboloidal mirrors have a 12 cm focal length, a 17 cm distance was used between the sapphire lenses and the paraboloidal mirrors to compensate for the wavelength-dependent diffraction and to optimize the response of the system at the peak of the measured spectrum. After recollimation by the mirror, we obtained beam diameters (10–70 mm) proportional to the wavelength; therefore, all of the frequencies propagated with the same 25 mrad divergence. After freely propagating 50 cm to the second mirror, all the frequencies were focused to the same 5-mm-diam spot at the entrance to the second sap-

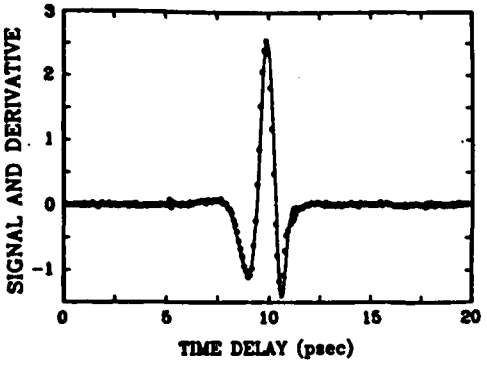

FIG. 3. Numerical derivative (dots) of the measured pulse with the simple gap [Fig. 2(b)] compared to the measured pulse (solid line) with the ultrafast dipolar antenna [Fig. 2(a)].

phire lens. This lens then focused the beam onto the ultrafast dipolar antenna or the simple gap. To first order the collection efficiency of the emitted radiation is almost complete and is independent of frequency. However, a detailed calculation shows a slight frequency dependence for the beam divergence and the resulting coupling between the transmitter and receiver. The total path length was 80 cm from transmitter to detector; 75 cm of this path was in an enclosure purged with dry nitrogen in order to prevent absorption of the terahertz beam by water vapor in the laboratory air. Because the focal diameters produced by the lens are proportional to wavelength, the focus can be considered as a series of concentric overlapping disks of increasing diameters corresponding to the increasing wavelengths.

Figures 2(a) and 2(b) display the detected terahertz radiation pulses measured with the ultrafast antenna and the simple gap, respectively. Both of these high signal-to-noise measurements of the transmitted pulses, after 80 cm of free propagation, were made in single 2 min scans of the relative time delay between the excitation and detection pulses. The measured voltages were calibrated by comparing the time-resolved signal with the photocurrent generated with a known dc bias voltage applied to the receiver. When the antenna was used as the transmitter, the signal strength increased by four times (with no loss in speed), compared to the "sliding contact" emitter, for which a charged coplanar transmission line with 15 μm separation was photoconductively shorted by the laser pulses.[4] This increase was due to the higher photocurrent and larger transient dipole moment of the antenna. Because the signal strength is proportional to the electric field, the factor of four increase in signal corresponds to the transmitter radiating 16 times more power. Compared to the previous demonstration,[4] which used only the sapphire lenses, the addition of the collimating paraboloidal mirror reduced the beam divergence to 25 mrad from an average divergence of 100 mrad. This together with the focusing paraboloidal mirror increased the power incident on the sapphire lens at the detector by another factor of 200. Consequently, as evidenced by the several millivolt amplitudes of the measured signals, the power incident on the detector has been increased by more than 3000 times compared to the earlier work.[4]

Because the spatial extent of the ultrafast detector depicted in Fig. 1(b) is small compared to the focal spot diameter of the shortest wavelength, this detector measures the incident electric field. There is an enhancement in the measured signal of the short-wavelength components due to the fact that their relative focal spot diameters are smaller and their focused electric fields are stronger. This situation is not true for the simple gap whose length is large compared to the focal spot diameter of the longest wavelength. Consequently, the long simple gap integrates over all the focal spots and the frequency enhancement disappears. This is similar to the bow tie antenna, which (theoretically) has a flat frequency response.[11,13] Although the signal strengths from the two detectors are almost the same, the response of the simple gap is clearly slower. A comparison in Fig. 2(c) of the amplitude spectra of the two signals shows that for the ultrafast antenna the spectrum peaks at 0.5 THz and extends well beyond 1.2 THz, compared to the maximum at 0.35 THz for the gap.

It is instructive to take the ratio of these spectra as shown in Fig. 2(d), where the feature at low frequency is an artifact and can be ignored. The linear frequency dependence indicated by the solid line agrees with the above description of the linear frequency enhancement of the antenna. This result, combined with the phase shift of $\pi/2$ of the frequency components of Fig. 2(a) compared to those of .g. 2(b), leads to the conclusion that the signal measured by the ultrafast antenna is equal to the time derivative of the signal measured by the gap. This conclusion is confirmed by the result shown in Fig. 3, where the calculated time derivative of the gap signal is compared with that measured by the ultrafast antenna, and excellent agreement is obtained.

We acknowledge the excellent masks and wafer fabrication by Hoi Chan. This research was partially supported by the U. S. Office of Naval Research.

[1]H. Hertz, Weidemann's Ann. 34, 551 (1881); for a translation of this and related papers see H. Hertz, *Electric Waves*, translated by D. E. Jones (Dover, New York, 1962).
[2]D. H. Auston, K. P. Cheung, and P. R. Smith, Appl. Phys. Lett. 45, 284 (1984).
[3]Ch. Fattinger and D. Grischkowsky, Appl. Phys. Lett. 53, 1480 (1988).
[4]Ch. Fattinger and D. Grischkowsky, Appl. Phys. Lett. 54, 490 (1989).
[5]D. Grischkowsky, M. B. Ketchen, C-C. Chi, I. N. Duling III, N. J. Halas, J-M. Halbout, and P. G. May, IEEE J. Quantum Electron. QE-24, 221 (1988).
[6]G. Mourou, C. V. Stancampiano, A. Antonetti, and A. Orszag, Appl. Phys. Lett. 39, 295 (1981).
[7]R. Heidemann, Th. Pfeiffer, and D. Jäger, Electron. Lett. 19, 317 (1983).
[8]A. P. DeFonzo, M. Jarwala, and C. R. Lutz, Appl. Phys. Lett. 50, 1155 (1987).
[9]A. P. DeFonzo and C. R. Lutz, Appl. Phys. Lett. 51, 212 (1987).
[10]P. R. Smith, D. H. Auston, and M. C. Nuss, IEEE J. Quantum Electron. 24, 255 (1988).
[11]D. B. Rutledge, D. P. Neikirk, and D. P. Kasilingham, in *Infrared and Millimeter Waves*, edited by K. J. Button (Academic, New York, 1983), Vol. 10, Pt. II.
[12]F. E. Doany, D. Grischkowsky, and C-C. Chi, Appl. Phys. Lett. 50, 460 (1987).
[13]David B. Rutledge and Michael S. Muha, IEEE Trans. Antennas Propag. AP-30, 535 (1982).
[14]W. Lukosz, J. Opt. Soc. Am. 69, 1495 (1979).

Terahertz time-domain spectroscopy of water vapor

Martin van Exter, Ch. Fattinger, and D. Grischkowsky

IBM Watson Research Center, P.O. Box 218, Yorktown Heights, New York 10598

Received April 24, 1989; accepted August 3, 1989

We describe the application of a new high-brightness, terahertz-beam system to time-domain spectroscopy. By analyzing the propagation of terahertz electromagnetic pulses through water vapor, we have made what we believe are the most accurate measurements to date of the absorption cross sections of the water molecule for the nine strongest lines in the frequency range from 0.2 to 1.45 THz.

Recently several new sources of freely propagating electromagnetic pulses have been demonstrated[1–3]; the spectral content of these sources extends from low frequencies to the terahertz frequency range. Using an optical approach in which a transient Hertzian dipole was tightly coupled to a sapphire collimating lens, we produced beams of single-cycle 0.5-THz pulses.[3] With the addition of paraboloidal focusing and collimating mirrors,[4] the resulting system has high brightness and extremely high collection efficiency.

In this Letter we describe the application of this new high-brightness system to time-domain spectroscopy[5–8] by studying the propagation of terahertz beams through water vapor. Fourier analysis of the directly measured electric fields of the propagated pulses, with and without water vapor in the beam path, yields the absorption and dispersion of water vapor as a function of frequency. This technique has some powerful advantages in producing results that appear to be equivalent to those of traditional cw spectroscopy. First, the detection of the far-infrared radiation is extremely sensitive. Although the energy per terahertz pulse is very low (1 aJ), the 100-MHz repetition rate and the coherent detection allow us to determine the electric field of the propagated pulse with a signal-to-noise ratio of ~3000 for an integration time of 125 msec. In terms of average power this sensitivity exceeds that of liquid-helium-cooled bolometers[9] by more than 1000 times. Second, because of the gated and coherent detection, the thermal background that plagues traditional measurements in this frequency range[9] is observationally absent. These two advantages have enabled us to make what we believe are the most accurate measurements to date of the absorption cross sections of the nine strongest rotational transitions of water vapor in the frequency range from 0.2 THz (6.6 cm^{-1}) to 1.45 THz (48.4 cm^{-1}).

The terahertz radiation source[4] is illustrated in Fig. 1(a). The emitting dipolar antenna was located in the middle of a 20-mm-long transmission line consisting of two parallel 10-μm-wide aluminum lines separated from each other by 30 μm. The pattern was fabricated on an ion-implanted, silicon-on-sapphire wafer. The antenna was driven by photoconductively shorting the 5-μm antenna gap with 70-fsec pulses coming at a 100-MHz rate in a 1.5-mW beam from a colliding-pulse, mode-locked dye laser. The terahertz radiation detector[4] uses the same ultrafast antenna and terminating transmission line as the transmitter. During operation the antenna is driven by the incoming terahertz radiation pulse polarized parallel to the antenna. The induced time-dependent voltage across the antenna gap is measured by shorting the gap with the 70-fsec optical pulses in the detection beam and monitoring the collected charge (current) versus the time delay between the excitation and detection laser pulses.

The terahertz optics[4] illustrated in Fig. 1(b) consists of two matched crystalline magnesium oxide (MgO) spherical lenses in contact with the sapphire side of the silicon-on-sapphire chips located near the foci of two identical paraboloidal mirrors. The combination of the MgO lens and the paraboloidal mirror collimated the emitted radiation to beam diameters (10–70 mm) proportional to the wavelength and with a frequency-independent divergence of only 25 mrad. The second identical combination on the receiving end focused the terahertz beam onto the detector. The total path length from transmitter to receiver was 88 cm, of which 86 cm was located in an airtight enclosure in which the water-vapor content could be controlled.

Figure 2(a) displays the detected terahertz radiation pulses after propagating through 1 atm of pure nitrogen. This high signal-to-noise measurement with millivolts of signal was made in a single 10-min scan of the 200-psec relative time delay between the

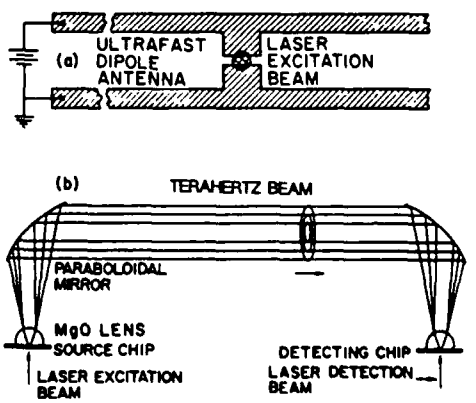

Fig. 1. (a) Ultrafast dipolar antenna. (b) Terahertz optics.

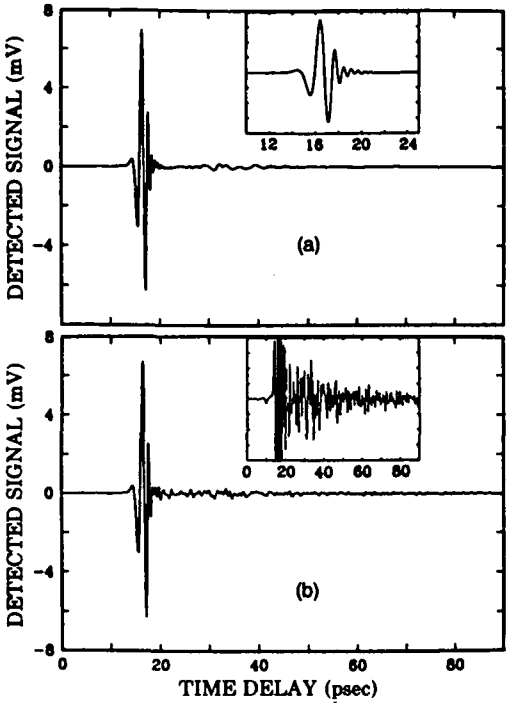

Fig. 2. (a) Measured electrical pulse of the freely propagating terahertz beam in pure nitrogen. The inset shows pulse on an expanded time scale. (b) Measured electrical pulse with 1.5 Torr of water vapor in the enclosure. The inset shows pulse on a 20× expanded vertical scale.

excitation and detection pulses. When 1.5 Torr of water vapor, corresponding to 8% humidity at 20.5°C, was added to the enclosure, the transmitted pulse changed to that shown in Fig. 2(b). The additional fast oscillations are caused by the combined action of the dispersion and absorption of the water-vapor lines. The slower and more erratic variations seen in both Figs. 2(a) and 2(b) result from reflections of the main pulse. They are reproducible and do not affect our data analysis, as they divide out in the frequency domain. The insets show the data on a 20× expanded vertical scale. Here, the oscillations are seen to decay approximately exponentially in time. For a low concentration of water vapor the observed decay corresponds to an average coherent relaxation time T_2.

The amplitude spectra of the full 200-psec scans corresponding to Figs. 2(a) and 2(b) are compared in Fig. 3(a), where the strong water-absorption lines are clearly observable. The additional structure on the spectra is not related to noise but results from reflections of the main pulse. At each line we have indicated two frequencies, our measured value and in parenthesis the accepted literature value.[10–16] Our measured line centers have an estimated error of ±0.001 THz. Within this bracket they agree with the literature values. We assign the systematic deviation of +0.1% to error in the calibration of our delay line. Our peak positions are obtained from a fit to the Fourier transform, assuming a Lorentzian line shape. The basic data are of sufficient accuracy to permit the determination of the peak position of one fifth of the 0.005-THz fundamental frequency given by the 200-psec scan duration. A numerical method of making the fit is to extend the scan artifically by the addition of zeros.[17] Using this approach, we extended the scan range to 600 psec and obtained the same line centers.

From the above spectra the corresponding absorption coefficients are displayed in Fig. 3(b). The vertical scale is the natural logarithm of the ratio of the two amplitude spectra shown in Fig. 3(a) and thus represents the amplitude absorption coefficient. In Table 1 we have converted the measured absorption into the commonly used peak-intensity absorption coefficient α_0 for a 1-m path (m^{-1}) at 100% humidity (18 Torr at 20.5°C) in 1 atm of nitrogen. These values were compiled from eight 10-min scans taken at humidities between 3% and 13%. The humidity was varied to accommodate the different line strengths.

Three lines demanded special attention. As the 1.097- and the 1.113-THz lines are relatively close together, we corrected for the overlap to get their line strengths. The measured line shape of the 1.163-THz line is asymmetric owing to the presence of two weaker modes at 1.153 and 1.158 THz. Using the theoretical strengths of these modes, we also corrected the measured absorption of this line. With our high signal-to-noise ratio the relative strengths of the lines could be determined to better than 10% with the actual uncertainty indicated in Table 1. We used a commercial

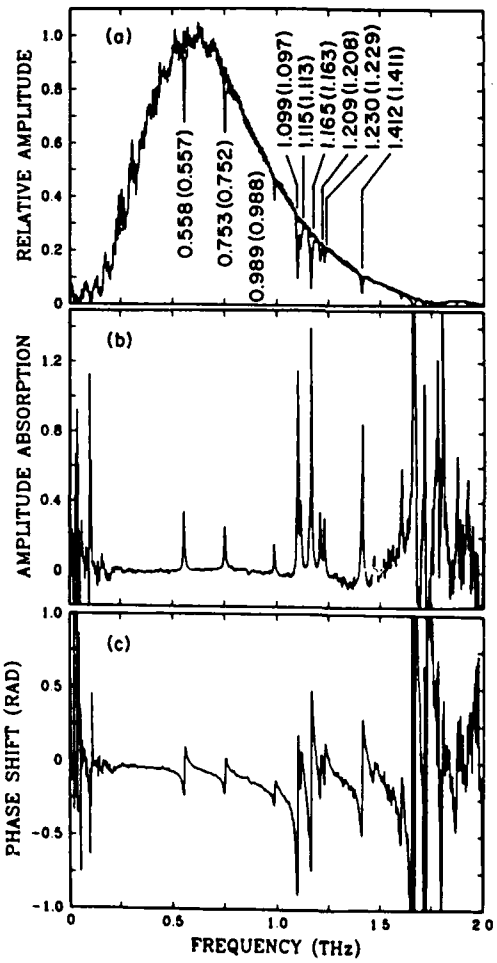

Fig. 3. (a) Amplitude spectra of Figs. 2(b) and 2(c). (b) Amplitude absorption coefficient obtained from Fig. 3(a). (c) Relative phase of the spectral components of Fig. 3(a).

Table 1. Comparison of Our Experimental Results with Theoretical Predictions for the Indicated Lines (in terahertz)[a]

Line	Exp α_0	10	11	12	13*	14*	15*	16*
0.557	9.4 (2)	9.6	9.9	8.6	4.6	10.8		9.7
0.752	6.9 (4)	6.8	6.9	5.9	5.1	7.1		6.8
0.988	5.0 (4)	5.0	5.1	4.3	2.2	5.3	5.1	5.0
1.097	32.0 (10)	33.8	34.3		33.8	33.8	33.8	33.8
1.113	10.1 (7)	10.2	10.5		1.5	10.3	10.1	10.3
1.163	37.9 (14)	38.2	39.1		36.7	38.6	35.9	38.2
1.208	9.8 (7)	12.9			14.7	12.1	11.2	12.8
1.229	8.5 (7)	10.0			7.1	10.5	9.7	10.0
1.410	23.1 (30)	30.5			45.9	31.6	29.4	30.2

[a] Asterisks indicate relative values only.

hygrometer (Fischer Scientific 11-661-7A) to determine the relative humidity inside the enclosure, and, using that value, we evaluated the absolute absorption strength to within 10%. In the last seven columns of Table 1 we present theoretical values for the peak absorption coefficient α_0 extracted from the literature. The values of Ref. 10 appear to be the most reliable, as they result from a substantial compilation of data. Because Ref. 10 cites the absorption cross section integrated over each line, we used the linewidths as calculated in Ref. 18 to convert to peak absorption. Our data are in good agreement with those of Refs. 10–12, although the measured α_0 of the high-frequency lines appears to be low. To indicate that they are relative values only, the last four columns are marked with asterisks. We have normalized these values with respect to the 1.097-THz transition. In order to convert the line strengths of Ref. 16 into absorption coefficients, one must take the frequency dependence, linewidth, Boltzmann factors, and spin statistical weights into account.[19] The absorption strengths of Ref. 13 are the only ones that show strong disagreement with our measurements.

As the technique described directly probes the electric field, we also obtain the measured phase shift plotted in Fig. 3(c). The Kramers–Kronig relations couple this phase shift to the absorption, and there is indeed excellent agreement between the two; as expected for a Lorentzian line, the magnitude of the jump in phase experienced at each resonance equals the peak absorption.

Two competing far-infrared spectroscopic techniques are microwave spectroscopy, based on harmonic generation and mixing, and Fourier-transform spectroscopy. With microwave techniques the frequencies of the rotational transitions of water molecules have been determined with extreme accuracy.[16] However, it is difficult to determine the line strengths, and consequently they are described by the adjectives weak and strong. Common practice is to calculate the absorption strength from a model that uses input parameters deduced from the frequency data.[10–16] In comparing time-domain spectroscopy with Fourier-transform spectroscopy, it should be clear that the frequency resolutions of these techniques are similar, as they are both based on a scanning delay line. Although for now Fourier-transform spectroscopy is superior above 1.5 THz, the limited power of the radiation sources and the problems with the thermal background favor time-domain spectroscopy below 1.0 THz.

We acknowledge informative discussions with Søren Keiding concerning the calculations of line strengths, and we thank Hoi Chan for the excellent masks and wafer fabrication. This research was partially supported by the U.S. Office of Naval Research.

References

1. A. P. DeFonzo, M. Jarwala, and C. R. Lutz, Appl. Phys. Lett. **50**, 1155 (1987); A. P. DeFonzo and C. R. Lutz, Appl. Phys. Lett. **51**, 212 (1987).
2. P. R. Smith, D. H. Auston, and M. C. Nuss, IEEE J. Quantum Electron. **24**, 255 (1988).
3. Ch. Fattinger and D. Grischkowsky, Appl. Phys. Lett. **53**, 1480 (1988); **54**, 490 (1989).
4. M. van Exter, Ch. Fattinger, and D. Grischkowsky, Appl. Phys. Lett. **55**, 337 (1989).
5. K. P. Cheung and D. H. Auston, Infrared Phys. **26**, 23 (1986).
6. D. Grischkowsky, C.-C. Chi, I. N. Duling III, W. J. Gallagher, M. B. Ketchen, and R. Sprik, in *Laser Spectroscopy VIII*, W. Persson and S. Svanberg, eds. (Springer-Verlag, New York, 1987).
7. D. Grischkowsky, in *Proceedings of the Fourth International Conference on Infrared Physics*, R. Kesselring and F. K. Kneubuhl, eds. (ETH, Zurich, 1988).
8. Y. Pastol, G. Arjavalingam, J.-M. Halbout, and G. V. Kopcsay, Appl. Phys. Lett. **54**, 307 (1989).
9. C. Johnson, F. J. Low, and A. W. Davidson, Opt. Eng. **19**, 255 (1980).
10. J. M. Flaud, C. Camy-Peyret, and R. A. Toth, *Water Vapour Line Parameters from Microwave to Medium Infrared* (Pergamon, Oxford, 1981).
11. D. E. Burch, J. Opt. Soc. Am. **58**, 1383 (1968).
12. H. J. Liebe, Radio Sci. **20**, 1069 (1985).
13. R. T. Hall, D. Vrabec, and J. M. Dowling, Appl. Opt. **5**, 1147 (1966).
14. D. E. Gray, ed., *American Institute of Physics Handbook* (McGraw-Hill, New York, 1972).
15. J. Kauppinen, T. Karkkainen, and E. Kyro, J. Mol. Spectrosc. **71**, 15 (1978).
16. F. C. De Lucia and P. Helminger, Int. J. Infrared Millim. Waves **4**, 505 (1983).
17. P. R. Griffiths, *Chemical Infrared Fourier Transform Spectroscopy* (Wiley, New York, 1975).
18. W. S. Benedict and L. D. Kaplan, J. Chem. Phys. **30**, 388 (1959).
19. C. H. Townes and A. L. Schawlow, *Microwave Spectroscopy* (McGraw-Hill, New York, 1955), see Eqs. (4-22) and (4-28).

Measurements of the phase shift and reshaping of terahertz pulses due to total internal reflection

Søren R. Keiding and D. Grischkowsky

IBM Watson Research Center, P.O. Box 218, Yorktown Heights, New York 10598

Received July 26, 1989; accepted October 20, 1989

Using time-domain spectroscopic techniques with freely propagating electromagnetic beams of terahertz pulses, we have measured the phase shift and reshaping of subpicosecond pulses due to total internal reflection from a crystalline quartz prism. Our measured value of the phase shift is in excellent agreement with the theoretical prediction.

The reshaping of ultrashort electromagnetic pulses due to the phase change that occurs on total internal reflection (TIR) was first demonstrated by Cheung and Auston.[1] As their source of ultrashort far-infrared pulses, they generated an electromagnetic shock wave by driving the optical rectification effect in a nonlinear dielectric material with an ultrashort laser pulse.[2,3] In their experiments[1] they measured the reshaping of this shock wave after a TIR at the boundary of the nonlinear crystal.

A recent observation of electromagnetic shock waves emitted by surface-dipole distributions propagating on a dielectric surface[4] permitted the indirect measurement of the phase shift due to TIR. In that study the shock wave was the sum of a directly radiated term and a phase-shifted term from a TIR component. The good agreement between theory and experiment[4] confirmed the theoretical model that relied heavily on the pulse-reshaping effect due to the TIR phase shift.

In this Letter we report direct observations of the pulse reshaping due to TIR of freely propagating, low-divergence beams of subpicosecond terahertz pulses. In order to compare experiment and theory as precisely as possible, we used the new high-brightness terahertz beam source[5] together with a crystalline quartz prism in the TIR geometry. We observed strong reshaping of the propagating terahertz pulse compared with the incident pulse. With the technique of time-domain spectroscopy,[3,6] a comparison of the Fourier transforms of the incident and reflected pulses allows us to extract the TIR phase shift, which agrees with the theoretical prediction to within our experimental error of 2%.

The experiment is illustrated schematically in Fig. 1. The system is driven by the 70-fsec, 625-nm pulses from a compensated colliding-pulse mode-locked dye laser operating with a pulse repetition rate of 100 MHz and producing an average power of 5 mW in the driving beam. As previously described,[5] this beam is focused onto a micrometer-sized dipole antenna terminated by a coplanar transmission line fabricated on an ion-implanted silicon-on-sapphire (SOS) wafer. There is a bias voltage of 10 V across the line and also across the antenna gap. The driving laser pulses are focused on the gap and thereby short the antenna and produce a transient Hertzian dipole that radiates a terahertz pulse into the sapphire substrate.[5-7] The peak transient current in the antenna is approximately 0.01 A, corresponding to an average current of 0.5 μA. This radiation is then collimated to an approximately 5-mm beam diameter by a spherical sapphire lens in contact with the sapphire surface. The center of a truncated 9.5-mm-diameter sphere (lens) is 2.3 mm above the ultrafast dipolar antenna located at the focus of the lens. Because the output face of the lens is in the radiation zone for the frequency range of interest, the antenna pattern on the output face is the same for all frequencies. The effect of the lens is to collimate this pattern into a plane wave. From this point the beam can be considered as a superposition of waves diffracting from a 5-mm soft circular aperture. Although the 75-mm-aperture paraboloidal mirrors have a 12-cm focal length, a 17-cm distance was used between the sapphire lenses and the paraboloidal mirrors to compensate for the wavelength-dependent diffraction and to optimize the response of the system at the peak of the measured spectrum. It is important to note that because the incident beam diameter at the collimating mirror is proportional to the wavelength, a frequency-independent divergence is obtained after the collimation by the paraboloidal mirror.[5]

The experiment consists in measuring two reflec-

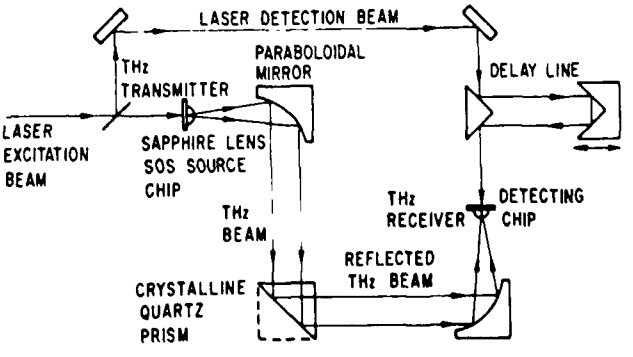

Fig. 1. Schematic diagram of experiment.

0146-9592/90/010048-03$2.00/0 © 1990 Optical Society of America

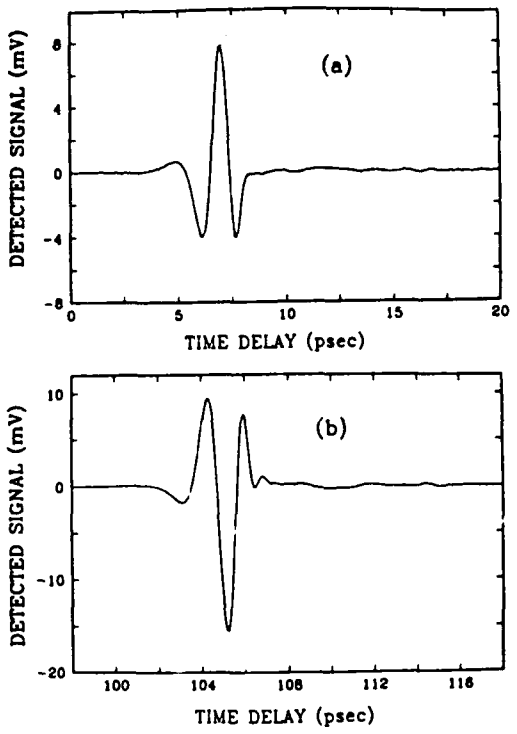

Fig. 2. (a) Reference pulse reflected from the front surface of the quartz prism at the position indicated by the dashed line in Fig. 1. (b) TIR pulse from the quartz prism oriented as shown by the solid line in Fig. 1.

tions from the crystalline quartz right-angle prism. The *C* axis of the crystal is perpendicular to the triangular plane, i.e., perpendicular to the plane of the diagram of Fig. 1. The transient Hertzian dipolar source is oriented so that the linear polarization of the terahertz beam is perpendicular to the *C* axis of the crystal and is in the plane of the diagram. The initial reference pulse is obtained with the prism oriented as shown by the dashed line in Fig. 1, so that the reflection from the dielectric interface is reflected to the second paraboloidal mirror, which focuses the reflected beam onto a second identical sapphire lens. This lens further focuses the terahertz beam onto the detector consisting of a second identical antenna assembly. At the detector the incident terahertz pulses bias the antenna gap. Consequently, an electric current can be obtained if the gap is shorted by means of an ultrashort light pulse in the presence of the terahertz pulse. The measurements consist of monitoring the collected current versus the relative time delay between the excitation and sampling light pulses. The totally internally reflected pulse is measured in a similar way by simply rotating the prism to the position shown by the solid line in Fig. 1.

The input (reference) pulse shown in Fig. 2(a) is the measured reflected terahertz pulse from the surface of the quartz prism oriented as shown by the dashed line in Fig. 1. Because the dispersion of the index of refraction of quartz is relatively small, this front surface reflection, to a good approximation, does not change the incident pulse shape. This measurement was made in a single 150-sec scan of the relative time delay between the excitation and detection pulses and has a signal-to-noise ratio of better than 250:1. The relatively large signal amplitude of 12 mV was calibrated by adjusting a dc bias voltage across the detector to obtain the same photocurrent. The ultrafast subpicosecond response of the system is evident from the observed pulse shape, where the pulse width (FWHM) of the main signal is approximately 0.8 psec.

When the position of the prism was oriented as shown by the solid line in Fig. 1, we observed the totally internally reflected pulse shown in Fig. 2(b). Because of the relatively low dispersion of the index of refraction of quartz, the normal-incidence reflections do not distort the transmitted propagating pulse. These reflections only attenuate the pulse and thereby do not affect the relative phase of the frequency com-

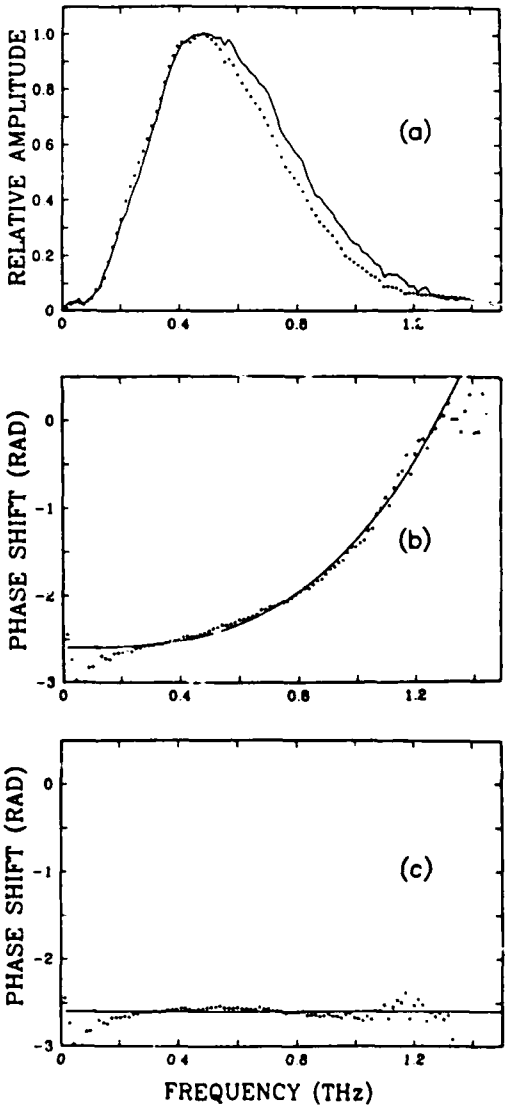

Fig. 3. (a) Normalized amplitude spectra of Figs. 2(a) (solid curve) and 2(b) (dotted curve). (b) The relative phase in radians of the spectral components of the (TIR) pulse of Fig. 2(b) with respect to the reference pulse of Fig. 2(a); the solid curve describes the constant TIR phase shift plus the effect of a quadratic frequency dependence of the index of refraction of crystalline quartz. (c) The relative phase in radians of Fig. 2(b) with respect to Fig. 2(a) compensated for the dispersion of crystalline quartz.

ponents of the transmitted pulse. In addition to the comparative increase in signal strength due to the total reflection, the pulse shape changes significantly. The polarity is reversed, the lobes on either side of the main pulse no longer have the same strength, and structure appears on the trailing edge. These changes are due to the frequency-independent TIR phase shift that occurs on the reflection at the internal surface of the prism and to the frequency-dependent absorption and dispersion of crystalline quartz.

The normalized amplitude spectra of the two pulses of Fig. 2 are shown in Fig. 3(a) and extend from low frequencies to beyond 1 THz. A slight absorption of the higher-frequency components is evident for the TIR pulses that traversed the 25-mm-long path within the quartz prism. For the entire bandwidth the measured amplitude absorption coefficient is less than 0.2 cm^{-1}.

The relative phase of the spectral components of the TIR pulse with respect to those of the reference pulse is shown by the dotted curve in Fig. 3(b). To obtain these results, the pulses were first numerically overlapped in time to eliminate the linear phase shift due to $n_o(0)$ and then the complex Fourier transforms were made. The relative phase is considered to be accurate in the frequency range from 0.2 to 1.2 THz. Outside this range the amplitudes of the spectral components are too low and the relative phase shows considerable scatter as it drops into the noise level of the measurement. In addition to the TIR phase shift, the strong frequency-dependent phase shift is due to the frequency-dependent index of refraction of crystalline quartz. Incidentally, Fig. 3(b) presents what is to our knowledge the most precise measurement to date of the dispersion of quartz in this frequency range. The calculated solid curve corresponds to a constant TIR phase shift plus a quadratic frequency dependence of the index of quartz. The index of quartz has been assumed[8] to be of the form $n_o(f) = n_o(0) + Af^2$, where f is the frequency in terahertz and A describes the strength of the dispersion. As shown in the figure, our experimental data are well fitted by the value $A = 0.0024/(\mathrm{THz})^2$, in agreement with that obtained at higher frequencies.[8]

Subtracting the quadratic dependence, we obtain the TIR phase shift shown in Fig. 3(c). In accordance with the reality of the measured field, i.e., no imaginary component, the phase shift changes sign for negative frequencies. Here, in the frequency range from 0.2 to 1.2 THz, the resulting measured phase is independent of frequency and agrees well with the predicted value[9] of −2.55 rad shown by the horizontal line for an incident angle of 45°. Most of the data are contained within the band centered on the predicted value of 2.55 ± 0.05 rad, indicating the accuracy of our measurement. Experimentally, the incident angle was set accurately (to within 0.1°), because the TIR phase shift is strongly dependent on the incident angle and deviations of a few degrees show phase-shift changes of several tenths of a radian.[9] We have measured this sharp angular dependence, and our results agree with the theoretical predictions.

In summary, by using the powerful combination of time-domain spectroscopic techniques with high-brightness terahertz beams, we have performed what is to our knowledge the most accurate measurement to date of the frequency-independent TIR phase shift.

We acknowledge extensive and informative discussions with Ch. Fattinger and Martin van Exter. This research was partially supported by the U.S. Office of Naval Research.

References

1. K. P. Cheung and D. H. Auston, Opt. Lett. **10**, 218 (1985).
2. D. H. Auston, K. P. Cheung, J. A. Valdmanis, and D. A. Kleinman, Phys. Rev. Lett. **53**, 1555 (1984).
3. D. H. Auston and K. P. Cheung, J. Opt. Soc. Am. B **2**, 606 (1985).
4. Ch. Fattinger and D. Grischkowsky, Phys. Rev. Lett. **62**, 2961 (1989).
5. M. van Exter, Ch. Fattinger, and D. Grischkowsky, Appl. Phys. Lett. **55**, 337 (1989).
6. M. van Exter, Ch. Fattinger, and D. Grischkowsky, Opt. Lett. **14**, 1128 (1989).
7. Ch. Fattinger and D. Grischkowsky, Appl. Phys. Lett. **53**, 1480 (1988); **54**, 490 (1989).
8. E. E. Russell and E. E. Bell, J. Opt. Soc. Am. **57**, 341 (1967).
9. M. Born and E. Wolf, *Principles of Optics*, 6th ed. (Pergamon, Oxford, UK, 1980). The TIR phase shift was calculated using Eq. (60) on p. 49. For our case the quantity n in the equation is equal to $n = 1/n_o(0)$, where the index of air is taken to be unity and $n_o(0) = 2.106$. The angle of incidence is 45°, and in the experimental geometry the electric field is in the plane of incidence.

T-MTT/38/11//38470

Characterization of an Optoelectronic Terahertz Beam System

Martin van Exter
Daniel R. Grischkowsky

Reprinted from
IEEE TRANSACTIONS ON MICROWAVE THEORY AND TECHNIQUES
Vol. 38, No. 11, November 1990

Characterization of an Optoelectronic Terahertz Beam System

MARTIN VAN EXTER AND DANIEL R. GRISCHKOWSKY, SENIOR MEMBER, IEEE

Abstract—**We describe the performance of an optoelectronic THz beam system. The transmitter operation is based on the repetitive, subpicosecond laser excitation of a Hertzian dipole antenna embedded in a charged coplanar line. With this transmitter electromagnetic beams of 1/2 cycle THz pulses at a repetition rate of 100 MHz are produced. The associated optoelectronic receiver is gated in synchronism with the excitation of the transmitter by subpicosecond pulses from the same laser source. With this receiver, the 10 nW beams of THz pulses were observed with a signal-to-noise ratio greater than 10000:1. Several sources contributing to the noise of the receiver are discussed, together with ways to reduce them. With an integration time of 125 ms, a signal-to-noise ratio of 1 is obtained for a THz beam with an average power of 10^{-16} W. The receiver operates in the sampling mode and has a time resolution of 0.5 ps.**

I. INTRODUCTION

IN A SERIES of recent papers, the features and applications of a new high-brightness pulsed THz beam system have been reported [1]–[4]. The highest performance version of the system is based on repetitive, subpicosecond optical excitation of a Hertzian dipole antenna [3]–[5] embedded in a charged coplanar transmission line structure. The burst of radiation emitted by the resulting transient dipole is collimated by a THz optical system into a diffraction-limited beam and focused onto a similar receiver structure, where it induces a transient voltage and is detected. The THz optical system gives exceptionally tight coupling between the transmitter and receiver, while the excellent focusing properties preserve the subpicosecond time dependence of the source.

As mentioned previously [2]–[4], the combination of THz optics with the synchronously gated, optoelectronic detection process has exceptional sensitivity for repetitively pulsed beams of THz radiation. With lenses and mirrors it is possible to direct a large fraction of the radiation, emitted during the excitation of an optoelectronic device, onto a distant device. The transmitted waveforms have been measured with subpicosecond resolution and with signal-to-noise ratios of more than 10000:1. This result was obtained with a repetition rate of 100 MHz, an integration time of 125 ms, and an average power of 10 nW in the THz beam.

In this paper we present measurements and analysis of the total emitted power, the beam collection efficiency, and the limiting noise properties of the THz receiver. In particular, we show how the combination of THz optics with the optoelectronic, subpicosecond, synchronous gating of the receiver allows for the measurement of incident THz beams with peak powers far less than the incident room-temperature thermal radiation in the same frequency range. Methods to further improve the performance of the receiver are also discussed.

The exceptional sensitivity is due in part to the high performance of the THz optics. Via two stages of collimation a THz beam with a frequency-independent divergence of 25 mrad is obtained from the THz transmitter. The THz receiver with identical optical properties collects essentially all of this beam. The resulting tightly coupled system of the THz transmitter and receiver gives strong reception of the transmitted pulses of THz radiation after many meters of propagation.

Another reason for the exceptional sensitivity is that the optoelectronic gating changes the effective resistance of the receiving antenna from 22 MΩ in the off state to 550 Ω in the on state. The gating window of the on state lasts for approximately 0.6 ps. The duty cycle of 0.6×10^{-4} is given by the ratio of the 0.6 ps gating time to the period of the 100 MHz sampling rate. Consequently, the average resistance seen by a current amplifier directly connected to the receiving antenna is about 7 MΩ. Therefore, with respect to the current amplifier, the receiver has a high impedance together with a subpicosecond response.

A final important feature of the detection method is that it is a coherent process; the electric field of a repetitive pulse of THz radiation is directly measured. Because we synchronously detect a repetitive signal, the total charge (current) from the signal increases linearly with the number of sampling pulses, while the charge (current) from noise increases only as the square root of the number of pulses.

II. EXPERIMENTAL SETUP

The setup used to generate and detect beams of short pulses of THz radiation is presented in Fig. 1. The transmitting and receiving antennas are identical, each consisting of the metallic pattern shown in Fig. 1(a) [3], which

Manuscript received October 18, 1989; revised June 25, 1990. This work was supported in part by the U.S. Office of Naval Research.

M. van Exter was with the IBM Watson Research Center, P.O. Box 218, Yorktown Heights, NY 10598. He is now with the Huygens Laboratories, Postbus 9504, 2300 RA Leiden, the Netherlands.

D. R. Grischkowsky is with the IBM Watson Research Center, P.O. Box 218, Yorktown Heights, NY 10598.

IEEE Log Number 9038470.

0018-9480/90/1100-1684$01.00 ©1990 IEEE

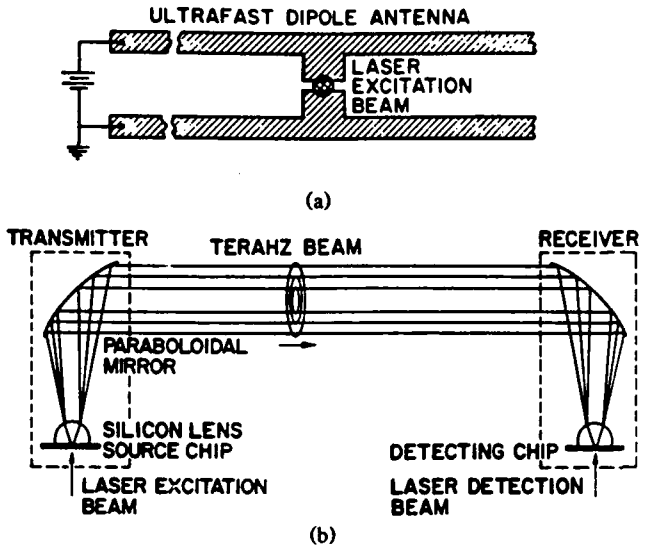

Fig. 1. (a) Ultrafast dipolar antenna. (b) Schematic diagrams of the THz transmitter and receiver.

has been fabricated on an ion-implanted silicon-on-sapphire (SOS) wafer. The 20-μm-wide antenna structure is located in the middle of a 20-mm-long coplanar transmission line consisting of two parallel 10-μm-wide, 1-μm-thick, 5 Ω/mm aluminum lines separated from each other by 30 μm. A colliding-pulse mode-locked (CPM) dye laser produces 623 nm, 70 fs pulses which are focused onto the 5-μm-wide photoconductive silicon gap between the two antenna arms. This 100 MHz periodic excitation causes pulsed, subpicosecond changes in the conductivity of the antenna gap. When a dc bias voltage of typically 10 V is applied to the transmitting antenna, these changes in conductivity result in pulses of electrical current through the antenna, and consequently bursts of electromagnetic radiation are produced. A large fraction of this radiation is emitted into the sapphire substrate in a cone normal to the interface [2] and is then collected and collimated by a dielectric lens attached to the back side (sapphire side) of the SOS wafer [1]–[4].

For the work reported here, the dielectric lenses were made of high-resistivity (10 k$\Omega\cdot$cm) crystalline silicon with a measured absorption of less than 0.05 cm^{-1} in our frequency range. The use of silicon gave significant improvement over the sapphire lenses previously used [1]–[3], although the 10% mismatch in dielectric constant between the silicon lens and the sapphire wafer causes a slight reflection. The center of the truncated 9.5-mm-diameter silicon sphere (lens) is 2.0 mm above the ultrafast antenna located at the focus of the lens.

After collimation by the silicon lens, the beam propagates and diffracts to a paraboloidal mirror, where the THz radiation is recollimated into a highly directional beam. Although the 70 mm aperture paraboloidal mirrors have a 12 cm focal length, a 16 cm distance was used between the silicon lenses and the mirrors to optimize the response of the system at the peak of the measured spectrum. While the high-frequency components of the THz pulses remain reasonably well collimated, the very low frequency components quickly diffract and illuminate the entire paraboloidal mirror, which presents a solid angle of 0.15 steradians to collect radiation from the source. After recollimation by the paraboloidal mirror, beam diameters (10–70 mm) proportional to the wavelength were obtained; thereafter, all of the frequencies propagated with the same 25 mrad divergence. The combination of the paraboloidal mirror and silicon lens (THz optics) and the antenna chip constitute the transmitter, the source of a highly directional, freely propagating beam of (sub)picosecond THz pulses. After a 50 cm propagation distance this THz beam is detected by an identical combination, the THz receiver, where the paraboloidal mirror focuses the beam onto a silicon lens, which focuses it onto a SOS antenna chip, similar to the one used in the emission process. The electric field of the focused THz radiation induces a transient bias voltage across the receiving antenna, directly connected to a low-noise current amplifier. The amplitude and time dependence of this transient voltage are obtained by measuring the collected charge (current) versus the time delay between the THz pulses and the CPM laser pulses that periodically gate the sensitivity of the receiver. The detection process with gated integration can be interpreted as a subpicosecond boxcar integrator.

III. Measurements

A typical time-resolved measurement is shown in Fig. 2(a). The clean pulse shape is a result of the fast action of the photoconductive switch at the antenna gap, the broad-band response of the ultrafast antennas, the broad-band THz optical transfer function of the lenses and paraboloidal mirrors, and the very low absorption and dispersion of the silicon lenses. The measured pulse width of only 0.5 ps (FWHM) is only an upper limit to the true pulse width, because no deconvolution has been applied to the measurement to take out the response time of the antenna gap. The value of 14 mV was established as a lower limit for the peak transient voltage across the gap; this was done by determining the required dc voltage for a photocurrent in the receiving antenna equal to the measured average current at optimum delay. The words *lower limit* indicate that the measured current results from a convolution of the transient voltage with the transient conductivity of the gate. In this regard, notice that the FWHM of the central spike is only 0.5 ps wide, compared with the 0.6 ps pulse width of the integrating gate. A deconvolution results in a peak transient voltage of 35 mV, which is about 2.5 times larger than the simple estimate mentioned above. The associated electrical pulse generated on the coplanar line by the excitation of the transmitting antenna is typically measured to be 1.0 ps in duration and close to 1 V in amplitude. Taking into account the response time of the measurement, the pulse on the line is considered to have a pulse width of about 0.7 ps with a rise time of the order of 0.3 ps and a longer

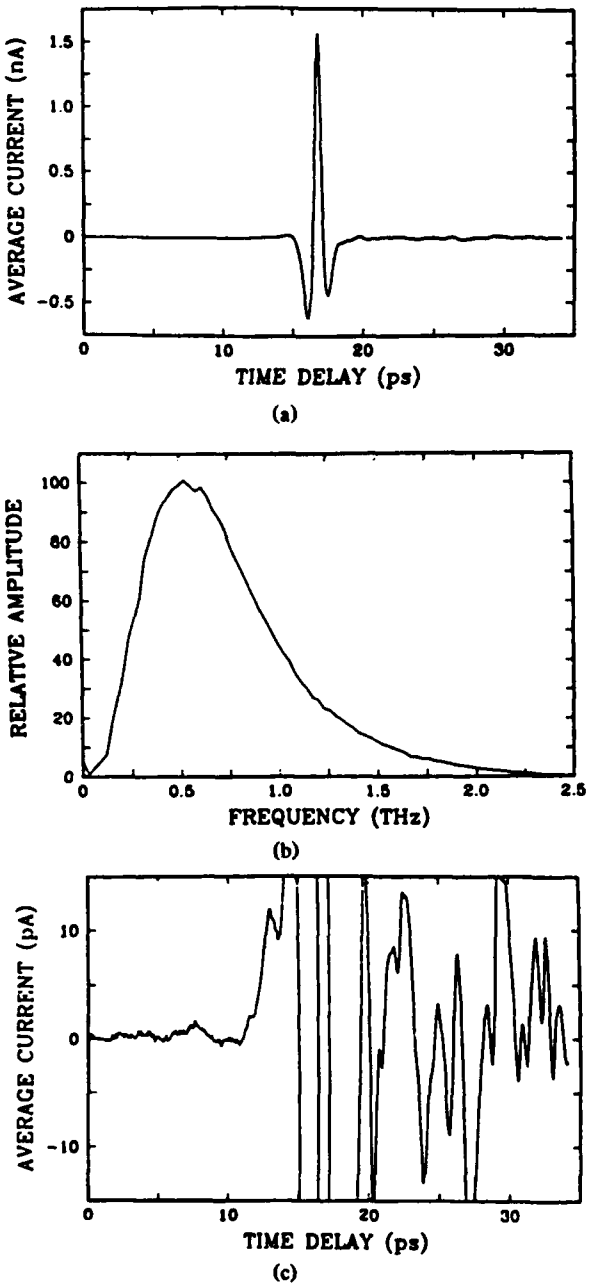

Fig. 2. (a) THz pulse measured by scanning the time delay between the optical gating pulses and the incident THz pulses, while monitoring the current induced in the THz receiver. (b) Amplitude spectrum of the measured pulse shape. (c) THz pulse on a 100 times expanded vertical scale.

fall time determined by the 0.6 ps carrier lifetime in implanted silicon [7].

In Fig. 2(b), the Fourier transform of the measured signal (Fig. 2(a)) is shown to stretch from about 0.1 to 2.0 THz. This represents only a lower limit to the true extent of the emitted radiation as it contains the frequency response of the receiver. At the low-frequency end, the efficiency of both emitter and receiver has been shown to be proportional to the length of the antenna, i.e., proportional to the separation between the two lines of the coplanar transmission line. For extremely low frequencies

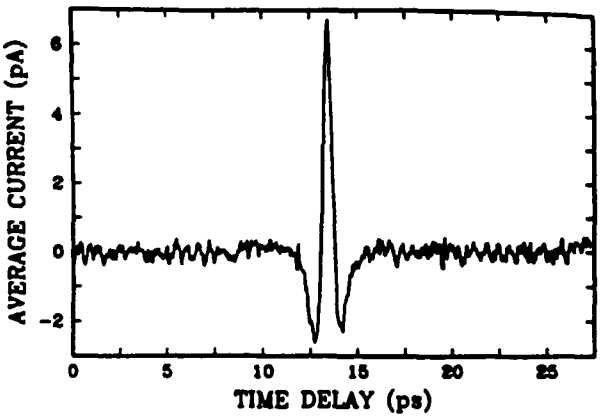

Fig. 3. Measured THz pulse with a 10^5 times reduction (compared with Fig. 2(a)) of the THz beam power.

the size of the paraboloidal mirrors will also limit the efficiency. For the high-frequency limit the efficiency of the antenna is strongly reduced when 1/2 the wavelength (in the dielectric) of the emitted radiation is no longer large compared with the antenna length. This frequency for our 30 μm antenna is 1.5 THz, so that the observed signal and corresponding spectrum are somewhat limited by the antenna response, which has dropped by 50% at this frequency. The high-frequency part of the spectrum is also limited by the finite rise time of the current transient and the nonideal imaging properties of the THz optics.

In Fig. 2(c), the time-resolved signal is shown on a vertical scale that has been expanded by a factor of 100. The structure observable after the main pulse is reproducible and is due to reflections of the electrical pulse on the transmission line, reflections of the THz pulse from the various dielectric interfaces, and absorption and dispersion of water vapor [4] in the 1 cm path outside the vaportight box placed around most of the setup. The observed noise in front of the main pulse is about 1.3×10^{-13} A rms for an integration time of 125 ms, corresponding to an integration bandwidth of 1 Hz determined by a 12 dB/octave filter. An identical noise value is obtained when the far-infrared beam is completely blocked. The signal-to-noise ratio in this 4 minute scan is more than 10000:1. Another 4 minute scan is shown in Fig. 3, for which the intensity of the pump laser beam was reduced from the 6 mW normally used to only 15 μW. This 400-fold reduction in laser power led to a reduction in the transient photocurrent of 320, instead of the expected 400. The discrepancy indicates a slight nonlinearity due to the onset of saturation, related to the fact that the electrical pulses generated on the transmission line are quite strong (almost 1 V in either direction). This 320-fold reduction in photocurrent led to a reduction in the power of the THz beam by the factor 1.0×10^{-5}. However, despite this enormous reduction in power, the peak amplitude is still more than 30 times larger than the rms noise. Based on calculations presented in the next section we believe that the average power in the THz beam during this measurement was about 10^{-13} W. If the

power of the THz beam were even further reduced, the detection limit of the THz receiver would be reached at 1×10^{-16} W, for a signal-to-noise ratio of unity and a 125 ms integration time.

IV. Calculated Power in Terahertz Beam

Before we start a detailed analysis of the noise characteristics of the THz receiver, the emission and detection of the THz beam will be discussed in more detail. Below we will give an estimate of the power emitted by the transmitter, starting with the well-known equation for the power emitted by a harmonically oscillating dipole in free space. Several corrections have to be applied to this simple formula.

First of all, the current, generated in the transmitting antenna through the creation of photocarriers, is nonharmonic. To calculate the emitted power we decompose the transient current into its Fourier components, use the standard formula for each of these components, and finally perform the frequency integration. Most of the radiation is emitted in the rising edge of the transient current and not in the 0.6 ps exponential decay time of the conductivity, which is equal to the carrier lifetime for the radiation-damaged silicon [7]. Thus, the rise time is of vital importance and it proved to be slower than expected from the 70 fs laser pulse width. Using an exponential rise time as adjustable parameter, a good fit to the measured far-infrared spectrum was obtained with a rise time of slightly less than 200 fs. The reasons for the slow rise time are not presently understood. Tentative explanations involve carrier cooling effects, the frequency-dependent conductivity, radiation damping, and the circuit response.

As a second feature, it is important to note that the antenna is not an infinitely short dipole. The effective length of the antenna is probably more than the 30 μm separation between the lines and depends on the current flow from the antenna into the transmission line. In the calculations an effective length of 35 μm is used. This length is roughly equal to a half wavelength of 1.5 THz radiation in the dielectric, resulting in a decrease in emission efficiency of about 50% and limiting the high-frequency end of the integration.

As a last correction we mention that the antenna is situated at an interface between air and a dielectric medium with an index of refraction in the far infrared of n. It has been shown [8], that this situation results in an increase in emitted power by roughly a factor n when n is much bigger than 1. Furthermore, the emitted radiation is strongly directed into the dielectric and concentrated along the normal to the interface. The exact angular distribution of the radiation can be very complicated [2], [8], [9], making it difficult to estimate the fraction of emitted radiation that is collimated into the THz beam. A first consideration is the reflection loss that occurs when the radiation is coupled through the silicon lens into the air. This reflection loss is about 30% at normal incidence. However, the angle for total internal reflection for silicon is only 17°. Calculations show that with a spherical lens it is therefore impossible to capture more than 40% of the THz radiation. To estimate the actual fraction that ends up in the THz beam, a 5-mm-diameter diaphragm was placed in front of the silicon lens. As a result the power in the THz beam was reduced by roughly a factor 2. The diaphragm restricts the captured radiation to an emission cone of 19° (half angle). Calculations show the fraction of radiation within this cone to be only 7%, reflection losses included. Consequently, we estimate that without the diaphragm only 15% of the total emitted radiation ends up in the THz beam, the rest being lost by (total internal) reflection and lens aberration. The complicated field profile at the dielectric lens diffracts out upon propagation to the paraboloidal mirror, and the THz beam profile between the paraboloidal mirrors roughly resembles a (Gaussian) TEM_{00} mode for each of the frequency components, with the diameter increasing as a function of wavelength.

At a dc bias of 10 V and a laser power of 6 mW we find an average photocurrent of 1.1×10^{-6} A, corresponding to a peak current of about 1.8×10^{-2} A. Using this value and the method just described we calculate the total frequency-integrated power emitted by the transmitting antenna to be 75 nW. Using our previously derived value of 15% to describe the coupling efficiency, we obtain 11 nW in the collimated, freely propagating THz beam emitted from the transmitter.

An alternative estimate of the transmitted power can be obtained at the receiving antenna, by combining the measured amplitude of the incident far-infrared field with the measured size of the focal spot. The corrections that have to be applied are similar to those mentioned above for the transmitter.

First of all the response time of the receiving antenna is determined by its gating time and the rise time of the transient conductivity. The Lorentz reciprocity theorem shows that the frequency dependence of the receiving antenna should equal that of the transmitting antenna [10]. Second, the boundary condition results in a complicated angular sensitivity of the receiving antenna and an increase in electric field by the factor $2n/(n+1)$ for radiation incident perpendicular to the interface. As a third and a fourth correction we have to mention the loss of high-frequency components due to the size of the antenna and the reflection losses at the front surface of the dielectric lens.

Measurements show that the size of the focal spot on the receiving antenna is wavelength dependent, being larger for longer wavelengths. The measured (FWHM) diameters of the focal spots were about 180 μm at 1.0 THz, 280 μm at 0.5 THz, and 460 μm at 0.25 THz. The (deconvoluted) induced peak voltage of about 35 mV over the 35 μm antenna structure corresponds to a focused field of about 6 V/cm in the dielectric, if we correct for surface enhancement. These figures yield an average power of about 7 nW in the air incident on the dielectric focusing lens of the receiver. This value is in reasonable

agreement with the previously derived value of 11 nW from the point of view of the transmitter.

An alternative analysis makes use of the concept of antenna impedance, defined as the ratio of the emitted power over the mean square of the current. In this respect it is important to notice that the current is constant along the antenna structure, which makes it a more efficient emitter than the related center-fed antenna [11]. The interface increases the antenna impedance and we find a value of 12 Ω at 0.6 THz for our situation. From the transmitter point of view, a peak current of about 1.8×10^{-2} A is pulsed through the antenna. If we assume that the current and emitted power were concentrated in a narrow band around 0.6 THz, then the emitted peak power would simply be I^2R, and the average emitted power would be about 17 nW, a number that includes the aforementioned 15% coupling efficiency into the THz beam and the 0.6×10^{-4} duty cycle. From the 35 mV induced voltage at the receiving antenna, one can derive an average incident power of 4.5 nW in a similar way. It was only a rough approximation to assume that all radiation was concentrated around the 0.6 THz peak of the spectrum. When we take the proper frequency integrations into account together with the corrections mentioned above, we arrive at 11 nW for the emitted power and 3.5 nW for the received power at the receiving antenna. Taking into account the 30% reflection at the silicon lens, the value obtained from calculations at the receiving antenna gives 5 nW incident on the silicon lens.

Another useful parameter is the ratio of the voltage induced in the receiving antenna to the current in the transmitting antenna. This frequency-dependent ratio is called the mutual impedance [11], [12]. For perfect coupling the mutual impedance should equal the impedance of the (identical) antennas [12]. From our measurements we extract a mutual impedance of about 3 Ω at 0.6 THz, corresponding to 25% amplitude coupling between the transmitter and the receiver for this frequency.

By reasoning from both the transmitter and the receiver point of view, we calculated the average power in the far-infrared beam to be about 11 nW and 5 nW or 7 nW, respectively. For the purposes of the discussion to follow, we consider the average transmitted power in the THz beam to be 10 nW, and we believe that this value is within a factor 2 of the actual value. This average power is comparable to that of conventional thermal sources [13], but the peak power of our source is orders of magnitude larger.

V. Noise in the Receiver

In this section we will present an analysis of the noise of the THz receiver. The following noise analysis is generally applicable to any type of photoconductive switch, although the actual numbers will depend on the type of device. If we were to destroy the directionality of the receiver by removing the paraboloidal mirror and the add-on silicon lens, the noise characteristics of the antenna/switch would in fact be unchanged. However, the sensitivity of the receiver for the THz beam would be drastically reduced.

Experimentally, we measured the receiver noise with a frequency analyzer (Hewlett Packard 3585B) connected to the output of a low-noise current amplifier (Ithaco 1211). The amplifier was in turn connected to the receiving antenna via the terminating coplanar transmission line. This arrangement allowed the investigated noise to be separated from the small pickup of harmonics of the line current. An alternative approach was to measure the fluctuations on the output of the lock-in amplifier that was also connected to the current amplifier (CA). These fluctuations were then converted to an rms current at the input terminals of the current amplifier and could thus be compared with the noise floor (in dBm) measured with the spectrum analyzer.

In the absence of the CPM laser beam, the noise of the first receiving antenna chip investigated was 1.5×10^{-13} A rms for a 125 ms integration time on the lock-in (−73 dBm, with the CA at a setting of 10^{-8} V/A and a bandwidth of 10 Hz). That this value was due to the thermal Johnson noise, also called Nyquist noise, could be demonstrated by replacing the antenna chip by an ordinary resistor of identical value (0.7 MΩ). The easiest way to reduce this noise is to strip the silicon from the areas of the chip that are not illuminated by the laser during normal operation. Such an antenna chip with stripped silicon showed a much increased resistance of 22 MΩ in the off state. For this antenna the noise measurement gave about 3.9×10^{-14} A rms (125 ms), being only slightly affected by the much lower, open-ended current noise of the CA of 1.5×10^{-14} A rms.

When a 6 mW laser beam was focused on the antenna gap, the noise increased to 2.2×10^{-13} A rms (125 ms) for the first antenna chip and to 1.3×10^{-13} A rms for the second stripped antenna chip. For the second chip we could show that the amplitude of the additional noise was proportional to the square root of the laser power. A likely candidate for this additional noise is the Johnson noise arising from the thermally driven random motion of electrons. Each laser pulse temporarily reduces the resistance between the two lines of the terminating coplanar transmission line. During the 0.6 ps switching time the resistance is typically about 550 Ω. The integrated thermal noise power scales with the average conductivity, which in our situation is reduced from 22 MΩ to about 7 MΩ. Thus, we would expect this noise to be 4.8×10^{-14} A rms (125 ms, 1 Hz). However, at 6 mW the measured noise power was equal to the Johnson noise of a 1 MΩ resistor and not that of the measured average resistance of 7 MΩ. Consequently there must be additional noise sources, some of which are described below. The measured antenna noise can also be interpreted as a random effective voltage and charge transfer at each shot of the laser. The 1.3×10^{-13} A rms (125 ms) noise level corresponds to a shot-to-shot effective voltage of 4.2 mV. This value seems to be very large, but results only in a charge transfer of 4.6×10^{-18} C or roughly 30 electrons per shot,

while the incident laser beam creates about 10^8 electrons per shot.

In the experiment it was noticed that, even though no bias voltage was applied to the receiving antenna, the focused laser beam still gave rise to a constant photocurrent of about 3 nA, as if the antenna were biased with about 30 mV. We think this might be due to a nonohmic contact between the silicon and the metallic antenna and terminating transmission line. Although this stray photocurrent does not show up in the signal it can lead to additional noise. First of all the laser power is not perfectly stable, but experiences fluctuations of about $\Delta I/I = 1.0\times10^{-5}/\sqrt{\text{Hz}}$ at the 1 kHz modulation frequency. The noise arising from these fluctuations will definitely contribute but cannot be the dominant noise source, because if it were the noise amplitude should be directly proportional to the laser power. Second, the 3 nA stray current will lead to quantum noise of about 3×10^{-14} A ($RC = 125$ ms). We estimate both noise sources arising from this stray current to be of the same order of magnitude as the expected Johnson noise.

VI. Thermal Background Radiation

The classic broad-band detector for the (far) infrared is the bolometer. This device is strongly affected by thermal noise, which sets serious limitations on its sensitivity [6], [14]. It has been shown [14] that the noise equivalent power (NEP) of temperature sensors in general can never be less than 8×10^{-12} W (125 ms) at room temperature. Therefore bolometers are usually operated at 4.2 K or lower. At 4.2 K their NEP[1] is typically 1×10^{-13} W/$\sqrt{\text{Hz}}$ [6].

The gated and coherent nature of our THz receiver dramatically reduces its sensitivity to thermal background radiation. We will now estimate the noise contribution on our antenna arising from this thermal background. The combined action of thermal far-infrared radiation, with an energy of about kT per mode, from low frequency to the high-frequency response limit of the receiver induces a random voltage across the receiving antenna which is converted into a current and detected. This random voltage is $\sqrt{(4kTR)}$ in V/$\sqrt{\text{Hz}}$, where R is the characteristic impedance of the antenna [15], [16]. We estimated the charge transfer due to the thermal background at room temperature to be about 2.5×10^{-19} coulomb (C) at each shot of the laser. This corresponds to an effective pickup voltage of about 0.23 mV, during the 0.6 ps gate. Because the thermal radiation is incoherent and the pickup voltage for successive shots is unrelated, the net charge transfer across the antenna gap can be viewed as a random walk. The noise in the average current created by the thermal background should thus be about 7×10^{-15} A (125 ms, 100 MHz repetition rate), or roughly a factor 7 lower than the expected Johnson noise. Via a similar calculation we obtain the random charge transfer due to the quantum fluctuations, having a power density of $h\nu$ per mode, to be roughly 5×10^{-20} C per shot of the laser, corresponding to an effective voltage of 0.05 mV and a current noise of 1.4×10^{-15} A (125 ms). Both values depend strongly on the frequency response of the gate and thus on the rise time of the transient conductivity. This dependence occurs because the noise power at high frequencies is much larger than that at low frequencies, due to the quadratic increase of the density of electromagnetic modes with frequency. Consequently the above-mentioned noise values are only rough estimates, but they do provide important points of reference for the sensitivity of the THz receiver. The noise arising from the thermal background and the quantum fluctuation would remain unchanged if the paraboloidal mirror and add-on lens were removed from the receiver, as this only changes its directionality and the receiving antenna "sees" the same temperature in all directions.

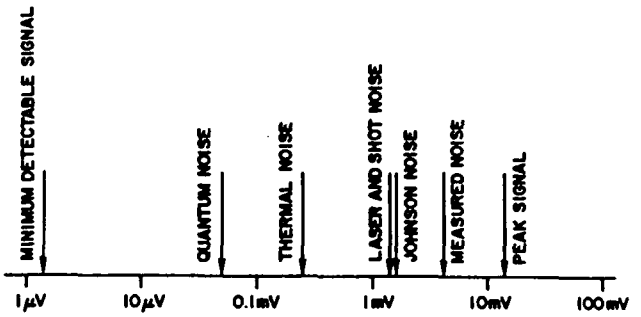

Fig. 4. Logarithmic presentation of the measured peak signal, the minimum detectable signal, and the discussed noise sources, in terms of the induced voltage across the receiving antenna.

VII. Discussion and Summary

At this point we want to review and compare some relevant figures. The THz receiver detects, with signal-to-noise ratios of approximately 10000:1, subpicosecond, 14 mV pulses coming at a 100 MHz repetition rate in a highly directional beam of THz radiation with an average power of 10 nW. Consequently, the detection limit for these repetitive pulses is about 1.4 μV. However, it has just been shown that the sampled voltage, during a single 0.6 ps gating pulse, on the receiving antenna due to the thermal background is about 0.23 mV and due to the vacuum fluctuations is 0.05 mV. Thus, in terms of instantaneous voltages, the receiver can detect 1/160 of the thermal background and 1/35 of the vacuum fluctuations. Beams of THz radiation can be detected with peak powers of only 4×10^{-5} that of the incident thermal radiation. This impressive performance is due to the high directionality of the THz receiver and to the fact that the thermal noise is incoherent and adds randomly for successive gating pulses, while the signal propagating in the THz beam is coherent and scales linearly with the number of gating pulses. Fig. 4 graphically presents the various noise

[1]As explained in [15], a coherent detector measures amplitude; therefore, the NEP is proportional to the measurement bandwidth. In contrast to this, an incoherent detector measures power; therefore, the NEP is proportional to the square root of the measurement bandwidth.

sources and the signal amplitude in terms of the effective induced voltage at each gating pulse.

The generation and detection of the terahertz (far-infrared) radiation is coherent; therefore the THz receiver is intrinsically much more sensitive than the incoherent bolometer. With respect to this comparison it should be clear that the bolometer can measure the average power in the repetitively pulsed THz beam. However, our synchronously gated and coherent detection method cannot directly measure incoherent THz beams. The only detectable effect of an incoherent beam on our detector would be an increase in the noise on the receiving antenna. Another consideration is whether the gated detector can detect a single frequency wave. In the absence of synchronization between monochromatic radiation and a high harmonic of the 100 MHz gating rate, the gated detection will yield a beat signal which averages to zero. Even if the CW wave is synchronized, a large reduction in sensitivity will occur, because of the limited duty factor of 0.6×10^{-4}. With respect to the above comment, it is still appropriate to compare the detector with a radio receiver, which in fact it is, although the antenna is only 35 μm long and the device is operated in this nonconventional gated mode. For a good radio the NEP can be as low as 10^{-19} W/Hz (see [17]), 1000 times lower than for our receiver. To compare our detector with a radio it is instructive to interpret the gated operation of the receiver in the frequency domain. Here, the 10 ns periodic gating of the receiver results in the simultaneous detection of thousands of narrow frequency bands separated by the 100 MHz rate and with a THz roll-off determined by the 0.6 ps gating time. This results in broad-band performance together with the sensitivity increase due to coherent detection. This picture also shows why the influence of thermal (incoherent) radiation is so small. The receiver is only sensitive to radiation close (within 1 Hz for a 125 ms integration time) to the 100 MHz multiples of the comb.

The performance of a radio deteriorates when the impedance of the lead from the antenna to the radio is not matched with that of the antenna itself or when the lead is lossy. The laser gating pulses reduce the resistance between the lines to 550 Ω, which definitely is not matched with the antenna impedance, which we calculated to be about 12 Ω at 0.6 THz. A better match is obtained for longer antennas. Changing both transmitting and receiving antenna to a structure with lines separated by 50 μm did indeed increase the peak signal by more than a factor of 2, while the noise was not affected. However, increasing the size of the antenna leads to a reduction in the speed of the device. Furthermore, the way the THz pulses are detected, by making the gap between the antenna stubs conductive, is based on real resistance and thus by definition is lossy. Only the creation of a complete short could result in loss-free coupling to the transmission line, a coupling that would be optimum if the antenna impedance were matched to that of the transmission line. At room temperature the ultimate performance of the THz receiver would then be determined by the fluctuations in thermal background.

In this paper we have described the performance of an optoelectronic system for the generation and detection of beams of 1/2 cycle pulses of THz (far-infrared) radiation. The THz transmitter operation is based on repetitive, subpicosecond laser excitation of a Hertzian dipole antenna embedded in a charged coplanar line. The associated optoelectronic receiver is gated in synchronism with the excitation of the transmitter by subpicosecond pulses from the same laser source. With this transmitter 10 nW (average power) highly directional electromagnetic beams, consisting of 0.5 ps pulses of THz radiation with a repetition rate of 100 MHz, are generated. After freely propagating to the receiver, these beams can be detected with a signal-to-noise ratio of 10000:1 and with a sampling time resolution of 0.5 ps. We have discussed several different sources of noise in the present receiver design, which for an integration time of 125 ms can detect repetitive subpicosecond pulses in a beam with an average power as low as 10^{-16} W. We have shown how the thermal noise will eventually limit the performance of an ultimate receiver. Our receiver is more noisy in amplitude than this ultimate device by a factor of approximately 20. The reasons for that are reasonably well understood, and efforts are being made to improve the system performance.

Acknowledgment

The authors acknowledge the excellent masks and wafer fabrication by H. Chan.

References

[1] Ch. Fattinger and D. Grischkowsky, "Point source teraHertz optics," *Appl. Phys. Lett.*, vol. 53, p. 1480, 1988; "THz beams," vol. 54, p. 490, 1989.

[2] Ch. Fattinger and D. Grischkowsky, "Beams of teraHertz electromagnetic pulses," in *Proc. Picosecond Electronics and Optoelectronics Topical Meeting* (Salt Lake City, UT), Mar. 8–10, 1989, p. 225.

[3] M. van Exter, Ch. Fattinger, and D. Grischkowsky, "High-brightness teraHertz beams characterized with an ultrafast detector," *Appl. Phys. Lett.*, vol. 55, p. 337, 1989.

[4] M. van Exter, Ch. Fattinger, and D. Grischkowsky, "TeraHertz time domain spectroscopy of water vapor," *Opt. Lett.*, vol. 14, p. 1128, 1989.

[5] P. R. Smith, D. H. Auston, and M. C. Nuss, "Subpicosecond photoconducting dipole antennas," *IEEE J. Quantum Electron.*, vol. 24, p. 255, 1988.

[6] C. Johnson, F. J. Low, and A. W. Davidson, "Germanium and germanium-diamond bolometers operated at 4.2 K, 2.0 K, 1.2 K, 0.3 K, and 0.1 K," *Opt. Engr.*, vol. 19, p. 255, 1980.

[7] F. E. Doany, D. Grischkowsky, and C. C. Chi, "Carrier lifetime versus ion-implantation dose in silicon on sapphire," *Appl. Phys. Lett.*, vol. 50, p. 460, 1987.

[8] W. Lukosz and R. E. Kunz, "Light emission by magnetic and electric dipoles close to a plane interface. I. Total radiated power," *J. Opt. Soc. Amer.*, vol. 67, p. 1607, 1977.

[9] D. B. Rutledge and M. S. Muha, "Imaging antenna arrays," *IEEE Trans. Antennas Propagat.*, vol. AP-30, p. 535, 1982.

[10] G. D. Monteath, *Applications of the Electromagnetic Reciprocity Principle*. Oxford: Pergamon Press, 1973.

[11] L. V. Blake, *Antennas*. New York: Wiley, 1966.

[12] T. A. Milligan, *Modern Antenna Design*. New York: McGraw-Hill, 1985.

[13] J. G. Zissis and W. L. Wolfe, *The Infrared Handbook*. Washington, DC: NTIS, 1978.

[14] R. C. Jones, "The ultimate sensitivity of radiation detectors," *J. Opt. Soc. Amer.*, vol. 37, p. 879, 1947.
[15] F. R. Arams, *Infrared to Millimeter Wavelength Detectors*. Norwood, MA: Artech House, 1973.
[16] B. M. Oliver, "Thermal and quantum noise," *Proc. IEEE*, vol. 53, p. 436, 1965.
[17] W. H. Hayward, *Introduction to Radio Frequency Design*. Englewood Cliffs, NJ: Prentice-Hall, 1982.

✠

Martin van Exter was born in the Netherlands in June 1961. He received the Ph.D. degree in physics in 1988 from the University of Amsterdam, where he worked on time-resolved stimulated Raman spectroscopy and the dynamics of surface plasmon polaritons.

At the IBM T. J. Watson Research Center, Yorktown Heights, NY, he studied the generation and detection of short pulses of THz radiation and their application in broad-band spectroscopy. He is currently working on semiconductor lasers at the University of Leiden.

Daniel R. Grischkowsky (A'84–SM'90) was born in St. Helens, OR, on April 17, 1940. He received a bachelor's degree from Oregon State University in 1962 and the Ph.D degree in physics from Columbia University in 1968. His thesis work, supervised by S. R. Hartmann, involved electron spin resonance investigations and led to the explanation of the observed dependence of photon echoes in ruby on the direction of the applied magnetic field.

In 1969 he joined the IBM Research Division at the Watson Research Center at Yorktown Heights, NY, where he now manages the Ultrafast Science with Lasers Group. His initial experimental and theoretical research involved studying the interaction between near-resonant light and the two-level system. The adiabatic following model, which he originally proposed as a result of these studies, subsequently explained the observed effects of self-focusing, self-defocusing, self-steepening, and slow group velocities in vapors of two-level systems (alkali metals). His experimental and theoretical studies of the nonlinear propagation of picosecond laser pulses in single-mode optical fibers led to the concept of enhanced frequency chirping and the associated optical-fiber pulse compressor and to the experimental observations of gray solitons and optical intensity shocks. His most recent work has involved the generation and application of subpicosecond electrical pulses on transmission lines. An important part of this work has been the observation of terahertz radiation from the generation site and Cerenkov radiation from the propagating electrical pulses. These studies have resulted in a new source of pulsed terahertz beams.

Dr. Grischkowsky is a fellow of the Optical Society of America and the American Physical Society. He was awarded the Boris Pregel Award for Applied Science and Technology (1985) by The New York Academy of Sciences for his invention of the optical fiber pulse compressor. He received the R. W. Wood Prize (1989) from the Optical Society of America for his pulse propagation studies in optical fibers and their use for generating ultrashort pulses of light.

Optical and electronic properties of doped silicon from 0.1 to 2 THz

Martin van Exter and D. Grischkowsky
IBM Watson Research Center, P.O. Box 218, Yorktown Heights, New York 10598

(Received 11 December 1989; accepted for publication 14 February 1990)

Using a source of freely propagating subpicosecond pulses of THz radiation, we have measured the absorption and dispersion of both *N*- and *P*-type, 1 Ω cm silicon from 0.1 to 2 THz. These results give the corresponding frequency-dependent complex conductance over the widest frequency range to date. The data provide a complete view on the dynamics of both electrons and holes and are well fit by the simple Drude relationship.

The dynamics of carriers in semiconductors is important from both the scientific as well as the technical point of view. The most interesting phenomena occur at frequencies comparable to either the plasma frequency or the damping rate.[1-7] Unfortunately, this usually occurs in the submillimeter region, which is difficult to reach with microwave[2,6] as well as with far-infrared[1,7] techniques. Below 100 GHz, microwave techniques have been used for single-frequency studies. The high-frequency behavior of semiconductors has been investigated with classical far-infrared spectroscopy.[1,4,7] However, for moderate doping, the strongest absorption of the free carriers lies below 2 THz, where classical far-infrared spectroscopy becomes very difficult. Consequently, the investigation of the most important frequency range from 0.1 to 2 THz has remained incomplete (1.5 THz = 50 cm^{-1} = 6.2 meV).

Recently a new system has become available for spectroscopic studies in the range from 0.1 to 2.0 THz.[8,9] This system is based on the optoelectronic generation and reception of a beam of subpicosecond THz pulses. By inserting a sample in the beam and comparing the shape of the original subpicosecond THz pulses with the shapes of pulses that have propagated through the sample, one is able to deduce the frequency-dependent absorption and dispersion.

In this letter we describe an application of the above time-domain spectroscopy technique to a complete measurement of the absorption and dispersion due to carriers in doped silicon. The measured samples were *N*- and P-doped, 1 Ω cm silicon. The dopants were phosphorus and boron, respectively, and the flat wafers had a (111) orientation. The frequency-dependent properties are shown to be completely due to the carriers and not to the host crystal. Our measurements extend from 0.1 to 2 THz and allow for the most comprehensive determination of the complex conductivity to date. To first order the results are well fit by the simple Drude theory, although slight deviations indicate that further refinements in the theory are needed.

The setup used to generate and detect the short pulses of THz radiation is depicted in Fig. 1(a) and has been described earlier.[8,9] The transmitter and receiver are identical, each consisting of a micron-sized dipole antenna imbedded in a coplanar transmission line and optoelectronically driven by 70 fs pulses from a colliding-pulse mode-locked dye laser. A large fraction of the generated pulses of THz radiation is captured by a silicon lens attached to the transmitting chip and is directed onto a paraboloidal mirror that recollimates the radiation into a low divergence beam. This THz beam is directed towards the receiver where it is focused onto the receiving antenna. The amplitude and time dependence of the transient voltage induced across the receiving antenna are obtained by measuring the collected charge (current) versus the time delay between the THz pulses and the laser pulses that synchronously gate the receiver. Such a measured transmitted THz pulse with no sample in place is shown in Fig. 1(b). The corresponding amplitude spectrum of this 0.5 ps full width at half maximum pulse is presented in Fig. 1(c) and illustrates the 2 THz bandwidth available for spectroscopy.

Figure 2(a) shows a THz pulse transmitted through a 283-μm-thick sample of 1.15 Ω cm, *N*-type silicon. The first

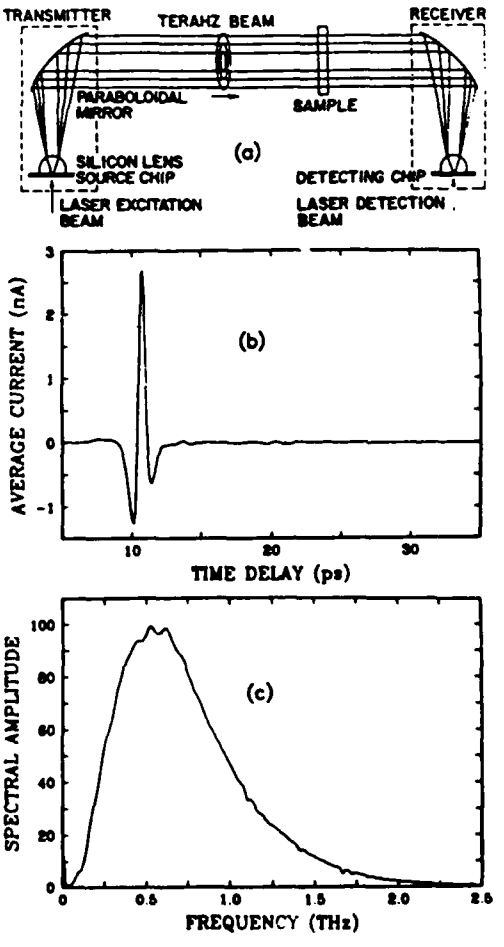

FIG. 1 (a) Schematic of the experiment; (b) measured transmitted THz pulse; (c) amplitude spectrum of (b).

 0003-6951/90/171694-03$02.00 © 1990 American Institute of Physics

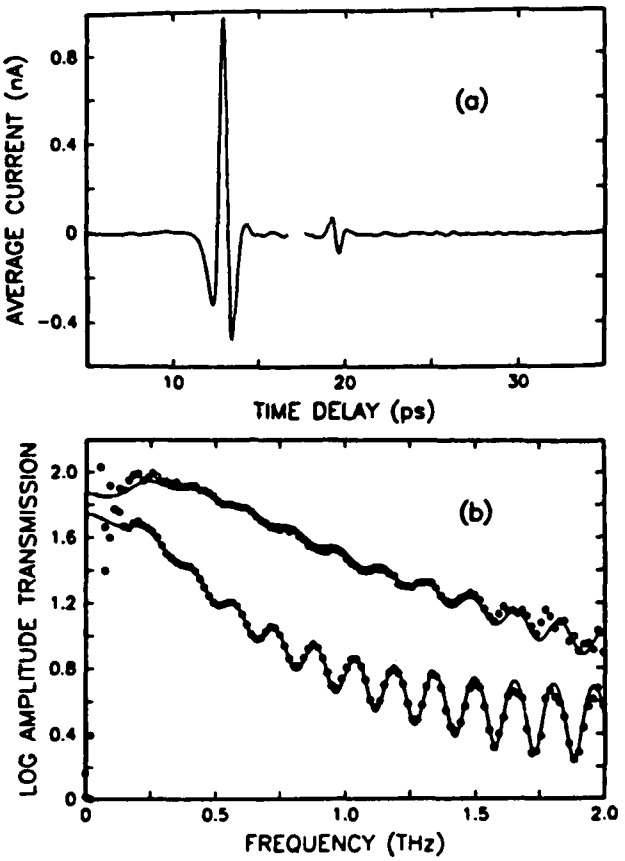

FIG. 2. (a) THz pulse transmitted through a 283-μm-thick wafer of 1.15 Ω cm, N-type silicon. (b) Logarithm of the amplitude transmission for a 283-μm-thick wafer of 1.15 Ω cm, N-type silicon (dots) and for a 258-μm-thick wafer of 0.92 Ω cm, P-type silicon (circles).

transient is the primary pulse that passed directly through the sample. Its peak amplitude is about 40% of that of the original pulse. The output pulse amplitude and shape are changed due to reflection losses, and the frequency-dependent absorption and dispersion of the sample. The second and barely resolvable third transients are THz pulses reflected inside the thin sample. Comparison of the Fourier transform of the single input pulse with that of the output pulse sequence from the doped silicon sample yields the frequency-dependent transmission plotted as $-\ln[(E_{\text{out}}(\omega)/E_{\text{in}}(\omega)]$ by the dots in Fig. 2(b). The open circles are measurements on a 258-μm-thick P-type sample that had a resistivity of 0.92 Ω cm. The multiple reflections are responsible for the oscillations in the frequency-dependent transmission of the sample. Similar oscillations are observed in the effective index of refraction, obtained by division of the phase shift of the transmitted spectral components by the length of the sample.

In order to quantitatively explain the above measurements, the index of refraction and absorption for undoped silicon was needed from 0.1 to 2.0 THz. Using time-domain spectroscopy, we have measured these quantities with high precision for a 20-mm-thick piece of float-zone-refined high-resistivity (10 kΩ cm) silicon. The index was found to be 3.415(2) and essentially constant over the entire frequency range, being in good agreement with the literature value of 3.416 at 1.0 THz.[10] The high-resistivity silicon was almost transparent over the entire frequency range, with a measured intensity absorption of <0.04 cm^{-1}. Consequently, the observed strong frequency dependence for doped silicon is due to the carriers and not to the host crystal.

The Drude model[5-7] treats the free carriers in a solid as classical point charges subject to random collisions. In this letter the simplest versus of the Drude model is adopted, in which the collision damping is independent of the carrier energy. According to the Drude model, the frequency-dependent complex dielectric constant ϵ, being the square of the complex index of refraction $n = n_r + in_i$, in SI units is

$$\epsilon = \epsilon_\infty + i\sigma/\omega\epsilon_0 = \epsilon_\infty - \omega_p^2/\omega(\omega + i\Gamma),$$

$$\sigma = \sigma_{dc} i\Gamma/(\omega + i\Gamma) = i\epsilon_\infty \omega_p^2/(\omega + i\Gamma),$$

where ϵ_∞ is the contribution of the bound electrons, $\Gamma = 1/\tau$ is the damping rate, and τ is the average collision time. The plasma angular frequency ω_p is defined by $\omega_p^2 = Ne^2/\epsilon_0 m$, where N is the number density of carriers, e is the electronic charge, ϵ_0 is the free-space permittivity, and m is the effective carrier mass. We have also presented the Drude result for the complex electric conductivity σ, where the dc conductivity σ_{dc} is given by $\sigma_{dc} = e\mu N$ with the mobility μ given by $\mu = e/m\Gamma$. The experimentally determined transmission is related to the above equations via the intensity absorption coefficient α, usually specified in cm^{-1}, which is $\alpha = n_i(4\pi/\lambda_0)$.

To include the effects of multiple reflections we fit the measurements with a model for the transmission through a reflective, lossy parallel slab of material with frequency-dependent optical properties described by the Drude model. The solid lines in Fig. 2(b) are theoretical fits. From the experimental data, both Drude parameters, the plasma angular frequency ω_p and the damping rate Γ, could be determined within 5% accuracy. For 0.92 Ω cm P-type silicon we found $\omega_p/2\pi = 1.75$ THz and $\Gamma/2\pi = 1.51$ THz, while for 1.15 Ω cm N-type silicon $\omega_p/2\pi = 1.01$ THz and $\Gamma/2\pi = 0.64$ THz. The measurements immediately show the different dynamic behavior of the electrons and the holes. For our situation of moderate doping and room temperature the damping rate Γ is mainly determined by carrier-phonon collisions,[2,4,11] a process that apparently is more efficient for holes than for electrons. A combination of the measured damping rates and the effective carrier masses, which have been measured to be $0.26m_0$ for the electrons and $0.37m_0$ on the average for the light and heavy holes,[1,12,13] where m_0 is the free-electron mass, yield mobilities of 1680 cm^2 V^{-1} s^{-1} for the electrons and 500 cm^2 V^{-1} s^{-1} for the holes. These values are higher than the literature values of 1400 and 400 expected for the doping levels of the N- and P-type silicon, respectively.[12,14] This disagreement may indicate the need for an extension of the simple Drude model; for example, many sophisticated models have been developed,[2,4,11] separating the carrier relaxation into both inter- and intravalley scattering with (acoustic and optic) phonons and with ionized impurities.

The second fit parameter, the plasma frequency, is proportional to the root of the ratio of the carrier density over the effective mass. The difference in plasma frequency between P- and N-type material mainly reflects the larger

doping needed in the *P*-type to compensate for the higher damping rate and to get the same dc conductivity. Combining the measured plasma frequencies with the respective effective carrier masses, we calculated a carrier density of $1.4\times10^{16}\,\mathrm{cm}^{-3}$ for the *P*-type and $3.3\times10^{15}\,\mathrm{cm}^{-3}$ for the *N*-type silicon. This is rather low compared to the doping levels of $1.8\times10^{16}\,\mathrm{cm}^{-3}$ and $4.6\times10^{15}\,\mathrm{cm}^{-3}$ specified by the manufacturer to $\pm 20\%$.

To facilitate interpretation of the data we removed the influence of reflections numerically, using the dielectric function obtained from the Drude fit. The correction, of which the result is shown in Fig. 3(a), is especially important for the very high frequencies, where the absorption is low and the interference fringes are strong, and for the very low frequencies, where the index of refraction becomes large. The absorption is seen to be quite strong, more than 2000 times greater than that of the host crystal. Below 0.15 THz the data become noisy due to the limited beam power, but the theoretically predicted drop in absorption at low frequencies is clearly observable. In Fig. 3(b), we present the obtained real part of the index of refraction versus frequency. This quantity is strongly frequency dependent, showing a clear minimum followed by a dramatic increase towards low frequencies. The agreement between this THz optical data and the simple Drude theory is exceptional.

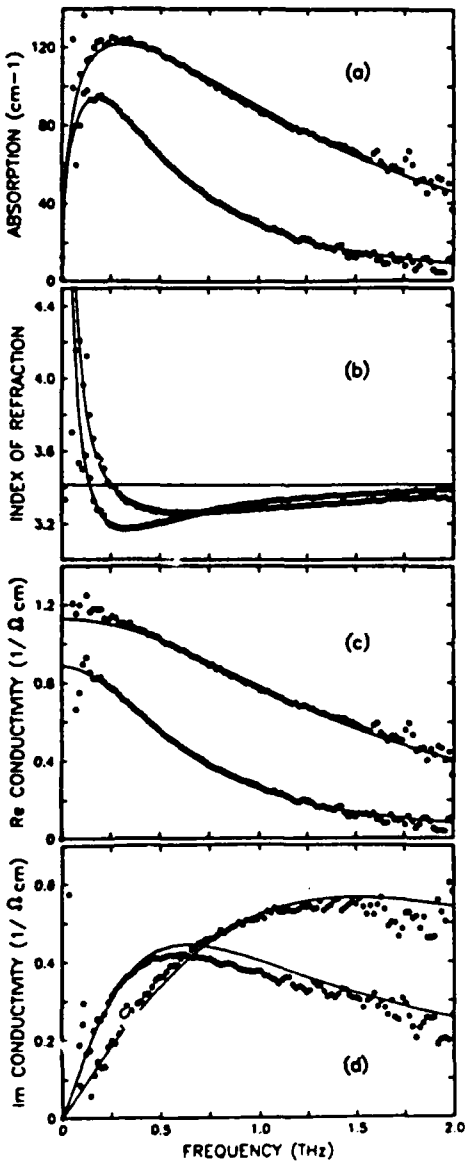

FIG. 3. Results for 1.15 Ω cm, *N*-type (dots) and 0.92 Ω cm, *P*-type (circles) silicon. (a) Intensity absorption calculated from the measured transmission of Fig. 2(b); (b) real part of the index of refraction; (c) real part of the electric conductivity; (d) imaginary part of the electric conductivity.

As the THz optical properties of the samples are largely determined by the carrier dynamics, we have indirectly measured the electric conductivity of the doped silicon. To link the optical measurements with electronics, the real part of the electric conductivity calculated from the optical data is shown in Fig. 3(c) and the imaginary part in Fig. 3(d). The real part is strongly frequency dependent, dropping monotonically from its dc peak to a reduced value at the highest measured frequency of 2 THz. The extrapolated dc conductivities are 0.89 Ω cm for the *P*-type material and 1.13 Ω cm for the *N* type, comparing favorably with the directly measured values of 0.92 Ω cm (*P* type) and 1.15 Ω cm (*N* type). The behavior of the imaginary part is completely different, increasing from zero at low frequencies, peaking at mid-range, and then showing a gradual decline. The agreement with the Drude theory of both the real and imaginary part of the conductivity is quite acceptable.

We acknowledge the excellent masks and wafer fabrication by Hoi Chan and the discussions with Søren Keiding. This research was partially supported by the U.S. Office of Naval Research.

[1]W. G. Spitzer and H. Y. Fan, Phys. Rev. **106**, 882 (1957).
[2]J. D. Holm and K. S. Champlin, J. Appl. Phys. **39**, 275 (1968).
[3]S. J. Allen Jr., D. C. Tsui, and F. DeRosa, Phys. Rev. Lett. **35**, 1359 (1975).
[4]M. Vindevoghel, J. Vindevoghel, and Y. Leroy, Infrared Phys. **15**, 161 (1975).
[5]N. W. Ashcroft and N. D. Mermin, *Solid State Physics* (Holt, Rinehart and Winston, New York, 1976).
[6]R. T. Kinasewitz and B. Senitzky, J. Appl. Phys. **54**, 3394 (1983).
[7]T. Ohba and S. Ikawa, J. Appl. Phys. **64**, 4141 (1988).
[8]M. van Exter, Ch. Fattinger, and D. Grischkowsky, Appl. Phys. Lett. **55**, 337 (1989).
[9]M. van Exter, Ch. Fattinger, and D. Grischkowsky, Opt Lett. **14**, 1128 (1989).
[10]E. V. Loewenstein, D. R. Smith, and R. L. Morgan, Appl. Opt. **12**, 398 (1973).
[11]P. A. Schumann Jr. and R. P. Phillips, Solid-State Electron. **10**, 943 (1967).
[12]S. M. Sze, *Physics of Semiconductor Devices* (Wiley, New York, 1981).
[13]R. N. Dexter, H. J. Zeiger, and B. Lax, Phys. Rev. **104**, 637 (1956).
[14]C. Jacoboni, C. Canali, G. Ottaviani, and A. Alberigi Quaranta, Solid-State Electron **20**, 77 (1977).

PHYSICAL REVIEW B VOLUME 41, NUMBER 17 15 JUNE 1990-I

Carrier dynamics of electrons and holes in moderately doped silicon

Martin van Exter and D. Grischkowsky
IBM Research Division, Thomas J. Watson Research Center, P.O. Box 218, Yorktown Heights, New York 10598
(Received 22 December 1989)

A time-domain spectroscopic technique, based on the generation and detection of a collimated beam of subpicosecond broadband terahertz pulses, is used to measure the absorption and dispersion of n- and p-type silicon, with resistivities of 0.1, 1, and 10 Ω cm in the submillimeter range of 0.1–2 THz. From the transmission measurements performed at room temperature and at 80 K, the absorption and dispersion, and concomitantly the full complex conductivity, of the doped silicon could be obtained. The results provide an accurate view on the dynamics of the electrons and the holes. Although the simple Drude model, with an energy-independent relaxation time, gives a surprisingly accurate description of the observed carrier dynamics, the measurements do show that some refinements are needed. An extended model, with an energy-dependent carrier-relaxation rate, can explain most of the observed deviations from the simple Drude model.

INTRODUCTION

For several decades physicists have studied the dynamics of carriers in semiconductors. A very interesting region for this study is the far-infrared or submillimeter region, where the frequency of the electromagnetic radiation is comparable to the carrier damping rate.[1–7] Unfortunately, this region is difficult to reach with available sources. In the microwave range below 100 GHz semiconductor samples have been investigated through insertion in oversized waveguides.[2] In these experiments it is important that the sample fits tightly in the waveguide, a situation that is never perfectly fulfilled, although the use of a circular TE_{01} mode reduces the problem dramatically.[2] A second complication is the variation in load experienced by the microwave source due to the reflections from the sample. Therefore, other groups have used horn-shaped transmitters and receivers to couple the microwave field into free space.[6] However, microwave techniques in general have the disadvantage that they are done at one single frequency or at best over a narrow frequency band. With the well-developed technique of classical far-infrared spectroscopy the high-frequency (above 2 THz) behavior of semiconductors has been thoroughly investigated.[1,4,7] However, for moderate doping, the strongest absorption of the free carriers lies below 2 THz, where classical far-infrared spectroscopy becomes difficult and time consuming, though some excellent studies have been performed.[3,4] Consequently, the investigation of the most important frequency range from 0.1 to 2 THz has remained incomplete.

Recently a new system has become available for spectroscopic studies in the range from 0.1 to 2 THz.[8–11] This system is based on the optoelectronic generation and reception of a beam of subpicosecond terahertz pulses. By inserting a sample in the beam and comparing the shape of the original subpicosecond terahertz pulses with the shapes of pulses that have propagated through the sample, one is able to deduce the frequency-dependent absorption and dispersion; this procedure is called time-domain spectroscopy.

In this paper we describe an application of time-domain spectroscopy with terahertz beams to a complete measurement of the absorption and dispersion due to carriers in doped silicon. The measured samples were n- and p-doped silicon wafers, having a ⟨111⟩ orientation and room-temperature resistivities of 0.1, 1, and 10 Ω cm. The frequency-dependent properties are shown to be completely due to the carriers and not to the host crystal. Our measurements extend from 0.1 to 2 THz and allow for the most comprehensive determination of the complex conductivity to date. To first order the results are reasonably well fit by the simple Drude theory for all the n-type and p-type samples and for both room temperature (293 K) and 80 K. Slight but significant deviations indicate further refinements in the theory are needed. We show how a model that takes the frequency dependence of the carrier relaxation into account can explain practically all the observed deviations.

THEORY

The Drude model[5–7] treats the free carriers in a solid as classical point charges subject to random collisions. In the first part of this paper the simplest version of the Drude model is adopted, in which the collision damping is independent of the carrier energy. The linear interaction between an isotropic medium and electromagnetic radiation is, in general, described by a frequency-dependent complex dielectric constant ϵ, being the square of the complex index of refraction $n = n_r + in_i$. According to the Drude model the dielectric constant in SI units is

$$\epsilon = \epsilon_\infty + \frac{i\sigma}{\omega\epsilon_0} = \epsilon_\infty - \frac{\omega_p^2}{\omega(\omega + i\Gamma)} ,$$

$$\sigma = \sigma_{dc}\frac{i\Gamma}{\omega + i\Gamma} = \frac{i\epsilon_0\omega_p^2}{\omega + i\Gamma} ,$$

where ϵ_∞ is the contribution of the dielectric, $\Gamma = 1/\tau$ is

 ©1990 The American Physical Society

the damping rate, and τ is the average collision time. The plasma angular frequency ω_p is defined by $\omega_p^2 = Ne^2/\epsilon_0 m$, where N is the number density of carriers, e is the electronic charge, ϵ_0 is the free-space permittivity, and m is the effective carrier mass. We have also presented the Drude result for the complex electric conductivity σ, where the dc conductivity σ_{dc} is given by $\sigma_{dc} = e\mu N$, with the mobility μ given by $\mu = e/m\Gamma$. The electric field at the peak of the terahertz pulse is only of the order of 0.1 V/cm, corresponding to an average energy in the terahertz beam of about 10 nW.[11] Clearly, this is small enough to validate the low-field expression for μ and to neglect joule heating. For the 80-K samples and the highest frequencies, the energy of the far-infrared photons becomes almost kT. Dumke[12] has shown that even for this case quantum effects give only a 1% correction compared to the classical model.

The effective carrier mass used in the Drude model represents the curvature of the energy-momentum relation of the carriers in silicon. Silicon has an indirect bandgap and the minimum of the conduction band is sixfold degenerate and close to the Brillouin zone in the $\langle 100 \rangle$ direction.[13] This asymmetry leads to the existence of a transverse and a longitudinal electron mass, m_t and m_l, respectively. The effective electron mass m_e is given by $(1/m_e) = (2/m_t + 1/m_l)/3$. Using cyclotron resonance[13,14] these masses have been measured to be $m_t = 0.19m_0$ and $m_l = 0.92m_0$, and thus $m_e = 0.26m_0$, where m_0 is the free-electron mass. The situation for the holes is more complicated, because there are three different valence bands around $k = 0$: there are light holes ($m_{lh} = 0.16m_0$) and heavy holes ($m_{hh} = 0.49m_0$) (Refs. 13 and 14) and there is an additional band split off due to spin-orbit interaction. The percentage of holes in the split-off band is about 2% at room temperature[15] and drops quickly when the temperature is lowered. In this article, the influence of this band is neglected. For parabolic bands the ratio of heavy and light holes is easily calculated and the effective hole mass that enters the Drude model is $m_h = (m_{hh}^{1.5} + m_{lh}^{1.5})/(m_{hh}^{0.5} + m_{lh}^{0.5})$ and thus is 0.37 m_0 (Refs. 1 and 13). This result is only valid to first order, as the heavy-hole band is nonparabolic and has a warped structure, which gives the effective hole mass a slight temperature dependence.[15,16]

Experimentally, we measure the amplitude transmission and the phase shift of terahertz radiation propagated through a flat sample. We convert the transmission into an intensity absorption coefficient α, which is related to the above equations via $\alpha = n_i(4\pi/\lambda_0)$. The measured phase shift is converted into the (real component of the) index of refraction, through division by the length of the sample. To link our optical measurements with high-speed electronics, we have also converted the experimental results into the complex high-frequency electrical conductivity $\sigma(\omega)$.

EXPERIMENTAL TECHNIQUE

The setup used to generate and detect the short pulses of terahertz radiation is depicted in Fig. 1 and has been described earlier.[8-11] For the room-temperature experiments we have used an identical transmitter and receiver. The dipole antenna, as shown in Fig. 1(a), consisted of two 20-μm-wide stubs separated by a 5-μm gap, sticking inwards from two 10-μm lines that were separated by 30 μm. This structure was fabricated on an ion-implanted silicon-on-sapphire (SOS) wafer. The conductivity of the gap region is periodically changed through optoelectronic excitation by the 623 nm, 70 fs pulses from a colliding-pulse mode-locked (CPM) dye laser. The resulting current transients in the biased (10-V) transmitting antenna generate pulses of terahertz radiation. A large fraction of the generated terahertz radiation is captured by a silicon lens attached to the transmitting chip and is directed onto a paraboloidal mirror that recollimates the radiation into a low-divergence beam. This terahertz beam is directed towards the receiver, where it is focused onto the receiving antenna. The amplitude and time dependence of the transient voltage induced across the receiving antenna are obtained by measuring the collected charge (current) versus the time delay between the terahertz pulses and the laser pulses that synchronously gate the receiver. Such a measured transmitted terahertz pulse with no sample in place is shown in Fig. 2(a). The corresponding amplitude spectrum of this 0.5-ps full width at half maximum (FWHM) pulse is presented in Fig. 2(c) and illustrates the 2-THz bandwidth available for spectroscopy.

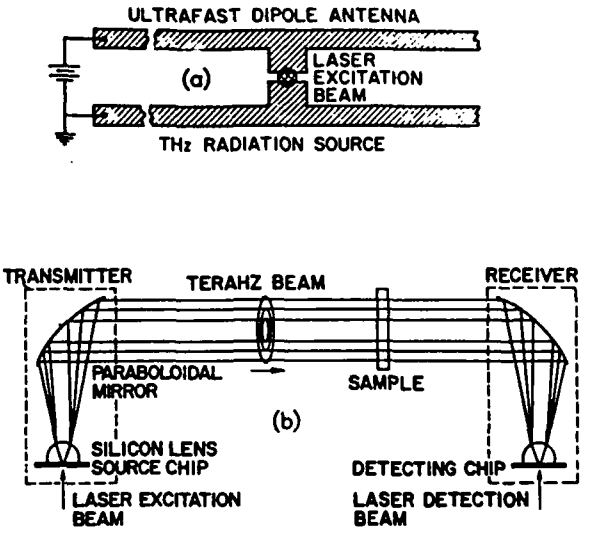

FIG. 1. (a) Antenna structure used in the experiment; (b) schematic for generation and detection of terahertz pulses.

The available frequency range proved to be ideally suited for the study of moderately-doped silicon at room temperature. However, on cooling down to 80 K the carrier dynamics becomes considerably slower and the interesting spectral features shift to lower frequencies. The small and fast antennas we used at room temperature are not efficient enough at low frequencies, and our first measurements were very noisy. We therefore changed the receiver to a structure similar to that shown in Fig. 1(a), but with 120-μm separation between the lines. The increased size of the antenna enhances the signal at low frequencies, where the detected spectral amplitude is pro-

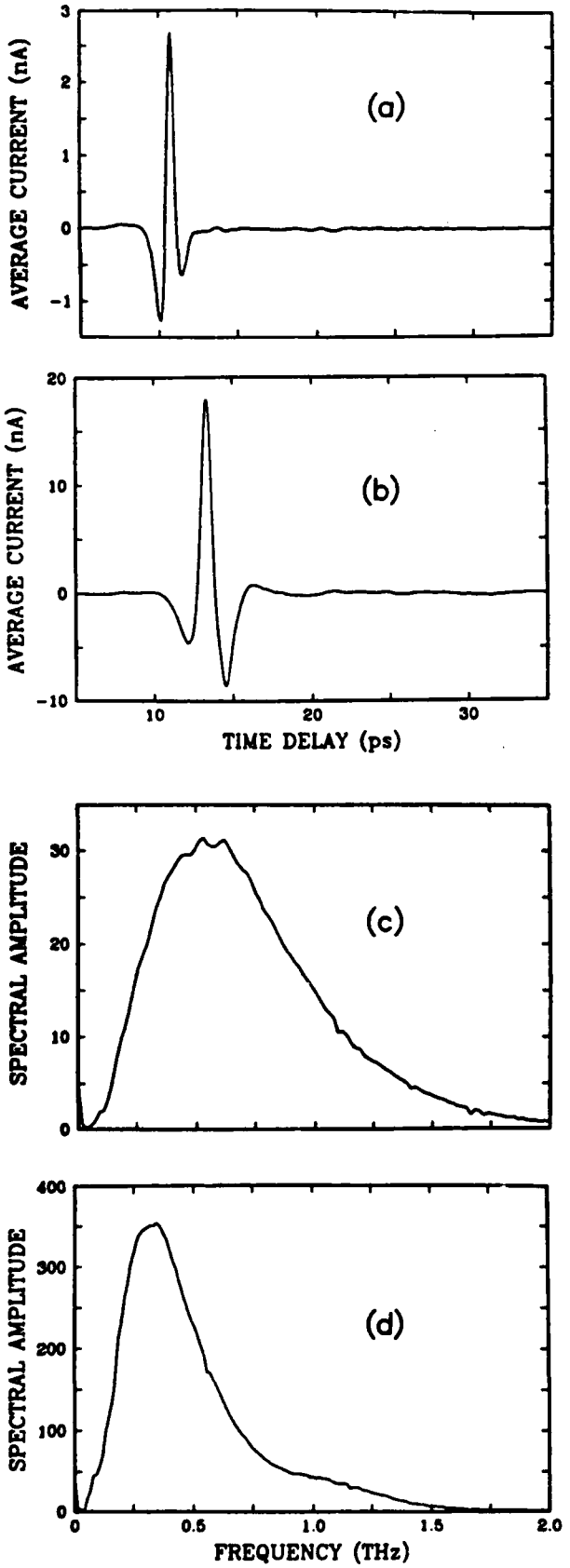

FIG. 2. (a) Terahertz pulse transmitted and detected with identical (10-30-10) antennas; (b) terahertz pulse generated with a (10-50-10) intrinsic GaAs transmitter and detected with a (10-120-10) implanted silicon receiver; (c) amplitude spectrum of (a); (d) amplitude spectrum of (b).

portional to the effective antenna length. The size of the transmitting antenna was increased to a (10-50-10) structure. The electromagnetic (EM) field radiated by a transient current is proportional to the time derivative of the current, in the far field and in the dipole approximation. Therefore, most terahertz radiation will be emitted during the fast rise time of the current transient and not during the slower fall time, being determined by the carrier lifetime of 0.6 ps in implanted silicon.[17] Experimentally, it proved to be advantageous to fabricate the transmitting antenna on an intrinsic GaAs wafer, instead of the usual ion-implanted SOS wafer. The use of GaAS increased the peak amplitude of the terahertz pulse by a factor of 5, together with a slight increase in bandwidth. The terahertz pulse measured with this (10-50-10) GaAs transmitter and a (10-120-10) implanted silicon receiver is shown as Fig. 2(b) and the related spectrum is shown as Fig. 2(d). In Figs. 2(c) and 2(d) the same units are used, showing the advantage of long antennas below 0.5 THz. Unfortunately, the slower speed of the long antennas limits the usefulness of the (cold) high-frequency transmission data to 1.5 THz.

The terahertz beam, propagating from transmitter to receiver, has a complicated cross section, because the low-frequency components are more spread out than the high-frequency components. To remove the outer edges, the terahertz beam was passed through a 20-mm-diameter hole in a thin metal sheet positioned between the transmitter and the receiver. This reduced the peak signal by less than 10% and allowed us tc use samples of moderate size. The room-temperature transmission measurements on doped silicon were performed by completely covering this circular hole by a flat wafer and monitoring the change in shape of the transmitted pulse. For the measurements at 80 K, a small dewar with crystalline quartz windows was centered between the transmitter and receiver. The metal sample holder inside the dewar also had a 20-mm-diameter opening. The reflection losses at the windows were 25% in total. The absorption of the two $\frac{3}{8}$-in.-thick crystalline quartz windows is small below 1 THz, but increases rapidly from about 15% at 1 THz to almost 50% at 1.5 THz. The dewar was a homemade liquid nitrogen container with a long cylindrical opening, in the middle of which the thin silicon wafer was mounted, using indium for thermal contact. The average equilibrium temperature of 80 K for our samples was measured for a typical cooling cycle of a thin silicon wafer, by a calibrated diode thermometer mounted at the center of the wafer.

In order to quantitatively explain the measurements on doped silicon, the index of refraction and absorption for undoped silicon was needed from 0.1 to 2.0 THz. Using time domain spectroscopy, we have measured these quantities with high precision for a 20-mm-thick piece of float-zone-refined, high-resistivity (10 kΩ cm) silicon. The index was found to be 3.415 (Ref. 2) and essentially constant over the entire frequency range, being in good agreement with the literature value of 3.416 at 1.0 THz.[18] Using a thinner piece of silicon that fit in our dewar, we determined the index of refraction at 80 K to be 3.386.[5] This change is in reasonable agreement with the radio-

frequency value of $\Delta n = -0.044$ (from 293 down to 77 K) mentioned in (Ref. 19) and $\Delta n = 0.000\,20\ \mathrm{K}^{-1}$ given in Ref. 20 (around 293 K at 25 cm^{-1}). The high-resistivity silicon was almost transparent over the entire frequency range, with a measured intensity absorption of less than 0.04 cm^{-1}.

MEASUREMENT EXAMPLE

We will now describe the results of transmission measurements on a 283-μm-thick, 25-mm-diameter wafer of 1.15 Ω cm, n-type silicon at room temperature. This serves as an example of the possibilities and problems associated with the system and demonstrates the method of analysis used for all six wafers (10, 1, and 0.1 Ω cm, n, and p type) at 293 as well as 80 K. For the other samples we will only present the final results. The pulse sequence transmitted through the 1.15 Ω cm, n-type silicon sample is shown in Fig. 3(a). The first transient is the primary pulse that passed directly through the sample. Its peak amplitude is about 40% of that of the original pulse. The output pulse amplitude and shape are changed due to reflection losses, and the frequency-dependent absorption and dispersion of the sample. The second and barely-resolvable third transients are terahertz pulses reflected inside the thin sample. Comparison of the Fourier transform of the single input pulse with that of the output pulse sequence from the doped silicon sample yields the frequency-dependent transmission, plotted as $-\ln[E_{\mathrm{out}}(\omega)/E_{\mathrm{in}}(\omega)]$ by the circles in Fig. 3(b). The multiple reflections are responsible for the oscillations in the frequency-dependent transmission of the wafer. Similar oscillations are also observed in the effective index of refraction obtained by division of the phase shift of the transmitted spectral components by the thickness of the wafer, which is plotted in Fig. 3(c) as circles. To include all these effects, we fit the measurements with a model for the transmission through a reflective, lossy parallel slab of material with frequency-dependent optical properties described by the Drude model. The solid lines in Figs. 3(b) and 3(c), are theoretical fits to the lossy slab model, using the two Drude parameters, the plasma angular frequency ω_p and the damping rate Γ. From the fit to the experimental data both ω_p and Γ could be determined within 10% accuracy, using the eye to judge the fit quality.

To facilitate interpretation of the data, we have removed the influence of reflections numerically, using the dielectric constant obtained from the Drude fit. The results of the corrections are shown as dots in Figs. 3(b) and 3(c) and do not depend critically on the fit parameters. The corrections are especially important for the very high frequencies, where the absorption is low and the interference fringes are strong, and for the very low frequencies, where the index of refraction becomes large. Below 0.15 THz the data becomes noisy due to the limited beam power, but the theoretically predicted minimum in the real part of the index of refraction followed by a dramatic rise towards low frequencies is clearly observable. Pure, high-resistivity silicon shows practically no absorption and hardly any frequency dependence of its index of refraction. Consequently, the observed strong frequency dependence for doped silicon is due to the carriers and not to the host crystal.

In Figs. 4(a) and 4(b) we have presented, respectively, the intensity absorption and the real part of the index of refraction for the discussed 1.15 Ω cm, n-type silicon (dots) and for 0.92 Ω cm, p-type silicon (circles) at 293 K. As the terahertz optical properties of the samples are largely determined by the carrier dynamics, we have indirectly measured the electric conductivity of the doped silicon. To link our measurements with electronics, the real part of the electric conductivity calculated from the optical data is shown in Fig. 4(c) and the imaginary part is shown in Fig. 4(d). The real part of the conductivity is strongly frequency dependent, dropping monotonically from its dc peak to the reduced value at the highest-measured frequency of 2 THz. In Table I the dc conduc-

TABLE I. Parameters used to fit the measurements in Figs. 4–8 with simple Drude theory. The columns indicate the wafer type p or n, the resistivity $1/\sigma_{\mathrm{dc}}$ (Ω cm) as measured by the four-point contact method at room temperature, the temperature T, the low-frequency resistivity $1/\sigma_{\mathrm{dc}}$ (Ω cm) as extrapolated from the fitted curves, the measured plasma frequency $\omega_p/2\pi$ (THz), the measured damping rate $\Gamma/2\pi$ (THz), and the resulting mobility μ (cm/V s) determined by Γ, and carrier density $N(\mathrm{cm}^{-3})$ determined by ω_p.

Type	$1/\sigma_{\mathrm{dc}}$	T	$1/\sigma_{\mathrm{dc}}$	$\omega_p/2\pi$	$\Gamma/2\pi$	μ	N
p	9.0	293 K	9.3	0.48	1.19	640	1.1×10^{15}
p	0.92	293 K	0.89	1.75	1.51	500	1.4×10^{16}
p	0.164	293 K					
n	8.1	293 K	8.2	0.36	0.59	1820	4.2×10^{14}
n	1.15	293 K	1.13	1.01	0.64	1680	3.3×10^{15}
n	0.129	293 K					
p	9.0	80 K	1.67	0.37	0.127	5960	6.3×10^{14}
p	0.92	80 K	0.42	0.92	0.198	3820	3.9×10^{15}
p	0.164	80 K	0.294	1.80	0.53	1430	1.5×10^{16}
n	8.1	80 K	1.45	0.33	0.088	12 200	3.5×10^{14}
n	1.15	80 K	0.32	0.78	0.107	10 100	2.0×10^{15}
n	0.129	80 K	0.180	2.00	0.40	2690	1.3×10^{16}

tivity extrapolated from the optical results is compared with a direct measurement at room temperature using the four-point contact method.[21] This independent check on the derived Drude parameters shows excellent agreement. The behavior of the imaginary part of the conductivity is completely different, increasing from zero at low frequencies, peaking at midrange and then showing a gradual decline. The calculation of the imaginary part of the conductivity depends critically on the thickness of the sample. For that reason the calculated value might be as

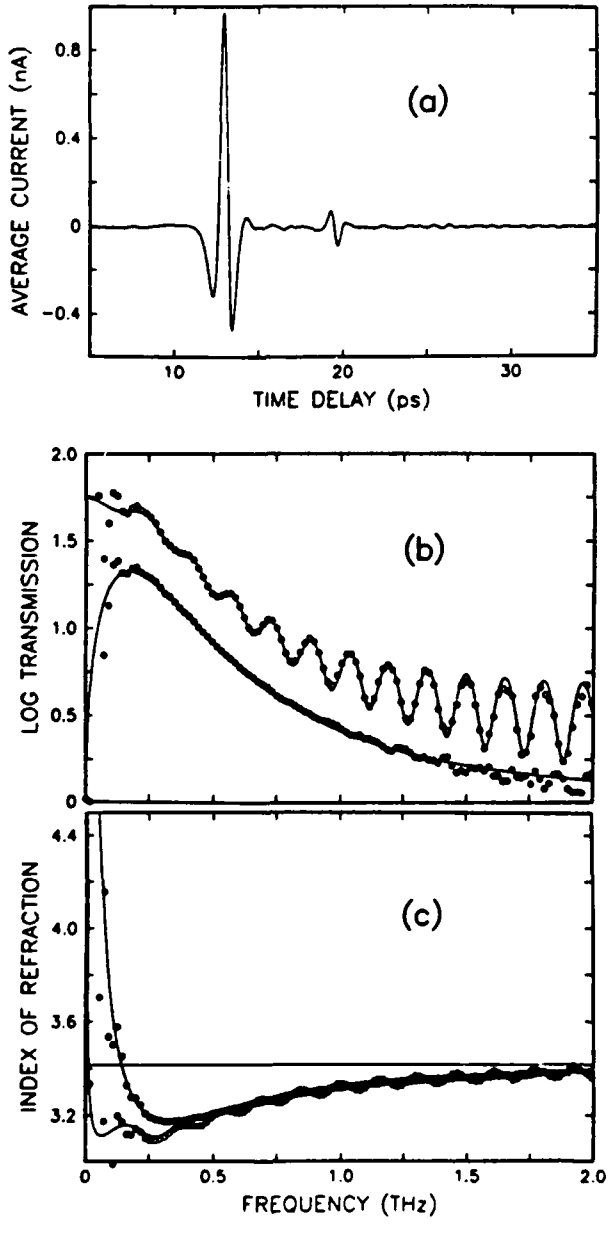

FIG. 3. (a) Terahertz pulse transmitted through a 283-μm-thick wafer of 1.15 Ω cm, n-type silicon at room temperature; (b) logarithm of the amplitude transmission for this sample (circles) and the amplitude transmission numerically corrected for reflections (dots); (c) effective index of refraction, derived by division of the measured phase shift of the transmitted terahertz pulses by the length of the sample (circles) and the index of refraction corrected for reflections (dots).

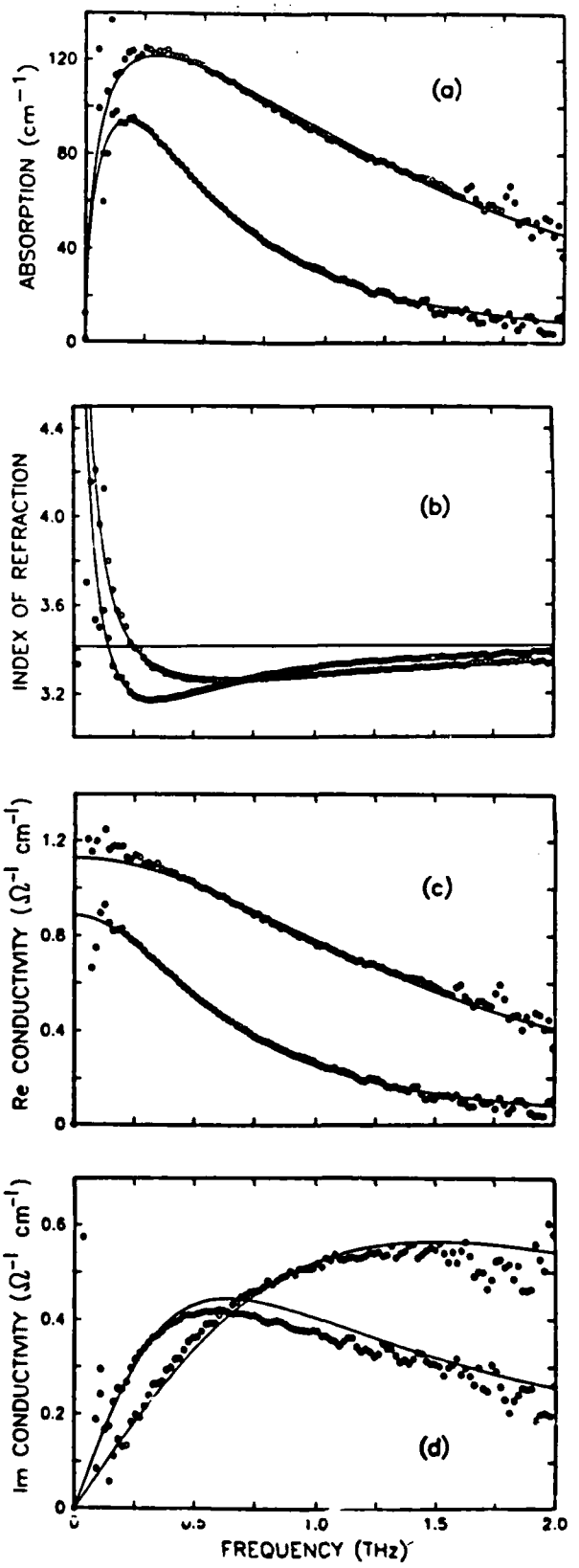

FIG. 4. Results for 1.15 Ω cm, n-type (dots) and 0.92 Ω cm, p-type (circles) silicon at room temperature. Solid lines describe simple Drude theory with parameters from Table I. (a) Intensity absorption; (b) real part of the index of refraction; (c) real part of the electric conductivity; (d) imaginary part of the electric conductivity.

much as 10% off from the actual value. Keeping this in mind, the agreement with the Drude theory of both the real and imaginary part of the conductivity is quite acceptable.

RESULTS

The measurements of 1 Ω cm, *p*- and *n*-type silicon immediately show the different dynamic behavior of the electrons and the holes. At room temperature the damping rate Γ in these moderately doped samples is mainly determined by carrier-phonon collisions,[2,4,22] a process that apparently is more efficient for holes than for electrons. The results for a 1.459-mm-thick disc of 8.1 Ω cm, *n*-type silicon and a 1.479-mm-thick disc of 9.0 Ω cm, *p*-type silicon are shown as Fig. 5 and are also presented in Table I. The damping rate in these samples was slightly less than in the 1 Ω cm samples. At room temperature the 260-μm-thick, 0.1 Ω cm silicon samples we investigated were practically opaque and showed an amplitude transmission of less than 0.1%. The transmitted pulses were too weak to analyze properly, and for room temperature the 0.1 Ω cm columns in Table I unfortunately remain blank.

Combining the measured damping rates with the effective carrier masses, yields mobilities of 1680 $cm^2V^{-1}s^{-1}$ for the electrons in the 1.15 Ω cm sample and 1820 $cm^2V^{-1}s^{-1}$ for the 8.05 Ω cm sample. These values are higher than the literature value, which is 1450 $cm^2V^{-1}s^{-1}$ for intrinsic silicon and decreases monotonically as the doping level increases.[13,23,24] Usually the carrier mobility is determined either directly in a time-of-flight experiment,[23] or via the Hall effect. Hall measurements should be used with care, because they determine the so-called Hall mobility, which differs from the (electric) mobility by the Hall factor. This factor depends on the ratio of longitudinal over transverse carrier mass, as well as on the model-dependent factor $\langle\tau^2\rangle/\langle\tau\rangle^2$, where $\langle\ \rangle$ signifies an average over the carrier distribution.[24,25] For the hole mobility we find 500 $cm^2V^{-1}s^{-1}$ for the 0.92 Ω cm sample and 640 $cm^2V^{-1}s^{-1}$ for the 9.0 Ω cm sample. These values are also higher than the literature value of 450 $cm^2V^{-1}s^{-1}$ for intrinsic silicon.[13] If we stick to the simple Drude model we are facing a clear disagreement between the damping rate extracted from the transmission experiments and the mobility extracted from other experiments. This discrepancy supports an energy dependence of the carrier collision time as will be discussed at the end of this paper.

The carrier density of the various samples can be easily calculated from the measured plasma frequency with the use of the literature value for the effective mass. The difference in plasma frequency between *p*- and *n*-type samples mainly reflects the larger doping needed in the *p*-type to compensate for the higher damping rate and get the same dc conductivity. The carrier densities we calculate are presented in Table I. They are rather low compared to the doping levels of 1.4×10^{15}, 1.8×10^{16}, and 2.9×10^{17} cm^{-3} for the 10, 1, and 0.1 Ω cm, *p*-type silicon, respectively, and 7.0×10^{14}, 4.6×10^{15}, and 6.6×10^{16} cm^{-3} for the 10, 1, and 0.1 Ω cm, *n*-type sil-

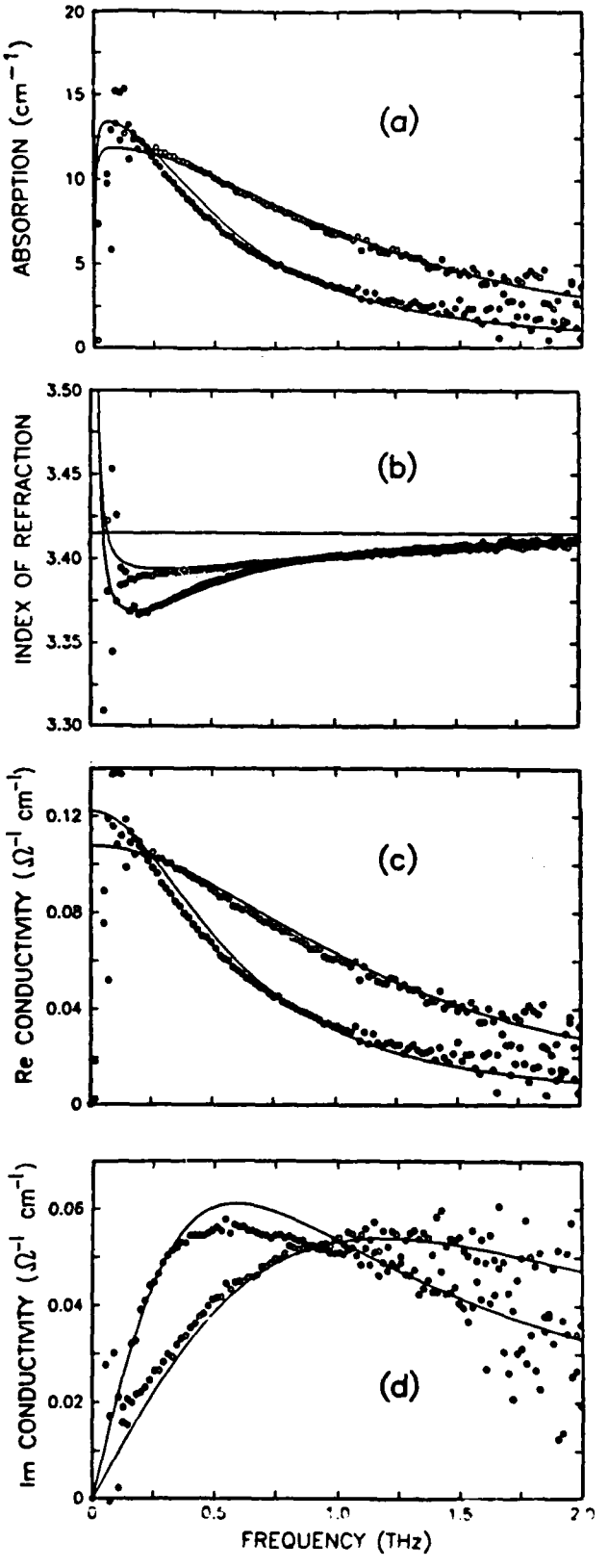

FIG. 5. Results for 8.1 Ω cm, *n*-type (dots) and 9.0 Ω cm, *p*-type (circles) silicon at room temperature. Solid lines describe simple Drude theory with parameters from Table I. (a) Intensity absorption; (b) real part of the index of refraction; (c) real part of the electric conductivity; (d) imaginary part of the electric conductivity.

icon, given by the manufacturer (Virginia semiconductor) with an error margin of 20%.

It is interesting to point out that σ_{dc}, calculated from the relationship $\sigma_{dc}=e\mu N$ with μ and N obtained from Table I, agrees exceptionally well with both σ_{dc} obtained by extrapolating the $\mathrm{Re}\sigma(\omega)$ curve and σ_{dc} as measured by the four-probe method. Thus, with respect to the above comments concerning μ and N, it appears that the simple Drude model overestimates μ, but that it underestimates N by the same percentage. The end result is that σ_{dc}, is given accurately.

Figures 6–8 show the results of terahertz transmission measurements on the previously mentioned doped silicon samples at the cryogenic temperature of 80 K. At this temperature the average amplitude transmission of the 0.129 Ω cm, *n* type and the 0.164 Ω cm, *p*-type sample has risen to about 4% and can now be easily analyzed. Upon cooling, the spectral features of all the samples have shifted to lower frequencies and the frequency dependence has become even more pronounced. The peaks have increased and sharpened and the minima have deepened and narrowed. At the highest measured frequency of 1.5 THz, the optical effects due to the carriers are monotonically disappearing in the 10 and 1 Ω cm samples. Upon cooling the dc conductivity of the 10 and 1 Ω cm samples have increased, while the falloff towards increasing frequency has steepened. However, for the 0.1 Ω cm samples, due to their proportionally more severe carrier trapping at the dopant, the conductivities have significantly decreased. The Drude parameters derived from these measurements are presented in Table I. The slower carrier dynamics is reflected in the strong reduction in damping rate Γ. The decrease in plasma frequency signifies a reduction in carrier density N related to carrier trapping at the dopant. For all the samples the measured decrease in N agrees well with that calculated due to the change in temperature and the corresponding shift of the Fermi level, using a value of 45 meV for the ionization energy of both the phosphorus dopant used in *n*-type silicon and the boron used in *p*-type silicon.[13]

The quality of the Drude fit for the cold samples is not as precise as for the room temperature samples. The deviations are best observed for the *p*-type material. For the 10 Ω cm silicon the index of refraction dropped more than expected and did not show the usual increase towards low frequencies [Fig. 6(b)], perhaps due to the large increase in noise below 0.1 THz. For the 1 Ω cm, *p*-type silicon (Fig. 7), the measured absorption at high frequencies is larger than predicted by the Drude model, while it is slightly less at lower frequencies. Additionally, the measured minimum in the index of refraction, plotted in Fig. 7(b), comes at a lower frequency than expected from the Drude model. For the more heavily doped 0.1 Ω cm silicon the same deviations from the Drude model show up, but are more severe (Fig. 8). The deviations between the theoretical curves and the measurements could not be removed through variation of the two fit parameters, which should also fit both the absorption and the index of refraction data. The deviations are reproducible from run to run and thus signify a disagreement with the simple Drude model for the cold samples. This

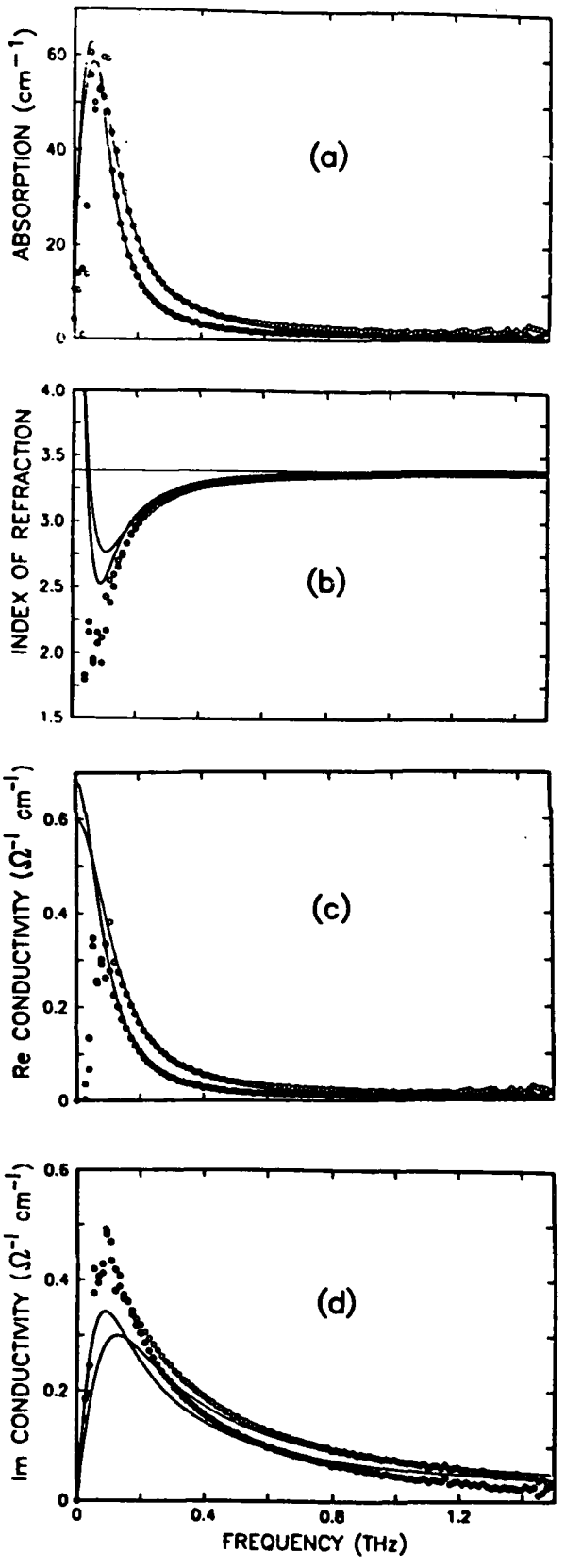

FIG. 6. Results for 8.1 Ω cm, *n*-type (dots) and 9.0 Ω cm, *p*-type (circles) silicon at 80 K. Solid lines describe simple Drude theory with parameters from Table I. (a) Intensity absorption; (b) real part of the index of refraction; (c) real part of the electric conductivity; (d) imaginary part of the electric conductivity.

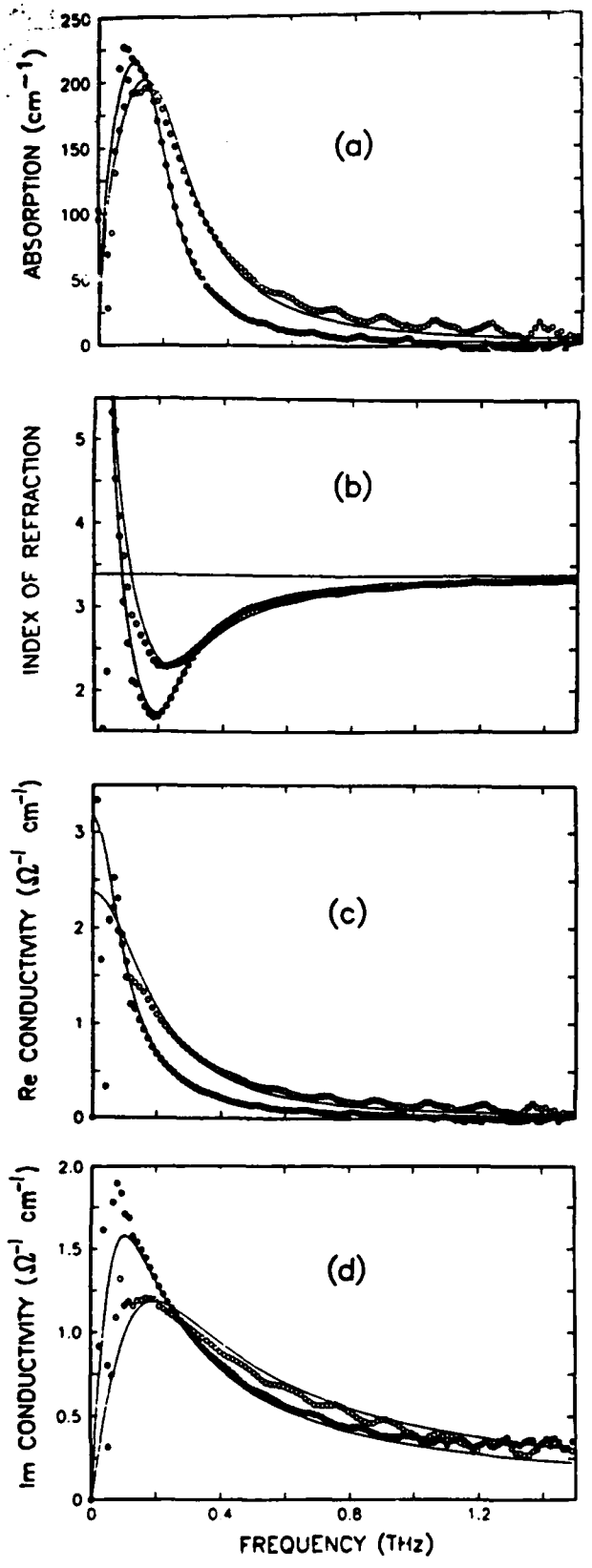

FIG. 7. Results for 1.15 Ω cm, *n*-type (dots) and 0.92 Ω cm, *p*-type (circles) silicon at 80 K. Solid lines describe simple Drude theory with parameters from Table I. (a) Intensity absorption; (b) real part of the index of refraction; (c) real part of the electric conductivity; (d) imaginary part of the electric conductivity.

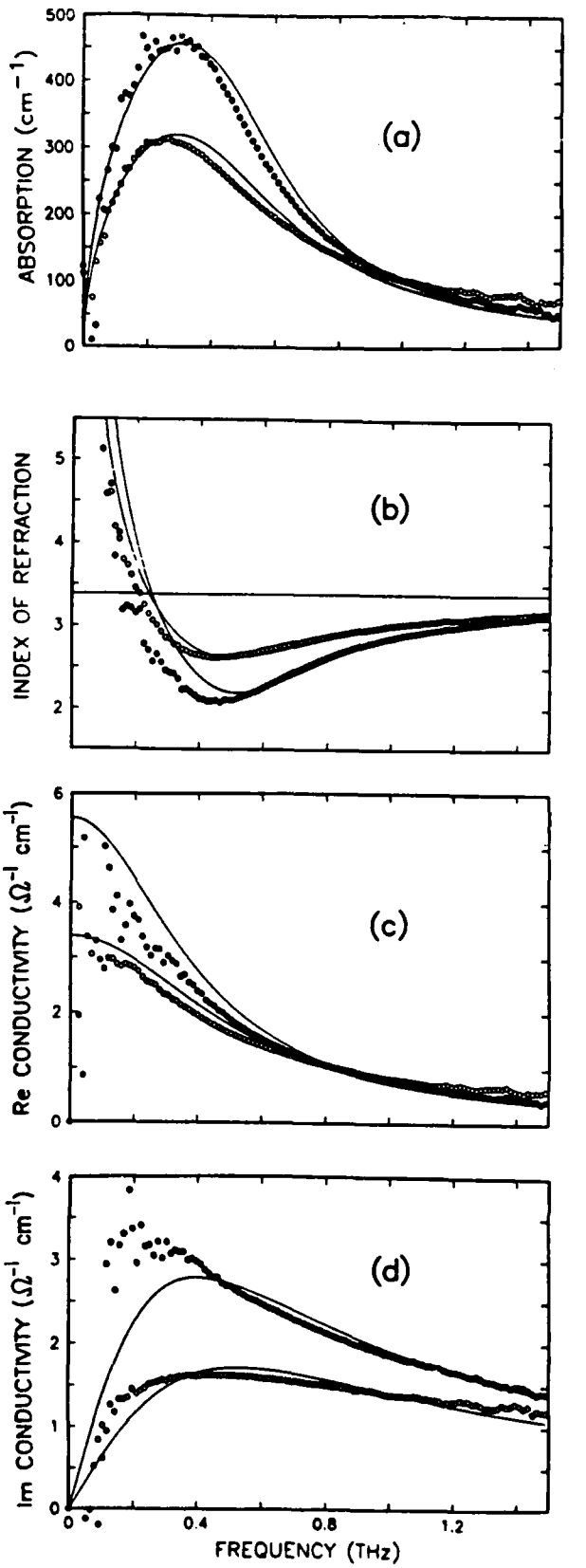

FIG. 8. Results for 0.129 Ω cm, *n*-type (dots) and 0.164 Ω cm, *p*-type (circles) silicon at 80 K. Solid lines describe simple Drude theory with parameters from Table I. (a) Intensity absorption; (b) real part of the index of refraction; (c) real part of the electric conductivity; (d) imaginary part of the electric conductivity.

discrepancy is considered to be due to an energy dependence of the collision time. In the following section we will briefly discuss an extended model for the carrier dynamics, which distinguishes between scattering with phonons and scattering with ionized impurities. A complication we will not take into account is the existence of both light holes and heavy holes and holes in the splitoff valence band, all of which may display a different dynamic behavior.

EXTENDED MODEL AND CONCLUSIONS

Many sophisticated models have been developed to give a more accurate description of the carrier dynamics that goes beyond the simple Drude model.[2,4,25–31] In these models the carrier relaxation is split into both intervalley and intravalley phonon scattering and scattering with the ionized impurities. Additionally, the interaction with the lattice is split into scattering from acoustic phonons and optic phonons. The many parameters involved make these extended models complicated to work with. Consequently, as a first-order approximation, we have analyzed our data with the more transparent simple Drude model.

We will now discuss the qualitative changes resulting from the energy dependence of the carrier relaxation. Theory predicts[27,28,32] that the efficiency of electron-phonon collision increases with the carrier energy to the power 0.5, because the mean free path for electron-phonon interaction is independent of carrier energy. In contrast, the carrier scattering from ionized impurities is more efficient at lower energies, scales roughly as the carrier energy to the power -1.5, and will dominate at low temperatures.[27,28,32] The damping rate of carriers with energy E relative to the extreme of the band is thus given by

$$\Gamma(E)=\Gamma_l(E/kT_0)^{0.5}+\Gamma_i(E/kT_0)^{-1.5}\,,$$

where the coupling constants Γ_l and Γ_i characterize the efficiency of scattering with the lattice and the ionized impurities, respectively, and depend on temperature and doping. T_0 is a normalization parameter, with the dimension temperature. In this way both Γ_l and Γ_i have the same dimension as the energy-independent damping rate used in the simple Drude model. The optical and electric properties of the doped semiconductor can now be evaluated by using the Drude result for each carrier energy and integrating over the conduction (or valence) band, as shown by the three examples in Figs. 9(a)–9(d). Using the Boltzmann transport equation one can show that,[5,28,29,32]

$$\sigma=\sigma_{dc}\left\langle\frac{i\Gamma(E)}{\omega+i\Gamma(E)}\right\rangle=i\epsilon_0\omega_p^2\left\langle\frac{1}{\omega+i\Gamma(E)}\right\rangle\,,$$

where $\langle\ \rangle$ denotes an average weighted by the product of the distribution of the carriers times their energy. For a parabolic band the weight factor is $E^{1.5}e^{-(E/kT)}$. The dc conductivity is given by $\sigma_{dc}=(e^2N/m)\langle 1/\Gamma\rangle$ and the relation between σ and ϵ remains unchanged.

Inserting the energy-dependent damping rate into the equation for the frequency-dependent conductivity, one

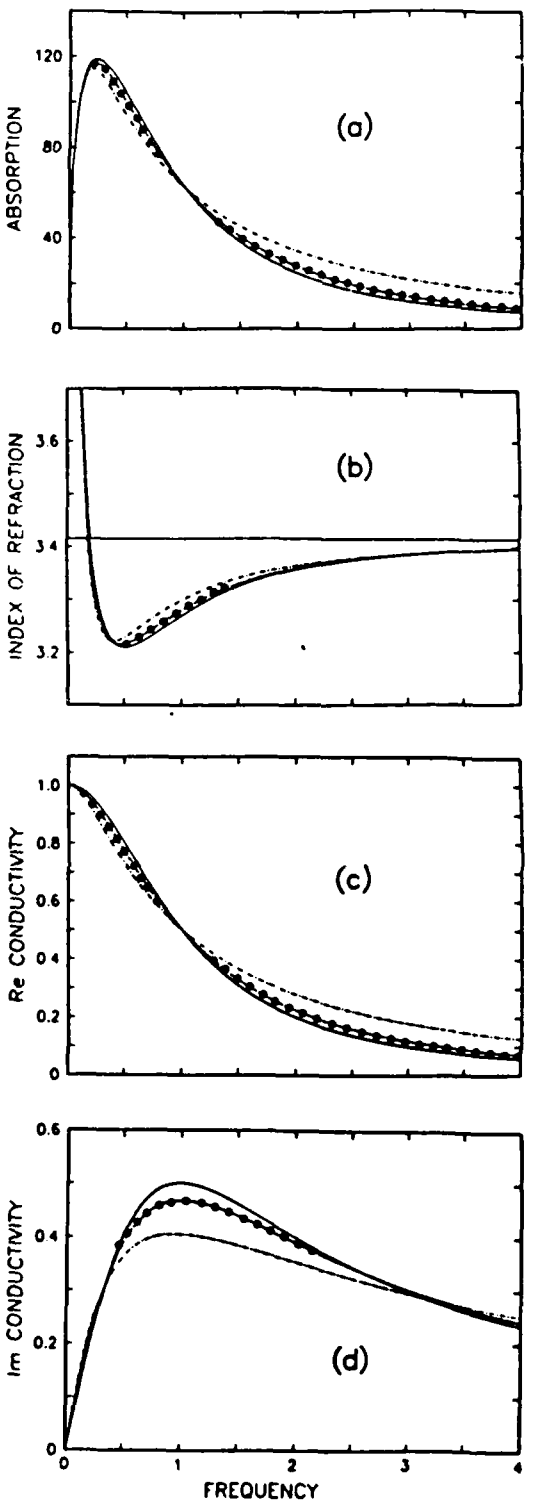

FIG. 9. Calculated optical and electronic properties for three different models for the carrier dynamics. The simple Drude model with an energy-independent damping rate is indicated by the solid line. The dotted curve describes phonon scattering only, with $\Gamma(E)$ proportional to $E^{0.5}$. The dashed curve describes scattering with impurities, with $\Gamma(E)$ proportional to $E^{-1.5}$. The coupling constants and carrier densities are adjusted to give identical dc conductivities and similar half-widths for the curves of $\mathrm{Re}\sigma(\omega)$; (a) intensity absorption; (b) real part of the index of refraction; (c) real part of the electric conductivity; (d) imaginary part of the electric conductivity.

can evaluate certain universal curves[4] for, e.g., the $\mathrm{Re}\sigma(\omega)$ versus ω relation. The scaling behavior of this function is simple, and it is easily adjusted to a specific case. A change in carrier density, e.g., only affects the conductivity axis, but leaves the frequency dependence untouched. If both coupling constants are increased by the same factor, the $\mathrm{Re}\sigma(\omega)$ versus ω curve flattens out, but retains its specific shape. The three curves in Fig. 9(c) show the calculated real part of the conductivity for the simple Drude model, for phonon scattering only ($\Gamma_l=0.8, \Gamma_i=0$) and for impurity scattering only ($\Gamma_l=0, \Gamma_i=6.8$). Both axes are in arbitrary units, but can be easily adjusted to a specific case as explained above. The coupling constants Γ_l and Γ_i were adjusted to give the same half-width for the three curves. The area under the $\mathrm{Re}\sigma(\omega)$ versus ω curve is directly proportional to the carrier density and independent of the functional dependence of the carrier damping rate. It is interesting to note that we had to increase the carrier density by 6% for the pure phonon-scattering process and by as much as 51% for the pure impurity scattering case to obtain the same dc conductivity as in the simple Drude model. This shows that when real data, which presumably includes both phonon and impurity scattering, is fit with a simple Drude model, using the dc conductivity and the half-width as fit criteria, one will always underestimate the carrier density and thereby overestimate the mobility. This is in agreement with our results for the room-temperature samples. In the Figs. 9(a), 9(b), and 9(d), we have plotted the other terahertz properties for the same three cases. The deviations from the simple Drude model are most dramatic for pure impurity scattering and are qualitatively similar to the deviations observed in the experimental data, being most dramatic for the 80-K 0.1 Ω cm silicon. The absorption is too small at low frequencies and too large at high frequencies, and the minimum in the index of refraction comes at lower frequencies than expected from the Drude theory, while it is slightly high in the midfrequency range. A careful inspection of the room-temperature data shows similar, but much smaller, deviations. This gives us confidence that time-resolved spectroscopy in the frequency range from 0.1 to 2 THz is a very sensitive method to study the dynamics of carriers in semiconductors, allowing one to separate and individually observe their various relaxation channels.

ACKNOWLEDGMENTS

We acknowledge informative discussions with Søren Keiding and the excellent masks and wafer fabrication by Hoi Chan. This research was partially supported by the U.S. Office of Naval Research.

[1]W. G. Spitzer and H. Y. Fan, Phys. Rev. **106**, 882 (1957).
[2]J. D. Holm and K. S. Champlin, J. Appl. Phys. **39**, 275 (1968).
[3]S. J. Allen, Jr., D. C. Tsui, and F. DeRosa, Phys. Rev. Lett. **35**, 1359 (1975).
[4]M. Vindevoghel, J. Vindevoghel, and Y. Leroy, Infrared Phys. **15**, 161 (1975).
[5]N. W. Ashcroft and N. D. Mermin, *Solid State Physics* (Holt, Rinehart, and Winston, New York, 1976).
[6]R. T. Kinasewitz and B. Senitzky, J. Appl. Phys. **54**, 3394 (1983).
[7]T. Ohba and S. Ikawa, J. Appl. Phys. **64**, 4141 (1988).
[8]Ch. Fattinger and D. Grischkowsky, Appl. Phys. Lett. **53**, 1480 (1988); **54**, 490 (1989).
[9]M. van Exter, Ch. Fattinger, and D. Grischkowsky, Appl. Phys. Lett. **55**, 337 (1989).
[10]M. van Exter, Ch. Fattinger, and D. Grischkowsky, Opt. Lett. **14**, 1128 (1989).
[11]M. van Exter and D. Grischkowsky, IEEE Trans. Microwave Theory Tech. (to be published).
[12]W. P. Dumke, Phys. Rev. **124**, 1813 (1961).
[13]S. M. Sze, *Physics of Semiconductor Devices* (Wiley, New York, 1981).
[14]R. N. Dexter, H. J. Zeiger, and B. Lax, Phys. Rev. **104**, 637 (1956).
[15]G. Ottaviani, L. Reggiani, C. Canali, F. Nava, and A. Albergi-Quaranta, Phys. Rev. B **12**, 3318 (1975).
[16]H. Miyazawa, K. Suzuki, and H. Maeda, Phys. Rev. **131**, 2442 (1963).
[17]F. E. Doany, D. Grischkowsky, and C. C. Chi, Appl. Phys. Lett. **50**, 460 (1987).
[18]E. V. Loewenstein, D. R. Smith, and R. L. Morgan, Appl. Opt. **12**, 398 (1973).
[19]M. Cardona, W. Paul, and H. Brooks, in *Solid State Physics in Electronics and Telecommunications, Proceedings of the International Conference on Solid State Physics in Electronics and Communications, Brussels, 1958,* edited by M. Desirant and J. L. Michiels (Academic, London, 1960), Vol. 1, p. 206.
[20]J. R. Birch, Infrared Phys. **18**, 613 (1978).
[21]L. B. Valdes, Proc. IRE **42**, 420 (1954).
[22]C. Jacoboni, C. Canali, G. Ottaviani, and A. Alberigi-Quaranta, Solid State Electron. **20**, 77 (1977).
[23]M. B. Prince, Phys. Rev. **92**, 681 (1953), **93**, 1204 (1954).
[24]F. Mousty, P. Ostoja, and L. Passari, J. Appl. Phys. **45**, 4576 (1974).
[25]C. Herring and E. Vogt, Phys. Rev. **101**, 944 (1956).
[26]D. Long and J. Myers, Phys. Rev. **120**, 39 (1960).
[27]D. Long, Phys. Rev. **120**, 2024 (1960).
[28]J. M. Ziman, *Electrons and Phonons* (Oxford University Press, London, 1960).
[29]P. A. Schumann, Jr. and R. P. Phillips, Solid State Electron. **10**, 943 (1967).
[30]P. K. Basu and B. R. Nag, Phys. Status Solidi B **53**, K61 (1972).
[31]E. Barta, Infrared Phys. **17**, 111 (1977).
[32]R. A. Smith, *Semiconductors* (Cambridge University Press, London, 1959).